Biofunctionalisation of calcium phosphate nanoparticles for applications in molecular biology and biomedicine

A dissertation submitted to

the Faculty of Chemistry

at the

University of Duisburg-Essen

in attainment for the academic degree of

doctor of natural science

–Dr. rer. nat.–

Duisburg-Essen

by

M. Sc. Mathis Kopp

born in Kamen

Faculty of Chemistry at the University of Duisburg-Essen

Institute for Inorganic Chemistry

Germany

„ To My Lovely Wife and her Parents “

Autor	Mathis Kopp, geb. Nitschke
	geboren am 22.11.1985 in Kamen (Westf.)
Angefertigt an	Universität Duisburg-Essen
	Fakultät für Chemie
	Institut für Anorganische Chemie
	Prof. Dr. M. Epple

Bearbeitungszeit	Januar 2015 – Dezember 2017

Gutachter	Prof. Dr. Matthias Epple
	Prof. Dr. Shirley Knauer
Prüfungsvorsitzender	Prof. Dr. Oliver J. Schmitz

Tag der Disputation	04.06.2018

“The most beautiful experience we can have is the mysterious. It is the fundamental emotion that stands at the cradle of true art and true science.”

— Albert Einstein

Contents

List of figures

1 Introduction

Since its conceptual foundation in 1959 by Richard Feynman, the field of nanotechnology has experienced a dramatical acceleration in the history of human mankind.[1] Even in the last decades, it has evolved into a widely encompassing technology that is involved in nearly every field of scientific research and the daily human life. Nanotechnology finds many applications in the metal and alloying industry and microchip fabrication, and has entered the sectors of the health, hygienic and cosmetic market of daily products. The main reason for this broad applicable range is that materials with nanoscale features present unique characteristics, otherwise absent at a macroscopic level.[2] To give an idea about this, the prominent example of finely distributed colloidal dispersions of spherical gold nanoparticles (<100 nm) can emit fluorescence of different wavelengths where colours ranging from violet to red of the visible spectra. It is also famous for its surface plasmon resonance absorbance at 525 nm, whereas gold as bulk material show none of these properties.[3,4] Such nanoparticular materials range on a scale from 1 to 100 nm in diameter, which is one billionth of a meter ($1 \cdot 10^{-9}$ m). More than 150,000 nanotechnology-related scientific research articles have been published worldwide in 2016.[5] This immense number highlights and reflects the high interest and the importance of this technology. Understandably, nanotechnology is considered to be the answer of mankind's future problems, solving those problems of the next decades of the 21st century. Indeed, the research and innovation department of the European Commission published the successfully accomplished research projects in nanomaterials, nanoelectronics and nanomedicine, giving answers to many of the major problems of the future. Especially the young science nanomedicine has drawn much attention since its evolvement in the 1990´s. It is a modern multi-interdisciplinary rapidly growing scientific research field driven by a tremendous progress in techniques derived from the development of an array of ultramicroscopic devices and studies of cellular molecular and finally atom-sized structures in biology, chemistry and physics in the 20th century.[6] Today, nanomedicine comprises many applications, including nanoimaging, lab-on-a-chip for nano-diagnostic, nanocapsules for complementary cancer treatment with hyperthermia, thermoablation and radiotherapy methods. Especially, the biocompatible nanomaterials, e.g. liposomes,

calcium phosphate nanoparticles as drugs, vaccines and gene vehicles for therapy have caught significant interest.[6] However, these are only a few examples of what nanotechnology may be capable of. The future direction for this paramount section in science and medical treatment is remains to be promising and multifaceted.[6] For instance, in the last decade inorganic calcium phosphate nanoparticles (CaP) have drawn notable attention due to their possible application in nano- and biomedicine as biocompatible, biodegradable and low toxic nanocarriers for vaccinations (against viral infections), targeted drug delivery, nano-imaging, photodynamic therapy (PDT) and gene modulating purposes (gene silencing and transfection).[7-11] This work is primarily focused on the synthesis, characterisation of bio-functionalised calcium phosphate nanoparticles and their use in molecular biology and biomedical applications considering the range of functionalisation possibilities and behaviour in cell culture. This work is further focusing on the cellular uptake of calcium phosphate nanoparticles and investigate their role as a tool for cell targeting, protein delivery, vaccination or transfection.

2 Theory

In the following section, the theoretical background of this thesis is described to provide the reader with the necessary knowledge to be able to follow the performed experiments and subsequent explanations. In the first chapter, the principles of colloidal chemistry are discussed. The second chapter will give an overview into calcium phosphate particles and explain their application in nanomedicine and biomedicine. Further chapters are focussed on the different biological disciplines and methodologies that are related to this work.

2.1 Colloidal chemistry

2.1.1 Colloids

The term colloid describes a fine dispersion in one of the three physical fundamental states in another one (i.e. solid/liquid, gas/liquid, solid/solid) and is called colloidal system. A dispersion is a heterogeneous mixture of at least two chemically inactive substances, which are not or only hardly soluble in each other. Herein, one or more substances (disperse phase) are finely divided into another continuous substance (continuous phase).[12] The IUPAC describes a dispersion as a "*material comprising more than one phase where at least one of the phases consists of finely divided phase domains, often in the colloidal size range, dispersed throughout a continuous phase*".[13] Various examples of colloidal systems are known that include aerosols, emulsions, colloidal suspensions and association colloids.[14,15] Bone, a bio-colloid, for example is a dispersion of apatite (disperse phase) and collagen (continuous phase). Within a colloidal system, like nanoparticles dispersed in water, the colloidal stability of a dispersion is influenced by different processes.[12,16] From a stable colloidal dispersion, the system may destabilise through particle adhesion, forming aggregates of successively increasing size, which settle out by gravity force.[16] Alternatively, instead of aggregate formation, the system stability can also be disrupted by gravity influenced sedimentation. The process of the initial aggregate formation is called flocculation, while the aggregate is called a floc.[16] A floc can further coagulate and finally separate into two phases by sedimentation. The flocculation process is reversible, whereas a coagulated system ends in its phase separation, depending on the aggregate changes to a much denser form. The aggregates usually separate out,

if they are more dense than the continuous phase, by sedimentation or if they are less dense than the medium by creaming (Figure 2-1).[16]

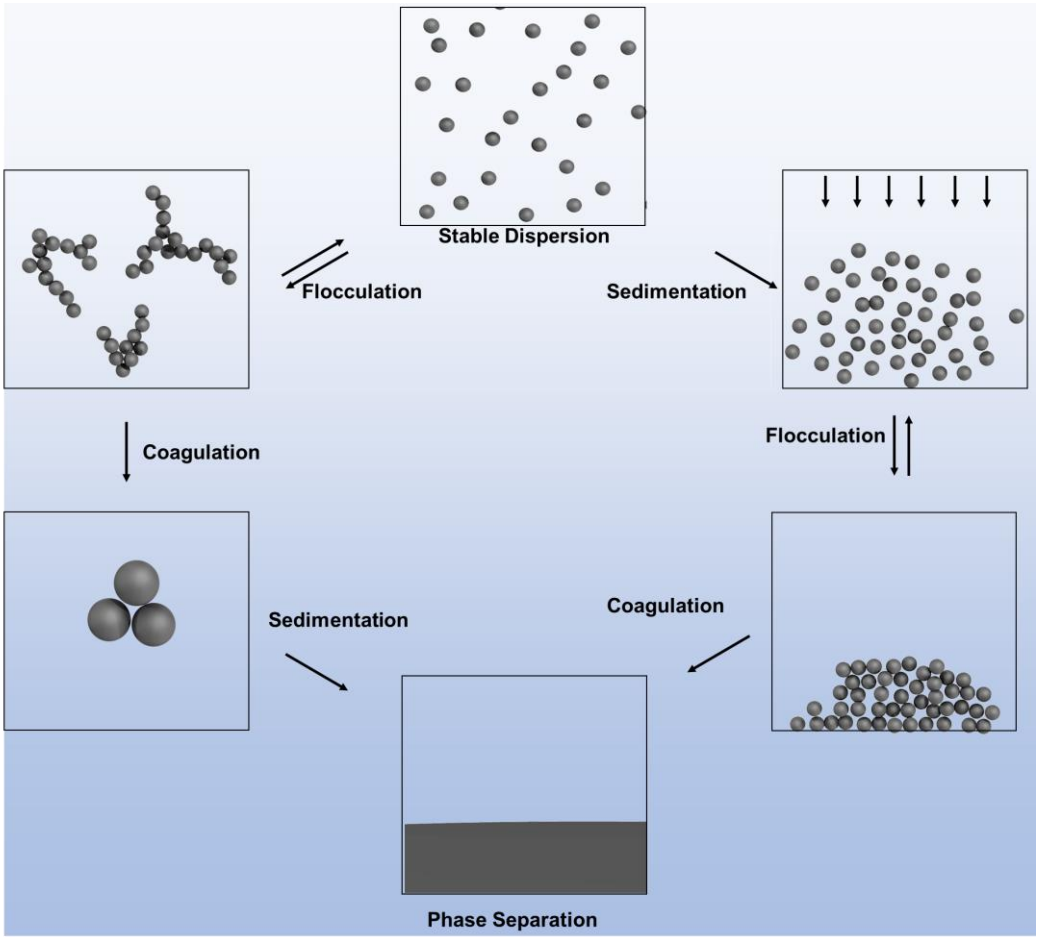

Figure 2-1: Processes influence the colloidal stability.
From a stable dispersion, the system can be either destabilised by flocculation or sedimentation. Flocculation is a reversible process. Thus, flocculated systems can be returned into a stable colloidal system. Coagulated systems end in the phase separation of the system.

2.1.2 Colloidal stability and DLVO theory

The colloidal stability of a particle dispersion can be described by the DLVO theory. The DLVO theory was first developed by Boris Derjaguin. It was then extended together with Lev Landau and later with Evert Verwey and Jan Overbeek (DLVO).[17-19] The theory describes the interactions between colloid particles, including Brownian motion, gravity, convection and Van der Waals forces, and their aggregation behaviour.[20] This theory can also be applied on nanoparticles and reflects the cornerstone of understanding the prevailing interactions within a colloid system.[20] Furthermore, this theory is also being used to rationalise the interacting forces acting between interfaces or planar substrates to interpret particle deposition to planar substrates.[20] Initially, the theory was formulated for symmetric systems of two identical surfaces, corresponding to the case of the homoaggregation which reflects the aggregation of identical particles.[20] The asymmetric case of this concept, the aggregation for different particles (heteroaggregation) was later extended to the two different interfaces.[20]

In general, the DLVO theory assumes that the stability of a colloid or particle dispersion is given by the total potential energy of all interacting forces. The colloidal system between two particles is then given as the sum of the different interacting forces and can be described as a function of their potential energy:

$$V_T = V_D + V_H + V_S \qquad \text{Eq. 1}$$

With V_T: total potential energy; V_D: repulsive electrostatic potential energy (Debye-Term); V_H: Hamaker potential or attractive Van der Waals potential energy and V_S: steric potential.

This equation reflects the particles 'potential energy depending on the separation distance to each other.

The attractive Van der Waals potential is given as:

$$V_H = -\frac{A_{12}\, r}{12 x k_B T} \qquad \text{Eq. 2}$$

With A: Hamaker constant; *r*: radius of the particles; *x*: distance between the particles' surfaces; k_B: Boltzmann constant and *T*: temperature.

The double layer repulsive force is considered by the repulsive electrostatic potential energy which is given by:

$$V_D = \frac{2\pi e_0 \varepsilon r \varphi^2 \ln\left(1+e^{-\frac{x}{k^{-1}}}\right)}{(k_B T)} \qquad \text{Eq. 3}$$

With e_0: permittivity of free space; ε: dielectric constant of the solvent; φ: surface potential; k_B: Boltzmann constant; *T*: temperature; k^{-1}: a function of the ionic strength; *I* also known as the Debye length which considers the charge carrier's net electrostatic interactions in solution, and how far those electrostatic interactions persist.[21]

$$k^{-1} = \sqrt{\frac{\varepsilon_0 \varepsilon k_B T}{2 N_A e^2 I}};\ I = \sum_{j=1}^{n} c_j z_j^2 \qquad \text{Eq. 4-5}$$

With N_A: Avogadro number; e: elementary charge; *c*: molar concentration; *z*: charge of ion; *j*: ion identification number.

The last term V_S of Eq. 1 is the potential energy due to the solvent. It usually only makes a marginal contribution to the total potential energy over the last few nanometres of separation and also reflects the steric interaction between the particles within a solvent.[16] It is given as follows :

$$V_S = 30 N_A 4\pi \frac{r\Gamma^2 (0.5-\chi)\left(1-\frac{x}{2\delta}\right)^2}{(\rho^2 \mathrm{MVol})} \qquad \text{Eq. 6}$$

With Γ: Absorbed weight; χ: Flory-Huggins term; δ: layer thickness; ρ: density of the particles; MVol: molar volume.

By plotting the three different potential energies, scenarios influencing the colloidal stability can be described (Figure 2-2).

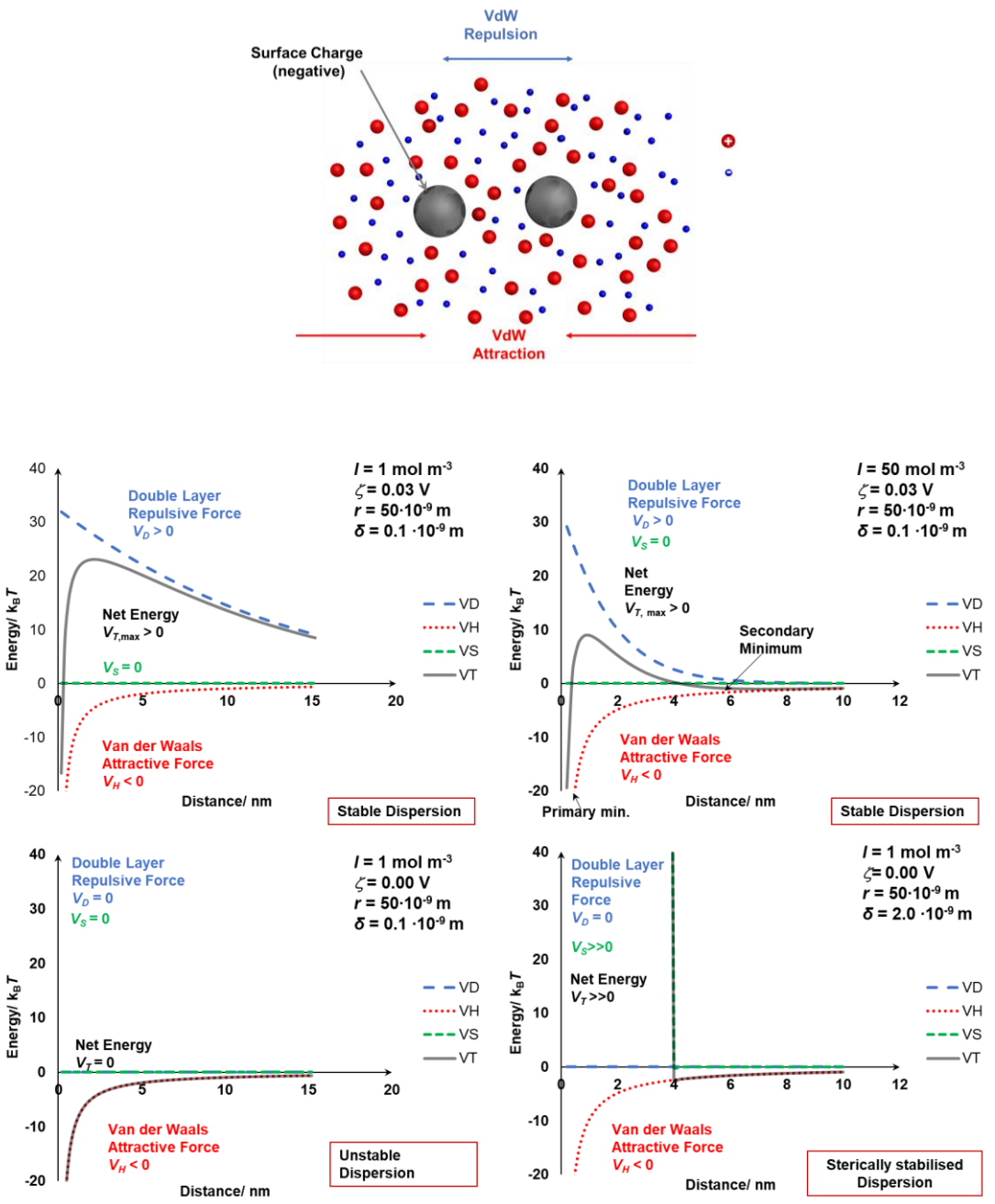

Figure 2-2: Schematic interaction of two particles in a solvent and DLVO plots with different colloidal conditions.

I: ionic strength, ζ: zeta potential, r: particles radius, δ: Debye length. Four different cases of colloidal instability and stability. Upper left, dispersion is stabilised by repulsive forces (marked as grey line). Upper right, ionic strength is highly increased, and the steric potential V_S is decreased to zero, leading to the stabilisation of the colloidal system by attractive (secondary minimum) and repulsive attraction to a certain distance. Lower bottom left, predominating attractive forces between two particles directing the colloidal system to collapse (agglomerate). Lower bottom right, the steric potential is much larger than zero. This is the case when molecules e.g. a stabilising branched polycation demands much steric space.

In a stable dispersion, the particles that have a sufficiently high repulsion force will resist flocculation, due to the fact that the net energy barrier is too high to overcome. If two particles are brought together too close to each other, e.g. by increasing the temperature or increasing the ionic strength, the Van der Waals attractive forces will lead to a destabilisation of the colloidal system by the incoming contact of both particles and the dispersion starts to flocculate. It is well accepted that a dispersion with a repulsion energy barrier of 25 $k_B T$ is stable.[22] In a particular case, where the ionic strength is increased, it is possible to create a secondary stabilising minimum. In a system where no repulsion forces (V_D = 0) are present, the colloidal system will collapse and lead to phase separation. A colloidal system can also be sterically stabilised. In that case, the layer thickness of each particle is much larger, resulting in a steric hindrance and repulsion of each particle to another. This case is also realised by using polycationic polymers e.g. polyethyleneimine or carboxymethyl cellulose to stabilise calcium phosphate nanoparticles.[23,24]

Therefore, in a colloidal system there are two general mechanisms that counteract the attractive Van der Waals attraction forces. On one hand, particles in a colloidal system can be stabilised by coating them with steric exigent polymers which prevent them from agglomeration. In the case of a charged polymer the particles can also be stabilised by the electrostatic repulsion. The electrostatic stabilisation of two equally charged particles is the balance between the attraction and repulsion of the electrical double-layer surrounding each particle (Figure 2-3).[23,24]

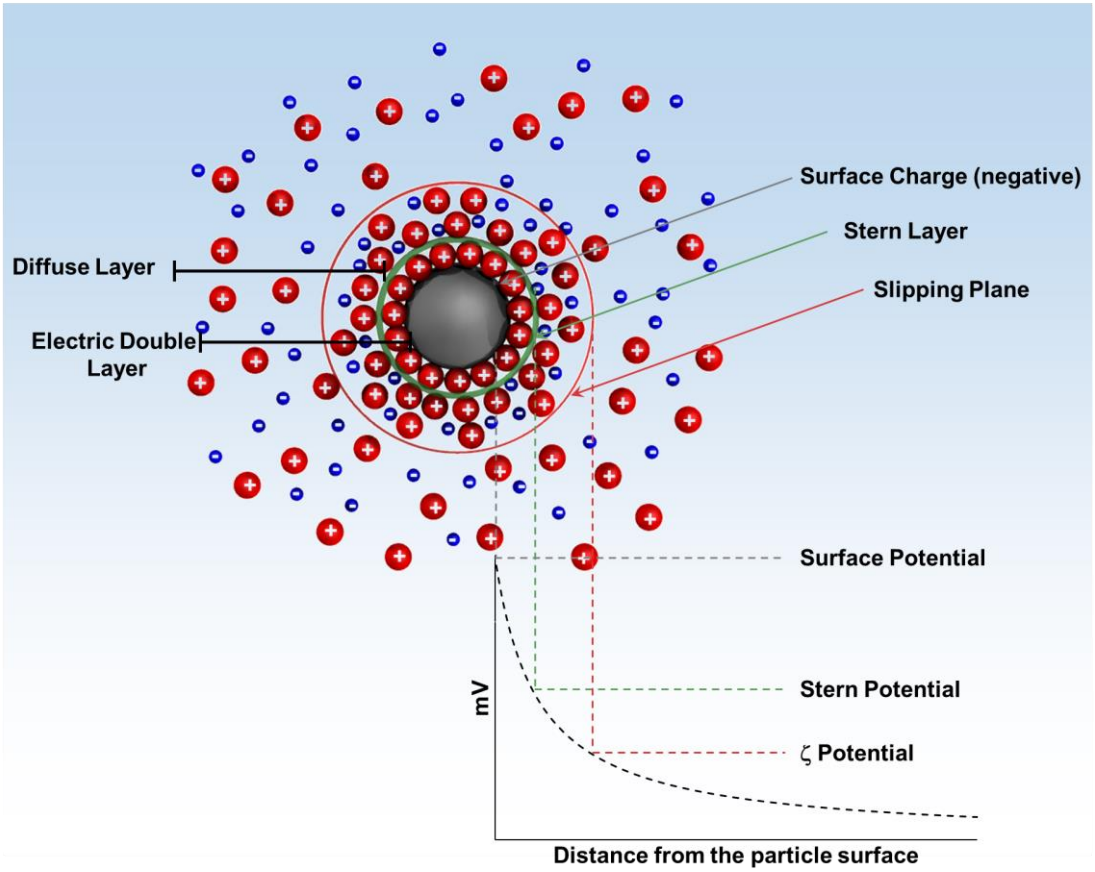

Figure 2-3: Electric double layer of a particle.

This surrounding layer is made of two parts; a Stern layer forms the inner region, ions within are strongly bound while a diffuse layer builds the outer region, both are less firmly associated.[16] There is a notional boundary between these layers and the surface of the particles forming a stable entity.[16] Ions within the boundary will also move e.g. by gravity or Brownian motion, while those ions beyond the boundary will stay with the bulk dispersant.[16] The potential on the surface of the hydrodynamic shear (slippling plane) is the zeta potential (ζ).[16] A potential can be calculated in the dependence of the distance to the surface of the particle for each boundary. The zeta potential magnitude gives an indication of the potential colloidal stability of system. The particles in a colloid system that have either a large negative or positive zeta potential tend to agglomerate less due to the repulsion of equally charged particles. Contrary, if the particles have a low zeta potential, no force will prevent the particles from flocculation or agglomeration.[16] Within a moderate stable dispersion the zeta

potential is either >+30 or >-30 mV (Table 2-1). Dispersions with a higher zeta potentials than ± 30 mV are assumed to be stable.[16]

Interestingly, those particles that have a density greater than the continuous phase, even though they are dispersed, will sediment due to the gravity force.[16]

Table 2-1: Influence on the stability behaviour of the colloids by the ζ-potential.

ζ-potential /mV	**Stability behaviour of the colloid**
0 - ±5,	Rapid coagulation or flocculation
±10 - ±30	Incipient instability
±30 - ±40	Moderate stability
±40 - ±60	Good stability
> ±61	Excellent stability

2.2 Calcium phosphate nanoparticles

2.2.1 Hydroxyapatite

In nature, the main mineral component of biological hard tissues, like bone (65-70%), dentin (70%) or enamel (97%), is mainly comprised of calcium and phosphate (CaP) in form of hydroxyapatite (HAP).[25-30] HAP is a member of the apatite group, $M_5(ZO_4)_3X$, where M is either a divalent cation of the alkaline earth metals (Mg^{2+}, Ca^{2+}, Sr^{2+}, Ba^{2+}) or of the transition metals (Zn^{2+}, Cd^{2+}) or either of the metalloids (Pb^{2+}), while ZO_4 stand for PO_4^{3-}, CO_3^{2-} or SO_4^{2-}; and X represents OH^-, F^- or Cl^-.[31] Therefore, HAP is described by the formula as $Ca_5(PO_4)_3(OH)$, but is also usually written as $Ca_{10}(PO_4)_6(OH)_2$ (Figure 2-4).[32] It has a bipyramidal orientation with a mixture of ionic and covalent bonds.[33] Furthermore it belongs to the hexagonal crystal system ($a_0 = b_0 = 9.432$ Å, $c_0 = 6.881$ Å; α = β = 90°, γ = 120°) and to the space group $P6_3/m$.[34,35]

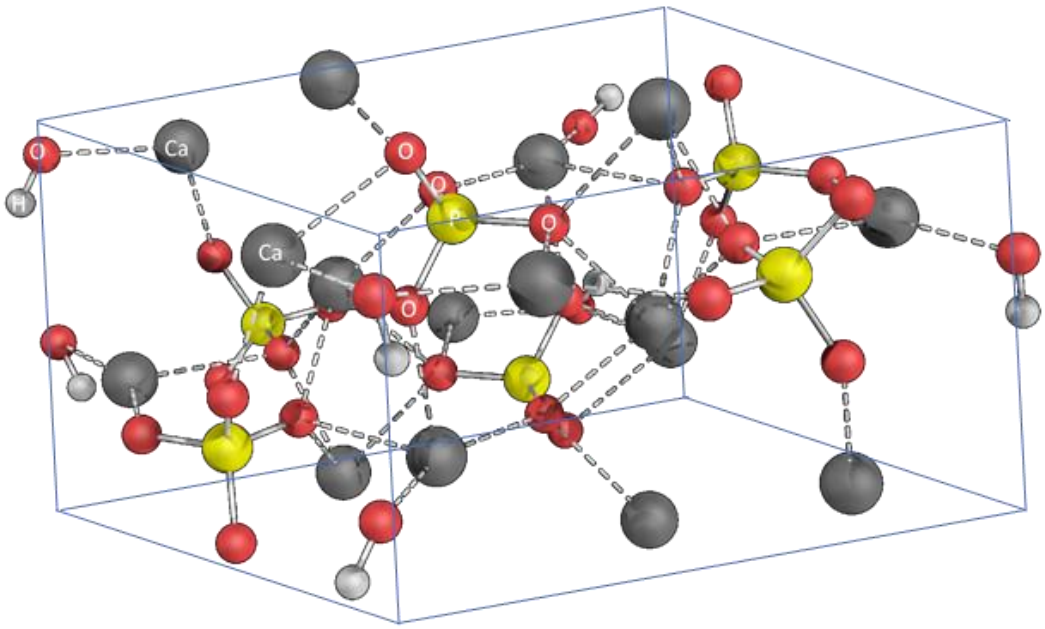

Figure 2-4: Crystal unit cell of HAP.
HAP $Ca_5(PO_4)_3(OH)$ belongs to the hexagonal crystal system with the $P6_3/m$ space group (PDB: HAP1).

In bone, small hydroxyapatite crystals are formed with approximately 200 Å in their largest dimension.[36] As bone matures, larger hydroxyapatite crystals are formed reducing the level of impurities by monovalent and divalent ions (e.g. Na^+, Mg^{2+}, Sr^{2+},

K^+, CO_3^{2-}).[36] Calcium phosphate can form different phases depending on the pH value, stoichiometry, and temperature with specific configurations and properties, ranging from the least water-soluble phase, the tetracalcium phosphate $Ca_4(PO_4)_2O$ (Ca/P ratio 2.0, through HAP (Ca/P ratio 1.67) and with the most water-soluble monocalcium phosphate $Ca(H_2PO_4)_2{\cdot}H_2O$ (Ca/P ratio 0.5).[23]

2.2.2 Calcium phosphate nanoparticles synthesis and applications

Nowadays, calcium phosphate nanoparticles can be obtained by a various number of synthesis methods in different sizes, shapes and morphologies.[37-43] Based on their very good biodegradability and biocompatibility, calcium phosphate nanoparticles can be used as carriers for different biomolecules, including DNA, RNA, proteins, peptides, oligonucleotides or even small organic molecules which adsorb on the surface by electrostatic or hydrophobic interaction.[31] In nanoparticulate dispersed form, it can be used to easily transport a desired cargo across a cell membrane for numerous biomedical applications (e.g. gene silencing, transfection or vaccination).[44-51] The cost-efficient and easy precipitation of alkaline solutions (e.g. pH 9, at room temperature) of Ca^{2+} and PO_4^{3-} salts e.g. $Ca(NO_3)_2$ and $(NH_4)_2PO_4$, is a fast way to obtain calcium phosphate nanoparticles and was also used during this work.[52-54] The following scheme sketches the preparation of calcium phosphate nanoparticles. After step 2, the primary dispersion CaP/PEI can be loaded with a desired cargo molecule, optimally with a counteracting molecule to the colloidal stabiliser, and is finished by a second layer of calcium phosphate and PEI. Finally, non-adsorbed molecules or ions are removed by ultracentrifugation and the remaining pellet is redispersed in water by ultrasonication.

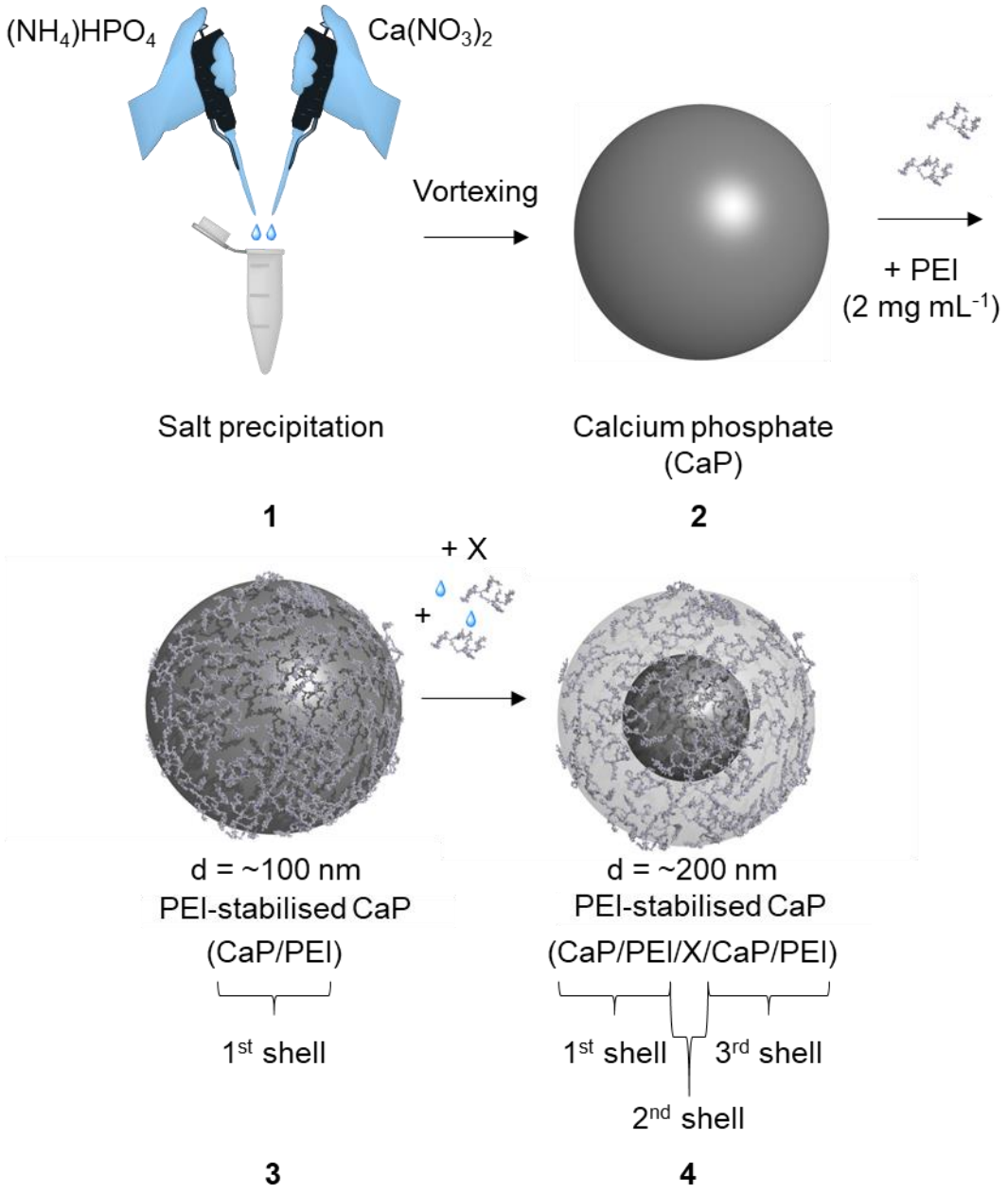

Figure 2-5: Representative synthesis scheme of single- and triple-shell calcium phosphate nanoparticles.
1 salt precipitation, 2 calcium phosphate core; 3 PEI stabilised Calcium phosphate core; 4 triple-shell variant is obtained by the repetition of the steps 1-3. X= cargo of interest e.g. protein, nucleic acid, drug, adjuvant

Furthermore, another shell can be formed by the simple addition of calcium and phosphate salt followed by an additional coating with a colloidal stabiliser e.g. PEI (Figure 2-5). The method can also be varied by the substitution of the colloidal stabilising polyelectrolyte by e.g. oligonucleotides, carboxymethyl cellulose and others e.g. CMC (Figure 2-6).[44,45,55]

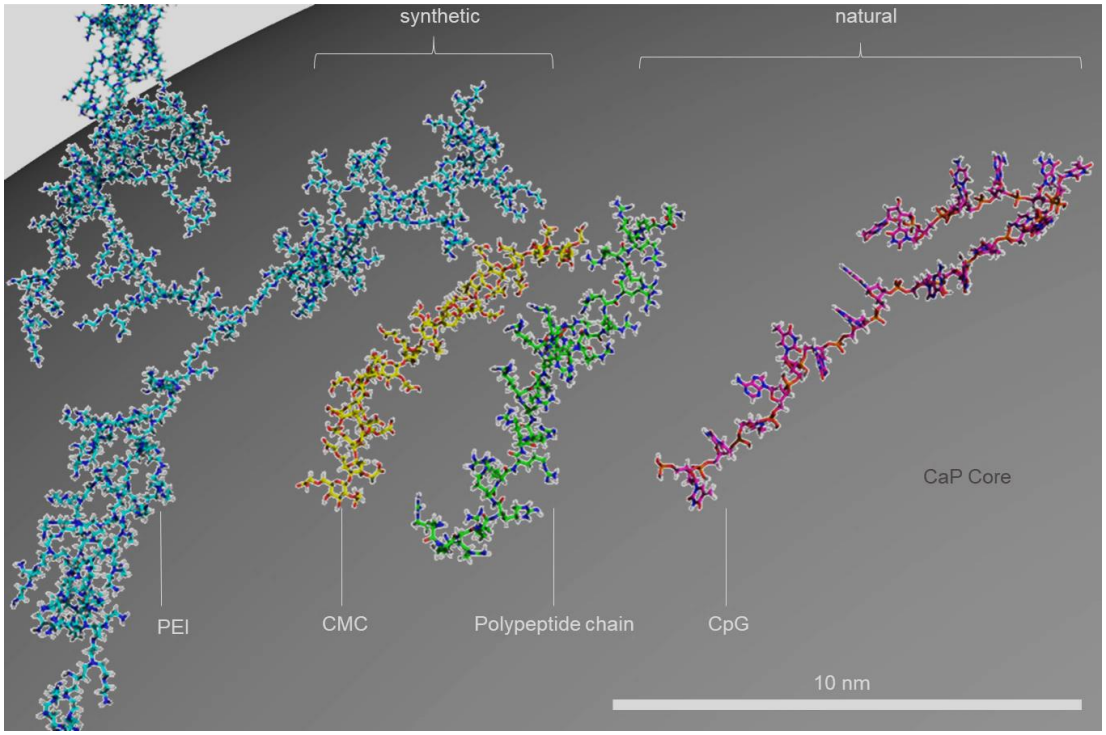

Figure 2-6: CaP stabilised nanoparticles by different synthetic or natural colloidal stabilisers. From left to right; A single PEI-molecule (25 kDa), CMC, polypeptide chain, oligonucleotide CpG and a calcium phosphate core with 100 nm in diameter. Different colloidal stabilising agents. Scale bar 10 nm.

Such colloidal stabilising polyelectrolytes are origin-specific divided into either natural or synthetic polyelectrolytes. Especially the charge of the stabilising polyelectrolyte agent determines the charge on the particles' surface and particularly in dispersed form. Therefore, it also determines which kind of biomolecule can be loaded after the first precipitation and colloidal stabilisation of the surface (Step 1-2). HAP is rather less soluble in aqueous solutions at pH 7-10 than acidic pH. The amphiphilic and positively charged PEI stabilises the CaP core by coordinating the PO_4^{3-} and Ca^{2+} ions through ionic and Van der Waals interactions (Figure 2.7).[56,57]

The particles can be further characterised according to their colloid-chemical properties. Especially the zeta potential gives information about the surface charge of a particle in a disperse system and reflects equally the used stabilising polyelectrolyte. Figure 2-7 shows a model of possible interactions between the positively charged polyethyleneimine and the surface of the calcium phosphate nanoparticle.

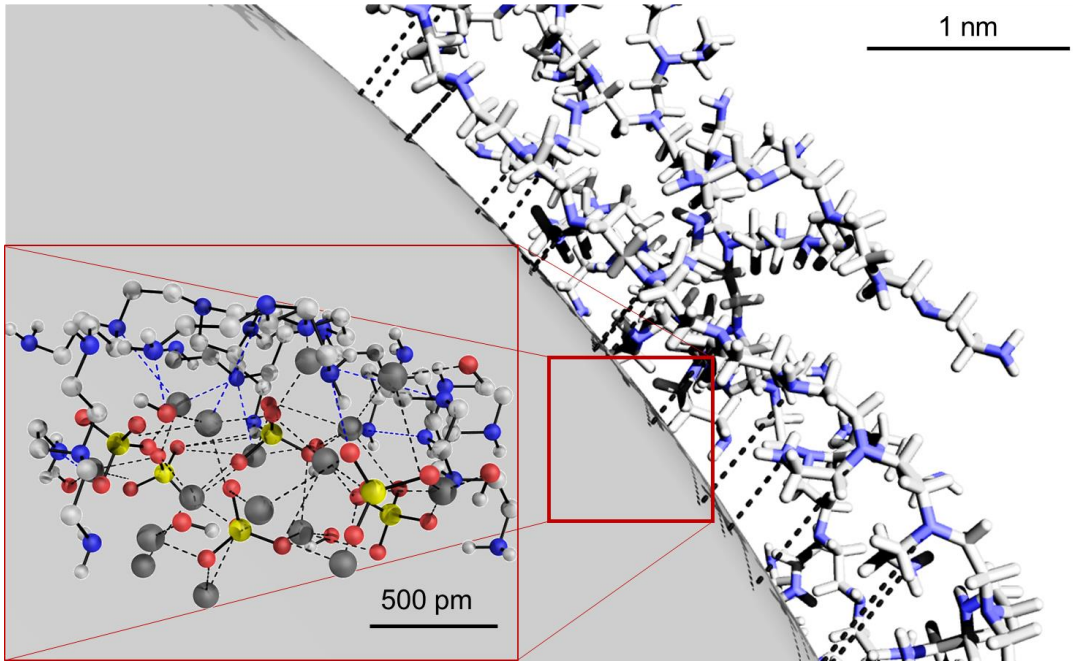

Figure 2-7: Illustration of the CaP/PEI interface.
PEI stabilises the CaP core by ionic interaction. Protonated primary amines coordinating the orthophosphate ions while the lone electron pair coordinates the calcium ions. In left lower corner, a close-up of the interface (sphere colour code: Blue = nitrogen, dark grey = Ca^{2+}, yellow = PO_4^{3-}, white = hydrogen, grey = carbon, red= oxygen).

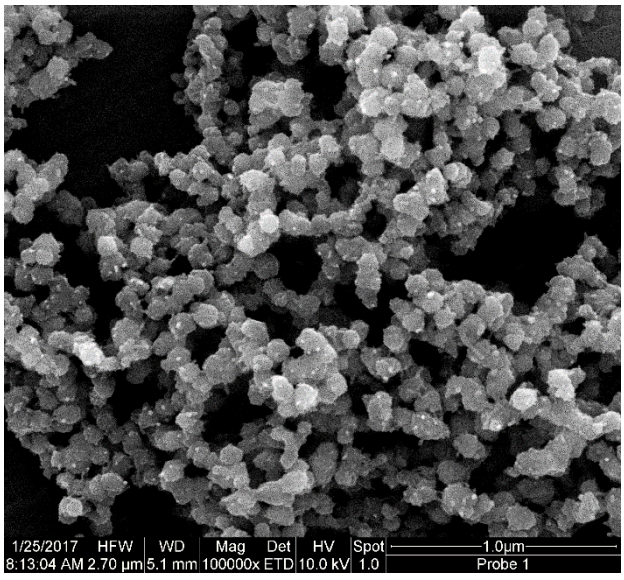

Figure 2-8: Representative SEM Image of single-shell calcium phosphate nanoparticles CaP/PEI with an average diameter of 146 nm.

Various modifications of the synthesis of calcium phosphate nanoparticles has been developed for different purposes. They have been exploited for the delivery of antigens, proteins, DNA, adjuvants and biological relevant molecules.[51,52] Stable

dispersions of either biomolecule loaded or non-loaded calcium phosphate nanoparticles can also be encapsulated through a thin silica shell by the Stoeber method (Figure 2-9).[58] This condensation reaction is usually catalysed by traces of ammonia. It also works with simple addition of aqueous solutions e.g. calcium phosphate nanoparticle dispersions.[59,60] This method allows the formation of a calcium phosphate core silica shell interface.[58,61] The surface of such calcium phosphate silica shell encapsulated nanoparticles can be modified by the additional condensation of (3-mercaptopropyl)-trimethoxysilane (MPS) or (3-aminopropyl)-triethoxysilane (APTES). This leads to thiol- or amino-functionalised silica shells and gives an addressable functionalised surface for common conjugation chemistry e.g. succimidyl ester or maleimide activated molecules (Figure 2-10).[61] A prominent example is the sulfo-succinimidyl-4-(N-maleimidomethyl)cyclohexane-1-carboxylate (Sulfo-SMCC) hetereo-specific which is a bifunctional cross-linker that addresses amino and thiol groups.

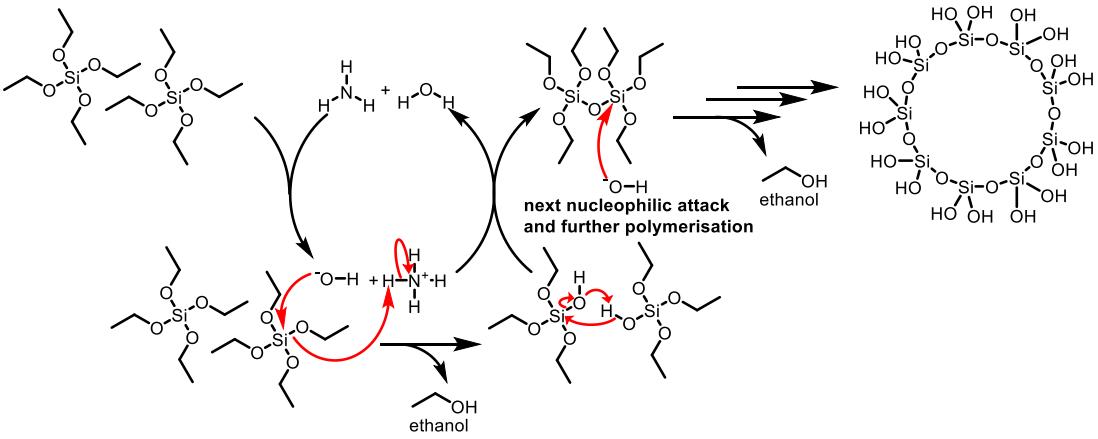

Figure 2-9: Mechanism of the ammonia catalysed silanisation.

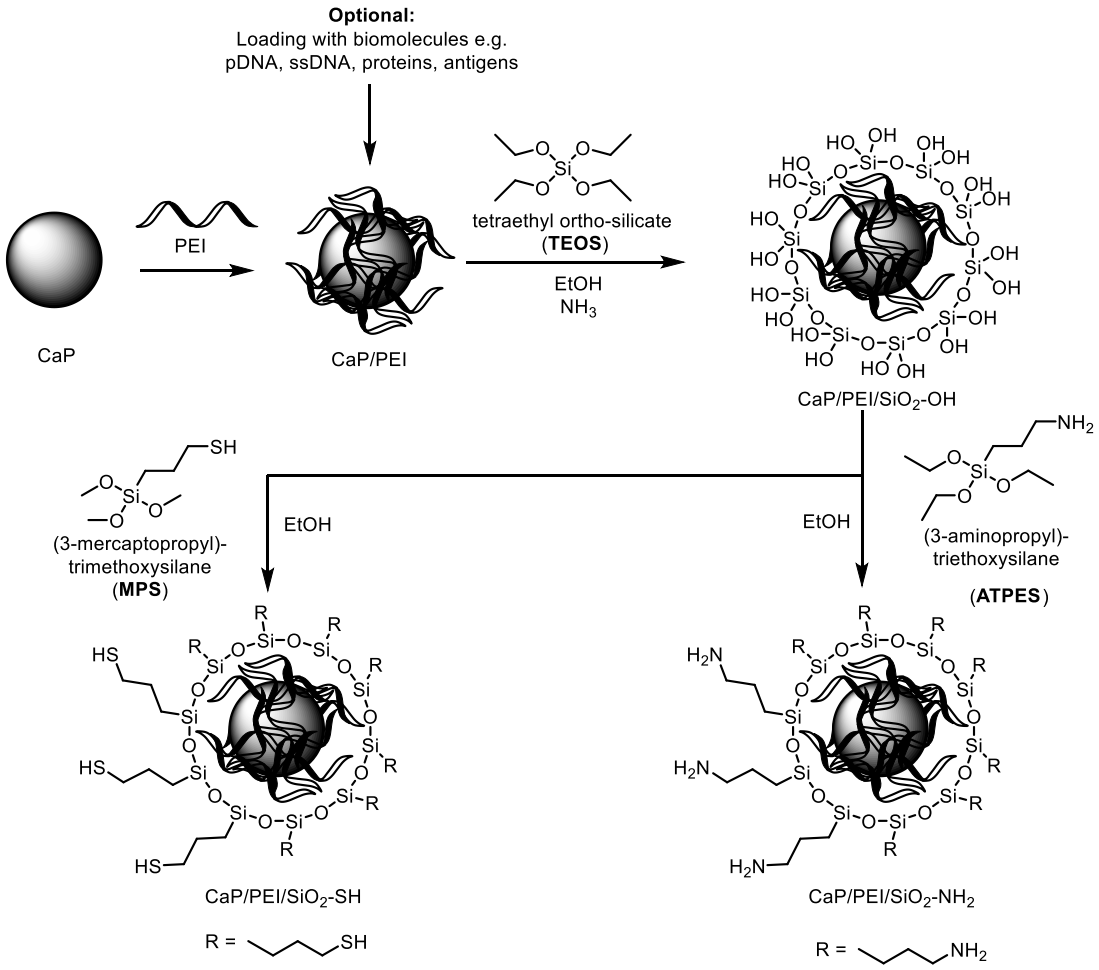

Figure 2-10: Synthesis scheme of silanised calcium phosphate nanoparticles.
After the precipitation and colloidal stabilisation (here PEI) of nascent calcium phosphate nanoparticles, the dispersion can optionally be loaded with biomolecules, including plasmid DNA (pDNA), single stranded DNA (ssDNA), proteins or antigens. Then, the dispersion is given to the Stoeber solution, containing a mixture of TEOS and ammonia dissolved in ethanol (EtOH). After purification by ultracentrifugation, the dispersion is redispersed with water and applied to a mixture of MPS or APTES in EtOH. The final mixture is again purified via ultracentrifugation and redispersion.

The encapsulation by a silica shell of the calcium phosphate nanoparticles was first published by Kozlova *et al*..[61] The simultaneous incorporation of bioactive molecules by the adhesion onto the surface of the calcium phosphate nanoparticle core and the possible surface modification (e.g. amine, thiol) of the silica shell (e.g. maleimide or NHS-ester activated biomolecules) giving a multimodal vehicle system with many biomedical applications. Thus, these particle systems have been used successfully for the gene and drug delivery, as well for the vaccination against different viruses.[61] Beside the previously described synthesis by fast precipitation, these kind of nanoparticles have been used in this work for vaccinal application.

2.3 Biomedical and molecular biology applications of nanoparticles

Many examples for the application of nanoparticles in biomedicine and molecular biology have been listed since the development of nanotechnology. Albumin-bound or liposome-formulated nanoparticles like Abraxane® (paclitaxel) or Doxil® (doxorubicin), with an average diameter of ~10 nm or ~100 nm, respectively, have even found their way into the global market after FDA drug approval for the treatment of metastatic breast or ovarian cancer, respectively.[62-65] Both nanoparticular drugs use the enlarged surface to volume ratio which is basically leading to a better loading efficiency of the transported drug. These two examples show that differences in drug formulation compared to the free drug can have improved impacts on its circulation and resistance time. Furthermore, chemical modifications like the PEGylation, in the case of Doxil, leads to a less renal excretion of the anticancer drug.[66,67] Beside these successful nanoparticular-like examples for drug delivery, nanoparticles in biomedicine have further been used and studied as vehicles for imaging, sensing or to understand biological processes.[68] Further examples are polymeric NPs, iron oxide NPs, quantum dots or gold NPs.[68] The control of the chemical modifications with accessible functional moieties like amine, alkyne, azide or thiol groups turn nanoparticles into a tailor-made and adjustable biomedical tool. It can be decorated likewise with nearly any functionality over the corresponding and well-known cross-coupling ligation reactions (EDC/NHS, [3+2] cycloaddition (azide and alkyne) or Michael addition).[58,69-72] Especially in a therapeutic and biomedical approach, the anchoring of cell targeting antibodies or aptamers is an often desired goal in cancer and other therapies.[58,69-72] Calcium phosphate nanoparticles can also be a good choice for the investigation of biological processes. As previously mentioned, the low toxic side effects and the good biocompatibility of synthetic HAP turn calcium phosphate nanoparticles into a multipurpose biomedical tool for the transport of biomedically relevant molecules across the cell membrane. Therefore, calcium phosphate nanoparticles have been exploited for antibody directed cell targeting, photodynamic therapy (PDT), DNA transfection, gene silencing and drug delivery. The easy synthesis, adjustable polymeric stabilisation by either negatively or positively charged biocompatible polymers makes it cost-efficient and versatile applicable. Silanisation of the CaP core

allows further decoration of maleimide or NHS-activated molecules, giving aris to many biomedical and molecular biology applications.

2.4 Endocytosis and uptake of nanoparticles

Beside the active and diffusion driven transport of water and small solutes, larger molecules like proteins or objects larger than 1 µm are generally unable to cross the cell membrane on their own. Eukaryotic cells use two different processes to maintain cellular homeostasis: the processes of exocytosis (from Greek *exo*, outside, and *kytos*, cell), exporting bulky molecules such as indigestible polysaccharides or proteins, while endocytosis (from Greek *endo*, inside) deals with the internalisation of substances.[73] Both are membrane trafficking processes in which endocytosis is involved in the cellular internalisation and sorting of extracellular molecules, plasma membrane proteins and lipids.[74] Endocytosis is vital for a several number of cellular functions, including nutrient uptake, cell adhesion and migration, receptor signalling, pathogen entry and cell polarity. It therefore regulates e.g. receptor-mediated signalling (including signalling from receptor tyrosine kinases and G protein-coupled receptors).[74] Endocytosis comprises the two major processes phagocytosis and pinocytosis.[74,75] Phagocytosis is used to internalise pathogens or objects larger than 1 µm. Pinocytosis is also known as cell drinking, it can be further distinguished into four mechanistically and cargo size-dependent different internalisation routes. The first is pinocytotic internalisation pathway is macropinocytosis which is highly active in dendritic cells and macrophages, capturing most of surrounding antigens. It is also relevant for the cell migration and tumour metastasis and represents an entry point exploited by a variety of pathogens.[76] Other pathways are mediated specifically by surface receptors that are associated with the recruitment of clathrin molecules forming a clathrin-coated pit. Non-specific endocytosis by caveolin lead also to a caveolin-coated pit (Figure 2-11).[77] All these uptake pathways can be addressed by a distinct functionalisation of engineered nanoparticles. For the calcium phosphate nanoparticles, macropinocytosis as well as clathrin-dependent and caveolin-dependent endocytosis pathways were shown to be the main uptake routes for these kinds of nanoparticles.[58,78-80] Next to the uptake of nanoparticles, its desired effect also depends on its intracellular processing. In the case of DNA introduction, particles

need to reach the nucleus in order to be read by the cells´ protein biosynthesis machinery.

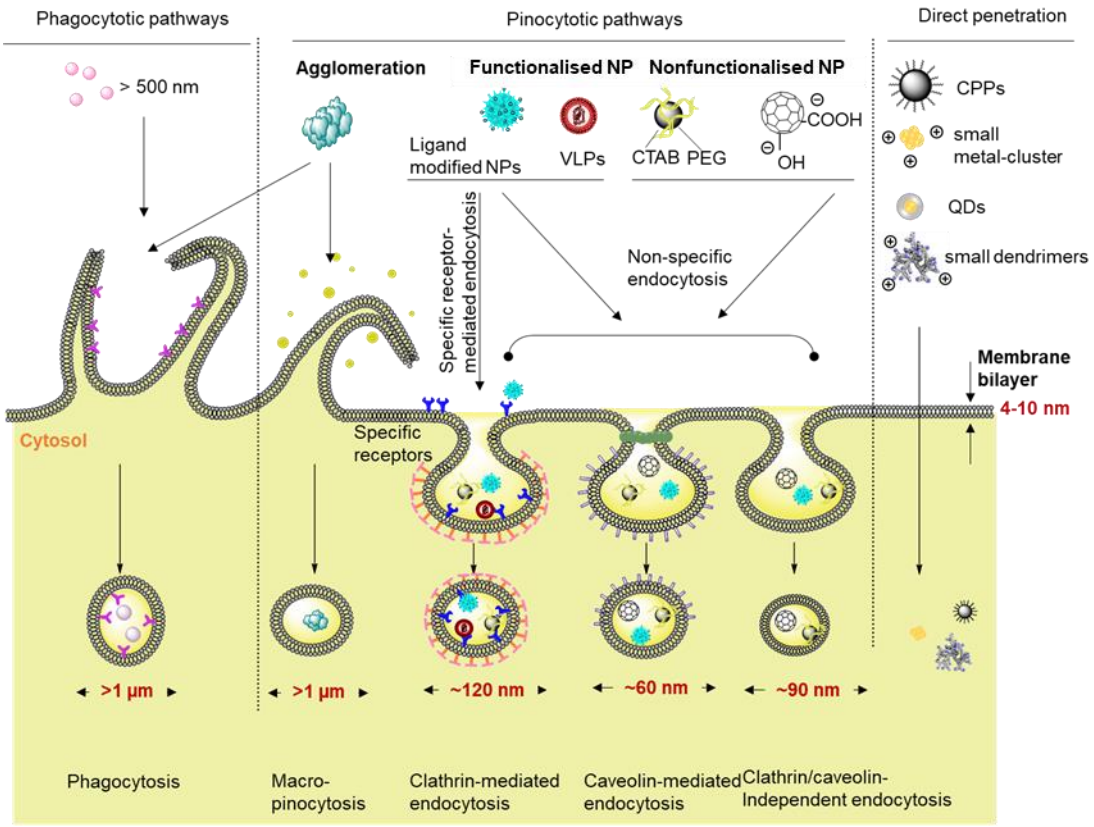

Figure 2-11: Particle size dependent uptake mechanism of different nanoparticles.
Different functionalised, shaped and sized nanoparticles are differently taken up by endocytotic pathways. Macroscopic substances (>500 nm) like proteins, polysaccharides or pathogens are mainly taken up by phagocytosis or macropinocytosis, forming vesicles larger than 1 µm in diameter. Smaller objects, especially nanoparticles are taken up by pinocytotitic endocytosis pathways distinguishable in clathrin- or caveolin-dependent mediated endocytosis or independent of those two. The formed vesicles range from 120 – 60 nm in diameter (Retraced from Ref.).[81]

2.5 Intracellular transport of nanoparticles

The route nanomaterials enter the cell determines the intracellular processing of engineered nanoscopic materials for biomedical purposes. Substances internalised by phagocytosis are degraded faster than clathrin- or caveolin-dependent endocytosed materials. Even more, the transport over the caveolin-dependent endocytosis can lead to an escape of degradation by lysosomes.[77] Independent of the endocytosis pathway, substances are primarily vesicular enclosed and interact with sorting endosomes. At this stage, the cargo is sorted to different organelles like the dictyosome or can be matured to a degrading lysosome which is later transported out of the cell.[82,83] Up to now, not much is known about the intracellular processing of internalised nanomaterials but it is assumed that the exogenous and cell-foreign material is proceeded by the endosomal lysosomal pathway for their degradation. It is well known that biological fluids e.g. blood or nutrition medium contacting nanomaterials are instantly coated by layers of solubilised proteins covering the nanomaterial by adhesion. These surrounding protein layers are also known as protein corona, a protein corona can be composed of a unique set of proteins from the surrounded media which also relies on the nanomaterials' chemical properties e.g. hydrophobicity, hydrophilicity or functionality. Protein coronas are assumed to influence the processing of applied nanomaterials.[84-86]

2.6 Molecular biology

2.6.1 Gene vectors

Genes composed of circular self-contained double stranded DNA are called plasmids. In general, plasmids are exchanged between prokaryotes like bacteria to mediate additional genetic information like antibiotic resistance or other beneficial attributes.[345] In molecular biology, plasmids are used to introduce a desired genetic information by transfection encoding a desired protein.

2.6.2 Transfection

Transfection is the introduction of a desired genetic information. The transfection can be either realised by viral infection or by DNA carrying cationic liposomes. In this study liposome-based transfections were carried out as control experiments, using Lipofectamine 2000 (Invitrogen, Thermo Fisher Scientific). It can be distinguished between two forms of transfections, namely the transient and the stable transfection. The transient transfection describes the temporary gene expression of an introduced nucleic acid, either DNA or RNA, whereas the stable transfection is the permanent genetic modification of the recipient cell. The mechanism of liposomal transfection is exploiting the formation of nucleic acid lipoplexes that are internalised by endocytosis and released into the cytoplasm where the cell is delivering the nucleic acid to the nucleus.[87]

2.6.1 *In vitro* transcription

In vitro transcription (IVT) is a template-directed (cDNA) synthesis of RNA molecules of any sequence from short DNA oligonucleotides to those of several kilobases under the control of a constitutive bacteriophage promoter sequence (e.g. from the T7 coliphage).[88] It can yield µg to mg quantities of RNA.[88] *In vitro* transcripts have a large number of applications including analytical techniques (e.g. hybridisation analysis), structural studies (for NMR and X-ray crystallography), in biochemical and genetic studies (e.g. as antisense reagents), or as functional molecules (ribozymes and aptamers).[88] The well-accepted theory of the IVT reaction is shown and explained in Figure 2-12. IVT is normally carried out with the promotor-corresponding RNA polymerase (T7 RNA polymerase for the T7 Promotor). Polymerases usually have a

distinct error rate in RNA synthesis. The average error rate of a common RNA polymerase ranges between 0.0001 or 0.00001%, which is one mistake per 10^4 or 10^5 nucleotides. This error rate is about 10^5 times higher than that of a DNA polymerase. The much lower fidelity of the RNA synthesis is tolerable because mistakes are not transmitted to progeny.[89] Many RNA transcripts are synthesised from genes, but only a few defective transcripts are unlikely to be harmful for the organism.[89]

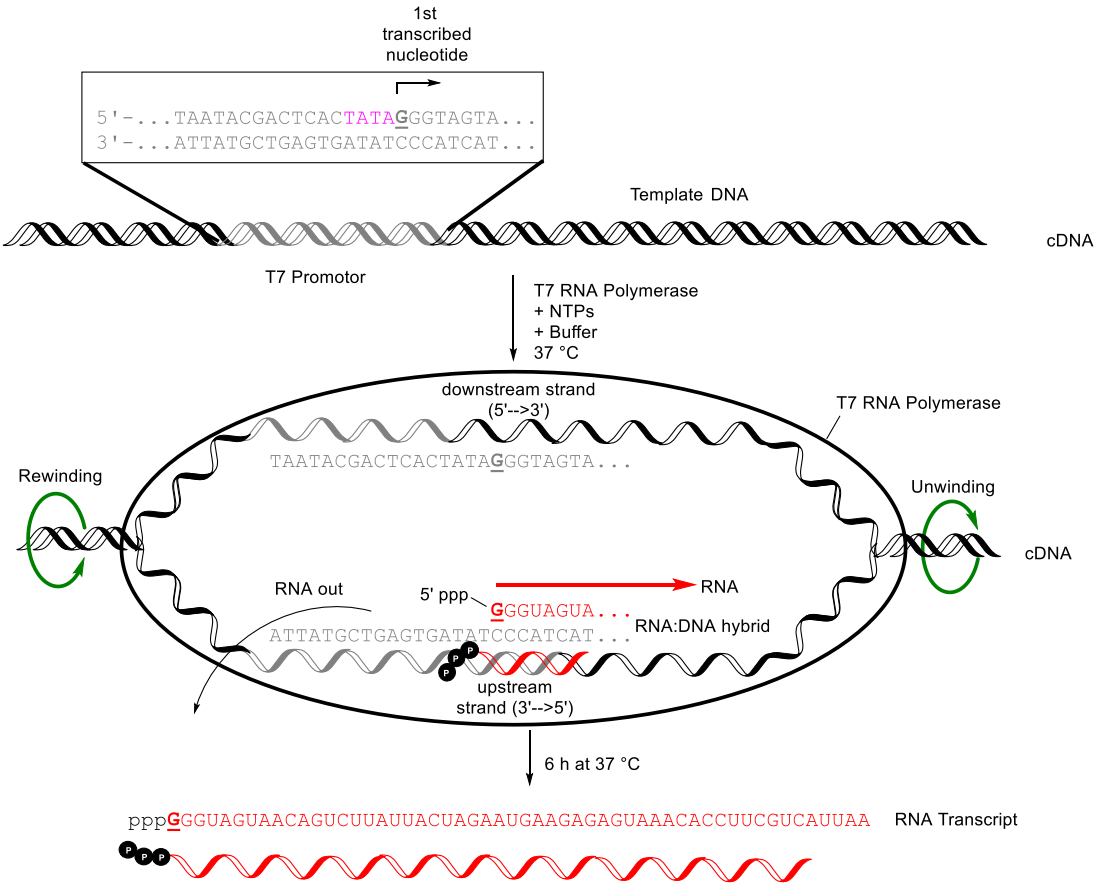

Figure 2-12: *In vitro* transcription.
The *in vitro* transcription needs a bacteriophage T7 RNA polymerase that recognises and binds to the upstream localised constitutive promotor sequence (T7 Promotor), reading a coding template DNA (cDNA). Furthermore, a NTPs Mix (ATP, CTP, GTP, UTP) and an appropriate transcription buffer is needed as well. The T7 RNA polymerase binds to its promotor sequence, recognising the DNA template counterpart. It initiates the insertion of complementary NTPs. A guanosine triphosphate right after the consensus initiator sequence TATA (TATA box) is the first transcribed ribonucleotide. During its way down the template upstream strand, the T7 RNA polymerase is constantly unwinding and rewinding the cDNA after each new inserted ribonucleotide. At the same time, the nascent RNA strand leaves the RNA polymerase in the opposite direction giving a 5'→3' synthesised RNA transcript.

The cDNA templates for IVT are used as run-off templates. RNA polymerase runs off the template after reading its template and ensures a correct reading or rather

termination of the template. IVT templates can be either generated by plasmid amplification in a suitable bacterial hosts (e.g. *E. coli*) and subsequent plasmid linearisation by restriction enzymes or by PCR amplification to generate a run-off template (Figure 2-13).[90]

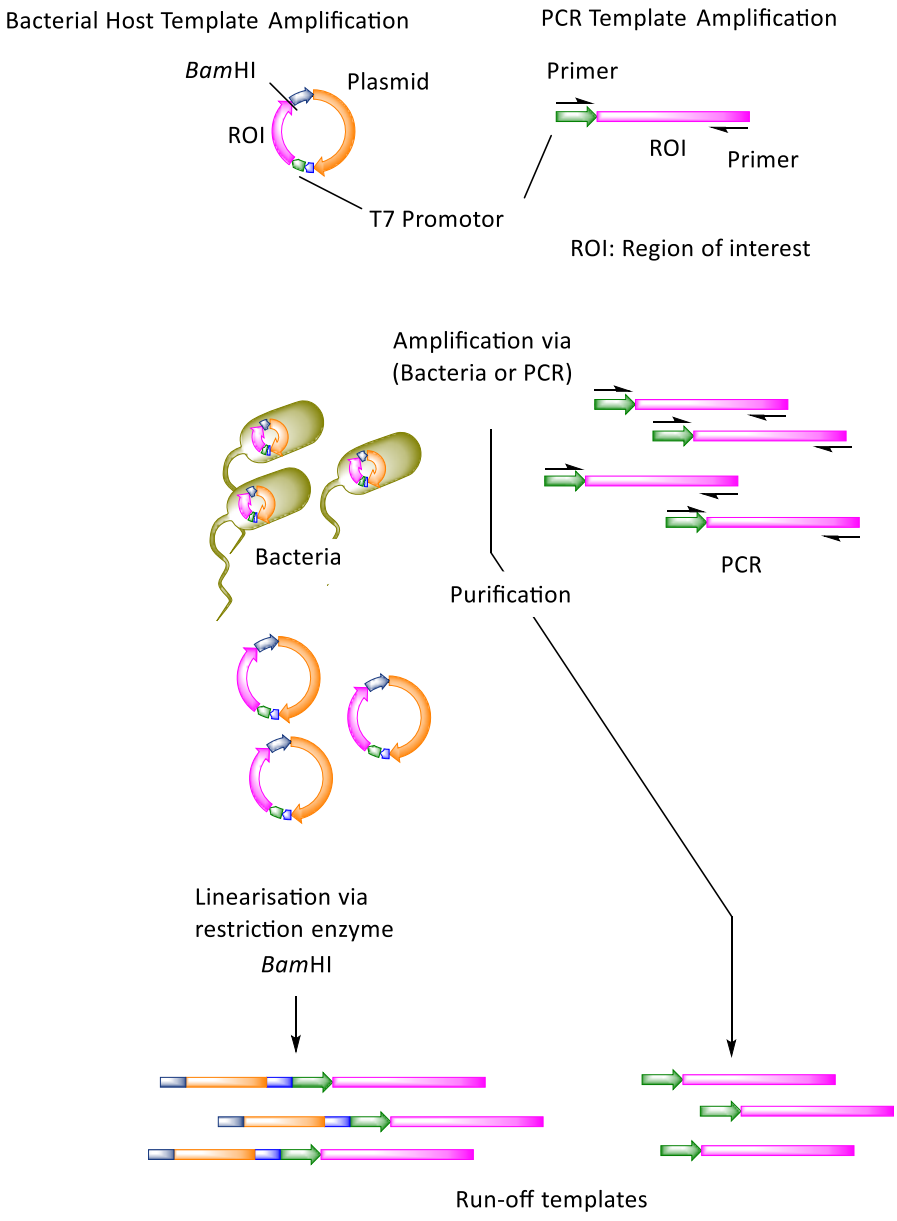

Figure 2-13: Run-off template generation.
Templates for subsequent IVT reaction are generally produced as run-off templates and can either be prepared by bacterial plasmid amplification followed by purification and restriction enzyme mediated plasmid linearisation, or by PCR amplification with site specific flanking primers at the T7 promotor and the ROI.

Templates containing plasmids are easy to handle and store and can be produced in several milligram quantities. A disadvantage of this amplification method is the necessary restriction enzyme mediated linearisation after purification that can result in incomplete digestion and leads to overlong and wrong transcripts.[90] Templates generated by PCR are also easy to handle and store, but cannot be produced in that large quantity as the plasmid amplification does. The advantage of this method is that no overlong transcripts can be produced although the template for the PCR can be originated from plasmid DNA. Resulting interferences for the IVT can be circumvented using *Dpn*I which is a restriction enzyme that recognises and digests methylated plasmid DNA. Plasmids inside a bacterial host usually have methylated DNA to protect plasmid DNA from nuclease-mediated self-digestion. After a PCR, *Dpn*I is generally exploited to remove parental plasmid DNA to avoid any interferences in the IVT. Enzymatic removal of template DNA is also carried out after each IVT with an DNA specific nuclease (DNase).[90]

2.6.2 Aptamers

Aptamers are highly selective and specific binding RNA or DNA sequences comprised of up to 120 nucleotides (nts). They are generated *in vitro* by an iterative selection process (systematic evolution of ligands by exponential enrichment (SELEX)) to bind with high affinity and specificity to a given target (Figure 2-14).[91,92] Herein, a library of randomised DNA or RNA sequences (10^{15} sequences), which are constantly flanked by specific primers, are used to bind an immobilised analyte (binding). The analyte molecule can differ, ranging from large targets such as proteins over peptides, complex molecules to drugs and organic small molecules or even metal ions.[93,94] Non-binding sequences are rinsed from the analyte by different washing steps (rinsing). Bound aptamers are eluted and then amplified by a polymerase chain reaction (PCR). After the selection and strand separation, sequences are DNA-sequenced and mutated randomly, generating a new diverse library of DNA or RNA sequences which are used for the next SELEX round. Thus, binding sequences with optimised binding specificity are selected. Five to ten rounds of binding, rinsing, elution, amplification, separation and mutation are needed to obtain the final DNA

or RNA aptamer with a significant high affinity for considerably differing molecules.[93,94]

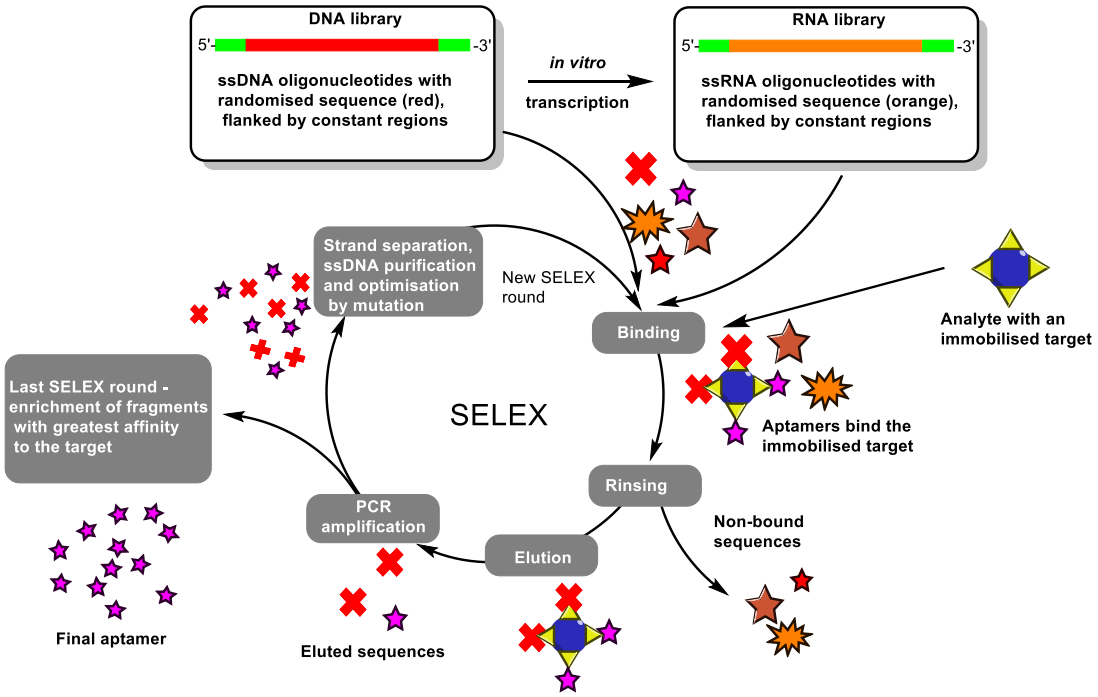

Figure 2-14: SELEX process.
A DNA or RNA library is incubated with an analyte of choice e.g. protein, peptide or metal ions. Non-bound sequences are washed away from the immobilised analyte using different washing conditions. The remaining bound sequences are eluted and separated. After the DNA sequencing, the selected sequences are mutated to optimise the binding affinity. A newly generated library comprised of initially found sequences and the mutants are introduced to a subsequent SELEX round. Generally, after 5-10 iterative rounds the final aptamer is obtained.

The high affinity and specificity of aptamers (e.g. 10^{-10} to 10^{-9} mol L^{-1}) to target molecules is related to their uniquely folded three-dimensional structure. It has nowadays led to a number of different applications, including flow cytometry staining, activating signalling pathways through cell surface receptor ligation, drug or siRNA delivery, blocking protein-protein interactions, and inhibiting enzyme function, which demonstrated a flexible and wide application range in medicine or diagnostics.[95,96] For example, aptamer-based therapeutics against diverse diseases, including cancer, are currently undergoing clinical trials, with one already approved for clinical use (i.e. Macugen®).[97] Therefore, aptamers have also been known as an alternative for antibodies combining some advantages over antibodies, but are less commonly used due to the patent claims from the early 90s´ (Table 2-2).[98-100]

Table 2-2: Comparison between aptamers and antibodies

Characteristics	Aptamers	Antibodies
Specificity and affinity	High (pM to nM)	High (pM to nM)
Development Time (Delivery of 1st production batch)	~1-3 months	~4-6 months
Molecular weight	8-25 kDa	~150 kDa
Tissue barrier penetration	+++ (due to smaller size)	+
Immunogenicity	-	+++ (even with humanised antibodies)
Thermal stability	++	-
Modification potential	Easy, unlimited	Difficult, limited
Manufacture	Chemical synthesis, IVT	Mammalian cell systems
Batch-to-batch variation	Low	High
Production time	Hours	Days to month
Production cost	$	$$$
Ranges of targets	Proteins and non-protein molecules	Limited to immunogenic proteins

Table was adapted from Ref..[101-104]

The SELEX patent has expired recently and therefore newly founded biotech-companies are making process in developing new aptamer-based functional molecules for the prementioned applications.[105]

2.6.3 RNA imaging aptamers - Spinach and Broccoli

The Jaffrey lab developed two fluorophore specific binding RNA aptamers for the visualisation of RNA.[106] The RNA aptamers, Spinach and Broccoli recognise and bind to a small fluorophore molecule, the 3,5-difluoro-4-hydroybenzylidene imidazolinone (DFHBI). DFHBI is cell-permeable and closely derived from the autocatalytically formed (by Ser^{65}, Tyr^{66} and Gly^{67}) GFP chromophore. It mimics the green fluorescence of GFP in complex with both RNA aptamers, forming a G-quadruplex which surrounds the fluorophore.[107] The binding event is visualised by emitting fluorescence of the DFHBI/RNA aptamer complex under a certain wavelength excitation. DFHBI was further derivatised, resulting in much brighter and more stable fluorophores with a prolonged fluorescence life time (Figure 2-15).[108]

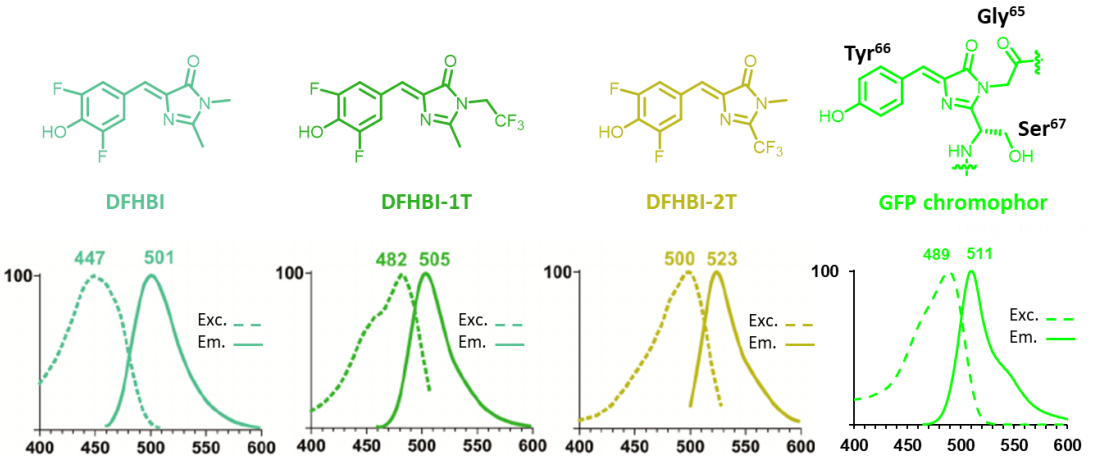

Figure 2-15: DFHBI and derivatives versus GFP chromophore.
Spinach and Broccoli bind to these fluorophores, forming a fluorescent active G-quadruplex with certain fluorescence spectroscopic characteristics.

In comparison to GFP, RNA-aptamer-DFHBI is not irreversibly photobleached under light exposure, but instead DFHBI undergoes a reversible conversion to a non-fluorescent state and the signal recovers spontaneously in the dark.[109,110] This feature allows the RNA-related monitoring of molecular biology processes such as transcription, translation, ribozymes, RNA-protein interactions or RNA-RNA interactions.[111-114] The encoding gene for the RNA aptamer for example can be attached to a gene of interest which allows both the monitoring and studying of the protein expression on the RNA level in eukaryotic cells.[115] The RNA aptamer, dimeric Broccoli (dBroccoli), was derived from a former imaging aptamer called Spinach aptamer and has a brighter fluorescence signal due to the two units of Broccoli. It is even much more stable when inserted into the viral scaffold F30.[116] In this study dBroccoli was used to analyse the protein expression and DNA translation in a calcium phosphate nanoparticle transfected cell line.

2.6.4 F30 Scaffold and F30-2xdBroccoli

The performance of dimeric Broccoli (dBroccoli) can be further enhanced using a stabilising scaffold such as F30 which is a highly stable viral ϕ29 three-way junction RNA motif that improves the Broccoli fluorescence by inserting two encoding copies into the junction sites, giving F30-2xdBroccoli (Figure 2-16).

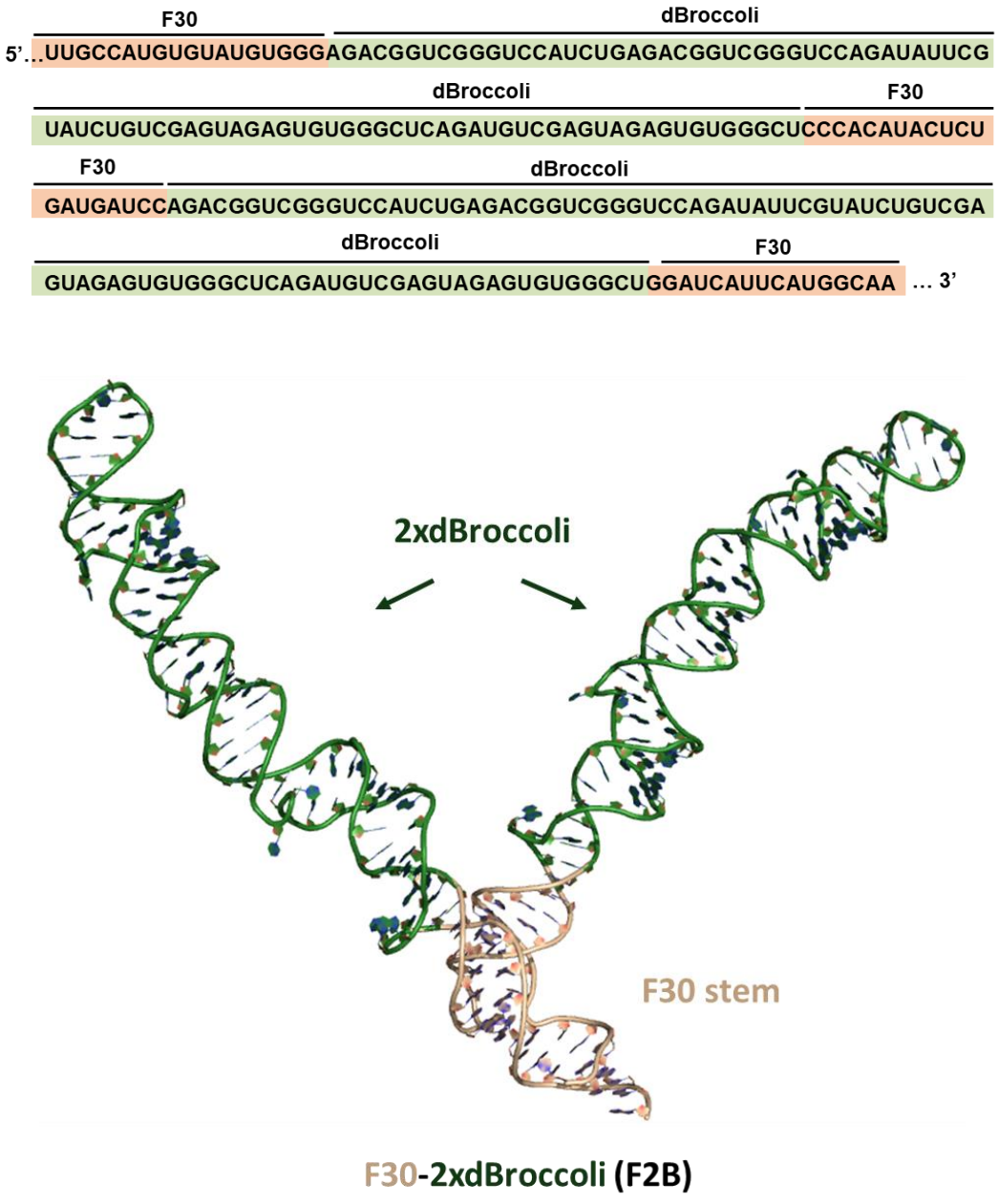

Figure 2-16: Sequence and structure of F30-2xdBroccoli.
Image of the sequence was redrawn from Ref.[117] The structure was generated through RNAComposer.[320]

Furthermore, the scaffold shows minimal or no cleavage in bacterial or mammalian cells.[117] Since the three-dimensional structure of an aptamer is of tremendous importance for its function, the F30 scaffold serves as a folding helper and forces the inserted copies into the right three-dimensional structure. F30-2xdBroccoli was used in order to visualise the RNA transcription of a fluorescent protein.

2.7 Immune system and immune responses

The immune system is a complex network and encompasses organs, tissues, cells and specialised molecules protecting and defending the living organism from harmful substances, malignant body´s own cells, pathogens and diseases. It can be classified into distinct immune responses, such as innate immunity and adaptive immunity, or humoral immunity and cell-mediated immunity.[118] The innate immune responses or humoral immunity are found in all classes of plants and animals and provide a rapid first line of defence from infection in an antigen-independent and non-specific manner.[119] Skin, epithelia, mucosa, tears, oral cavity, respiratory tract, stomach, and small and large intestines are the first anatomical and physiological barriers of the immune system and play an important role in the defence against pathogenic infections.[120]

A vital and critical role-playing part of the immune system is the lymphatic system comprising a connected network of lymphoid organs and lymphatic vessels. It is divided into the central lymphoid (thymus and bone marrow) and the peripheral lymphoid system (spleen, lymph nodes, and mucosa-associated lymphoid tissues (MALT)).[120,121] All immune cells are derived by haematopoiesis from multipotential haematopoietic stem cells (MHSC) (Figure 2-17).

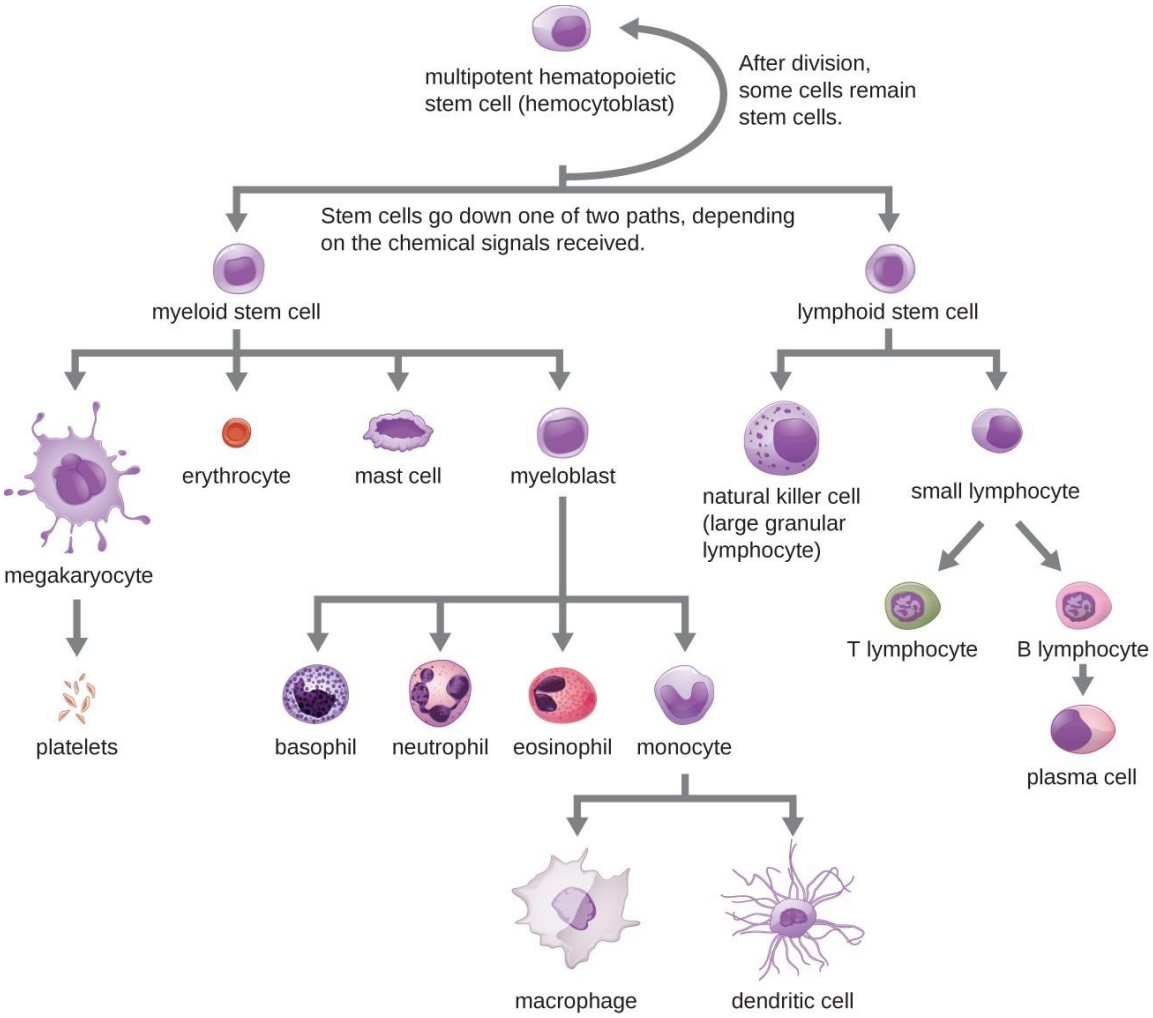

Figure 2-17. Process of haematopoiesis.
All immune cells are derived from multipotential haematopoietic stem cells (haemocytoblasts) by haematopoiesis. Haemocytoblasts differentiate by specific cytokines either into a common lymphoid or myeloid progenitor. Under specific cytokine stimulation, progenitors differentiate between specialised cells. (Image was taken from Ref.[122]).

Haematopoiesis involves the differentiation of MHSC between myeloid-derived cells (megakaryocytes, erythrocytes, mast cells, myoblasts, basophils, eosinophils, neutrophils, monocytes, dendritic cells and macrophages) and lymphoid-derived cells (granulocytes, natural killer cells (NK), small lymphocytes, B lymphocytes, T lymphocytes) depending on the stimulating cytokines received.[122] Each of these immune cells play a specific and vital role in the orchestra of the immune system (Table 2-3).

Table 2-3: Immune cells and their function.

Cell type	Erythrocytes	Dendritic cells	Monocytes/ Macro-phages	Neutrophils	Eosinophils	Basophils	Mast cells	NK cells	CD8+T cells	CD4+T cells	γβT cells	B cells
Origin		Myeloid						Lymphoid				
Morpho-logy	 Erythrocytes	 Agranulocytes		 Granulocytes								
Major sub-types	Erythrocytes	Leukocytes						Agranulocytes				
Cells per µL and (range)	5.2 million (4.4-6.0 million)	13-37	455 (200-950)	4150 (1800-7300)	165 (0-700)	44 (0-150)	n.d.	2185 (1500-4000)				
Function	O_2 transport	Antigen presentation, secretion of interleukins	Antigen presentation, phagocytosis	Phagocytotic; particularly effective against bacteria	Phagocytotic extracellular digestion	Pro-inflammation	Immunity, inflammation	Cytotoxicity		Regulation		Antibody production, antigen presentation
Appear-ance	Flattened biconcave disk, no nucleus; pale red	Veiled, dendritic, single nucleus	Largest leukocyte, spherical	Nucleus lobes	Nucleus two-lobed		Single nucleus	Spherical cells with a single, mainly large, nucleus occupying much of the cell´s volume				

Table was adapted from Ref..[122,123]

The process of lymphoid-derived immune cell differentiation is called lymphopoiesis, separated into T, B, NK and dendritic cells (DC) lymphopoiesis. T lymphopoiesis takes place in the thymus, where only 2-4% of the initially migrated precursor cells undergo a successful T lymphocyte maturation. 96-98% of the cells die through apoptosis and are phagocytosed by macrophages in the thymus.[124] Fully differentiated T lymphocytes either CD8+T (Killer cells), CD4+T (Helper cells), or γβT cells are then transported through the circulation system to the peripheral lymphoid organs e.g. lymph nodes or spleen.[124] B-lymphocytes are differentiated in the bone marrow and partially in spleen. The spleen represents the largest peripheral lymphoid organ and can be divided into the blood-containing red pulp and the white pulp, which is full of lymphoid cells. The red pulp efficiently removes pathogens, cellular debris as well as aged erythrocytes from the blood by abundantly present macrophages. The white pulp is a highly organised lymphoid region. It is composed of separate areas for B cells and T cells and is responsible for the initiation of adaptive immune responses. Areas for B cells and T cells are surrounded by a discrete subset of macrophages and B cell containing marginal zone. Whereas blood flows freely through the marginal zone, in which also macrophages and dendritic cells catch foreign antigens, the white pulp itself is excluded from the bloodstream.[125] The lymphoid organ, the mucosa-associated lymphoid tissues (MALT), contain a number of various immune cells, including CD8+ and CD4+ T cells, B cells, eosinophils, mast cells, macrophages, DCs and plasma cells. It is part of more than 50% of the components (i.e. genitourinary tract, bronchus and gut) of the entire human body. Its main function is the production of immunoglobulin E (IgE) and A (IgA) as part of the innate immune system.[23,126]

The innate immune system is mainly composed of myeloid lymphocytes, such as macrophages, neutrophils, basophils, mast cells and NK cells: These cells are the first response to an intruding pathogen. For example, macrophages reside in every tissue of the body, such as osteoclasts, microglia and Kupffer cells, internalizing pathogens and apoptotic cells and produce immune effector molecules. Beside their key role in host protection, they also contribute to the pathogenesis of degenerative and inflammatory diseases. Macrophages are derived from monocytes which are rapidly recruited through effector molecules, such as IFNγ, prostaglandins, and leucotrienes,

to damaged or infected tissues and differentiate into tissue macrophages.[127] They show a remarkable plasticity and adopt pro- or anti-inflammatory phenotypes in response to environmental signals.[127-129] Neutrophils can produce toxic antimicrobial mediators or engulf bacteria directly and are rapidly recruited to infected tissues. They are a major effector of acute and also chronic inflammation and are the first lymphocyte to be recruited to a source of disease or infection.[130] Eosinophils are perceived as terminally differentiated cytotoxic effector cells. They promote homeostasis through the release of their cytotoxic granule cationic proteins and contribute to the pathogenesis of different diseases and parasitic infections.[131] Basophils account for less than 1% of peripheral blood leukocytes and are the least common type of granulocyte.[132] They are defined by three major characteristics: the presence of basophilic granules in the cytoplasm, the surface expression of the high-affinity Fc receptor for IgE (FcεRI) and the release of chemical mediators e.g. histamine.[132] Under certain pathological conditions, such as allergic disorders and parasite infections, basophils are recruited to peripheral tissues from the bloodstream.[132] Mast cells share many of these characteristics. They are involved into pro-inflammatory responses to allergens, contribute to the protection against pathogens and are activated by anaphylatoxin peptides C3a and C5a.[129,133] Natural killer cells connect features from the innate and adaptive immune system. Through a large set of surface-presented cell receptors, NK cells can distinguish between infected cells, damaged or even tumour cells, from normal cells.[134] They mainly produce cytotoxic molecules to eliminate affected cells.[134]

The molecular detection of pathogens through innate immune cells is a complex issue. Several families of pattern-recognition receptors (PRRs) and an array of signalling molecules play a pivotal role in the expression of key factors that mediate the host immune responses. A classical innate immune response to microbial products through distinct families of PRR leads to complex intracellular signalling, designed to eliminate invading pathogens. The family of PRRs comprises the toll-like receptors (TLRs), which recognise conserved molecular patterns. These are derived from bacteria, fungi, protozoa and viruses. The C-type lectin receptors (the CLRs) sense fungi, and the RIG-I-like and DNA-dependent activator of IRFs

receptors (the RLRs and DAI), sensing viral nucleic acids in the cytosol or the NOD-like receptors (the NLRs) sensing bacterial products and endogenous products released by dying cells. These receptors, together with kinases, transcription factors and possibly other molecules create multi-protein signalling platforms that recruit adaptor molecules and lead to the expression of immune response regulating key factors. These include interferon Type I (TypeI-I IFN), pro-inflammatory interleukin 1β (Pro-IL-1β), and pro-inflammatory cytokines (Figure 2-18).[135]

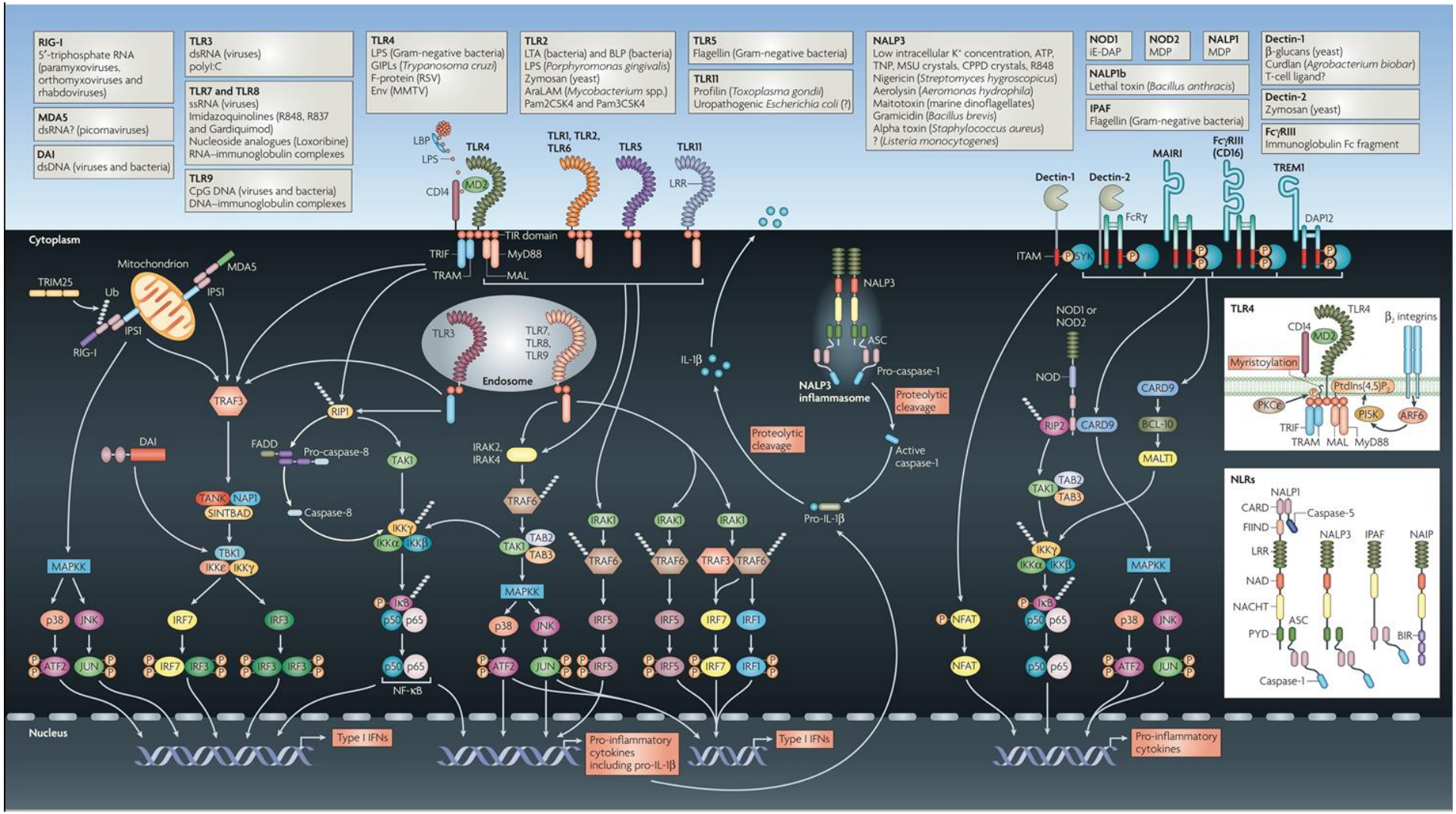

Figure 2-18: Sensing and signalling in innate immunity.
Image was free of permission and taken from Ref..[135]

Some of these factors, such as Pro-IL-1β require further processing by Caspase-1, a protease that catalyse the cleavage of Pro-IL-1β to IL-1β and is member of the NLR family.[135]

The release of cytokines leads to the recruitment of neutrophils (the first innate response to an intruding pathogen). In return macrophages are then recruited by neutrophils, sensing the release of effector molecules from neutrophils.[136] Then, macrophages begin to secrete colony-stimulating factors that lead to the proliferation, differentiation and recruitment of myeloid derived leucocytes from the bone marrow to the source of infection.[137]

Another critical role-playing defence system of the innate immune system against common pathogens is the complement system.[138] The complement system comprises more than 30 proteins in the plasma and on the cell surfaces, amounting to more than 3 g L^{-1} , constituting more than 15% of the globular fraction of plasma and can be activated through 3 major pathways: classical, lectin and alternative pathway.[138] The classical pathway is initiated by antigen/antibody immune complex formation and occurs when C1q binds to the F_c region of complement-fixing antibodies, IgM and IgG_1 which are generally attached to pathogenic surfaces during an innate immune response.[138] Binding leads to an inhibition of the toxic effects or infectivity of the intruding pathogen.[139] Complex formation initialises an efficient proteolytic cascade in which C1r and C1s are autocatalytically activated and cleave C4 and C2 into larger (C4b, C2a) and smaller (C4a, C2b) fragments (Figure 2-19).[138] Once cleaved, the larger fragments associate onto pathogenic surfaces and form the complex C4bC2a. This complex cleaves C3 (C3 convertase). Conversion of C3 by the C3 convertase is the converging point of all complement activation cascades. Here, C3 is cleaved into C3a and C3b, anaphylatoxin and opsonin and as well as into other products.[138,140] C3b can form stable covalent bonds to hydroxyl groups on proximate carbohydrates and proteins by an internally exposed thioester.[138] Through this 'tagging' activity, the complement system detects effectively microorganisms as foreign, leading to further complement activation.[138]

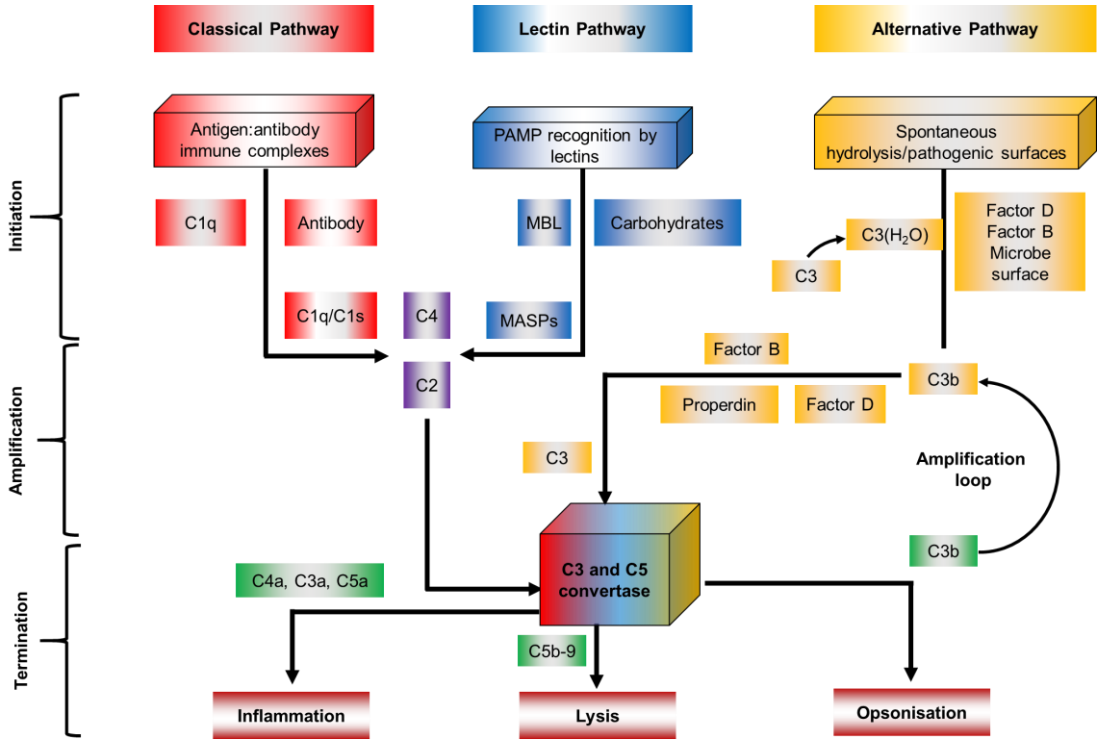

Figure 2-19: The complement system.
The complement system comprises three different proteolytic cascades: classical, lectin and alternative pathway. Each of them is divided in initiation, amplification and termination. All cascades share a converging point in which C3 or C5 convertases are formed, cleaving the corresponding substrates to give anaphylatoxins (C4a/C3a/C5a), and initialise three kinds of innate immune response. Redrawn from Ref..[138]

The immunoglobulin-independent lectin pathway functions in an analogous way, but employs germline-encoded PRRs, such as mannose-binding lectin (MBL). MBL focusses on highly conserved pathogen-associated molecular patterns (PAMPs), such as lipoteichoic acid of ´gram-positive bacteria, endotoxin or lipopolysaccharide of gram-negative bacteria, and β-glucan of fungi.[138] MBL activates the MBL-associated serine proteases (MASPs) and cleaves C4, C2 and the products form the classical and the lectin pathway C3 convertase, C4bC2a. C4bC2a cleaves C3 into C3b and C3a. C3b can further associate with C4bC2a, giving the C5 convertase of both pathways, C4bC2aC3b.[138]

The alternative pathway (AP) is initially activated by a spontaneous hydrolysis of AP C3 convertase to (C3(H_2O)). Together with the Factors B and D, the protease is proteolytically cleaved. The products activate AP C3 convertase (C3bBb) and AP C5 convertase (C3bBbC3b).[138]

Whereas macrophages, neutrophils of the innate immune system, together with the complement system provide a first line of defense against many common microorganisms and pathogens, some other infectious organisms and pathogens cannot be eliminated or recognised. They evade the innate immune system.[140]

Herein, the adaptive immune system has evolved a more versatile defense against subsequent reinfection with the same pathogen.[140] The critical role-playing cells of the adaptive immune system are macrophages, T and B lymphocytes and antigen presenting cells such as dendritic cells, or antigen-presenting cells (APC). Macrophages serve as a crucial important mediator between the innate and adaptive immune system. The engulfing and digestion of bacteria by macrophages leads to a secretion of chemokines and cytokines, and contribute to the T lymphocyte recruitment and activation.[140]

However, immature dendritic cells initialise an adaptive immune response by pathogen ingestion. They derive from the same bone marrow precursor as macrophages and are specialised long-living phagocytic cells which are resident in most tissues. After migration from the bone marrow through the lymph to the regional lymph nodes, immature dendritic cells survey the local environment for pathogens and interact with recirculating naive lymphocytes.[140]

Surface-presented receptors of the immature dendritic cells recognise common pathogenic materials, such as proteoglycans from bacteria. They stimulate the dendritic cells to ingest and digest the pathogen intracellularly. Immature cells take up constantly any other circulating pathogenic material, such as virus particles or bacteria, through the receptor-independent macropinocytosis.[140] The internalisation of a pathogen from an infection source induces the activation of the dendritic cells which initialise the transport of all pathogen-drained antigens to the peripheral lymphoid organs through the afferent lymphatics. Within, dendritic cells mature into APCs, secreting cytokines to recruit and activate pathogen-specific T-lymphocytes CD4+ and CD8+. They present the antigen in complex with major histocompatibility complex (MHC) molecules to the CD4+ (MHC Class II) and CD8+ (MHC Class I) T lymphocytes. This leads to the priming, activation, and proliferation of these primary naive cells.[140-143] Some of the naive CD4 T cells proliferate to T memory cells,

which persists in the lymph nodes for up to 10 years and are in charge of the enhanced immune response against the same pathogen.[140-143]

In the next step, T cells leave the lymphoid tissue and activate B cells (plasma cells) by presenting the pathogen antigen. B-cells initialise the gene expression of new specific and neutralising antibodies such as immunoglobulin G (IgG) and release them into the blood stream and tissue fluids. CD4+ T cells promote the cell-mediated immune response by activating B cells, wheras CD8+ T cells eliminate virus-infected or malignant cells.[140-143] Beside IgG, six classes of antibodies are known, including IgA, IgD, IgE, IgM, IgW and IgY. IgG marks an experienced infection or vaccination of the body and is produced by the adaptive immune system. It mediates the clearance of pathogens from the blood and is stored for a long period of time. IgA and IgD play an important role in pathogen recognition and B-cell stimulation, while IgE and IgM protect against intruding parasites and pathogens. IgW and IgY are found in sharks and chickens.[119,140-143]

2.8 Viruses

2.8.1 Herpesviridae

Infectious diseases caused by the viruses of the herpesviridae family are widely spread across vertebrate (e.g. humans, apes, cats) and invertebrate species (e.g. molluscs).[144] Though the symptoms of an infection can differ significantly, all subtypes of this virus family share the same particle morphology and molecular biological properties.[145] The large double-stranded linear DNA genome of herpes simplex viruses is replicated in the nucleus of an infected cell, where the first phases of the viral morphogenesis take place.[146] The viral genome is harboured in an icosahedral nucleocapsid, surrounded by a protein layer called tegument, and is enclosed by a lipid bilayer envelope containing different glycoproteins (Figure 2-20).[147] During the replication of herpesviruses, the lipid bilayer envelope is primary generated by the nuclear membrane of infected cells, and later substituted by a membrane of the *trans*-Golgi apparatus.[147-149] All herpesviruses encode various enzymes which are activated during their nucleic acid metabolism and genome replication. Cells, in which the virus reproduction becomes lysogenic, die and the new virus particles are then released. After primary infection, all viruses of the herpesviridae persist lifelong in their hosts by establishing a latent infection interrupted by recurrent reactivations.[147] Nowadays, more than 200 herpesviruses have been identified, including eight human herpes viruses. Based on their cell specificity, self-replication and pathogenicity, herpesviruses are categorised into α–, β– or either into γ-herpesvirus subfamilies.

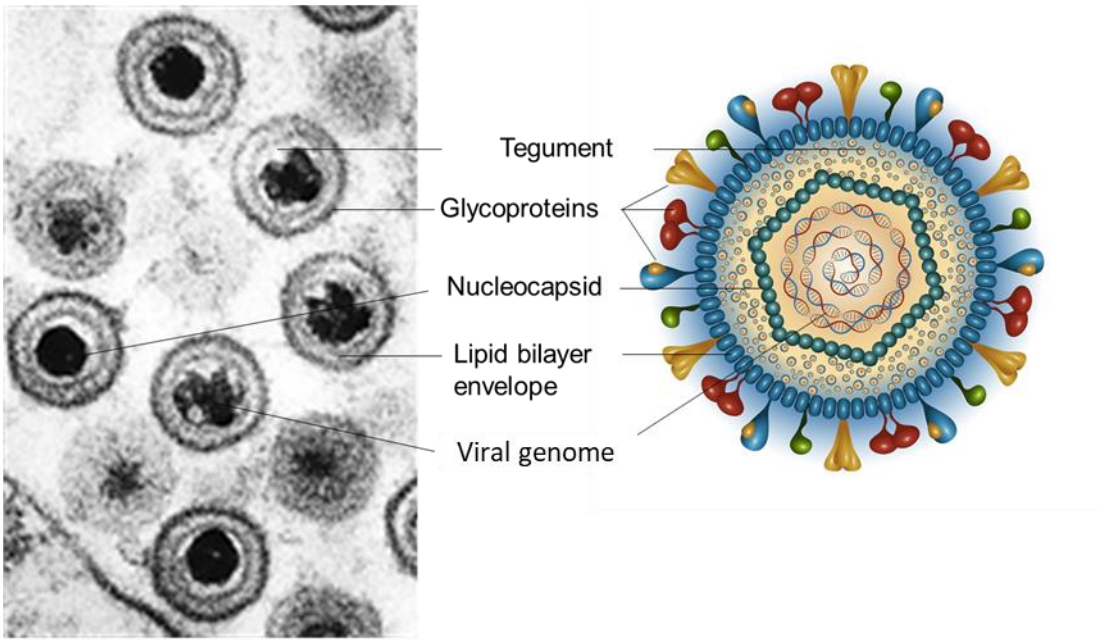

Figure 2-20 Virion structure of a herpes virus.
Herpes viruses are comprised of three major compartments; An icosahedral nucleocapsid, containing the densely coiled viral genome, the lipid bilayer envelope with embedded glycoproteins and a proteinaceous region between the nucleocapsid and the bilayer envelope called tegument.[147,150,151]

Predominantly, infectious diseases of the skin are caused by herpes simplex virus type 1 and 2 (HSV-1, -2) as well by the varicella zoster virus, which belong to the α-herpesvirus subfamily; the human cytomegalovirus (HCMV), HHV-6 and HHV-7, which belong to the β-herpesvirus subfamily; and the lymphatic system by the Epstein Barr virus, human herpes viruses type 6, 7 and 8, which belong to the γ–herpesvirus subfamily.[147,152]

2.8.1.1 Herpes simplex virus HSV-1

Together with the herpes simplex virus type 2 (HSV-2), HSV-1 is the archetypal member of the α–herpesvirus family.[151] Both viruses types have adapted well to the human body and are among the most ubiquitous of human infections that persist lifelong.[152,153] Since ancient times, sores forming skin diseases have been known and called *Herpes.* Interestingly, in the past centuries in human history, infections by the herpes simplex virus have been described many times. Even in the play *Romeo and Juliet* (1595). Herein William Shakespeare describes an obviously recurrent orofacial infection and later in 1763, Jean Astruc, the medical attendant of King Louis XV found evidences for genital herpes.[152] Beside the orofacial and genital herpes virus infections, which both can be caused by HSV-1, HSV-2 is almost exclusively sexual

transmitted, causing infection in the genital or anal area and it is less frequent than HSV-1 infections.[153,154] HSV-1 can cause further severe diseases when it infects the eyes (Herpetic Stromal Keratitis) or the central nervous system (Herpes Simplex Encephalitis) and can lead, untreated to life-threating infections in immunocompromised persons.[151,153-155] The World Health Organisation (WHO) has updated its fact sheet on Herpes Simplex Virus infections this year.[156] They have estimated that since 2012, 3.7 billion people under the age of 50 (67%) worldwide have a HSV-1 infection and the prevalence of the infected was the highest in Africa (87%) and the lowest in the whole of America (40-50%). In America 140 million people aged 15-49 years have genital HSV-1 infection, but prevalence varied substantially from region to region.[154,157] Today, HSV-1 infections are well-treated with antiviral DNA targeting chemotherapeutics composed of nucleoside derived antiviral drugs such as acyclovir (ACV), famciclovir (FCV), and valacyclovir (VCV). These are the most efficacious medications available for people with HSV infections. These medications can decrease the severity and frequency of symptoms but cannot cure the infection totally.[157] Furthermore, after two decades, an increasing incidence of ACV and multidrug-resistant strains in patients with corneal HSV-1 infections leading to Herpetic Stromal Keratitis (HSK) and more often results in blindness, has been reported and is still a major health problem of industrialised countries.[158-160] Latent HSV infections are considered invisible for the human immune system due to the well adaption of the virus which is reflected by the viral composition.[161] The human HSV-1 virion comprises three major structural elements. First, an icosahedral-shaped and 152-kbp large genome containing nucleocapsid. Second, the envelope that consists of a lipid bilayer with embedded glycoproteins, which mediate the infectivity. Third a region between the capsid and the envelope called the tegument, which contains over 20 proteins. It serves as a delivery compartment for proteins that are required in the early course of infection (Figure 2-21).[151,162]

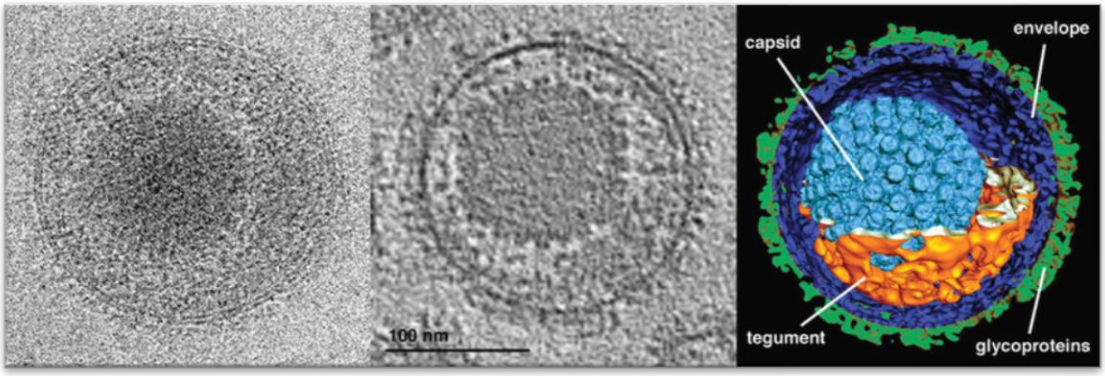

Figure 2-21: Tomographic reconstruction of herpes simplex virus 1 virions in vitreous ice.
Left, an electron-microscopic image of the architecture of the herpes simplex virus 1; middle, a cross section through the reconstructed and noise reduced tomogram; right, a detailed 3D structure of the herpes virion after the segmentation of its main components from the electron tomogram (with permission).[151,162]

The glycoproteins on the virion surface are responsible for the virus infectivity. Moreover, the HSV-1 can spread easily either by releasing virions from infected cells (cell-free spread) or by moving directly between adjacent cells without diffusing through the extracellular space (cell-to-cell spread).[159] The cell-to-cell spread enables the virus to bypass cellular barriers and to circumvent the classic recognition by neutralizing antibodies.[159] Here, the glycoproteins gD, gB, and gH/gL on the surface of HSV-1 are critically involved in the extracellular virus entry by the cell-to-cell spread process (Figure 2-20). To prevent the virus from cell-to-cell spreading, several viral glycoproteins gH, gD, and gB specific monoclonal antibodies have been raised in mice.[159] Based on gB-derived peptide sequences, Krawczyk *et al.* developed a gB-specific monoclonal antibody that exhibits strong HSV-neutralizing capacity and abrogates the viral cell-to-cell spread both *in vitro* and *in vivo* models.[159,163]

3 Results and discussion

3.1 *In vitro* imaging of mCherry-mRNA with F30-2xdBroccoli by calcium phosphate nanoparticle mediated transfection

In this study, the F30-2xdBroccoli RNA aptamer was used to label a plasmid-encoded cDNA of a fluorescent protein, mCherry, to study the time-resolved trafficking of mRNA translation and protein expression by fluorescence microscopy with the help of calcium phosphate nanoparticles. This study should elucidate the transcription and expression in human epidermal kidney cells HEK293T as a eukaryotic cell model using calcium phosphate nanoparticles as a transfection agent. This system was applied mainly to prokaryotic systems but is new to eukaryotic cells.

3.1.1 Construction of pCherries'n'Broccolies

The eukaryotic expression vector pcDNA3.3mCherry-F31-2xdBroccoli (pCherries'n'Broccoli or pChBr) was obtained by the HiFi DNA assembly cloning method.[164] pCherries'n'Broccolies has a pcDNA3.3 backbone that serves as a vector for subsequent cloning. The backbone was amplified through PCR from the pcDNA3.3_EGFP plasmid (Addgene, code #26822) by a high-fidelity DNA polymerase (Thermo Fisher). The following forward and reverse primers were used: 5'-TAA GCT GCC TTC TGC GGG-3' and 5'-GGT GGC TCT TAT ATT TCT TCT TAC TCT TC-3'. The inserts mCherry and F30-dBroccoli were also amplified via PCR from pcDNA3.3mCherry and pET28c-F30-2xdBroccolic (Addgene, #26822), respectively.

3.1.2 Engineering of F31 from F30

During the transcription from cDNA to RNA, RNA folds into distinct regulatory active structure motifs which are involved in the expression´s regulation of a protein in a living cell. A misfolded RNA structure motif might have a tremendous impact on a cell, e.g. toxification or even cell death.[165] For this reason, preserving the integrity of the secondary structure of RNA transcripts especially for the used 2xdBroccoli aptamer plays an important role. Furthermore, high specificity and affinity of aptamers is reflected by their 3D conformation. Aptamers which fold incorrectly do not recognise their target (here, DFHBI). The prediction of 2D structures of RNA with RNAfold[166] gives a good lead on how the nascent transcribed RNA is most likely folded

in cells. In a first attempt, the secondary structure of a full-length RNA transcript of mCherry-2xdBroccoli was analysed by the RNAfold prediction webtool.[166] The RNAfold analysis of the full-length transcript revealed a loss of the structural integrity of the attached F30-2xdBroccoli aptamer. The conserved structure motif of the aptamer was misfolded and showed low MFE base-pair probabilities compared to the expected F30-2xdBroccoli 2D structure (Figure 3.1 A). In detail, the secondary structure of one of the two dimeric broccoli aptamers remained properly folded while the scaffold F30 and the second dimeric Broccoli aptamer showed a poorly folded structure. The RNA transcript of mCherry and its 3'- and 5'-UTRs were also poorly folded and showed four structural matching regions indicating a non-functional or less readable mRNA of mCherry (Figure 3.1 B). The processing of such a construct for later cloning might lead to a poor outcome of fluorescent signals after transfection. To overcome this problem, engineering of the viral F30 scaffold was carried out. A good anchor point to modify the F30 scaffold is the elongation of its stem (Figure 3.1 A). With the addition of several complementary base-pairs within the stem region of the F30 scaffold, the stem should get a longer distance to the centre loop to retain the native folding structure of the full-length mCherry RNA transcript.

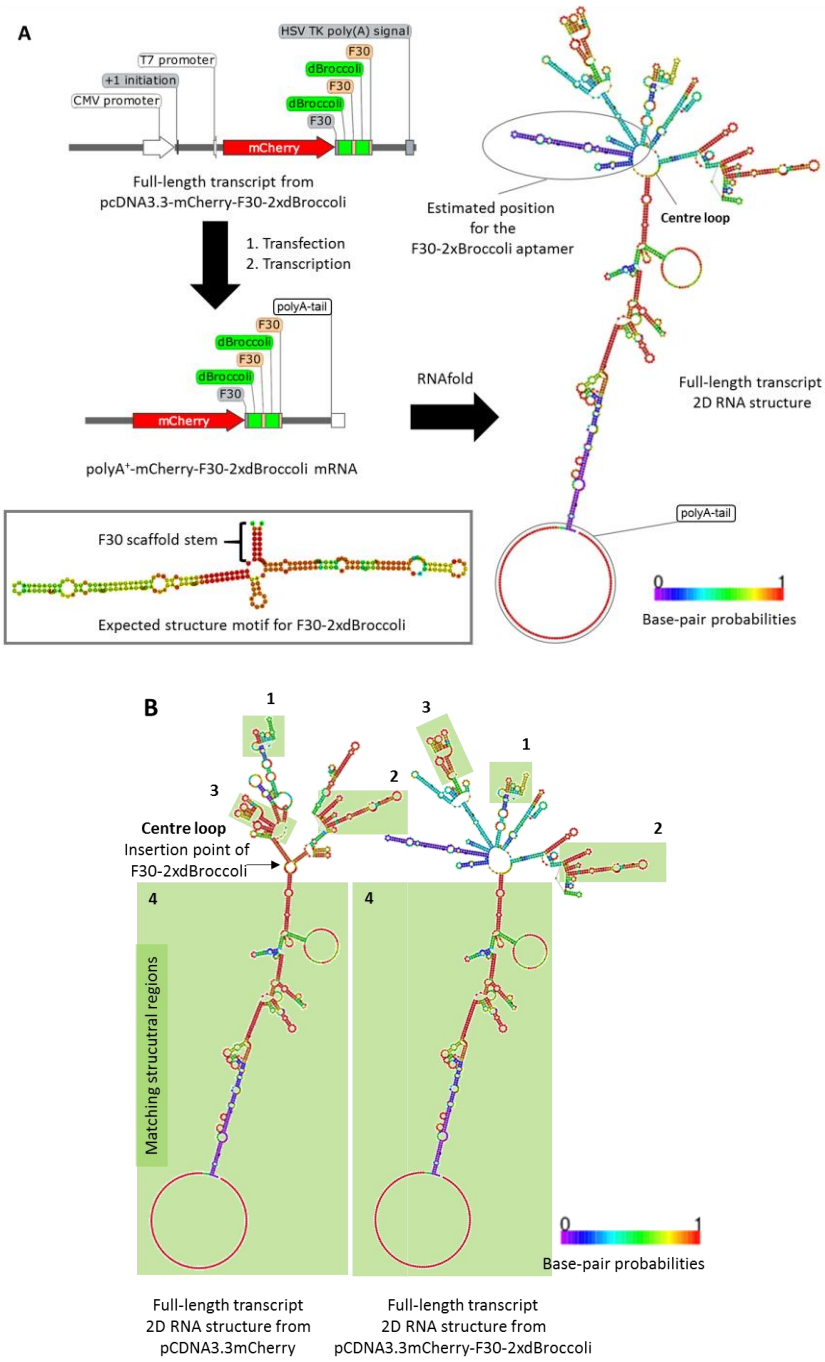

Figure 3-1: RNAfold analysis of the full-length transcript from pcDNA3.3mCherry-F30-2xdBroccoli. Structure analysis of the 2D folding of the full-length transcript from pcDNA3.3mCherry-F30-2xdBroccoli using RNAfold. A: After initial transfection and transcription, the transcript carries a posttranscriptional polyA-tail at the 3'-end and the 5´-UTRs. The computational RNAfold prediction of the full-length RNA transcript revealed a misfolded 2D RNA structure. For F30-2xBroccoli, one of the two dimeric broccoli aptamers is not or less folded with low base-pair probabilities for the given 2D RNA structure. A misfolded F30 scaffold, compared to the expected structure motif of F30-2xdBroccoli, is found at the estimated position for the F30-2xdBroccoli aptamer in the full-length transcript from pcDNA3.3mCherry-F30-2xdBroccoli. B: Comparison of both full-length RNA transcripts from pcDNA3.3mCherry and F30-2xdBroccoli elongated transcript. The RNA transcript from pcDNA3.3mCherry shows only four structural matching regions with the modified full-length transcript from pcDNA3.3mCherry-F30-2xdBroccoli indicating a non-functional RNA of mCherry after transfection.[166]

Thus, the elongation with complementary base pairs (e.g. GC), should have a beneficial effect on both the structural integrity of the F30-2xdBroccoli scaffold and the mCherry RNA structure. Therefore, an iterative analysis approach was performed that consists of repetitive cycles of RNAfold prediction, comparison, analysis and modification of the primary RNA sequence in the stem of the F30 scaffold.[166] Figure 3-2 shows the iterative RNA folding analysis approach. After nine cycles, the final modified F30 scaffold, F31, was obtained which showed an intact 2D RNA structure for the two dimeric broccoli aptamers and for mCherry. The obtained sequence was then used for later cloning through HiFi DNA assembly.

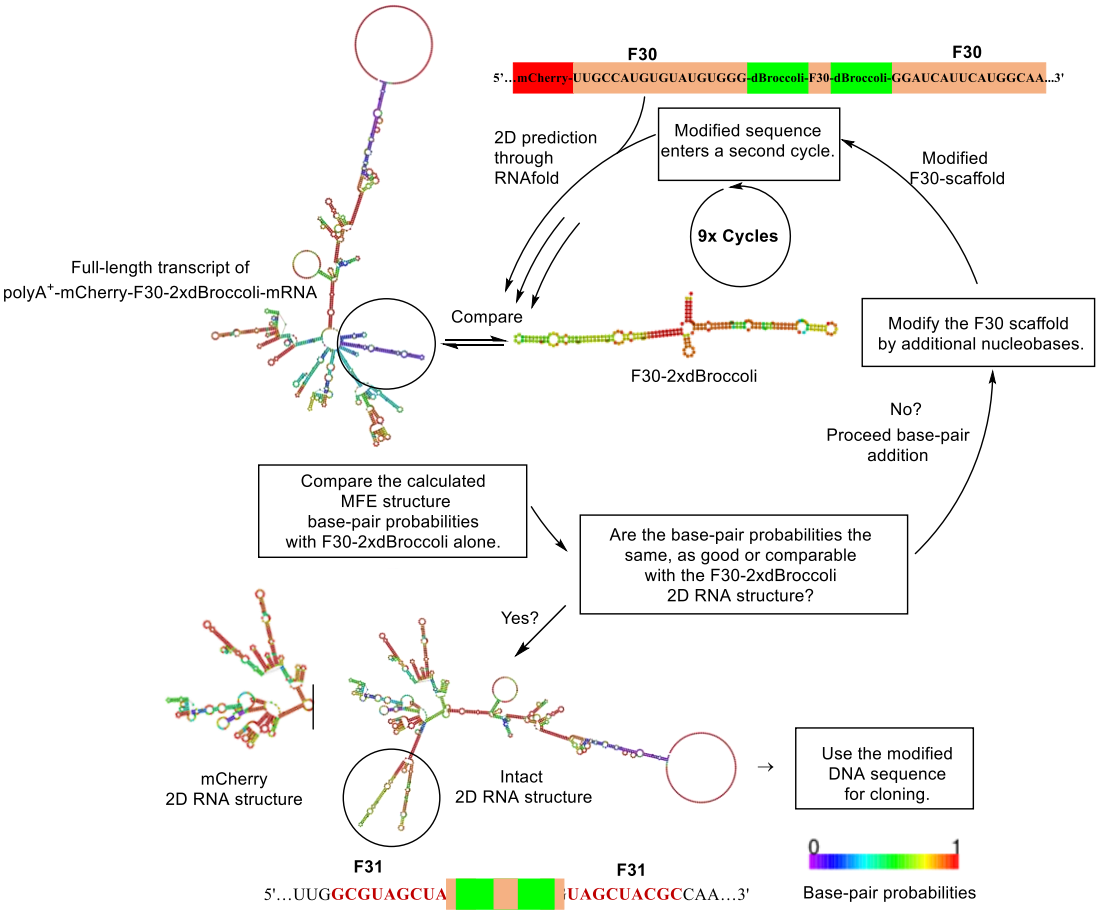

Figure 3-2: Engineering F31 from F30 by iterative cycles of 2D RNA structure prediction with RNAfold. An iterative 2D RNA folding analysis approach was used to obtain the engineered F30 scaffold F31. First, the primary sequence is pasted in the input line of RNAfold. The predicted structure is compared to the native structure of F30-2xdBroccoli and the overall structure of mCherry. Then, both predictions, native and modified, are analysed for structural similarities.

3.1.3 Generation of pCherries'n'Broccolies (pcDNA3.3-F31-2xdBroccoli-mCherry, pChBr)

The final construct was obtained through a HiFi DNA assembly.[164] The F31-2xdBroccoli insert was generated through a PCR extension from the plasmid pET28c-F30-2xdBroccoli. In a first PCR reaction, F30 was amplified with F31-Fwd (5'-TTG GCG TAG CTA CCA TGT GTA TGT GGG AGA-3') and F31-Rev (5'-CTT GGC GTA GCT ACC ATG AAT GAT CCA GCC C-3'), giving the PCR-product F31ext. The PCR product was purified by gel extraction and the concentration was determined through UV/Vis spectroscopy. Next, overhanging DNA strands of mCherry and pcDNA3.3 were added in a second PCR using the primer set F312xdBroccoliFwd (5'-GTA CAA GTA ATT GGC GTA GCT ACC ATG TG-3') and F312xdBroccoliRev (5'-GCC CCG CAG AAG GCA GCT TAC TTG GCG TAG). The PCR product was purified and kept on ice for subsequent cloning. The PCR product for mCherry was obtained with the primer mcherryFwd (5'-TAA GAA GAA ATA TAA GAG CCA CCA TGG TGA GCA AGG GCG AG-3') and mcherryRev (5'-GCT ACG CCA ATT ACT TGT ACA GCT CGT CCA TG-3') in an analogous way. The obtained three dsDNA fragments were assembled in one HiFi DNA assembly reaction using 1x HiFi DNA AssemblyMix and 0.03 pmol of pcDNA3.3, 0.06 pmol of mCherry, 0.15 pmol of F31-2xdBroccoli. The mixture was incubated for 15 min at 50 °C and diluted 1:4. 2 µL of this dilution were used for the transformation in *E. coli* XL1 Blue cells. After cPCR and DNA sequencing of the promising clones, one colony was chosen for the plasmid preparation in mg scale.

3.1.4 Construction of the control plasmid pBroccolies (pcDNA3.3-F31-2xdBroccoli, pBr)

The control plasmid pBroccolies (pcDNA3.3-F31-2xdBroccoli, pBr) was obtained by assembling 0.015 pmol of the pcDNA3.3 dsDNA fragment with 0.075 pmol of the PCR product F31Ctrl (contains the dsDNA overhangs to the backbone DNA). This was generated by a PCR extension with F312xdBrCrtlRev (5'-GCC CCG CAG AAG GCA GCT TAT TGG CGT AGC TAC CAT GAA TG-3') as reverse and F312xdBrCrtlFwd (5'- TAA GAA GAA ATA TAA GAG CCA CCT TGG CGT AGC TAC CAT GTG-3') as forward primer.

3.1.5 Test transfection with Lipofectamine 2000

To validate the plasmid integrity and its function, a qualitative transfection analysis was carried out. The plasmid was transfected in HEK293T cells using Lipofectamine 2000 (Thermo Fisher). Lipofectamine 2000 is known as the gold standard for plasmid transfection, but shows some cytotoxic effects to a number of cell lines.[167] The images of the test transfection are shown in Figure 3-3. Herein, 40,000 HEK293T cells per well were incubated with 1 µg DNA for 24 h following the manufacturers´ protocol. 30 min prior to the imaging by fluorescence microscopy, the cells were incubated with prewarmed imaging media (20 µM DFHBI + DMEM with no phenol red or vitamins and supplemented with 25 mM HEPES pH 7.4).

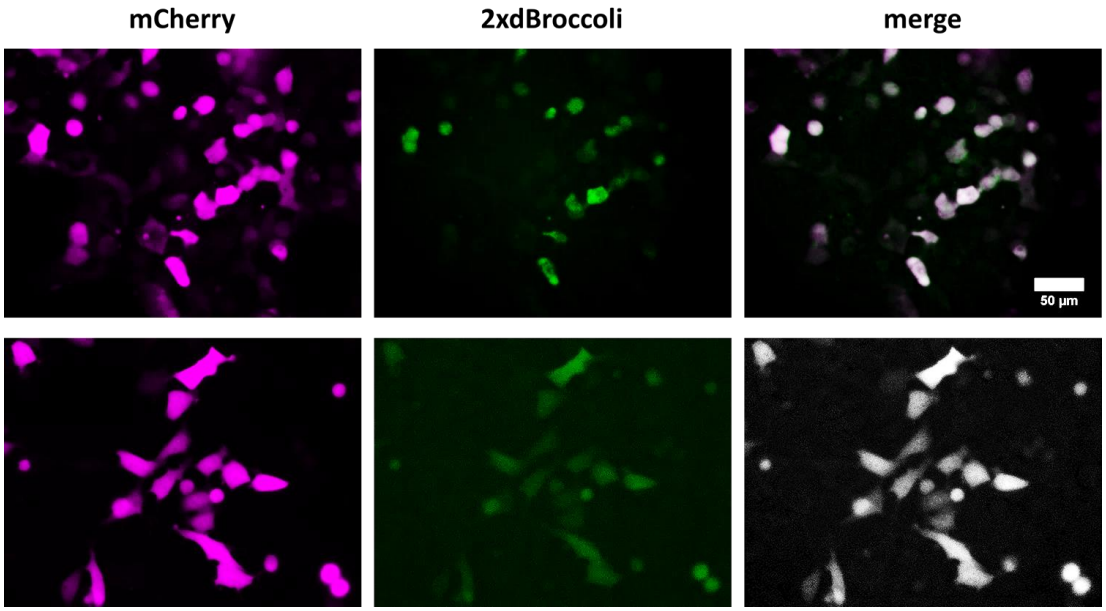

Figure 3-3: pCherries'n'Broccolies transfected cells with Lipofectamine 2000.
24 h after the transfection, HEK293T cells express the fluorescent protein mCherry properly (mangenta). On the mRNA level, dBroccoli is transcribed, indicated by the fluorescence-emitting DFHBI/2dBroccoli complex (green). Merged images of the cellular transcription and transcription (grey). (40x, scale bar 50 µm).

As depicted in Figure 3-3, the data indicates the full functionality and integrity of the designed plasmid pCherries'n'Broccolies (pChBr), visible by means of the red fluorescence from mCherry and the green fluorescence-emitting DFHBI/2xdBroccoli complex. Therefore, the rational designed plasmid for was successfully cloned and could later be used for the time-lapsed visualisation of mRNA transcription and protein translation.

The same experiment was repeated in the same manner for the control plasmid pBroccolies (pBr) which was obtained by an DNA assembly and does not contain the genetic mCherry cDNA, but in this case no positive fluorescent signals were detected (data not shown). It was assumed that the nascent mRNA of F31-2xdBroccoli is misfolded in the cell due to the flanking 5'- and 3'- untranslated regions (UTRs). These regions play a crucial role in the initiation and termination of gene expression, forming regulative secondary mRNA structures that control the reading of mRNA.[168] To ensure this, a time-lapsed nanoparticle-mediated transfection experiment was carried out with both plasmids.

3.1.6 Synthesis of CaP/pCherries'n'Brococlies/CaP/PEI and CaP/pBrococlies/CaP/PEI nanoparticles

For the nanoparticle-mediated transfection of pCherries'n'Broccolies or pBroccolies, plasmids were loaded separately on double-shell calcium phosphate nanoparticles. These nanoparticles have been used successfully in earlier eukaryotic transfection studies of pcDNA3.3eGFP, containing the genetic information for the green fluorescent protein eGFP.[45] Therefore, the plasmid-loaded calcium phosphate nanoparticles were synthesised as previously described.[45] Briefly, for each type of nanoparticle dispersion, 534 µL of 6.25 mM $Ca(NO_3)_2$ (pH 9) and 534 µL 3.74 mM of $(NH_4)_2PO_4$ (pH 9) were combined in a 5 mL tube and mixed continuously by rapid vortexing. Immediately, 174 µg of each plasmid (pCherries'n'Broccolies (pChBr, 4.5 mg mL^{-1}) and pBroccolies (pBr, 11.3 mg mL^{-1}) was added to the nascent CaP dispersion. Subsequently, the precipitation step with 534 µL of 6.25 mM $Ca(NO_3)_2$ (pH 9) and 534 µL of 3.74 mM $(NH_4)_2PO_4$ (pH 9) was repeated, obtaining a second DNA protective shell of calcium phosphate. Finally, the dispersion was stabilised by adding 90 µL PEI (2 g L^{-1}). The dispersion was removed from non-adsorbed reagents by centrifugation for 20 min at 21,000 g at 4 °C and finally redispersed by ultrasonication in 1 mL pure water. The DNA concentration on the nanoparticles was determined through UV spectroscopy from the supernatant, revealing a total nanoparticle-adsorbed DNA amount of 24.1 µg mL^{-1} (13.8% yield) for pChBr loaded and 20.9 µg mL^{-1} (12% yield) for pBr loaded calcium phosphate nanoparticles. These results correlate with earlier data and were comparably consistent.[45]

3.1.7 Characterisation of synthesised nanoparticles

The results of the colloidal characteristics are shown in Figure 3-4 and Table 3-1. The data of the DLS measurement pointed out an average diameter of 475 nm and revealed unstable nanoparticles regarding the PDI (0.4-0.5) and the zeta potential, (+6-10 mV). A pronounced degree of agglomeration and agglutination was observed through the SEM data (Figure3-4). However, the data is consistent with previously synthesised nanoparticles and should not influence the nanoparticle-mediated transfection as demonstrated before.[45]

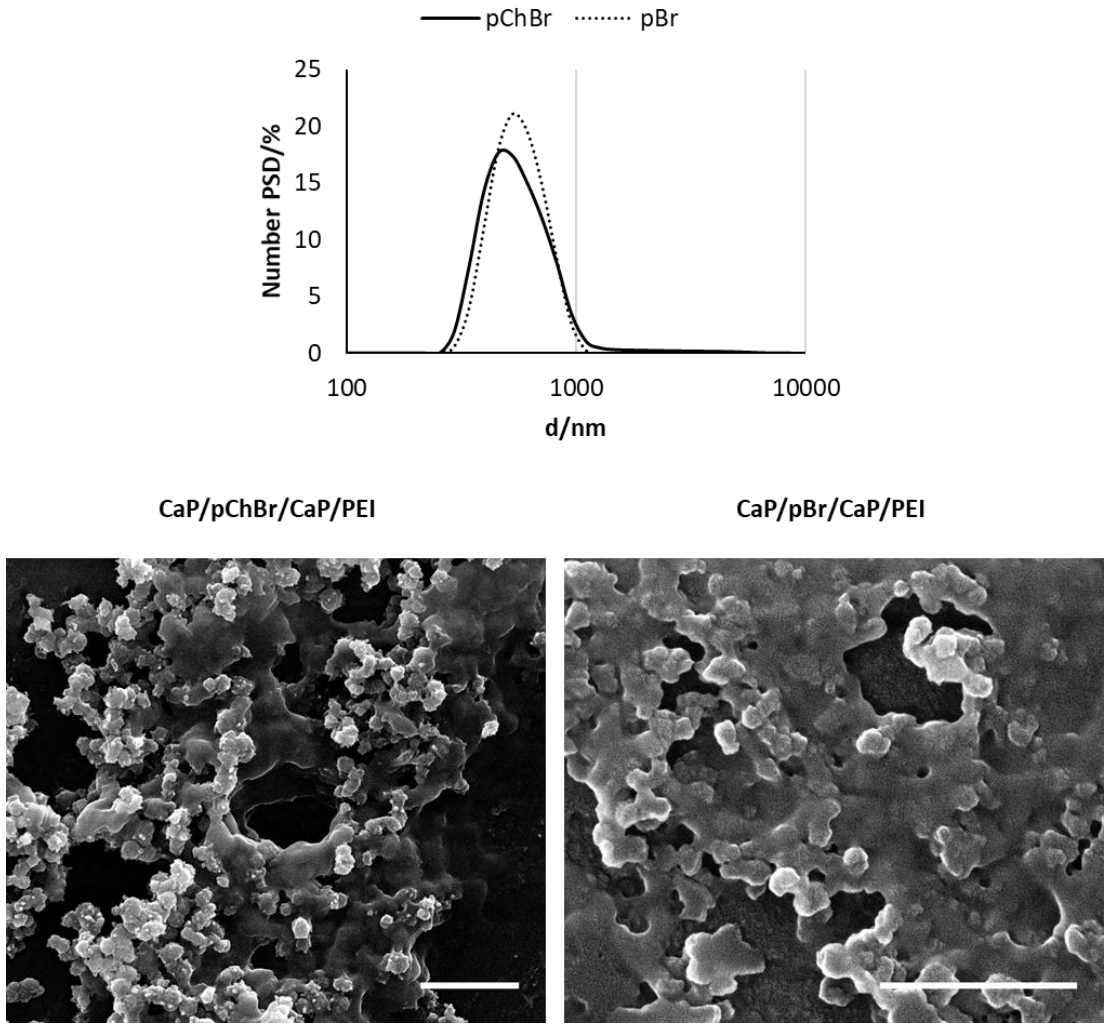

Figure 3-4: DLS and SEM results of the synthesised nanoparticles.
At the top, the DLS result of CaP/pChBr- and CaP/pBr/CaP/PEI. The broad PSD indicates a polydisperse suspension of each type of nanoparticle. Lower left, SEM images of CaP/pChBr/CaP/PEI nanoparticles, showing partially a spherical but not homogenous morphology. Lower right, SEM images of CaP/pBr/CaP/PEI nanoparticles, showing partially a spherical as well, but not homogenous morphology. Scale bar 500 nm.

The number of particles was calculated by using the equation Eq. 13 of chapter 5.5. The amount of Ca^{2+} was determined by AAS with 96.4 µg mL^{-1} for the pChBr loaded and with 78.4 µg mL^{-1} for the pBr loaded nanoparticles, giving the stoichiometrically calculated hydroxyapatite concentration of 242.1 µg mL^{-1} or 196.9 µg mL^{-1}, respectively. The nanoparticle concentration in 1 mL colloidal dispersion was computed from the calcium phosphate concentration and the density of hydroxyapatite (3,140 kg m^{-3}) under the assumption of spherical and uniformly shaped particles, taking the diameter from SEM (118 nm or 128 nm). In the case of the pChBr loaded nanoparticles, the calculated nanoparticle concentration was $8.96 \cdot 10^{10}$ particles mL^{-1} or $5.70 \cdot 10^{10}$ particles mL^{-1} in the case of pBr loaded nanoparticles.

Table 3-1: Characterisation of double-shell nanoparticles CaP/pChBr/CaP/PEI and CaP/pBr/CaP/PEI

Parameter	CaP/PEI/plasmid/CaP/PEI		
	pChBr	**pBr**	**Avg.**
Solid core diameter by SEM/nm	118	128	123
V(one nanoparticle; only CaP)/m^3	$8.6 \cdot 10^{-22}$	$1.1 \cdot 10^{-21}$	$9.7 \cdot 10^{-21}$
A(one nanoparticle; only CaP)/m^2	$4.4 \cdot 10^{-14}$	$5.1 \cdot 10^{-14}$	$4.8 \cdot 10^{-14}$
m(one nanoparticle; only CaP)/kg	$2.7 \cdot 10^{-18}$	$3.5 \cdot 10^{-18}$	$3.1 \cdot 10^{-18}$
w(Ca^{2+}) by AAS/µg mL^{-1} (= g m^{-3})	96.4	78.4	87.4
w($Ca_5(PO_4)_3OH$)/µg mL^{-1} (= g m^{-3})	242.1	196.9	219.5
N(nanoparticles)/number mL^{-1}	$8.96 \cdot 10^{10}$	$5.7 \cdot 10^{10}$	$7.2 \cdot 10^{10}$
MW(plasmid)/g mol^{-1}	$4.1 \cdot 10^{6}$	$3.7 \cdot 10^{6}$	$3.9 \cdot 10^{6}$
w(plasmid)/µg mL^{-1} (= g m^{-3})	24.1 (13.8% yield)	20.9 (12% yield)	20.9 (13% yield)
N(plasmid)/number mL^{-1}	$3.5 \cdot 10^{12}$	$3.4 \cdot 10^{12}$	$3.7 \cdot 10^{12}$
m(plasmid) per nanoparticle/kg	$2.7 \cdot 10^{-19}$	$3.7 \cdot 10^{-19}$	$3.1 \cdot 10^{-19}$
N(plasmid) per nanoparticle	39	60	51
Area occupied by plasmid/plasmid μm^{-2}	896	1160	1073
wt ratio plasmid to calcium phosphate	1:10.0	1:9.42	1:9.75
Hydrodynamic diameter by DLS/nm	475±22	483±323	475
PDI by DLS	0.437	0.541	0.489
Zetapotential by DLS/mV	10.8	6.9	8.9
Particle composition			
CaP/wt-%	90.9	90.4	90.7
Plasmid/wt-%	9.1	9.6	9.3

Together with the measured plasmid concentration from the supernatant (24.1 µg mL^{-1} or 20.9 µg mL^{-1}) and the molecular weight of each plasmid, the number of plasmid molecules per millilitre in the dispersion was calculated. A concentration of $3.5 \cdot 10^{12}$ plasmids mL^{-1} (pChBr) or $3.4 \cdot 10^{12}$ plasmids mL^{-1} (pBr) was computed for these dispersions. Further results of the characterisation of the synthesised nanoparticles are summarised in Table 3-1.

3.1.8 Live cell imaging of pChBr and pBr transfected cells

For the time-lapse monitoring with pCherries'n'Broccolies (pChBr), HEK293T cells were seeded on a four-chamber slide at 80,000 cells per well and were treated for 6 h at 37 °C (5% CO_2, humidified atmosphere) with 1-2 µg DNA (41-82 µL) or with $3.74\text{-}7.4 \cdot 10^9$ calcium phosphate nanoparticles per well which corresponds to about $4.7\text{-}9.4 \cdot 10^4$ particles per cell. The medium was vacuumed, and the cells were carefully washed twice with DPBS to remove non-incorporated nanoparticles. The medium was substituted with fresh prewarmed media containing 20 µM DFHBI. The cells were imaged with a Keyence Biorevo BZ-9000 microscope (Osaka, Japan) connected to a live-cell chamber (Tokai Inu) and equipped with an air objective S Plan Fluor ELWD 40×/0.60 OFN22 Ph2 WD 3.6±2.8 (Nikon, Japan). For the live-cell imaging, up to 6 imaging-positions were set to obtain an appropriate numeric coverage. Images were taken every hour over 32 h. Figure 3-5 shows the live-cell imaging results of HEK293T cells that were transfected with pChBr. The incidence of an upcoming fluorescence signal after 8 h implied the gene expression of mCherry and indicated the intake of the plasmid-loaded nanoparticles by the cells. Interestingly, no fluorescence-signal of the RNA-imaging aptamer was detected at that time-point, though mRNA is generally transcribed before its translation into a protein. This may be due to various reasons. First, after the DNA transcription, the nascent RNA is usually directly translocated into the cytoplasm and recruited by the ribosome for subsequent biosynthesis of a protein.[169,170] This may lead to an insufficient number of DFHBI-recognising RNA aptamers, resulting from a continuous mRNA recruitment and molecular competition by the protein synthesis machinery. Second, by this process, RNA is folded into distinct secondary structure motifs that may interfere with the nascent folding RNA aptamers. Third, by the intrinsic fluorescence of mCherry which is light-induced and

generated by the autocatalytic cyclo-isomerisation of three nearby amino acids in the β-barrel scaffold of mCherry. It is then compared to DFHBI which is not exclusively depended on the passive diffusion or the interaction between DFHBI and dBroccoli, leading to a less fluorescent signal of the dBroccoli/DFHBI complex.[171] However, a green fluorescent signal was detected 2 h later and signal was again detected 6 h later (16 h) (Figure 3-5), indicating the correct formation of the fluorescent active DFHBI/dBroccoli-complex. This corroborates the assumption of two competing complexes; the DFHBI/dBroccoli complex and the protein-synthesising ribosome. Herein, the mRNA transcription of mCherry'n'Broccolies is mediated by the CMV promotor. The viral-derived CMV promotor on the plasmid pChBr has been reported to mediate strong expression in various cellular systems, leading to an enhanced transcription of the plasmid encoded genes.[172,173] Thus, the ribosome might not able to translate the nascent mRNA completely into the protein, whereupon the interaction between DFHBI and dBroccoli is favoured and gives rise to the fluorescent signal. Over the whole observation time, from 16 to 32 h, both signals remained constant, but neither further expression of mCherry nor the transcription of dBroccoli in neighboured cells was observed. The total transfection efficiency of <2% is low compared to the lipo-based tested transfection. Among others, Neuhaus *et al*. could reveal that the transfection efficiency is mainly depended on the cell line that is used and also diverges when various transfection agents are applied.[45,174,175] As the lipo-based transfection revealed the latter mentioned result was obtained for the live cell-imaging of the nanoparticle-mediated plasmid transfection of Broccoli pBr (data not shown). Therefore, to obtain a functional plasmid that is transcribed properly in cells, a new plasmid without the 3'-and 5'-UTRs was designed.

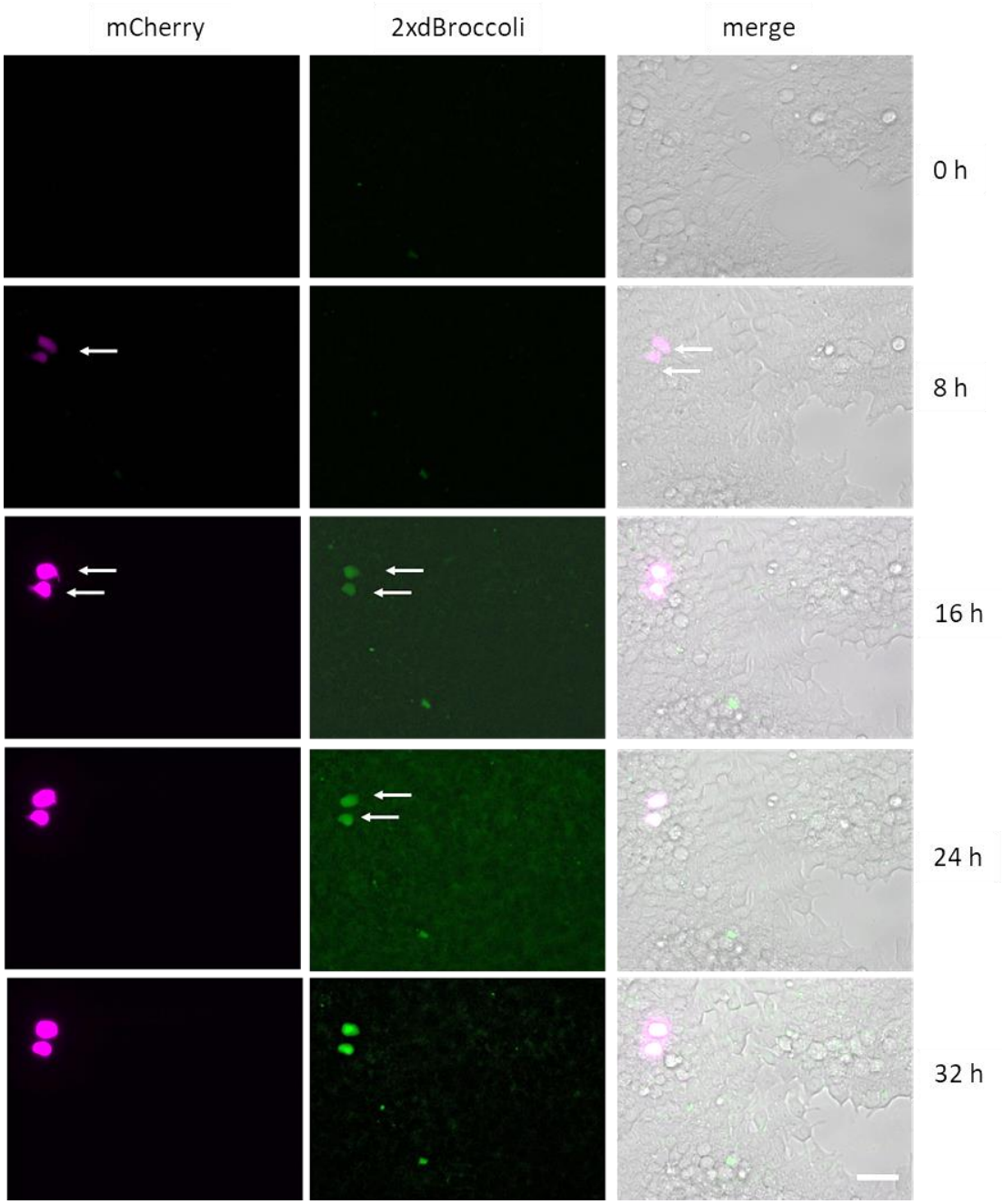

Figure 3-5: Live cell imaging of pChBr transfected cells with CaP/pChBr/CaP/PEI nanoparticles.
Live cell imaging was recorded for up to 32 h, HEK293T cells were seeded on a four-chamber slide at 80,000 cells well^{-1} and incubated for 6 h with pChBr loaded triple-shell calcium phosphate nanoparticles, containing 1-2 µg pChBr. Nanoparticles were removed, cells were washed twice with DPBS and re-cultivated with fresh media containing 20 µM DFHBI. Cells expressed the red fluorescence protein mCherry (magenta) after 8 h while the green fluorescence-emitting DFHBI/dBroccoli-complex (green) was formed 8 h later. (Scale-bar 50 µm, 40x magnification)

3.1.9 Design and construction of UTRs deleted control plasmid pΔBroccolies (pΔBr)

In the case of pCherrries'n'Broccolies (pChBr), the results clearly demonstrated that the 2D RNA prediction can be used to generate an aptamer labelled cDNA that folds correctly in cells. However, only poor results were obtained for the control plasmid pBroccolies (pBr) which indicate a misfolded secondary RNA structure of the inserted F31-2xBroccoli aptamer. In fact, pBroccolies is a mCherry truncated version of pCherries'n'Broccolies and is flanked by the same untranslated regions (UTRs). The secondary RNA structure of the 5'-UTR and 3'-UTR are important regulation factors in the orchestra of protein expression.[168] Whereas the secondary structures within the 5'-UTR are mostly responsible for the recruitment of the ribosome and the initiation of the protein expression. The secondary RNA structure within the 3'-UTR deals with its termination. Those structure elements can be important for the protein expression of a gene of interest but might be less important in the case of the production of a short RNA aptamer in cells since it is known that aptamers can fold improperly due to hybridisation with an adjacent sequence. The sequence of pBroccolies was cloned directly between the 5'-untranslated region (UTR) and the 3'-UTR of the pcDNA3.3 backbone (Figure 3-6).

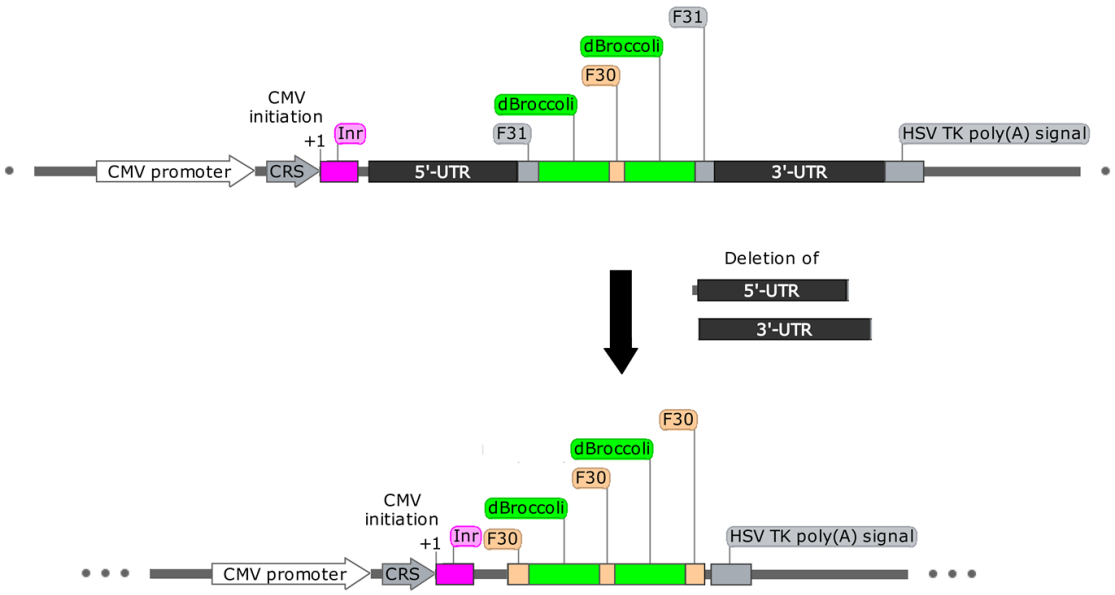

Figure 3-6: Generation of pΔBroccolies.
5'-UTRs and 3'-UTRs were deleted by DNA assembly.

Prior to the cloning, the RNA sequence was uploaded to the RNAfold TBI server to ensure the correct RNA folding. The new sequence without the UTRs was computed as stable which was indicated by a high base-pair probability and the correctly computed 2D RNA structure (Figure 3-7 A) whereas UTRs-containing sequence led to a misfolded structure (Figure 3-7 B). This corroborates the pre-assumed hypothesis of an UTRs-introduced misfolding of the RNA structure. Thus, the UTRs were deleted in pBr by a new DNA assembly with primers which do not contain the genetic information for the UTRs. To obtain the new plasmid, the HiFi-DNA Assembly kit from new England Biolabs was used, following the manufactures' protocol. Briefly, the control plasmid pΔBroccolies (pcDNA3.3-F31-2xdBroccoli ΔUTR's, pΔBr) was obtained by assembling 0.015 pmol of the backbone dsDNA pcDNAΔ3.3UTR's (contains dsDNA overhangs to 2xdBroccoli fragment) with 0.075 pmol of the PCR product 2xdBroccoli (contains the dsDNA overhangs to the backbone DNA).

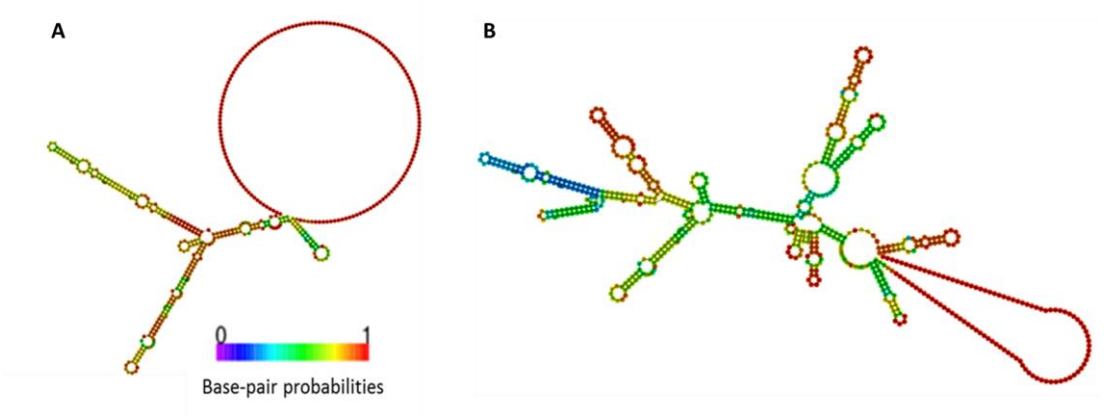

Figure 3-7: Secondary RNA structure prediction of the full transcripts Δ5'/3'-UTR-F31-2xdBroccoli-polyA$^+$ (A) in comparison to the previous RNA structure prediction (B) that contains the UTR's.
The comparison of two secondary RNA structure predictions: UTR deleted (A) and UTR containing (B). It shows that the characteristic secondary RNA structure of the imaging aptamer 2xdBroccoli is not folded when the plasmid harbours the cDNA of the 5'- and 3'-UTRs.

Herein, the backbone was amplified over PCR, using pcDNA3.3_Rev_Δ5'-UTR (5'-GAC GGT TCA CTA AAC GAG CTC TGC-3') as reverse and pcDNA3.3_Fwd _ Δ3'-UTR (5'-CGG CAA TAA AAA GAC AGA ATA AAA CG-3') as forward primer. The 2xdBroccoli insert was generated by a PCR amplification as well, using 2xdBroccoli-Fwd (5'-AGC TCG TTT AGT GAA CCG TCT TGC CAT GTG TAT GTG GG-3') as forward and 2xdBroccoli-Rev

(5'-ATT CTG TCT TTT TAT TGC CGC TTG CCA TGA ATG ATC CAG-3') as forward primer. After colony PCR a positive clone was chosen, and the sequence was verified via Sanger-DNA sequencing (Microsynth AG, Switzerland). The plasmid was multiplied in *E. coli* XL1-Blue and the purified plasmid was used for a test transfection.

3.1.10 Test transfection of pΔBr with Lipofectamine 2000

To verify the integrity and function of the plasmid pΔBr, a test transfection with Lipofectamine 2000 was carried out (Figure 3-8).

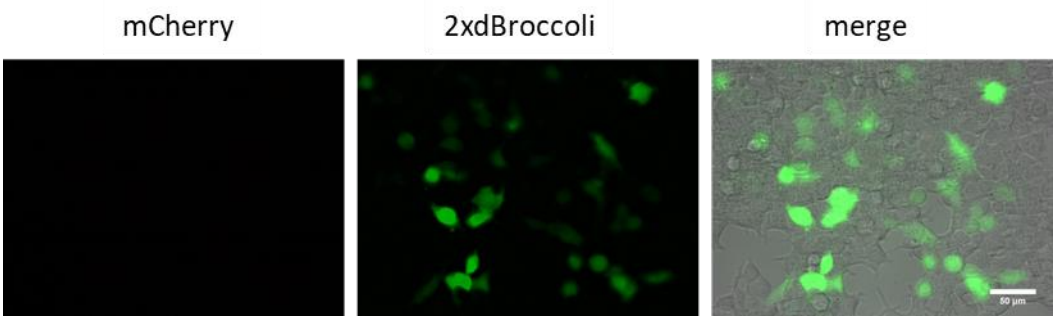

Figure 3-8: Transfection of 2.5 µg pΔBr with 3 µL Lipofectamine 2000.
HEK293T cells were seeded at $8 \cdot 10^4$ cells per well. After 72 h of incubation subsequent staining with DFHBI, cells express the RNA aptamer. (40x, Scale bar 50 µm)

After 72 h, cells were washed and re-cultured in DMEM + DFHBI for further 30 min in humidified atmosphere at 37 °C. The images demonstrate that about ~70% of the cells express the imagining RNA aptamer, implying the RNA aptamer F31-2xdBroccoli as properly folded in HEK293T cells. This corroborates the assumption that the RNA aptamer is affected by the flanking UTRs and leads to a misfolded secondary RNA structure. Since the transfection with CaP/DNA/CaP/PEI nanoparticles was not suitable for the nanoparticle-mediated transfection of pBr, another type of nanoparticles was synthesised that also simplifies the localisation of the cellular protein expression or transcription by including fluorescently labelled PEI-Cy5.

3.1.11 Synthesis of CaP/PEI-Cy5/DNA/CaP/PEI-Cy5

To simplify the localisation of cellular transcription and expression events, the nanoparticular DNA carrier system was modified by encapsulating the plasmid DNA between two calcium phosphate layers, stabilised by fluorescence labelled PEI-Cy5. The scheme of the synthesis is shown below (Figure 3-9)

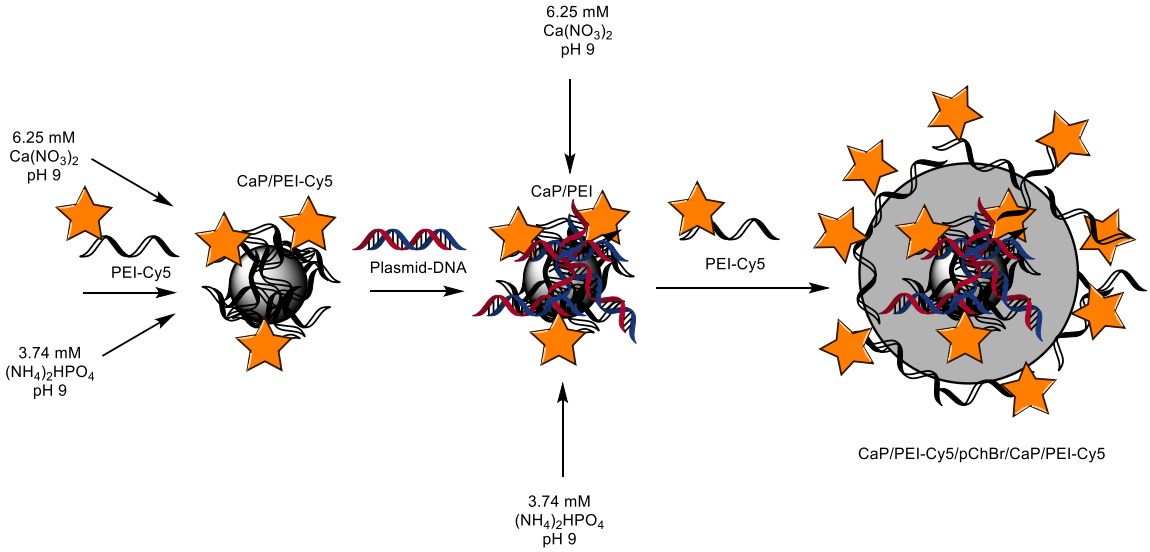

Figure 3-9: Synthesis scheme of CaP/PEI-Cy5/pChBr/CaP/PEI-Cy5 and CaP/PEI-Cy5/pΔBr/CaP/PEI-Cy5.

The synthesis of triple-shell calcium phosphate nanoparticles was carried out by mixing equivalent volumes of the corresponding salts and using PEI-Cy5 (volume ratio CaP-dispersion:PEI-Cy5, 5:1) instead of PEI to stabilise the colloidal system. To 1 mL of this dispersion, 20-40 µg of plasmid DNA was added and mixed thoroughly followed by another round of precipitation with the $(NH_4)_2PO_4$ and $Ca(NO_3)_2$ and stabilisation (Figure 3-9).

3.1.12 Characterisation of triple-shell nanoparticles

The results of the DLS measurements are displayed in Figure 3-11 and Table 3-2. The nanoparticles have an average size of about 87-117 nm showing a polydispersity index of 0.2-0.25 which is below the critical value of 0.3. Under the assumption of uniformly shaped and sized nanoparticles, the dispersion can be referred to as monodisperse. The zeta potential was about +25 mV, revealing a stable dispersion. About 145 µg mL^{-1} Ca^{2+} were determined through atomic absorption spectroscopy (AAS), giving a concentration of $1.4 \cdot 10^{11}$ nanoparticles mL^{-1} for pChBr loaded triple-shell calcium phosphate nanoparticles and $3.4 \cdot 10^{11}$ nanoparticles mL^{-1} for pΔBr. The DNA concentration on the nanoparticles was quantified by UV spectroscopy. The average amount of adsorbed DNA was approx. ~50% of the initially

applied plasmid DNA which corresponds to about 15 plasmids on one nanoparticle or $3.8 \cdot 10^{12}$ plasmids mL^{-1}.

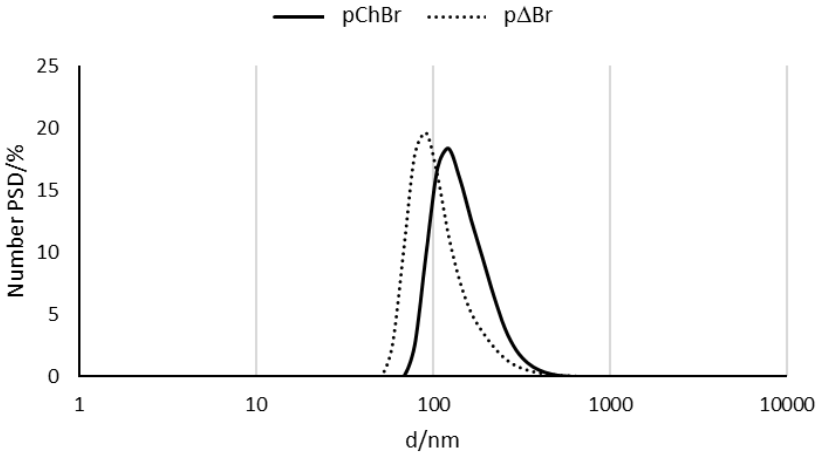

Figure 3-10: DLS measurement of CaP/PEI-Cy5/pChBr/CaP/PEI-Cy5 and CaP/PEI-Cy5/pΔBr/CaP/PEI-Cy5.

Table 3-2: Colloidal characteristics.

Parameter	CaP/PEI/plasmid/CaP/PEI		
	pChBr	**pΔBr**	**Avg.**
Hydrodynamic diameter by DLS/nm	117	87	102
V(one nanoparticle; only CaP)/m^3	$8.4 \cdot 10^{-22}$	$3.4 \cdot 10^{-22}$	$5.6 \cdot 10^{-22}$
A(one nanoparticle; only CaP)/m^2	$4.3 \cdot 10^{-14}$	$2.4 \cdot 10^{-14}$	$3.3 \cdot 10^{-14}$
m(one nanoparticle; only CaP)/kg	$2.6 \cdot 10^{-18}$	$1.1 \cdot 10^{-18}$	$1.7 \cdot 10^{-18}$
w(Ca^{2+}) by AAS/µg mL^{-1} (= g m^{-3})	143	147	145
w($Ca_5(PO_4)_3OH$)/µg mL^{-1} (= g m^{-3})	359.1	369.2	364.2
N(nanoparticles)/number mL^{-1}	$1.4 \cdot 10^{11}$	$3.4 \cdot 10^{11}$	$2.1 \cdot 10^{11}$
MW(plasmid)/g mol^{-1}	$4.13 \cdot 10^{6}$	$3.38 \cdot 10^{6}$	$3.76 \cdot 10^{6}$
w(plasmid)/µg mL^{-1} (= g m^{-3})	18.3 (46% yield)	20.9 (54% yield)	19.9 (50% yield)
N(plasmid)/number mL^{-1}	$2.7 \cdot 10^{12}$	$3.8 \cdot 10^{12}$	$3.2 \cdot 10^{12}$
m(plasmid) per nanoparticle/kg	$1.3 \cdot 10^{-19}$	$6.3 \cdot 10^{-20}$	$9.5 \cdot 10^{-20}$
N(plasmid) per nanoparticle	20	11	15–16
Area occupied by plasmid/plasmid µm^{-2}	455	470	459
wt ratio plasmid to calcium phosphate	1:19.6	1:17.3	1:9.5
PDI by DLS	0.222	0.257	0.237
Zetapotential by DLS/mV	25.7	24.7	25.2
Particle composition			
CaP/wt-%	95.2	94.5	94.8
plasmid/wt-%	4.8	5.5	5.2

3.1.13 Live cell imaging of pChBr and pΔBr transfected cells.

For the live cell imaging, the cells were treated in the same manner as described previously. Briefly, cells were seeded on a four-chamber slide with 80,000 cells per well and treated with 2 µg plasmid DNA or $2.39 \cdot 10^{10}$ nanoparticles per well. Images were recorded over 32 h (Figure 3-12). Even with the different nanoparticle type for the nanoparticle-mediated transfection of pChBr, the same results were obtained as indicated by the upcoming fluorescence. Cells express mCherry after 8 h while dBroccoli/DFHBI complex is formed 2 h later, after 10 h of incubation. No results were obtained for the control plasmid pΔBr which corroborates with the previous results.[45] It is assumed that dBroccoli is not properly folded inside the cell due the cDNA modification of the F30 scaffold to F31, which bears additional nucleotides to stabilise the construct pChBr. This has to be confirmed by future experiments.

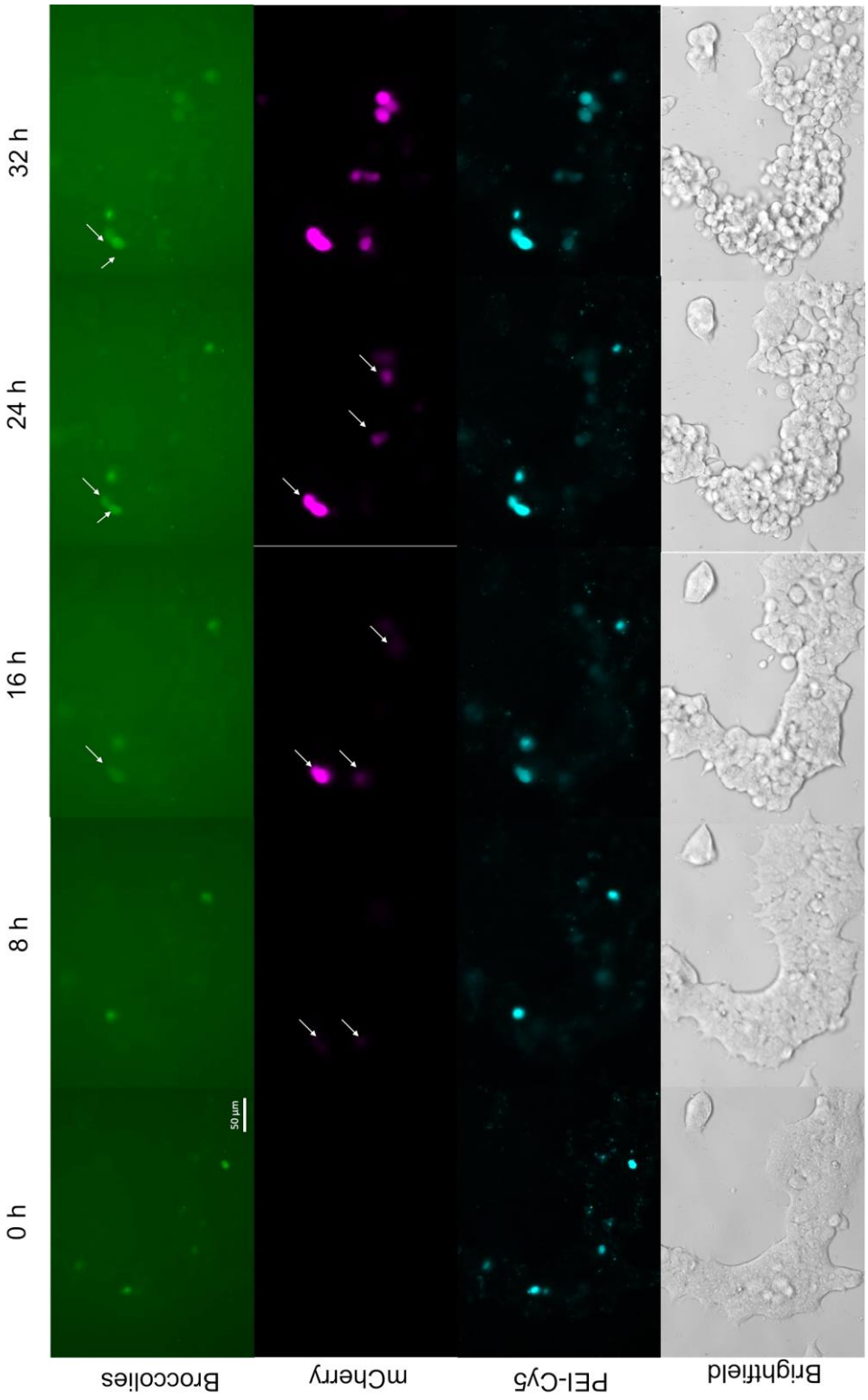

Figure 3-11: Transfection with CaP/PEI-Cy5/pChBr/CaP/PEI-Cy5.
Live cell imaging was recorded for up to 32 h. HEK293T cells were seeded on a four-chamber slide with 80,000 cells per well and incubated for 6 h with pChBr loaded triple-shell calcium phosphate nanoparticles, containing 2 µg pChBr. Nanoparticles were removed, cells were washed twice with DPBS and re-cultivated with fresh media containing 20 µM DFHBI. Cells expressed the red fluorescence protein mCherry (magenta) after 8 h while the green fluorescence-emitting DFHBI/dBroccoli-complex (green) was formed 8 h later. (Scale-bar 50 µm, 40x magnification).

After 16 h cells began to shrink, indicating the ongoing process of apoptosis. Apoptosis can lead to misinterpreted results since a round-shaped dead cell is visible as well in green fluorescent living cells, but the occurrence of the fluorescence signal came up much earlier indicating the opposite.

Interestingly, only a few cells were transfected (<2%), but this low transfection efficiency might enable to monitor single cells during transcription and translation of RNA aptamer labelled protein cDNA. However, transfection efficiency is as pre-mentioned influenced by many factors, including the mechanism of uptake and intracellular delivery routes, the chemical properties of the vector and the used transport system and cell lines.[176] Despite the central dogma of molecular biology (DNA→RNA→protein), the fluorescent signal of the protein was observed before the signal of the tagged RNA. Differences in brightness and bleaching of DFHBI, or the competition for the mRNA between the DFHBI/Broccoli complex-formation and the ribosome can be a reason for this result. Additionally, with lower particle dosages, the system benefits from the less toxicity of calcium phosphate nanoparticles compared to common transfection agents (e.g. Lipofectamine 2000). Other functional RNA can be labelled with this non-invasive fluorogenic tag to follow its uptake by calcium phosphate nanoparticles.

3.1.14 Summary

Here we have demonstrated the successful synthesis and fully colloidal characterisation of double and triple-shell calcium phosphate nanoparticles. Moreover, the successful design, cloning, and transfection of pCherries'n'Broccolies in eukaryotic cells was shown. A plasmid that encodes the fluorescent protein mCherry and the cDNA for the imaging RNA aptamer dBroccoli is adjacent to mCherry. The design of the plasmid was based on predicted secondary RNA folding structures, which led to the final construct pChBr. The designed plasmid was successfully used for the nanoparticle-mediated transfection with double- and triple-shell calcium phosphate nanoparticles and revealed a low transfection efficiency in both cases. The fluorescent signal of mCherry was observed before the signal for dBroccoli, which indicated a molecular competition for the nascent mRNA through the ribosome. The in parallel designed control plasmid pBr and pΔBr could not be

transfected due to misfolded RNA or modification at the F30 scaffold. Beside some needed optimisation, this system may then be useful to monitor single cells during transcription and translation of RNA aptamer labelled proteins.

3.2 HSV-1 antigen functionalised and CpG loaded calcium phosphate nanoparticles CaP/PEI/CpG^m/SiO_2-S-antigen

This work was a cooperation between the groups of Dr. Krawczyk and Prof. Dr. Epple. Results obtained by the cooperation partners have been clearly marked in the following chapters.

3.2.1 Relevance and motivation

The herpes simplex virus 1 is a life-long persistent and global viral infection of humans, causing serious diseases, such as HSV encephalitis or keratitis. These diseases can cause severe life-threatening damage to the brain or lead to blindness, or can even end in death when untreated.[159,177-179] Despite broadly available antiviral chemotherapeutics, upcoming HSV drug resistance stresses the urgency to develop new effective treatment alternatives.[159] The chokepoint for the infectivity and immunogenic invisibility of HSV-1 arises from the surface-presented glycoproteins gD, gB, and gH/gL which mediate the non-diffusive and direct transport of virions from infected to healthy cells.[159] This as cell-to-cell spread known process enables the bypassing of cellular barriers and circumvents the classic recognition by neutralising antibodies.[159] Therefore, glycoprotein specific antibodies may lead to an efficacious inhibition of viral cell-to-cell spread infections. Based on gB-derived antigenic peptides, Krawczyk *et al.* developed a gB-specific monoclonal antibody (mAb2c) that exhibits strong HSV-neutralising capacity and abrogates the viral cell-to-cell spread both *in vitro* and *in vivo* models.[159,163] In this study, three gB-derived antigenic peptides are immobilised onto the surface of CpG-loaded calcium phosphate nanoparticles. CpG (a TLR9 ligand) is known as a potent immune adjuvant and induces the production of inflammatory cytokines. By immunisation with gB-peptide functionalised and CpG-loaded calcium phosphate nanoparticles, the generation of new HSV-specific and neutralising antibodies was investigated in mice. Here, the synthesis and primarily immunisation results are shown.

3.2.2 Synthesis of HSV-1 antigen functionalised and CpG loaded calcium phosphate nanoparticles CaP/PEI/CpG^m/SiO_2-S-antigen

All syntheses were performed at room temperature. 20 mL sterile filtrated (0.2 µm) ultrapure water was filled into a 50 mL tube. By continuously stirring at 1000 rpm, 5 mL of 10.8 mM $(NH_4)_2HPO_4$ [pH 10] (Merck), 5 mL of 18.0 mM $[CH_3CH(OH)COO]_2Ca \cdot 5\ H_2O$ [pH 10] (Fluka) and 7 mL of 0.08 mM polyethyleneimine (25 kDa, Sigma Aldrich) were pumped into the water prefilled 50 mL tube for 1 min. The dispersion was stirred for further 20 min. 18 mL of the CaP/PEI dispersion were transferred into a new tube and 2.0 mL of mouse CpG (550 µg mL^{-1}), hereinafter CpG^m (ODN 1826, Invivogen, USA), were added to the dispersion and it was stirred for 30 min at 500 rpm. For the preparation of the silica-shell around the calcium phosphate nanoparticles, 10 mL of CaP/PEI were mixed with a Stoeber solution consisting of 40 mL EtOH (p.a.), 50 µL tetra orthosilicate (TEOS, Sigma) and 26 µL ammonia solution (30-33% (v/v), Carl Roth). The mixture was stirred overnight at 1000 rpm. CpG^m containing and silanised calcium phosphate nanoparticles were prepared by mixing 2x10 mL of CaP/PEI/CpG^m with two Stoeber solution consisting of 40 mL EtOH, 50 µL TEOS and 26 µL NH_3 (30-33% (v/v)) each. The mixtures were stirred at 1000 rpm overnight. The next day, the dispersions were divided over 6x26 mL ultracentrifugation tubes in 25 mL aliquots and were centrifugated at 30,000 rpm (SORAVALL, Ultra Series Thermo Scientific) for 30 min to remove non-reacted impurities. The pellets were washed briefly with 2 mL sterile filtrated ultrapure water and redispersed by ultrasonication (UP50H, Hielscher, Ultrasound Technology; sonotrode 3, cycle 0.8, amplitude 70%, 20 s) on ice in 5 mL sterile filtrated ultrapure water. The obtained fractions of CaP/PEI/CpG^m/SiO_2-OH and CaP/PEI/SiO_2-OH nanoparticles were combined separately. 5 mL of each type of nanoparticles were kept for later analysis and stored at 4 °C. Another 5 mL of CaP/PEI/SiO_2-OH nanoparticles were given to a mixture of 20 mL EtOH (p.a. grade), 25 µL (3-mercaptopropyl)trimethoxysilane (MPS) and stirred for 6-8 h at 500 rpm, while 10 mL and 5 mL of CaP/PEI/CpG^m/SiO_2-OH nanoparticles were given to a solution of 40 or 20 mL EtOH, 50 or 25 µL MPS and stirred for 6-8 h at 1000 or 500 rpm, respectively. 25 mL of the resulting dispersions of CaP/PEI/SiO_2-SH or

CaP/PEI/CpG^m/SiO_2-SH were evenly spread across the 26 mL ultracentrifugation tubes again and centrifugated at 30,000 rpm for 30 min. Pellets were washed briefly with 2 mL sterile ultrapure water and redispersed in 5 mL sterile ultrapure water by ultrasonication as described before, resulting in 15 mL of CaP/PEI/CpG^m/SiO_2-SH and 5 mL of CaP/PEI/SiO_2-SH calcium phosphate nanoparticles. Each type of nanoparticle was combined and stored at 4 °C for later coupling. Figure 3-12 down below shows a schematic representation of the synthesis.

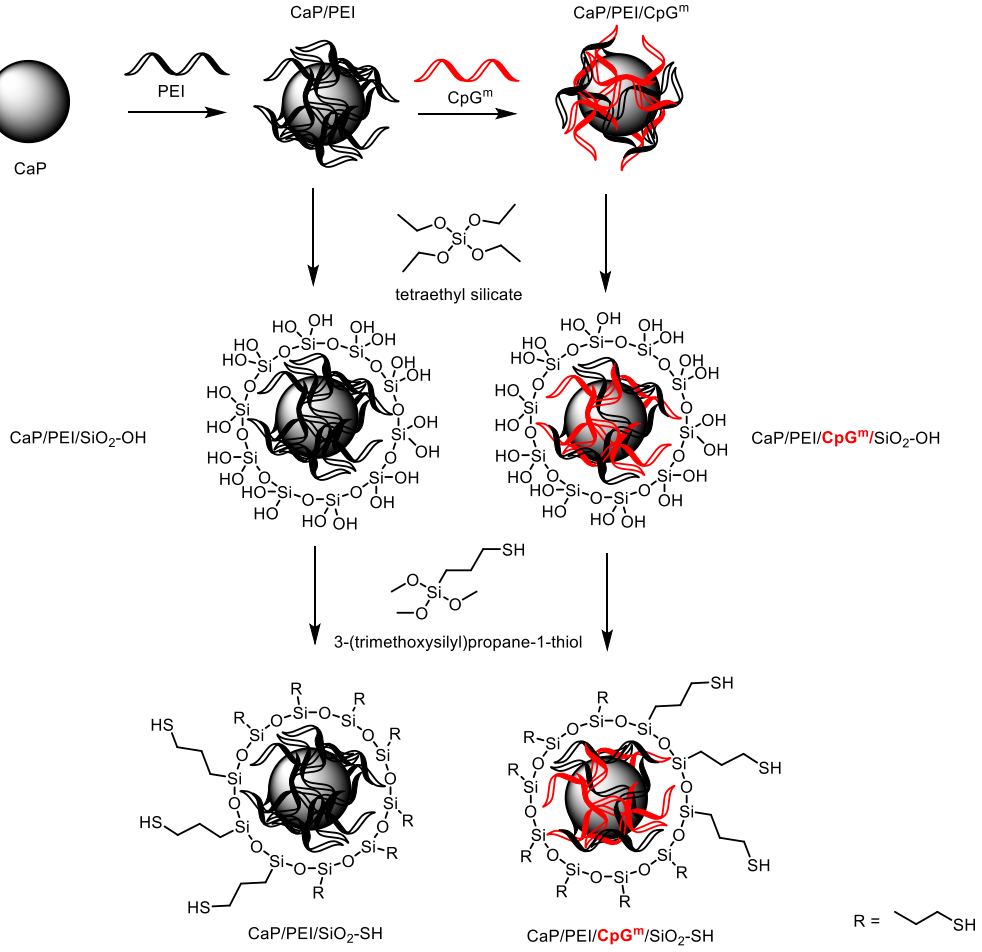

Figure 3-12: Synthesis of either CpG^m-loaded or unloaded, thiol-terminated and silica-coated calcium phosphate nanoparticles.

3.2.3 Coupling of HSV-1 antigens

During the synthesis of thiol-terminated calcium phosphate nanoparticles, the activation of the HSV-1 peptides was performed. HSV-1 antigens ME-2, P1_5, P2_5, and P3_5 were purchased from Peptides&Elephants (Potsdam, Germany). Sequences are shown in the table below.

Table 3-3: HSV-1 peptides that have been used in the syntheses of calcium phosphate nanoparticles

Peptide	Sequence	*MW*/ g mol^{-1}	aa	pI	Structure
ME-2	FEDaaFYGYRE*	1367.4	11	4.14	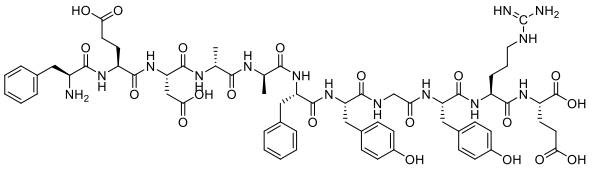
P1_5	PFYGYREGSHTEH	1579.3	13	6.02	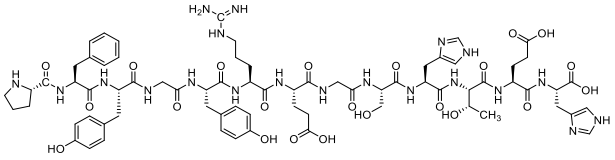
P2_5	PFYGYREGFEDF	1526.1	12	4.14	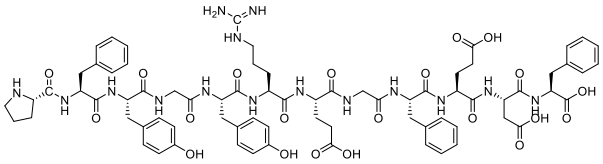
P3_5	QVWFGHRYSQFMG	1642.8	13	8.75	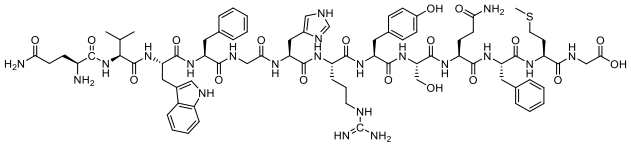

*Small single letter shows the code for D-alanin.

100 µg of each peptide were dissolved in 50 µL DPBS. The resulting concentration was determined via the NanoDrop2000c (Thermo Fisher Scientific) at $A_{280\ nm}$. It was activated with a molar excess of 12-16-fold with the water-soluble hetero-specific crosslinker sulfo-SMCC (Calbochem, Merck), 10 mg mL^{-1}, for 2 h at room temperature and was inverted gently every 20 min (Figure 3-13). Excess of the crosslinker was removed through three dialysis rounds using a Dialysis Mini Kit (1 kDa MWCO, GE Healthcare) against ice cold 500 mL DPBS for 2 h each, at 4 °C. After the dialysis, each activated peptide (approx. 240 µL) was given to 3 mL of CaP/PEI/CpG^{m}/SiO_2-SH calcium phosphate nanoparticles and incubated on ice overnight at 4 °C.

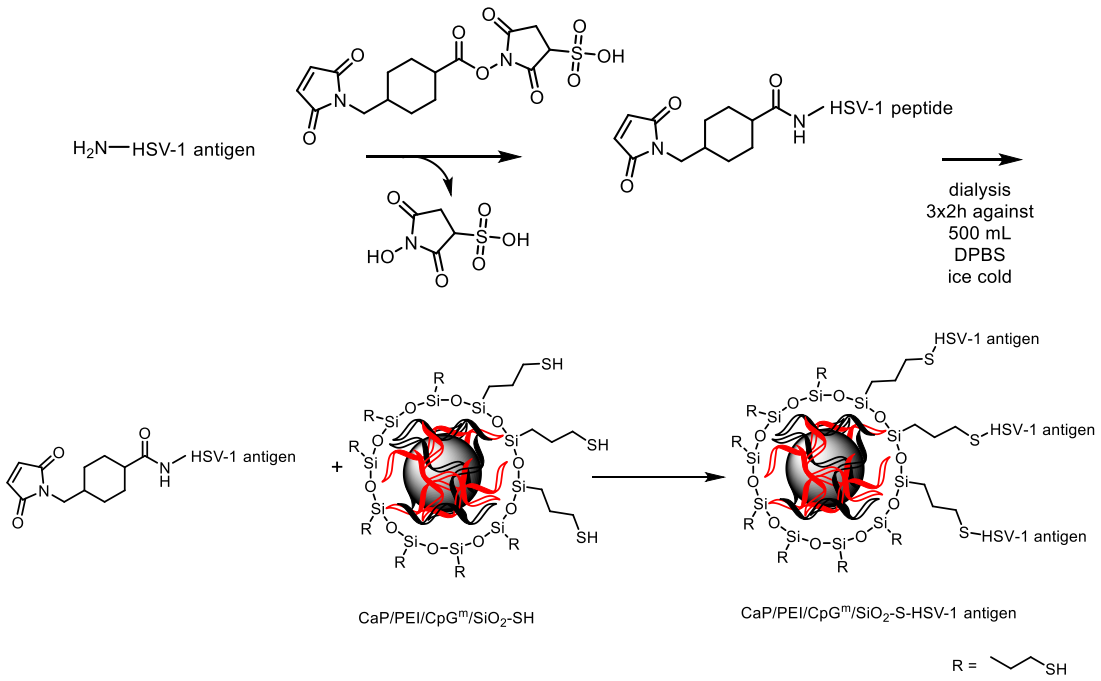

Figure 3-13: Activation and coupling of HSV-1 antigen onto thiol-functionalised calcium phosphate nanoparticles.
Primary amines within the peptides react with the NHS ester forming an amide bond between the HSV-1 antigen and the crosslinker SMCC attaching the antigen onto the surface of calcium phosphate nanoparticles.

The next day, unreacted compartments were removed by centrifugation for 30 min at 4 °C with 4696 g (Multifuge XR1, Thermo Scientific). The supernatants were transferred in new 15 mL collection tubes and kept on ice. The pellets were washed briefly with 1 mL of sterile filtrated ultrapure water and were redispersed in 3 mL each on ice by ultrasonication (UP50H, Hielscher, Ultrasound Technology; sonotrode MS3, cycle 0.8, amplitude 70%, 10 s), giving the following particle types shown in the below table (Table 3-4).

Table 3-4: Types of antigen functionalised calcium phosphate nanoparticles.

Code	Samples
A	CaP/PEI/SiO_2-OH
B	CaP/PEI/CpG^m/SiO_2-OH
C	CaP/PEI/SiO_2-SH
D	CaP/PEI/CpG^m/SiO_2-SH
E	CaP/PEI/CpG^m/SiO_2-S-ME-2
F	CaP/PEI/CpG^m/SiO_2-S-P1_5
G	CaP/PEI/CpG^m/SiO_2-S-P2_5
H	CaP/PEI/CpG^m/SiO_2-S-P3_5

3.2.4 Quantification of CpG^m

CpG^m was determined spectroscopically by using a NanoDrop2000c (Thermo Fisher) device. The supernatant of a 100 µL CaP/PEI/SiO_2-OH or CaP/PEI/SiO_2-SH calcium phosphate nanoparticle dispersion was used as a blank reference to ensure the subtraction of any possibly interfering background signal from the nanoparticles. Therefore, 100 µL of each dispersion was centrifugated at 20,000 g at 4 °C for 30 min. First CpG^m load quantification was performed by using 2 µL of a 100 µL supernatant of freshly centrifugated sample of CaP/PEI/CpG^m/SiO_2-OH calcium phosphate nanoparticle dispersion, giving the relative amount of the initially loss of CpG^m (3.1 µg mL^{-1}) after the first silanisation with TEOS . Therefore, 51.9 µg mL^{-1} was found on the surface of the silanised calcium phosphate nanoparticles. A second CpG^m load quantification was performed analogously, using the supernatant of the CaP/PEI/CpG^m/SiO_2-SH nanoparticles instead. Additionally, non-loaded calcium phosphate nanoparticles itself were used as a blank to determine the amount of adsorbed CpG^m of CpG^m-loaded nanoparticles. Thereby, 38 µg mL^{-1} of the initially used 55 µg mL^{-1} CpG^m were found, indicating that up to 70% of the CpG was adsorbed on the surface of the silica-coated calcium phosphate nanoparticles.

3.2.4.1 Quantification of bound HSV-1 antigens on the surface of calcium phosphate nanoparticles

The quantity of coupled peptides on the surface of the calcium phosphate nanoparticles was determined by using a NanoDrop2000c device, taking 2 µL of CaP/PEI/CpG^m/SiO_2-SH calcium phosphate nanoparticles as a blank and measure the absorption at A_{205nm}. The Lambert-Beer law and the peptide sequence specific extinction coefficient ε_{205} were used to calculate the concentration of bound peptides in µg mL^{-1}.[180] The peptide sequence specific extinction coefficient ε_{205} was calculated using the following equation:

$$\varepsilon_{205}=\Sigma(\varepsilon_i n_i)+\varepsilon_{bb}(r\text{-}1) \qquad \text{Eq. 7}$$

The coefficient ε_i describes the molar absorptivity of a specific amino acid side-chain residue, n_i is the number of this residue, ε_{bb} reflects the molar absorptivity of the backbone and *r* describes the length of the peptide. The molar absorptivity values at 205 nm are shown in Table 3-5. Therefore, the molar extinction coefficient can be calculated by the summation of the number of UV active residues of each HSV-1 peptide using the equation Eq. 7 (Table 3-5+6).

Table 3-5: Molar extinction at 205 nm (ε_{205}) for protein side chains.

Side chain/feature	ε_{205} /M^{-1} cm^{-1}
Tryptophan	20,400
Phenylalanine	8600
Tyrosine	6080
Histidine	5200
Methionine	1830
Arginine	1350
Cysteine	690
Asparagine	400
Glutamine	400
Cystine	2200
Backbone peptide bond	2780 ± 168

Table 3-6: Composition of HSV-1 antigens.

	Peptide composition			
Amino acid	**ME-2**	**P1_5**	**P2_5**	**P3_5**
Ala (A)	2 (18.2%)	0	0	0
Arg (R)	1 (9.1%)	1 (7.7%)	1 (8.3%)	1 (7.7%)
Asn (N)	0	0	0	0
Asp (D)	1 (9.1%)	0	1 (8.3%)	0
Cys (C)	0	0	0	0
Gln (Q)	0	0	0	2 (15.4%)
Glu (E)	2 (18.2%)	2 (15.4%)	2 (16.7%)	0
Gly (G)	1 (9.1%)	2 (15.4%)	2 (16.7%)	2
His (H)	0	2 (15.4%)	0	1 (7.7%)
Ile (I)	0	0	0	0
Leu (L)	0	0	0	0
Lys (K)	0	0	0	0
Met (M)	0	0	0	1 (7.7%)
Phe (F)	2 (18.2%)	1 (7.7%)	3 (25.0%)	2 (15.4%)
Pro (P)	0	1 (7.7%)	1 (8.3%)	0
Ser (S)	0	1 (7.7%)	0	1 (7.7%)
Thr (T)	0	1 (7.7%)	0	0
Trp (W)	0	0	0	1 (7.7%)
Tyr (Y)	2 (18.2%)	2 (15.4%)	2 (16.7%)	1 (7.7%)
Val (V)	0	0	0	1 (7.7%)
$\varepsilon_{205}=\Sigma(\varepsilon_i n_i)+\varepsilon_{bb}(r\text{-}1)$	58,510	65,870	69,890	86,220

The concentration is then given by the Lambert-Law:

$$A_{205}=\varepsilon_{205} c l \qquad \text{Eq. 8}$$

Where A is the absorbance, $\varepsilon_{205}$is the molar extincition coefficient at 205 nm, c the concentration in mol L^{-1} and l is the path length (1 mm).

$$\frac{A_{205}}{\varepsilon_{205} \cdot l} = c \text{ in mol } L^{-1}$$

$$\frac{A_{205}}{\varepsilon_{205} \cdot l} \cdot MW = w \text{ in g } L^{-1}$$

Where MW is the molecular weight and w is the mass concentration in g L^{-1}.

The absorbance at 205 nm was measured with the NanoDrop2000c device (Thermo Fisher Scientific, Waltham, USA) recording a whole spectrum from 200-850 nm to obtain the absorbance value at 205 nm. 2 µL of a freshly redispersed CaP/PEI/CpG^m/SiO_2-SH calcium phosphate nanoparticle dispersion was used as blank.

Thereafter, the peptide concentration of covalent bound antigens was measured by using 2 µL of the ME-2, P1_5, P2_5 or P3_5-functionalised calcium phosphate nanoparticle dispersion. By this method the following peptide quantities were found onto the surface of the calcium phosphate nanoparticles (Table 3-7).

Table 3-7: Amount of covalently attached peptides on the surface of thiol-terminated calcium phosphate nanoparticles.

HSV-1 peptide	Bound peptide/ µg mL^{-1}	Inital quantity/µg mL^{-1}	yield/%
ME-2	10.5	40.6	25.9
P1_5	40.0	46.7	85.7
P2_5	23.1	34.4	67.3
P3_5	4.95	18.9	26.2

3.2.5 Endotoxin quantitation and sterility assay

The outer membrane of gram-negative bacteria consists of a hydrophilic polysaccharide domain and a hydrophobic lipid domain in which the endotoxins or cytotoxic lipid polysaccharides (LPS) are found.[181] It is known that LPS plays a critical role in bacterial virulence.[182,183] In different mammalian cell types the mechanism of LPS-induced inflammation is triggered by a first binding event of LPS through a soluble LPS-binding protein, which transports the LPS to the Toll-like receptor (TLR4).[184] The TLR4-bound LPS recruits in turn MD2 and CD14, whereby a signalling cascade is initialised which activates the inflammation pathways.[185] Cells of the innate immune system e.g. monocytes and macrophages are express the TLR4 and respond highly sensitive to LPS stimulation.[186,187] The natural response of an inflammatory activated cell by LPS is the production of inflammatory factors like interleukins IL-1β, IL-6 or IL8. Beside of these inflammatory markers, it was found that LPS-stimulated cells also produce and secrete the tumour necrosis factor-α (TNFα) which can lead to apoptosis through the activation of the death inducing signalling complex.[188-192] Furthermore, in dependence on cell sensitivity at high concentrations, LPS can also directly kill cells.[193] The exposure to endotoxins can have severe and life-threating implications e.g. endotoxemia.[193] Thus, contaminated nanomaterials can lead to misinterpreted results when the inflammatory potency e.g. of a vaccine is tested.[193] Therefore, the production of sterile and endotoxin-free

nanoparticles is an important aspect for the desired biomedical application as a vaccine in mice. The endotoxin quantitation was performed with the LAL Chromogenic Endotoxin Quantitation Kit (Pierce, Thermo Fisher, Carlsbad), which is an endpoint determination assay, based on the conversion of a synthetic para-nitroanilline labelled peptide by an endotoxin activated protease. Smulders *et al.* analysed the usage of two types of endotoxin quantitation methods for different types of nanoparticles, including the LAL based assay for TiO_2, Ag, $CaCO_3$ and SiO_2-particles.[194] Therefore the LAL endotoxin assay was used. The results are depicted in the following figure and table (Figure 3-14 and Table 3-8A). They show that under the previously mentioned synthesis precautions, only very low concentrations of endotoxins were found in the final nanoparticle dispersions. The highest endotoxin concentration was found for the covalent antigen-functionalised calcium phosphate nanoparticles with 0.01 EU mL^{-1} compared to non-functionalised nanoparticles 0.003 EU mL^{-1}. The addition of D(+) trehalose, a cryoprotectant for subsequent lyophilisation of the particles normally leads to a slight increase of the endotoxin level, since trehalose is obtained from *Saccharomyces cervisiae.*[195]

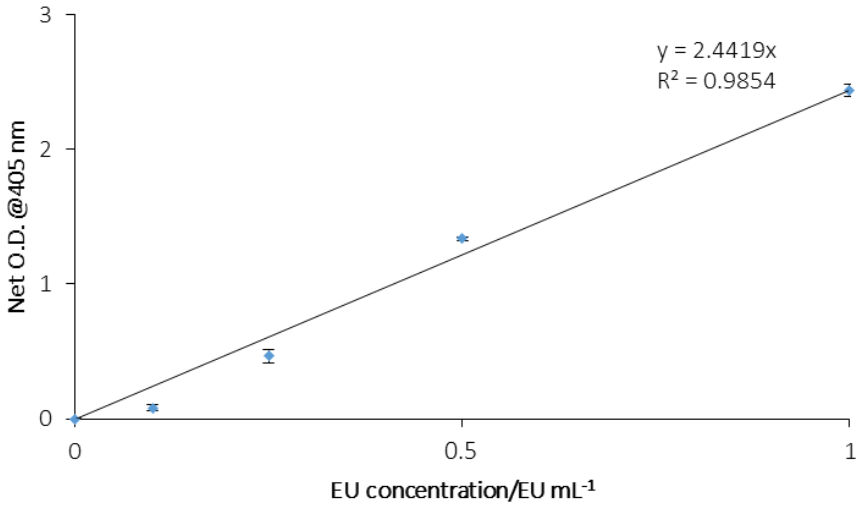

Figure 3-14: Endotoxin standard curve-regression plot of the LAL endotoxin assay.
Standard-regression line of the LAL endotoxin assay was recorded by the net OD at 405 nm. The correlation coefficient reflects the quality of the measured data, which showed an acceptable range concerning the manufactures protocol giving a value of R^2=1-0.98.

However, even after the addition of 20 mg mL^{-1} trehalose, the measured endotoxin concentrations were still within the reported and recommended range of medical

applied vaccines (Table 3-8B and Table 3-8C).[196] The data was additionally validated by a sterile test using blood-sheep agar that shows no bacterial contamination for none of the synthesised nanoparticles (Figure 3-15).

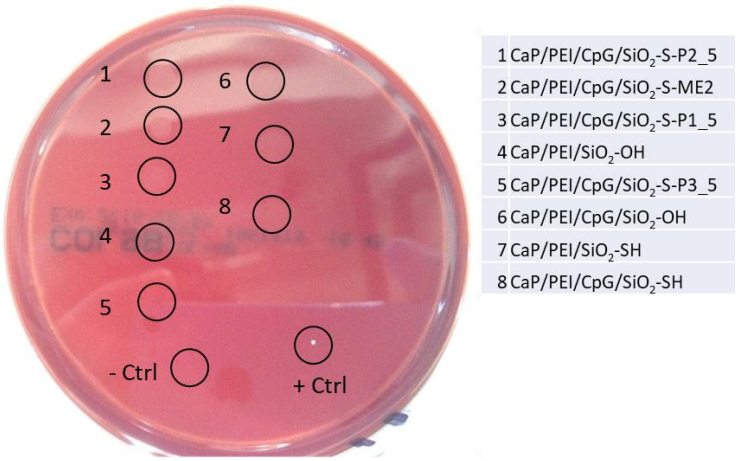

Figure 3-15: Sterility test on a sheep-blood agar.
Particles were incubated on a sheep-blood agar plate overnight at 37 °C. Neither non-functionalised nor CpG and functionalised calcium phosphate nanoparticles were contaminated. No colony forming units (cfu´s) were detected.

Interestingly, there is still no recommendation for an endotoxin level in biomedically applied nanomaterials due to the lack of appropriate analytic determination assays for the versatile and individual diversity of the used nanomaterials in research.[193,194,197,198] According to the values that are known from the regular applied vaccines compared to the synthesised calcium phosphate nanoparticles, it can be concluded that the previously sterile and pyrogen-free made precautions are efficacious in yielding pyrogen-free and sterile nanoparticles. They can be applied on future syntheses and will hopefully provide a useful protocol to enable the sterile synthesis of calcium phosphate nanoparticles.

Table 3-8: Contamination by endotoxins of the synthesised nanoparticles.
All synthesised particles were in the range of commonly applied vaccines.[196] A: Synthesised nanoparticles B: Commonly endotoxin level of medical used vaccines- C: different types of vaccines.

A

Particle type	EU mL^{-1} - Trehalose	EU mL^{-1} +Trehalose
CaP/PEI/SiO_2-OH	0.0041	0.0468
CaP/PEI/CpG/SiO_2-OH	0.0031	0.0335
CaP/PEI/SiO_2-SH	0.0037	0.0341
CaP/PEI/CpG/SiO_2-SH	0.0037	0.0341
CaP/PEI/CpG/SiO_2-S-ME2	0.0113	0.0417
CaP/PEI/CpG/SiO_2-S-P1_5	0.0086	0.039
CaP/PEI/CpG/SiO_2-S-P2_5	0.0147	0.0451
CaP/PEI/CpG/SiO_2-S-P3_5	0.0109	0.0413

B

Vaccine	Amount of Endotoxin
DTaP	< 100 EU $dose^{-1}$, 0.288–1390.8 EU mL^{-1}
DTaP	7600–181,640 EU mL^{-1}
Influenza	10–100 ng mL^{-1}, 0.304–380 EU mL^{-1}
HIB	<1.2–<12 EU $dose^{-1}$, 10.9–220.4 EU $dose^{-1}$
Prevnar	<0.21 EU $dose^{-1}$
Small Pox	Undetected
Rubella	Undetected
Polio	10 EU mL^{-1}
Rabies	Undetected—100 EU mL^{-1}
Mumps	100 EU mL^{-1}
Typhus	100,000 EU mL^{-1}
Cholera	1,000,000 EU mL^{-1}
Viral/nonviral vector	<10 EU mL^{-1}
	1 ng of endotoxin = 10 EU

C

Type	MREL (EU mL^{-1})
Gene vector	<10
Recombinant subunit	<20
Polysaccharide	<20
Live attenuated	<200
Inactivated	<500
Toxoida	<200,000

MREL: Maximum Recommended Endotoxin Levels

3.2.6 Characterisation

Antigen-functionalised calcium phosphate nanoparticles were characterised via DLS, SEM and UV-spectroscopy. DLS data is shown in Figure 3-16 and further calculated characteristics can be found in Table 3-9.

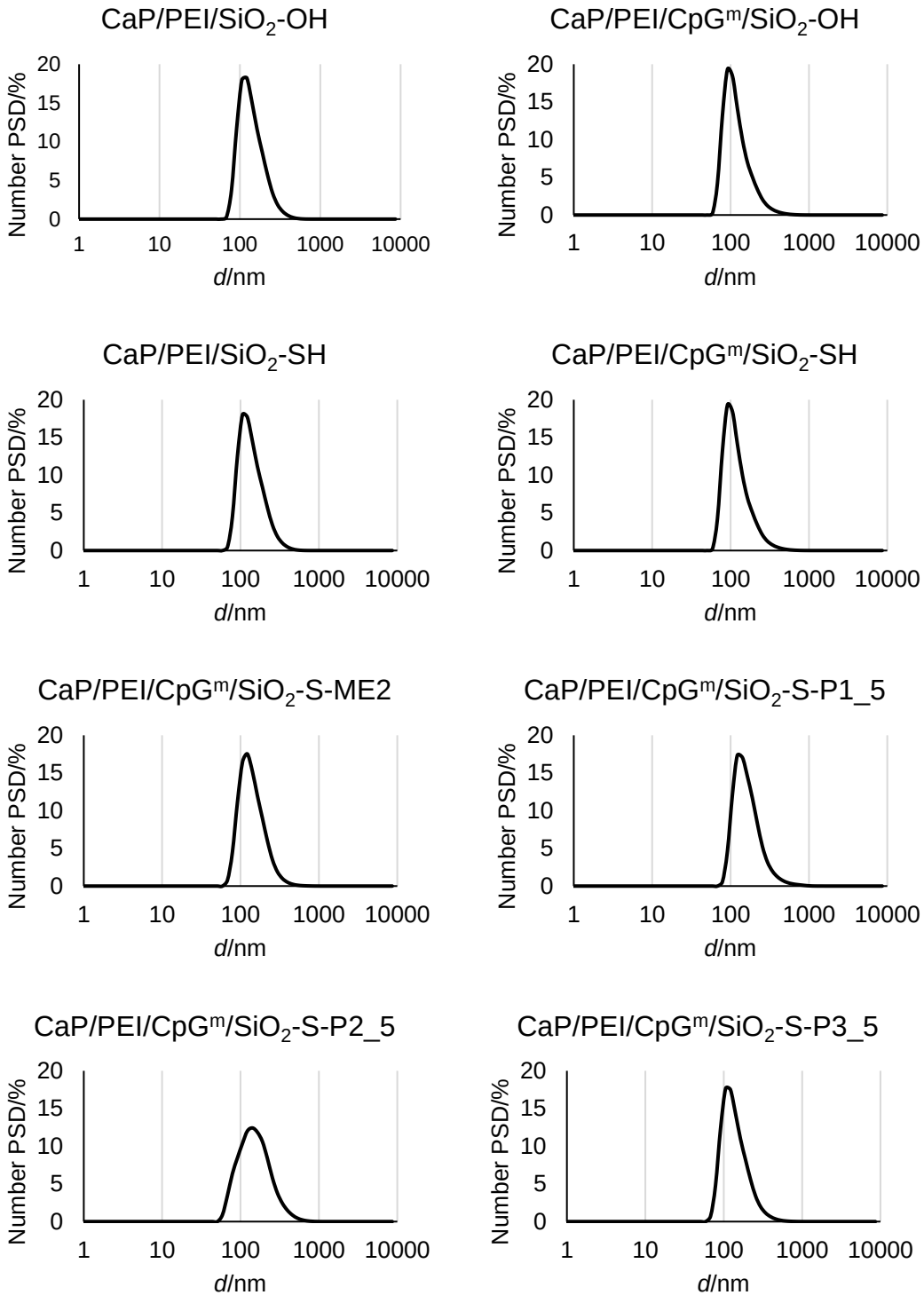

Figure 3-16: DLS results of the antigen functionalised calcium phosphate nanoparticles.

Table 3-9: Characteristics of antigen-functionalised calcium phosphate nanoparticles.

Particles	**-OH****	**-OH***	**-SH****	**-SH***	**ME2***	**P1_5***	**P2_5***	**P3_5***
Parameter	**A**	**B**	**C**	**D**	**E**	**F**	**G**	**H**
d_{SEM}[1]/nm	120±26	91±28	101±32	59±10	75±27	50±7	106±29	96±26
$V_{NP;\ only\ CaP}/\cdot10^{-22}m^3$	9.0	3.9	5.4	1.1	2.2	0.7	6.2	4.6
$A_{NP;\ only\ CaP}/\cdot10^{-14}m^2$	4.5	2.6	3.2	1.1	1.8	0.8	3.5	2.9
$m_{NP;\ only\ CaP}/\cdot10^{-18}kg$	2.8	1.2	1.7	0.3	0.7	0.2	2.0	1.5
$[Ca^{2+}]_{AAS}/\mu g\ mL^{-1}$	33.0	66.4	30	32.9	7.12	10.2	8.89	9.91
$[Ca_5(PO_4)_3OH]/\mu g\ mL^{-1}$	82.9	166.7	75.3	82.6	17.9	25.6	22.3	24.9
$\cdot10^{10}$ NPs mL^{-1}	2.9	13.5	4.5	24.5	2.6	12.5	1.1	1.7
$w(CpG^m)/\mu g\ mL^{-1}$	–	51.9	–	38.0	38.0	38.0	38.0	38.0
$\cdot10^{15}$ CpG^m mL^{-1}	–	4.9	–	3.6	3.6	3.6	3.6	3.6
$m(CpG^m)$ $NP^{-1}/\ 10^{-18}kg$	–	0.39	–	0.16	1.5	0.3	3.3	2.2
$\cdot10^4$ CpG^m NP^{-1}	–	3.7	–	1.5	13.9	2.9	31.5	21.0
CpG^m nm^{-2}	–	1.4	–	1.3	7.9	3.7	8.9	7.3
wt ratio (CpG^m:CaP)	–	1:3.2	–	1:2.2	1:0.5	1:0.7	1:0.6	1:0.7
w(antigen)/µg mL^{-1}	–	–	–	–	10.5	40.0	23.1	4.95
$\cdot10^{15}$antigens mL^{-1}	–	–	–	–	4.6	15	9.1	1.8
m(antigen) $NP^{-1}/\cdot10^{-19}kg$	–	–	–	–	4.1	3.2	20.2	2.9
$\cdot10^5$antigens NP^{-1}	–	–	–	–	1.8	1.2	7.9	1.1
antigens nm^{-2}	–	–	–	–	10	16	23	4
wt ratio (Antigen: CaP)	–	–	–	–	1:1.7	1:0.64	1:0.96	1:5.0
d_{DLS}[2]/nm	211	193	223	232	225	296	270	233
PDI_{DLS}	0.189	0.138	0.252	0.283	0.227	0.334	0.270	0.221
ζ_{DLS}/mV	17.9	21.9	22.0	21.5	24.3	26.3	23.7	26.2
Particle composition								
CaP/wt-%	100	76.3	100	68.5	26.9	24.7	26.8	36.7
CpG^m/wt-%	0	23.7	0	31.5	57.2	36.7	45.5	56
antigen/wt-%	0	0	0	0	15.8	38.6	27.7	7.3

[1]SEM diameter *d* was measured manually using ImageJ.
[2]DLS diameter *d* was measured in intensity given in a.u.
*Nanoparticles that were loaded with CpG^m: CaP/PEI/CpG^m/SiO_2-X-Y (X= O, S; Y=H, P1_5, P2_5, P3_5)
**CaP/PEI/SiO_2-X (X= OH, SH); unloaded nanoparticles

The colloidal characteristics of the synthesised nanoparticles are shown in Table 3-9. The PDI and zeta potential point out a monodisperse and stable dispersion. Except for P1_5 functionalised nanoparticles, the polydispersion index (PDI) quality value of <0.3 was not exceeded and the zeta potential ζ was about +23 mV. This may be due to the positively charged PEI dangling through the thin core-coating silica shell. The measured DLS diameter was increased after each antigen conjugation which might

indicate a successful attachment of the peptides to the surface of nanoparticles. SEM images demonstrated a uniformed and spherical shape of the nanoparticles and indicated only a small degree of agglomeration or agglutination (Figure 3-17). The number of calcium phosphate nanoparticles in one millilitre dispersion was calculated by using the solid core diameter from the SEM and the calcium concentration from the AAS. The AAS revealed a calcium concentration that ranges from 7-66 µg mL^{-1} which is corresponding to an equivalent hydroxyapatite concentration from 18-167 µg mL^{-1}. This gives a calculated particle concentration that ranges from about $1.1 \cdot 10^{10}$ to $2.4 \cdot 10^{11}$ NPs mL^{-1} (Table 3-9). For example, with the radius derived from the SEM data (r = 67 nm) for ME2-functionalised nanoparticles, the number of bound and adsorbed biomolecules can be calculated (Eq. 13 and Eq. 14, chapter 5.5). Therefore, ME2-functionalised nanoparticles were functionalised with $1.8 \cdot 10^5$ antigen molecules and loaded with $1.4 \cdot 10^5$ CpG^m molecules per nanoparticle, assuming a final CpG^m concentration of 38 µg mL^{-1} in every type of the antigen-functionalised nanoparticles and taking the measured bound peptide concentration from Table 3-7. Further results are shown in Table 3-9. The high number of molecules per particle might be explained by the low molecular weight of the applied molecules. CpG^m has a molecular weight of 6,364 g mol^{-1} and the antigenic peptides have an average molecular weight of ~1,500 g mol^{-1} which makes the molecules comparably small. These values are only an assumption since the number of peptide-captured thiols cannot directly be determined. Therefore, the number is only related to the molecules that adsorbed on the surface of each nanoparticle and might be less. However, dosages for the later immunisation were normalised to the concentration of peptides in µg mL^{-1} per dispersion and not by the numbers of covalently bound peptides per nanoparticle.

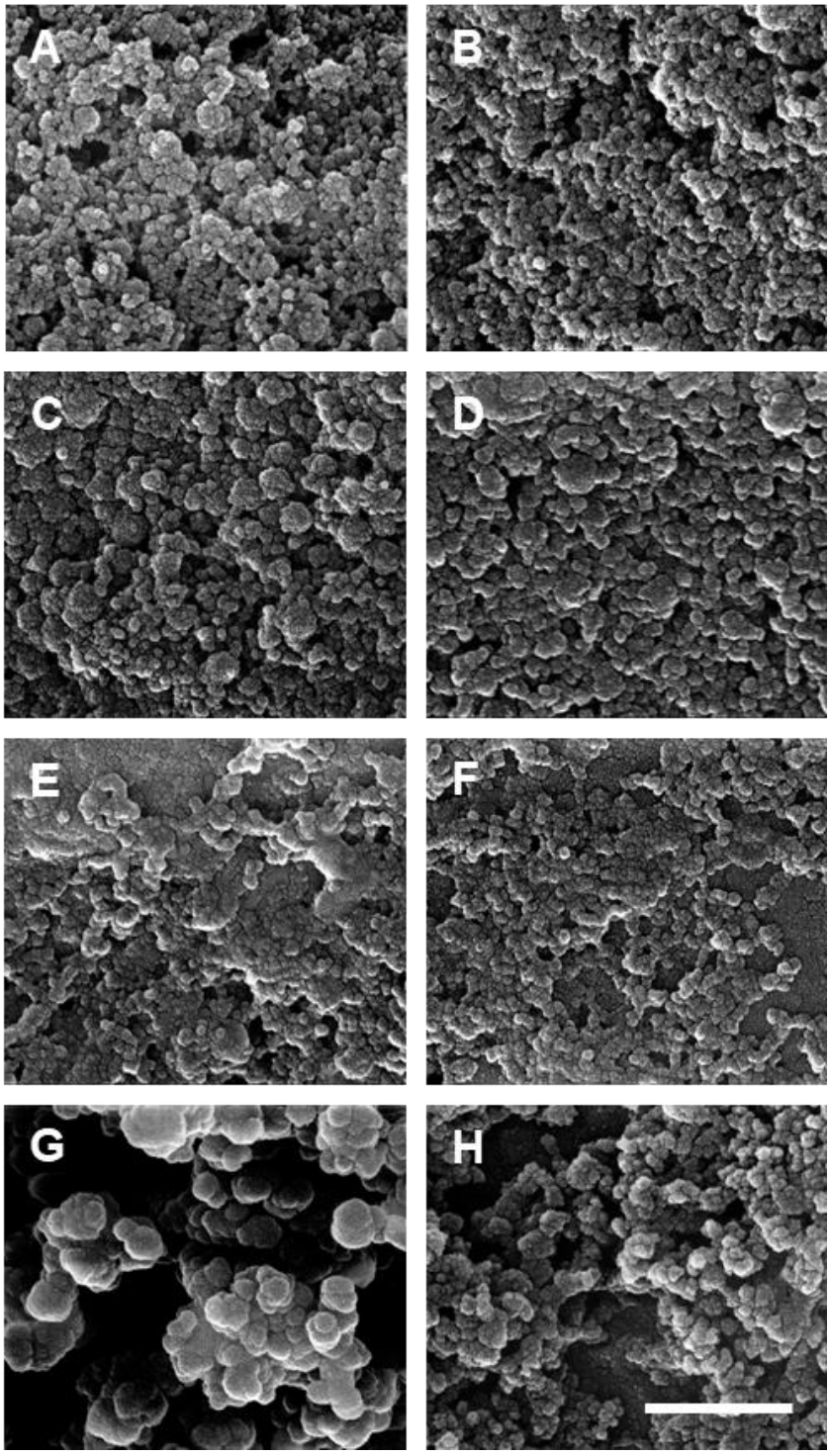

Figure 3-17: Scanning electron micrographs of antigen-functionalised calcium phosphate nanoparticles.
A: CaP/PEI/SiO_2-OH; B: CaP/PEI/SiO_2-SH; C: CaP/PEI/CpG^m/SiO_2-OH; D: CaP/PEI/CpG^m/SiO_2-SH; E: CaP/PEI/CpG^m/SiO_2-S-ME2; F: CaP/PEI/CpG^m/SiO_2-S-P1_5; G: CaP/PEI/CpG^m/SiO_2-S-P2_5
H: CaP/PEI/CpG^m/SiO_2-S-P3_5
All synthesised calcium phosphate nanoparticles have shown a spherical morphology. 200000x magnification, 20 kV. Scale bar 500 nm.

3.2.7 Immunisation experiments

The immunisation experiments were carried out by the group of Dr. Krawczyk at the Universitätsklinikum in Essen. Here, the first primarily results are presented.

To test the immuno-protective potential of the antigen-functionalised calcium phosphate nanoparticles, BALB/c mice (female, 8 weeks, Charles River) were treated prior to the infection with the antigen-functionalised nanoparticles. In parallel, mice were only immunised with the gB-peptides alone as a second control. Each of the four groups consisted of five animals, with one group as control included. Except the control group, each mouse received 60 µL of a mixture, containing CaP/PEI/CpG^m/SiO_2-S-antigen (P1_5, P2_5 or P3_5), MPL and Alum (Table 3-10) by *i.m.* thigh injection with either 10 µg of P1_5, P2_5 or P3_5, respectively. ME-2 was not tested in this experiment, due earlier not promising results.

Table 3-10: Vaccine composition.

Group	Mimotope CaP/PEI/CpG^m/SiO_2-X (Number of applied NPs)	Conc. ng µL^{-1}	NP Stock/ µL	Alum/ µL	MPL 1 mg mL^{-1}	Total+ void/ µL	*i.m.*/ µL	Peptide/ µg
1	P1_5 ($5.66 \cdot 10^8$)							
2	P2_5 ($6.67 \cdot 10^8$)	571.4	122.5	210	87.5	420	60	10
3	P3_5* ($8.73 \cdot 10^8$)							

*Only once injected

The immuno-stimulant adjuvants MPL and Alum were used to boost the murine immune response to the antigen-functionalised calcium phosphate nanoparticles. Immunisation was repeated on day 14 and day 28 (Figure 3-18). The nanoparticles with P5_3 were given only once due to insufficient amount of bound peptide on the nanoparticles. After each immunisation, 300 µL blood were taken. The procedure was repeated on day 42. Seven days prior to infection, 2.5 mg progesterone (Depo-Provera, Pharmacia) was subcutaneously injected into each mouse to enhance the viral susceptibility for the HSV-1 infection. On the day of the infection, murine vaginal mucosa was infected with HSV-1 F, using an appropriate lethal tissue culture infectious dose of $1 \cdot 10^5$ $TCID_{50}$ HSV virions. The murine vaginal mucosa was washed on day 1, 2, 4, 6, 8, and 30 days after the infection with 20 µL PBS and the vaginal lavages were frozen and kept for virus titer level endpoint determination. At the end

of the experiment, the mice were sacrificed and the lumbar- and sacral-ganglia were isolated. The presence of a viral latency was analysed by virus reactivation in cultured tissue cells and via PCR analysing virus related gene expression, such as the linker for activation of T-Cells (LAT) genes.

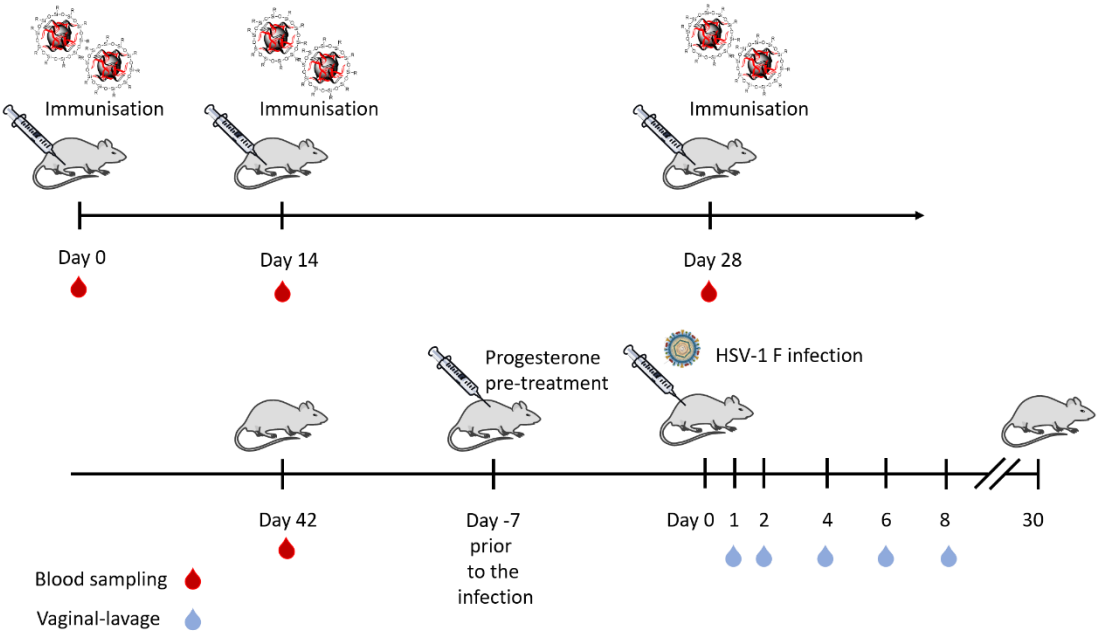

Figure 3-18: Time-line for the immunisation with antigen-functionalised calcium phosphate nanoparticles.
Mice were treated three times with 60 µL of an immunisation mixture, containing the antigen-functionalised calcium phosphate nanoparticles and additives. On each day of treatment and two weeks later, blood was taken from the mice, the sera were isolated and later analysed. Seven days prior to infection, the viral susceptibility was enhanced by subcutaneously administration of 2 mg of progesterone per mouse. Mice were infected with an appropriate lethal tissue culture infectious dose of $1 \cdot 10^5$ $TCID_{50}$ HSV virions. Murine vaginal lavages were collected over the whole observation to analyse the virus titer level by end-point determination.BW: Blood withdrawal.

To illustrate a sufficient protection against the herpes simplex virus, the potency of each gB-derived antigen was comparably analysed by the animal survival (Figure 3-19).

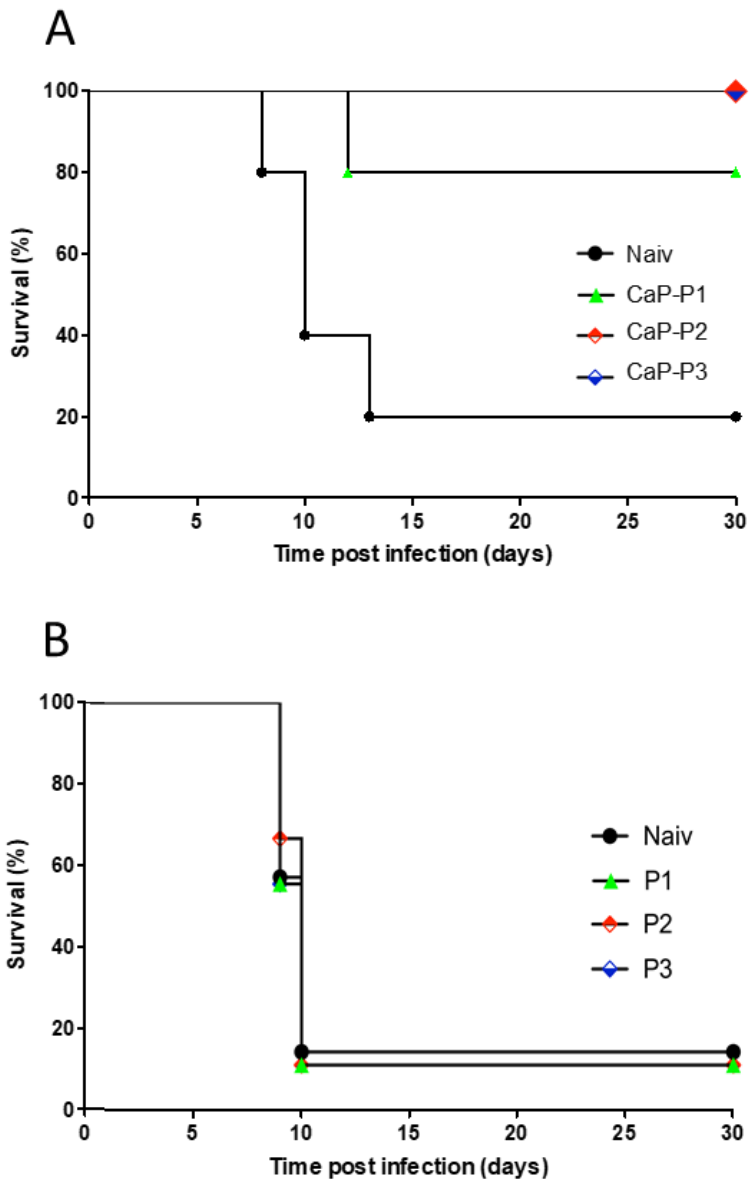

Figure 3-19: Survival of antigen-functionalised calcium phosphate nanoparticle and peptide immunised mice after HSV-1 F infection.
A: Mice (n=5) were immunised with antigen functionalised calcium phosphate nanoparticles formulated with Alum/MPL adjuvant. Immunisation was performed three times, every two weeks. Mice were intravaginally infected with a lethal dose (10^5 $TCID_{50}$) HSV-1 F and examined for HSV-1 infection for 30 days. B: Mice (n=5) were immunised with the antigens P1-_5-P3_5 with an appropriate amount of Alum/MPL adjuvant. Immunisation was performed analogously: three times, every two weeks. Mice were intravaginally infected with a lethal dose (10^5 $TCID_{50}$) HSV-1 F and examined for HSV-1 infection for 30 days.

The data indicates that the antigen-functionalised calcium phosphate nanoparticles provide a significant anti-viral protection compared to the untreated control group (naiv). Nearly all of non-immunised and peptide-immunised animals died relativlely

quickly within the first two weeks. Only 20% of the non-immunised animals survived. In comparison to the nanoparticle-treated animals, whereas almost all animals remained uninfluenced by the viral lethal infectious dose and survived. The P2_5 and P3_5-functionalised nanoparticles provided a noticeable animal survival (100%) followed by a slight decrease of P5_1 to 80%, showing to have a treatment-beneficial effect that is five times higher compared to the untreated case. The significant animal survival rate of antigen-functionalised nanoparticle treated animals indicates the production of strong HSV-1-neutralising antibodies and demonstrates a prophylactic anti-viral protection against HSV-1. Remarkably, P3_5-functionalised nanoparticles were only given once and lead to one of the highest survival rates over the whole observation time. Therefore, we think that our system provides an efficient antigen-presenting for vaccination purposes. However, the herein presented data needs to be validated by the results from further experiments, such as the virus titer endpoint determination and by the isolation and subsequent use of the in mouse produced antibodies in anti-viral *in vitro* assays. Instead of using CpG^m alone, which is indeed a potent immuno-activator of the innate immune system, a commercial and well-proven adjuvant mixture MPL+Alum was used for the immunisation. Therefore, we suggested that the combination of both may have led to a highly upregulated immune response to the nanoparticle conjugated peptides. Nevertheless, the primarily data gives a strong indication that the animal survival is resulted from the nanoparticle immunisation. Therefore, we assume that the murine immune system did respond positively to the covalently attached gB-derived peptides and induced the production of HSV-1-neutralising antibodies, inhibiting the virus infectiousness and lethal spread from cell-to-cell. To verify this, a cell-to-cell spread *in vitro* was carried out. Confluent Vero-cells were infected for 4 h with 400 TCID50 HSV-1 GFP reporter virus and were treated with the purified antibodies (100 µg mL^{-1}) from pooled blood samples (n=5) of day 28 and day 42. After 24 h images were recorded (Figure 3-20). The data indicates that the nanoparticle-presented peptides inhibited the cell-to-cell spread compared to the untreated case. Especially, the result of the peptide P2_5 was comparable to the control antibody mAb 2c.[158,159] The peptides P1_5 and P3_5 were also able to inhibit the cell-to-cell spread, but less efficiently. In these cases, some viral plaque formation occurred. This might be explained by a

missing optimisation of the antibody concentration. Therefore, an antibody titration might be useful for the future to determine the inhibitory concentration. However, the data shows a cell-to-cell spread inhibitory effect. This collaborates the suggestion that the animal survival is resulted from the positive respond of nanoparticle immunisation. Therefore, we conclude that the immunisation led to the production of HSV-1-neutralising antibodies, inhibiting the virus infectiousness and lethal spread from cell-to-cell.

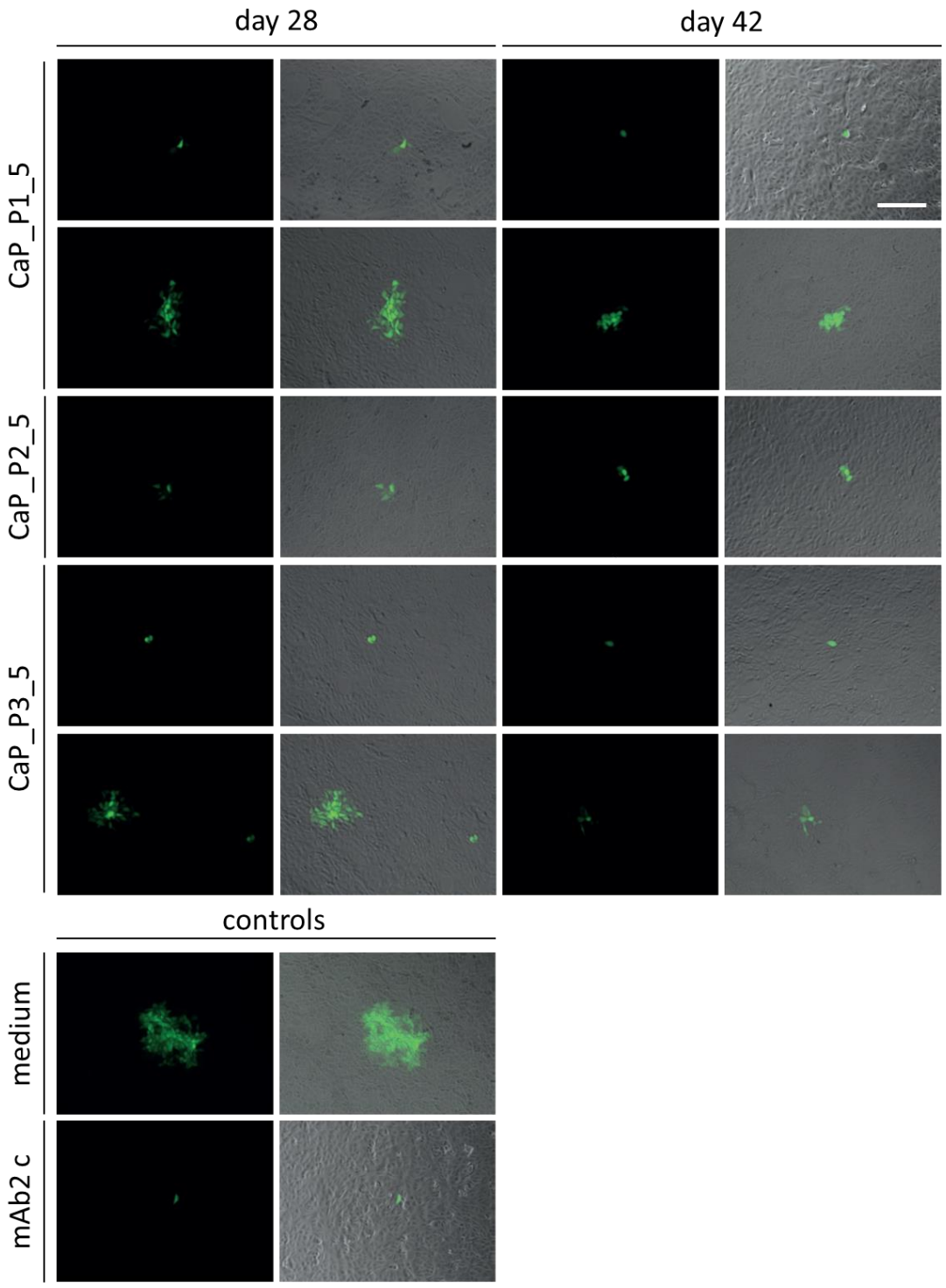

Figure 3-20: Inhibition of HSV-1 cell-to-cell spread by serum-derived antibodies from mice immunised with calcium phosphate nanoparticles.
Confluent Vero-cells were infected with 400 TCID50 HSV-1 GFP reporter virus. At 4 h post infection, inoculation medium was removed, and the cultures were inoculated with medium containing purified antibodies from mice immunised with CaP-nanoparticles CaP-P1 (day 28; 64.4 µg mL^{-1}, day 42; 189.4 µg mL^{-1}), CaP-P2 (day 28; 40.0 µg mL^{-1}, day 42; 72.5 µg mL^{-1}) or CaP-P3 (day 28; 50 µg mL^{-1}, day 42; 52.5 µg mL^{-1}). Antibodies were derived from pooled blood samples (n=5) taken at days 28 or 42 post immunisation. MAb2c at 500 nM was used as control. Pictures were taken 24 h post infection. Magnification = 100x. Scale bar 100 µm.

3.2.8 Summary

Here we have demonstrated the successful synthesis and full colloidal chemistry characterisation of four different antigen-conjugated calcium phosphate nanoparticles. The herein used antigenic and gB-derived synthetic peptides were effectively immobilised via hetero-specific cross-linking chemistry on a thin thiol-terminated silica-shell, coating the CpG^{m}-loaded calcium phosphate nanoparticle core. In all examined cases (P1_5-P3_5), this nanoparticle antigen-presenting vaccination system provided a pronounced and 4-5 times higher animal survival, ranging from 80-100%, compared to non- and peptide-immunised animals. This high animal survival rate indicated strongly that the murine immune system did respond positively to the antigen-functionalised nanoparticles and initiated the production of gB-specific antibodies, neutralising cell-to-cell spreading HSV virions. This was verified through the *in vitro* cell-to-cell spread assay.[158,159] Therefore, the organism was protected prophylactically. Interestingly, even one single dose of the P3_5-antigen-conjugated nanoparticles provided a sufficient protection against the viral herpetic infection over the whole observation time. This demonstrates, in turn, a good addressability of the nanoparticle-presented antigens and as well an easy recognition by the murine immune system. Therefore, the presented vaccination system may be an alternative to other nanoparticle-based carrier systems for future vaccination purposes.

3.3 Aggregation induced emitted fluorescence by a novel class of luminophores on calcium phosphate nanoparticles

Recently, a novel class of luminophores was established by Voskuhl *et. al.*.[199] The molecular structures of these luminophores are composed of a central terephalonitrile moiety flanked by two or four units of thioether-bonded benzene derivates (Figure 3-21A).

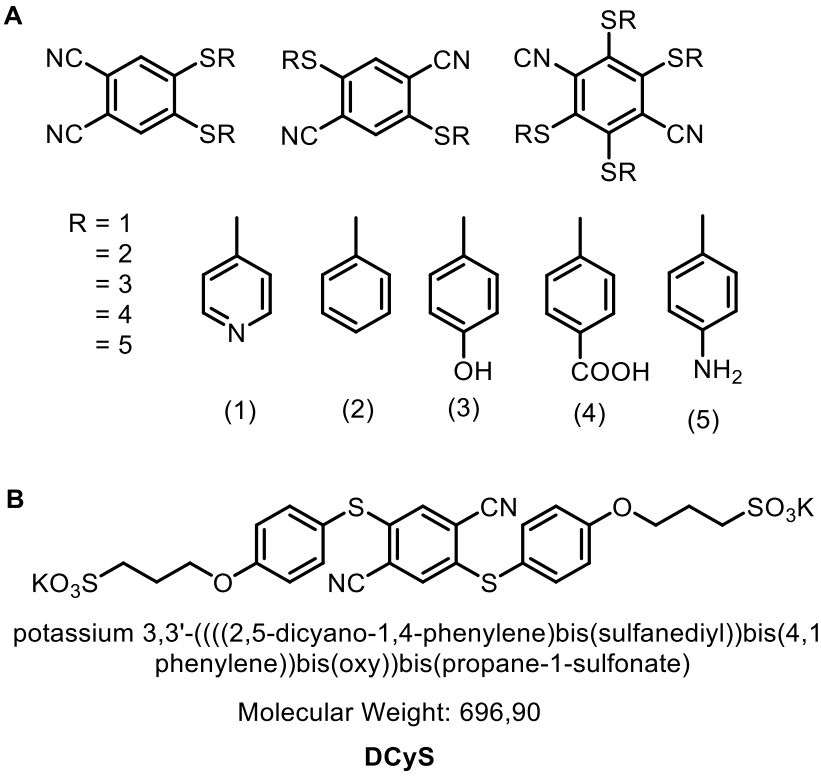

Figure 3-21: Different aggregation induced emitting luminophores (AIEL).
A: A set of possible modification of AIEL. B: Negatively charged AIEL, called DCyS which was used in this study.

These luminophores show an aggregation induced emitting luminescence (AIEL), by arresting the rotational degree of freedom of the σ thioether-bonds within the molecule. This can be realised by an appropriate interaction partner e.g. by a counter-ionic interaction partner (precipitation) or by complementary bonding through hydrophobic interactions. The AIELs have a broad potential application range, including the investigation of protein-protein interactions, usage as a diagnostic tool or as a molecular probe. In this proof of concept study, the cellular uptake of an AIEL was investigated using single-shell calcium phosphate nanoparticles.

3.3.1 Synthesis and characteristics of AIEL loaded calcium phosphate nanoparticles

Initially, a small set of different concentrations of the AIEL DCyS was screened to find a stable dispersion that could be used for later uptake analysis. Therefore, the negatively charged DCyS (Figure 3-21 B) was dissolved in DMSO, giving a 5 mM stock solution which was then diluted to give either 250 µM, 500 µM or 1000 µM of the AIEL in the final dispersion. Particles were synthesised following the synthesis scheme of the figure below (Figure 3-22).

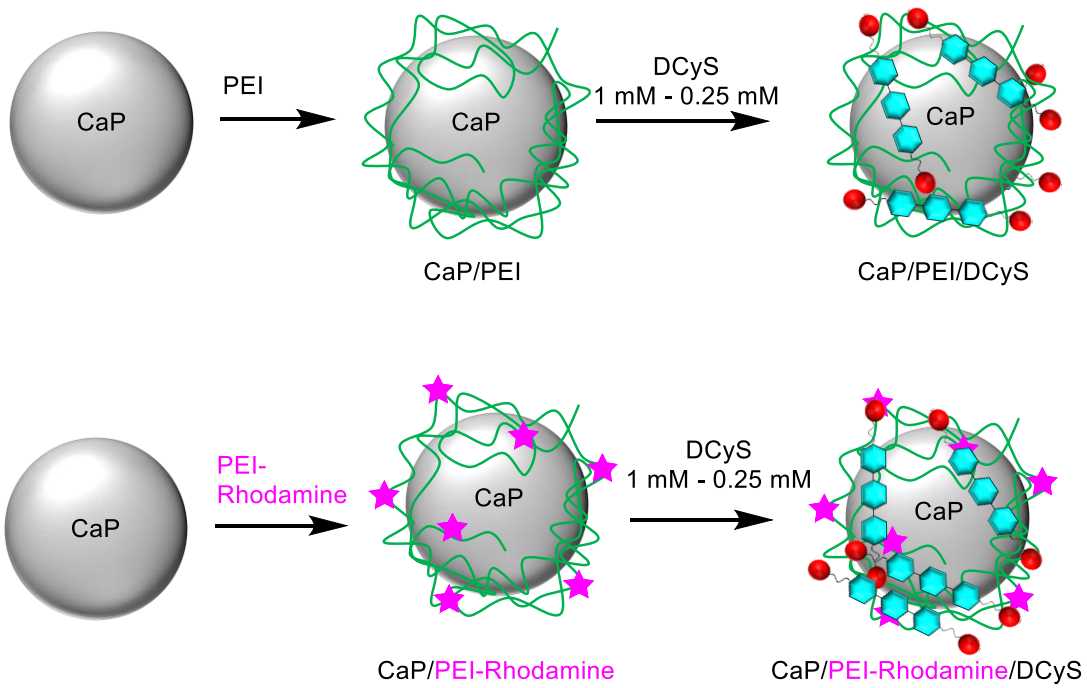

Figure 3-22: Synthesis scheme of AIEL loaded calcium phosphate nanoparticles.
A range of three different concentration was used for the nanoparticle synthesis (1 mM, 500 µM, 250 µM).

The primarily DLS results revealed that four of the six synthesised nanoparticles were not colloidal stable. Only the type of nanoparticles with the lowest amount of the AIEL (DCyS) showed a stable dispersion with a small degree of agglomeration (Figure 3-23 and Table 3-11A). The dispersion of CaP/PEI/DCyS loaded with 250 µM DCys (174 µg mL^{-1}) showed an average size distribution of 357 nm, while the PEI-Rhodamine stabilised particles showed a maximum of 242 nm. These results fit well to those of the SEM analysis (Figure 3-24). SEM images also revealed that the

PEI-Rhodamine stabilised particles were highly agglomerated and agglutinated. Thus, a precise size determination could not be carried out.

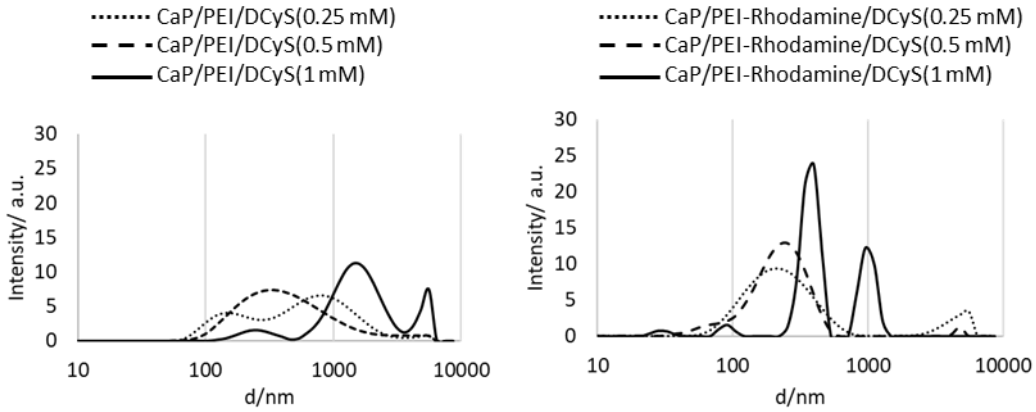

Figure 3-23: DLS measurement of the synthesised AIEL-loaded calcium phosphate nanoparticles. The with an increasing DCyS concentration. The data indicates that the dispersions of calcium phosphate were unstable in the case of an increased AIEL concentration reflected by the enlarged size of the hydrodynamic diameter. Only the lowest tested concentration of 250 µM DCyS showed good colloidal characteristics.

Therefore, the DCyS loaded and PEI-Rhodamine stabilised particles were assumed to have the same size as like the calcium phosphate nanoparticles stabilised by the non-fluorescently labelled PEI.

After the synthesis it turned out that the hydrodynamic diameter measured by DLS was enlarged with an increasing DCyS concentration. Here, the CaP/PEI-Rhodamine/DCyS(0.25 mM) showed the best colloidal characteristics. Therefore, these were used for the later uptake analysis. The UV/Vis spectroscopy for CaP/PEI-Rhodamine/DCyS(0.25 mM) indicated that over 95% (166 µg mL^{-1}) of the initially used compound was found on the surface of the particles (Figure 3-25). The AAS could reveal a calcium concentration of 106 µg mL^{-1} which corresponds to a hydroxyapatite concentration of 266.2 µg mL^{-1}. Together with a solid core diameter of 125 nm, the nanoparticle concentration was calculated to $8.3 \cdot 10^{10}$ nanoparticles per millilitre (NPs mL^{-1}) giving a total load of $1.7 \cdot 10^{6}$ DCyS (*MW*=691 g mol^{-1}) molecules on one single nanoparticle (DCyS NP^{-1}). By taking the number of AIEL molecules on one nanoparticle, the occupied area can be calculated. Then with a total area of $4.9 \cdot 10^{4}$ nm^2 per nanoparticle, it can be assumed that each nm^2 is occupied with 35 DCyS molecules. Further calculated colloidal and nanoparticular

characteristics for CaP/PEI-Rhodamine/DCyS(0.25 mM) nanoparticles are shown in Table 3-11B.

Table 3-11: DLS results and calculated characteristics of CaP/Rhodamine/DCyS(0.25 mM)
DLS results of the AIEL-loaded calcium phosphate nanoparticles. Different concentrations of the AIEL compound were used ranging from 0.25-1.0 mM.

A) Type of nanoparticle	**Size(DLS)/nm**	**PDI**	**ζ/mV**
CaP/PEI/DCyS (0.25 mM)	357.2 ±21.8	0.515	19.2±0.6
CaP/PEI/DCyS (0.5 mM)	323.7 ±3.5	0.410	20.0±0.3
CaP/PEI/DCyS (1 mM)	1622 ±44.5	0.475	19.3±1.3
CaP/PEI-Rhod/DCyS (0.25 mM)	242.2 ±19.1	0.305	22.7±0.8
CaP/PEI-Rhod/DCyS (0.5 mM)	281.7 ±16.4	0.357	22.6±0.8
CaP/PEI-Rhod/DCyS (1 mM)	5552 ±775.1	0.649	21.2±0.4

B) Parameter	**CaP/PEI-Rhod/DCyS (0.25 mM)**
SEM diameter by DLS/nm	125
V(one nanoparticle; only CaP)/m^3	$1.0 \cdot 10^{-21}$
A(one nanoparticle; only CaP)/m^2	$4.9 \cdot 10^{-14}$
m(one nanoparticle; only CaP)/kg	$3.2 \cdot 10^{-18}$
w(Ca^{2+}) by AAS/µg mL^{-1} (= g m^{-3})	106
w($Ca_5(PO_4)_3OH$)/µg mL^{-1} (= g m^{-3})	266.2
NPs mL^{-1}	$8.3 \cdot 10^{10}$
MW(DCyS)/g mol^{-1}	691
w(DCyS)/µg mL^{-1} (= g m^{-3})	166
DCyS molecules mL^{-1}	$1.4 \cdot 10^{17}$
m(DCyS) per nanoparticle/kg	$2.0 \cdot 10^{-18}$
DCyS molecules NP^{-1}	$1.7 \cdot 10^{6}$
DCyS molecules nm^{-2}	35
wt ratio DCyS to calcium phosphate	1:1.6
Particle composition	
CaP/wt-%	61.7
DCyS /wt-%	38.3

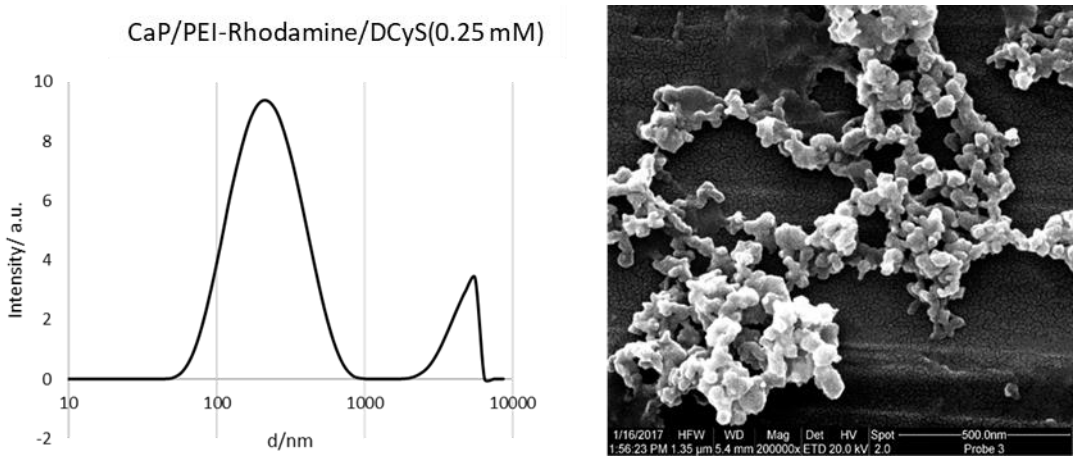

Figure 3-24: SEM images of CaP/PEI-Rhodamine/DCyS nanoparticles.
The average size of the DCyS loaded calcium phosphate nanoparticle was 125 nm and showed a small degree of aggregation. PEI-Rh stabilised particles were highly agglomerated thus a precise determination of the size was not possible. According to the similarities in size found by the DLS, it was assumed that the SEM data of the dispersion CaP/PEI-Rh/DCys(0.25 mM) has a similar size as like the dispersion of CaP/PEI/DCyS(0.25 mM).

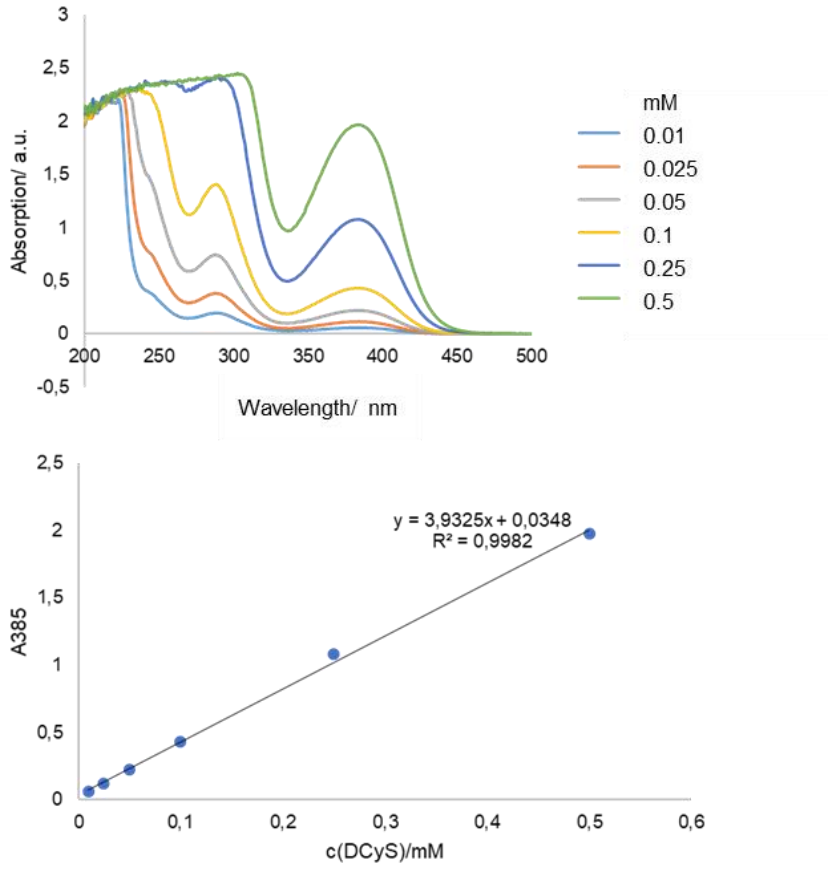

Figure 3-25: Absorption spectra and calibration curve of DCyS loaded calcium phosphate nanoparticles.
95% of the AIEL was found on the surface of the particles. The concentration value in the supernatant of the final dispersion was subtracted from the initial used amount of DCys, giving the final concentration of 166 µg mL^{-1} on the surface of the calcium phosphate nanoparticles.

The negatively charged AIEL is adsorbed on the positively charged PEI. To exclude a potential loss of the AIEL by positively charged counteracting ions, e.g. sodium chloride, the synthesised calcium phosphate nanoparticles were redispersed at various concentrations of NaCl, ranging from 0-150 mM NaCl and the changes of the fluorescence intensities were measured (Figure 3-26).

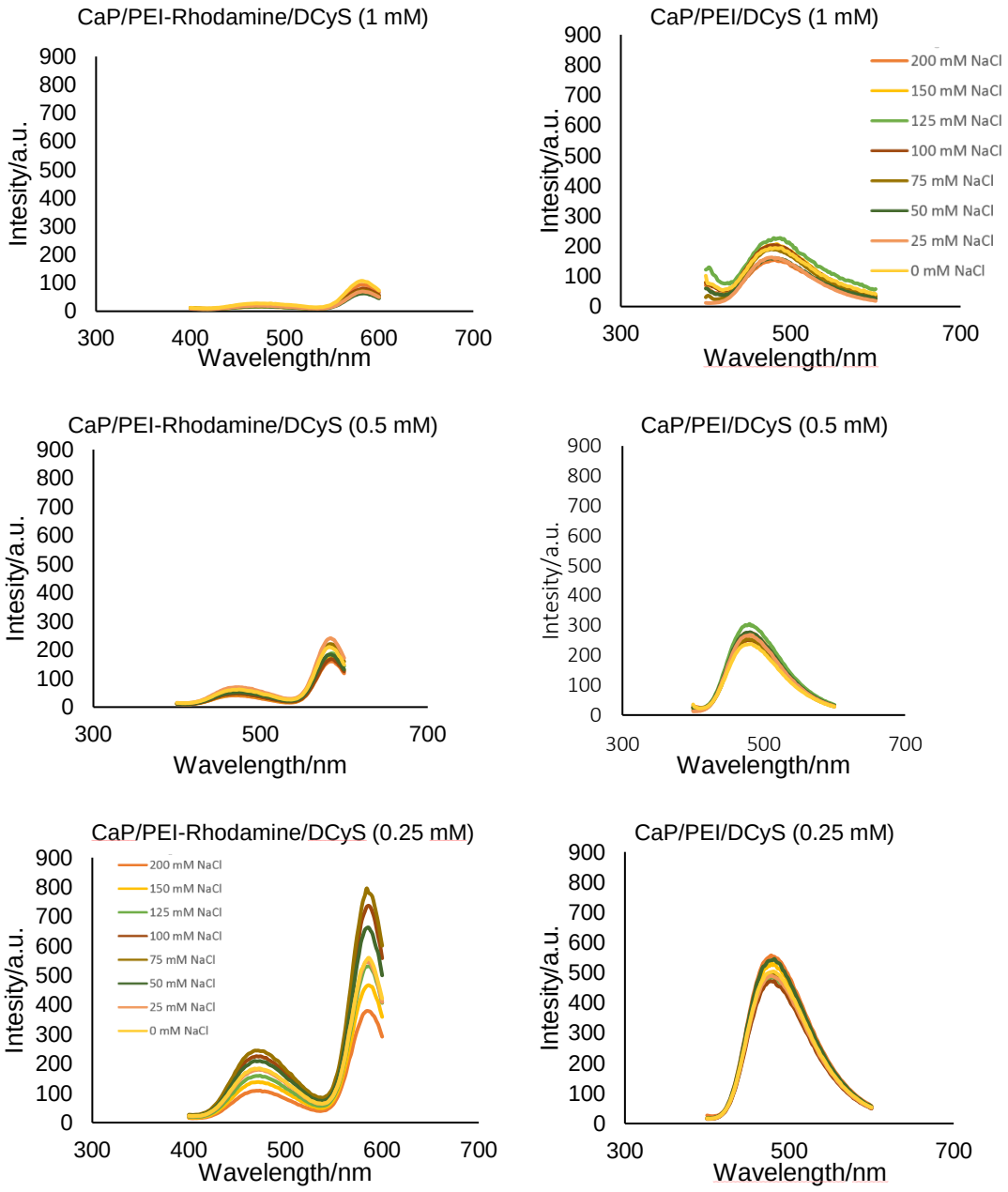

Figure 3-26: Sodium chloride dependency.
Left from top to down: CaP/PEI-Rhodamine/DCyS; Right from top to down: CaP/PEI/DyCS. AIEL-loaded nanoparticles were redispersed in distinct concentrations of sodium chloride ranging from 0-150 mM. No significant dependency was found for the used sodium chloride concentrations. Interestingly, the fluorescence intensity was decreased with increasing amounts of the AIEL probably due to some quenching effects. Fluorescence Exc. 350 nm Em. 480 nm DCyS, and 584 nm rhodamine.

The data revealed different concentrations of sodium chloride does not significantly influence the AIEL fluorescence intensity for almost any of the synthesised nanoparticles. Only the PEI-Rhodamine stabilised nanoparticles loaded with 0.25 mM of DCyS was influenced. Herein, the optimal NaCl concentration was 75 mM. Furthermore, a correlation between the used amount of AIEL was found depending on the final AIEL concentration. In final, the fluorescence intensity was clearly influenced, showing an increased fluorescence intensity with a decreasing AIEL concentration. This might be explained by the self-aggregation of the dye AIEL. The self-aggregation of dyes even at low concentrations leads to a significant energy transfer between the dyes resulting in severe quenching and low brightness implicating low fluorescence intensity.[200]

3.3.2 Uptake of DCyS loaded nanoparticles

For the uptake analysis, 50 µL (or $4.2 \cdot 10^9$ particles) CaP/PEI-Rhodamine/DCyS(0.25 mM) particles were used for the incubation with 25,000 HeLa cells per well which corresponds to about 168 particles per cell.

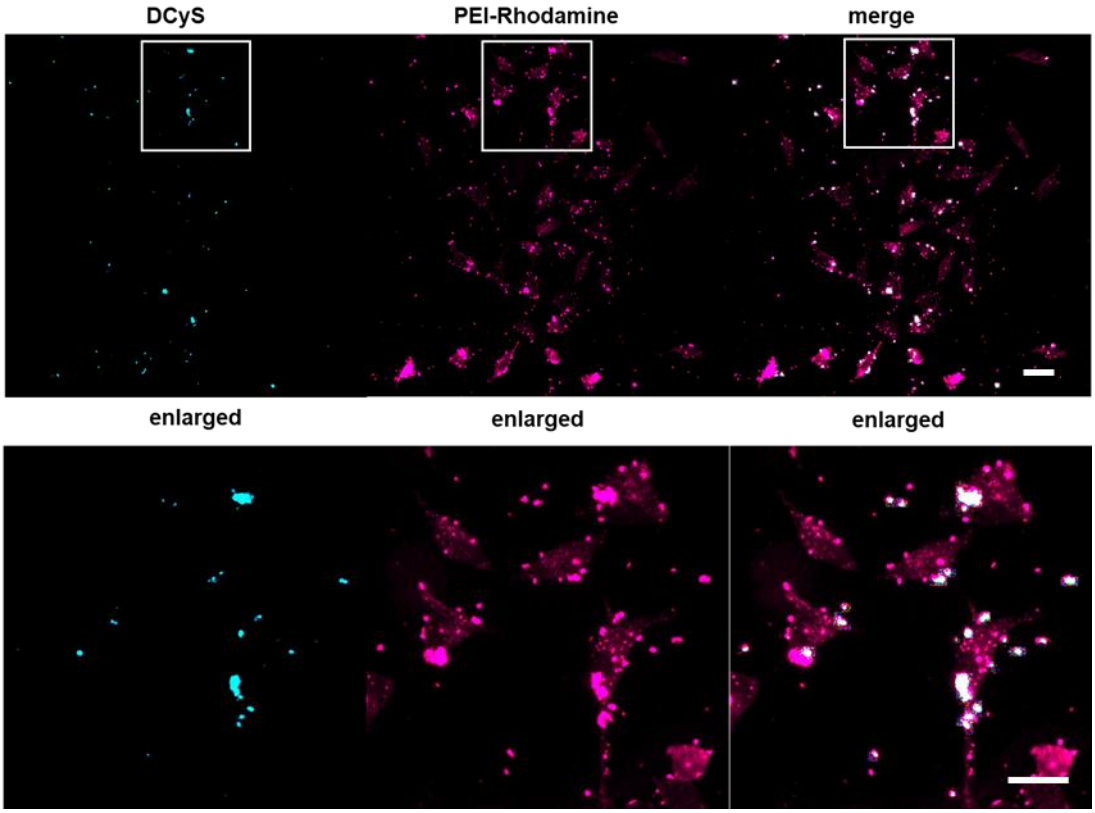

Figure 3-27: Incubation after 6 h. 25,000 cells per well were incubated for 6 h.
After 6 h incubation with $4.2 \cdot 10^9$ particles, cells were washed twice with PBS to remove excess material after that cells were imaged. Merging colours of the fluorescently labelled colloidal stabiliser PEI-Rhodamine (mangenta) and DCyS (cyan) indicate an uptake of the calcium phosphate nanoparticles by the cells. Scale bar 20 µm.

Cells were incubated for 6 h in DMEM under humidified atmosphere with 5% CO_2. After the incubation, cells were washed twice with PBS to remove excessive and nonincorporated materials from the cells. Then, the wells were refilled with medium and the cells were imaged with a Keyence Biorevo BZ-9000 microscope (Osaka, Japan). The results shown in Figure 3-27 indicate a slight uptake through the cells which is reflected by a diffuse distribution of the purple fluorescence signal (Rhodamine) and by the merging colours (white) coming from the DCyS (cyan) and fluorescently labelled PEI (purple). It further indicates that both molecules are

partially absorbed on the surface of the calcium phosphate nanoparticles since not all the fluorescence signals coming from PEI-Rhodamine are matching with those from the DCyS. Thus, it was assumable that some of the DCys was interacting with other binding partners in the medium during the incubation so that the DCyS was probably washed out after medium exchange. However, the results indicate an uptake of the DCyS-loaded nanoparticle through HeLa cells. Major purpose of this study was to verify a possible uptake of the AIEL through calcium phosphate nanoparticles.

The emitting fluorescence of the herein used AIEL is mainly caused by arrest of the rotational freedom degree of the two sulfonate acid groups within the molecule.[199] Obviously, these groups formed ionic bonds to the positively charged PEI covering the surface of the nanoparticles which can be derived from the observation of the cellular uptake analysis (merging colours). The experiment was repeated multiple times. In all cases, a clear detectable fluorescence signal from the AIEL was visible. Due to the anionic character of DCyS it was assumed that polyethyleneimine, a polycation, might also be able to deliver DCyS into cells with the help of cationic PEI/DCyS complexes. Therefore, PEI alone, which is also known as a transfection reagent, was also investigated through a time resolved uptake analysis for up to 16 h, following a standard PEI transfection protocol.[201] Herein, a different range of DCyS concentrations (0-200-µM in final) were used for the formation of PEI complexes (Figure 3-28). After 3 h, HeLa cells began to take up the DCyS/PEI complex starting with 75 µM of the AIEL. At 100 µM, the uptake of the DCyS indicated a reached intensity maximum at 3 and 6 h. The fluorescence signal intensity decreased with increasing AIEL concentration. A decreased cell confluence at 200 µM of the AIEL was observed that indicated some toxic side effects. After 6 h, the cells were washed with DPBS twice and incubated for further 16 h in fresh medium. After incubation, only a weak fluorescence signal remained. This indicates that the AIEL is probably transported out the cell via exocytosis.

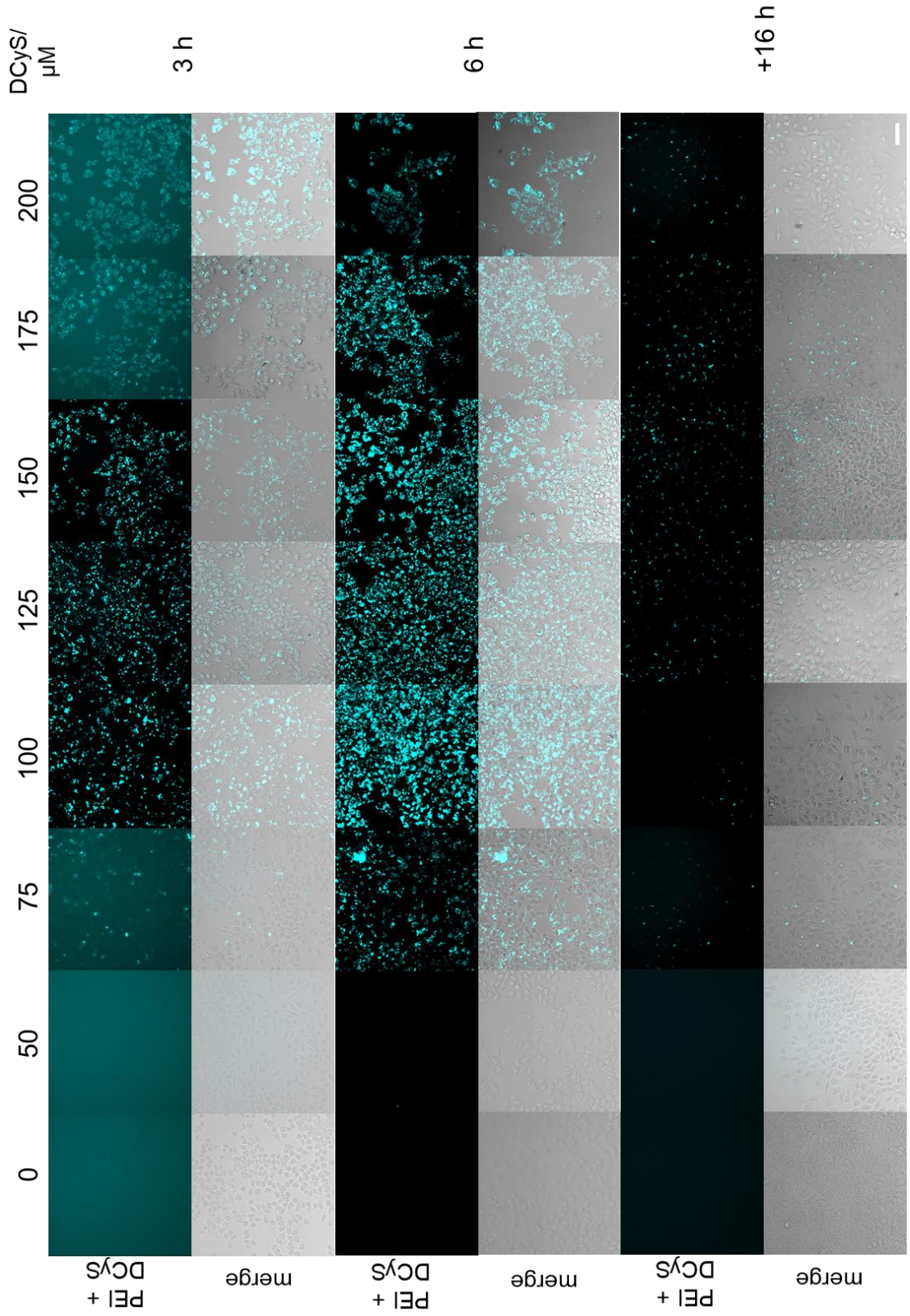

Figure 3-28: Uptake analysis with PEI/DCyS complexes.
Cells were incubated for 3 and 6 h. After 6 h, the cells were washed twice with DPBS, fresh medium was added and incubated for additional 16 h. Cells were imaged after each incubation timepoint. Scale bar 50 µm.

3.3.3 Summary

These primarily results have shown a feasible application of calcium phosphate nanoparticles as a carrier system for the AIEL transport across the cell membrane. The adsorption of AIEL was insignificantly impaired by varying sodium chloride concentrations, while using high AIEL concentrations lead to self-aggregation of the luminophore with AIEL resulting in severe quenching, low brightness and implicate low fluorescence intensity. Interestingly, the AIEL was also successfully transported in cells by PEI/AIEL-complexes revealing alternate ways for the dye transport.

However, further investigations need to be carried out e.g. how the cells do clear off the AIEL and which pathway is used. This experiment can be carried through vesicular markers, using small time intervals or time-lapse trafficking of the AIEL after the 6 h incubation and washing.

3.4 HBcAg loaded calcium phosphate nanoparticles

In this study, calcium phosphate nanoparticles have been used as a potential vaccine against the hepatitis B virus (HBV). This study was carried out in cooperation with the Institute of Virology in Wuhan. All *in vivo* studies in Caco-cells and bone marrow derived macrophages from femurs of C57BL/6 mice were carried out by Dr. Maohua Zhong and Dr. Ejuan Zhang from Wuhan. A recombinant version of salmonella flagellum protein, flagellin (rSF), 55 kDa, from the *salmonella enterica subsp.* was used as an immunogenic adjuvant in mice. The bacterial flagellin is a unique pathogen-associated molecular pattern (PAMP). PAMPs are easily recognised by the innate immune system.[202] It is also a potent activator (booster) of the innate and adaptive immune system in which the surface localised Toll-like receptor 5 (TLR5) and the cytosolic NOD-like receptor (NLR) protein 4 (NLRC4) receptors mediated immunogenicity is involved.[203,204] The stimulation of these receptors lead to the secretion of pro-inflammatory cytokines IL-8 and IL-1β in a broad range of cell types.[203,204] Together with a short and FITC-labelled antigenic peptide sequence (FITC-Ahx-NTNMGLKFRQLlWFH-OH, Pepscan Presto) from the nucleocapsid core protein HBcAg of HBV, they were loaded onto the surface of calcium phosphate nanoparticles and protected from protein degradation by a coating silica shell.[205] A truncated version of the SF protein (named as ΔL (DL)), 54 kDa, was used as a control and is non-immunogenic unable to activate the immunogenic TLR5 or NLR mediated pathways.[205]

3.4.1 Synthesis of Flagellin loaded calcium phosphate nanoparticles

The synthesis was carried out analogously as it is described by Kozlova *et al.* (Figure 3-29).[205] To estimate the peptide loading, after the final centrifugation the supernatant was kept and analysed by using the UV-spectroscopy, measuring the absorption at 480 nm of a FITC-labelled HBcAg antigenic peptide. The protein concentration was estimated via SDS PAGE, taking 50 µL of the final dispersion and applying the sample on a 13% SDS Gel, 100 V, 40 min.

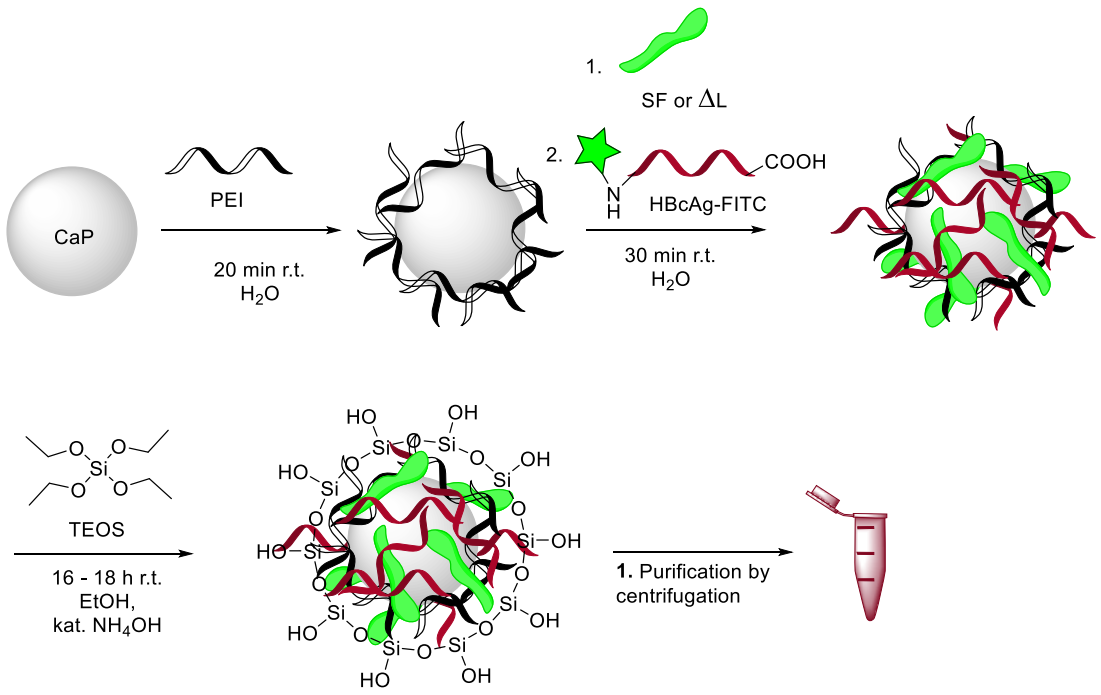

Figure 3-29: Synthesis of CaP/PEI/SF/HBcAg(FITC)/SiO_2-OH.
Synthesis of antigen, SF loaded and silica shell-coated calcium phosphate nanoparticles. First, calcium and phosphate were precipitated and polyelectrolytically stabilised by PEI, followed by the addition of the SF or ΔL (1 mg mL^{-1}) and the HBcAg and finally coated with a silica shell through the Stoeber process.

3.4.2 Characterisation

Four different types of calcium phosphate nanoparticles were synthesised: Unloaded nanoparticles are referred to as CaP/PEI/SiO_2 whereas the three other different types of antigen and either SF or DL loaded calcium phosphate nanoparticles are referred to as CaP/PEI/HBcAg-FITC/SiO_2, CaP/PEI/SF/HBcAg-FITC/SiO_2 or CaP/PEI/ΔL/HBcAg-FITC/SiO_2. The particles were analysed by DLS, SEM and UV/Vis spectroscopy. The DLS data and the corresponding SEM images are shown in Figure 3-30. All dispersions have shown colloidal stability which is indicated by the relative high and positive zeta potential. However, according to the dispersity, it can be concluded that only the unloaded particles have shown nearly monodispersed characteristics which is reflected by the PDI of 0.31 with a slight degree of agglomeration. The PDI of the loaded types of nanoparticles ranged from 0.35-0.47, indicating more agglomeration and polydispersity (Figure 3-30). However, the stability of all dispersions remained stable and the dispersions were used for later analysis.

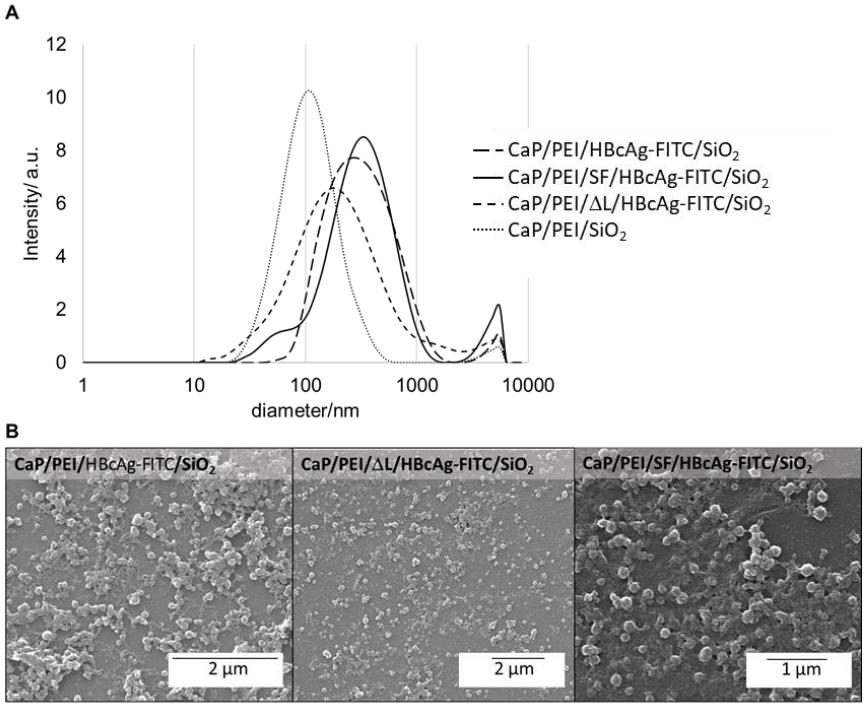

Particles (CaP/PEI/X; X= …)	**SiO_2**	**HBcAg-FITC/ SiO_2**	**rSF/HBcAg-FITC/ SiO_2**	**ΔL/HBcAg-FITC/ SiO_2**
Parameter				
d_{SEM}/nm	30±6	144±6	184±6	157±6
$V_{NP;\ only\ CaP}$/m^3	$1.4\cdot10^{-23}$	$1.6\cdot10^{-21}$	$3.3\cdot10^{-21}$	$2.0\cdot10^{-21}$
$A_{NP;\ only\ CaP}$/m^2	$2.8\cdot10^{-15}$	$6.5\cdot10^{-14}$	$1.1\cdot10^{-14}$	$7.7\cdot10^{-14}$
$m_{NP;\ only\ CaP}$/kg	$4.4\cdot10^{-20}$	$4.9\cdot10^{-18}$	$1.0\cdot10^{-18}$	$6.4\cdot10^{-18}$
$[Ca^{2+}]_{AAS}$/µg mL^{-1}	40.7	62.9	50.1	43.7
$[Ca_5(PO_4)_3OH]$/µg mL^{-1}	102.1	158.0	126.0	110.0
NPs mL^{-1}	$2.3\cdot10^{12}$	$3.2\cdot10^{10}$	$1.2\cdot10^{10}$	$1.7\cdot10^{10}$
w(protein)/µg mL^{-1}	–	–	300	300
MW(protein)/g mol^{-1}	–	–	55000	54000
protein mL^{-1}	–	–	$3.3\cdot10^{15}$	$3.3\cdot10^{15}$
m(protein) NP^{-1}/kg	–	–	$1.9\cdot10^{-17}$	$1.1\cdot10^{-17}$
protein NP^{-1}	–	–	$2.1\cdot10^{5}$	$1.3\cdot10^{5}$
protein nm^{-2}	–	–	2.0	1.6
wt ratio (protein:CaP)	–	–	1:0.42	1:0.36
w(HBcAg-FITC)/µg mL^{-1}	–	73.4	90.7	75.9
MW(HBcAg-FITC)/g mol^{-1}		2408	2408	2408
HBcAg-FITC mL^{-1}	–	$1.8\cdot10^{15}$	$2.3\cdot10^{15}$	$1.9\cdot10^{15}$
m(HBcAg-FITC) NP^{-1}/kg	–	$2.3\cdot10^{-18}$	$7.4\cdot10^{-18}$	$4.4\cdot10^{-18}$
HBcAg-FITC NP^{-1}	–	$5.7\cdot10^{4}$	$1.9\cdot10^{5}$	$1.1\cdot10^{5}$
HBcAg-FITC $µm^{-2}$	–	$8.8\cdot10^{5}$	$1.7\cdot10^{6}$	$1.4\cdot10^{6}$
wt ratio (HBcAg-FITC: CaP)	–	1:8.8	1:1.3	1:2.9
d_{DLS}/nm	106	270	264	145
PDI_{DLS}	0.307	0.349	0.441	0.468
ζ_{DLS}/mV	24.0±1.2	24.0±0.3	22.0±0.5	23.0±0.6
Particle composition				

CaP/wt-%	100	68.3	24.4	22.6
protein/wt-%	0	31.7	58.1	64.8
HBcAg-FITC/wt-%	0	0	17.6	15.6

Figure 3-30: Summary of the results.
A: DLS measurement. B: SEM images and summary of the nanoparticle characterisation. All synthesised calcium phosphate nanoparticles have shown a spherical morphology (HBcAg = HBcAg-FITC).

The average diameter size of the loaded nanoparticles ranged from 145-270 nm whereas the determination via SEM revealed an average size distribution that ranges from 144-184 nm in diameter (Figure 3-30). The amount of ΔL and SF onto the particles' surface was analysed by SDS PAGE and was carried out by Dr. Ejuan Zhang (data not shown). In both cases, it revealed a presumed protein concentration of 0.3 mg mL^{-1} which makes 300 µg of protein per mL dispersion. This gives a yield of about 75% of the initially used protein concentration of 400 µg mL^{-1} which is comparable with previous studies.[205] Together with the solid core radius of 72-92 nm from the SEM data and the calcium concentration determined by the AAS (67.2-80 µg mL^{-1}), corresponding to an equivalent hydroxyapatite concentration of 160-202 µg mL^{-1}, the number of protein molecules on the surface of one nanoparticle can be estimated. Thus, either 210,000 rSF or 130,000 ΔL molecules per single nanoparticle can be assumed on the surface of one single nanoparticle (Figure 3-30). In addition to the number of molecules per nanoparticle, the necessary and occupied area of the protein on the surface can be calculated giving 1.9 rSF and 1.6 ΔL protein molecules per nm^2 (Figure 3-30). The antigen loading was determined by UV/Vis spectroscopy, measuring the FITC absorption in the remaining supernatant after centrifugation of a small aliquot of a freshly prepared nanoparticle dispersion. Figure 3-31 shows the calibration curve of the antigen determination. Herein the absorbance at 480 nm was measured from the supernatants of the final dispersion to quantify the peptide concentration on the surface of the calcium phosphate nanoparticles.

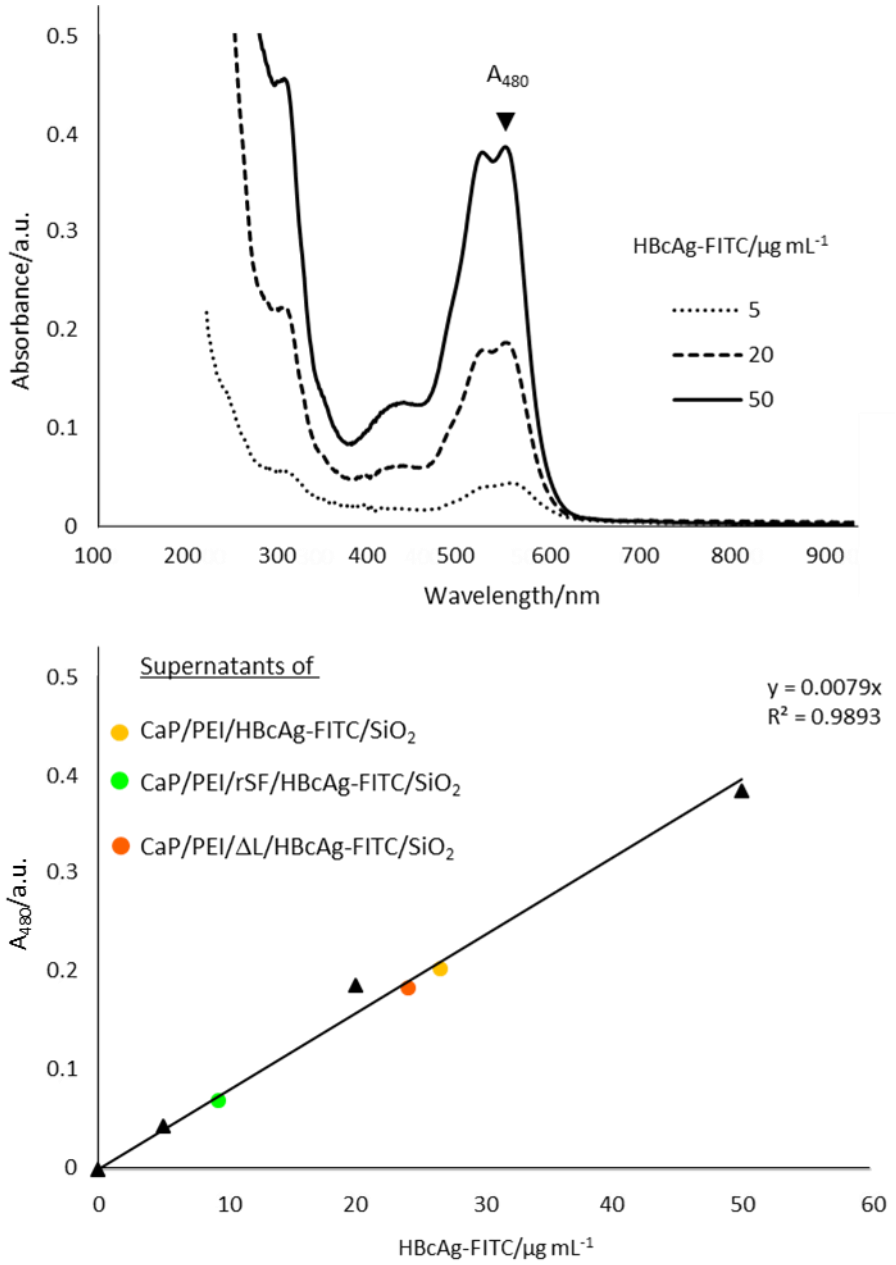

Figure 3-31: Antigen determination on the surface of calcium phosphate nanoparticles.
Upper section: Absorbance spectra of the calibration curve and samples of the supernatants after the final centrifugation step of each type of nanoparticle. Lower section: Calibration curve.

The calculated value was subtracted from the initial applied peptide concentration which was 100 µg mL^{-1}. Therefore, for the particles without any adjuvant, the concentration of the HBcAg-FITC antigen was 73.4 µg mL^{-1} whereas adjuvant-loaded nanoparticles have shown a comparable high amount of encapsulated HBV antigen, ranging from 75.9 µg mL^{-1} (ΔL-loaded) to 90.7 µg mL^{-1} (rSF-loaded). The difference might be explained through the different adjuvants that were used. In the case where no adjuvant or nonimmunogenic ΔL was used, it is noticeable that the amount of

antigen is slightly increased with the addition of ΔL. This increasing effect is also observed when the protein is switched to rSF. Herein, it can be assumed that the additional amino acids in rSF have a beneficial effect on the interaction between those two biomolecules i.e the adjuvant and the antigen.

This is also reflected by the number of molecules on the surface of each nanoparticle. Particularly, 57,000 HBcAg-FITC molecules per nanoparticle on the surface of CaP/PEI/HBcAg-FITC/SiO_2 can be calculated from the SEM and AAS data, which is less compared to the other types of nanoparticles CaP/PEI/rSF/HBcAg-FITC/SiO_2 (190,000 antigens per particle) and CaP/PEI/ΔL/HBcAg-FITC/SiO_2 (110,000 antigens per particle) (Figure 3-30+31). Herein, the occupied area of antigens can be assumed with $8.8 \cdot 10^5$ HBcAg-FITC molecules μm^{-2} (without adjuvant), $1.7 \cdot 10^6$ HBcAg-FITC molecules μm^{-2} (rSF-loaded) and $1.4 \cdot 10^6$ HBcAg-FITC molecules μm^{-2} (ΔL).

3.4.3 *In vitro* studies

In vitro and studies were carried out in Wuhan by the group of Prof. Dr. Huimin Yan. The TLR5 and NLRC4 activities of CaP/rSF/HBc-FITC/SiO_2 or CaP/ΔL/HBcAg-FITC/SiO_2 were measured by stimulating Caco-2 cells or peritoneal macrophages from and were quantified by the secretion of IL-8 or IL-1β using an enzyme-linked immunosorbent assay (ELISA). For the *in vitro* studies, human intestinal epithelial Caco-2 cells were grown in 300 µL DMEM supplemented with 10% FBS (Gibco, Darmstadt, Germany) and 100 U mL^{-1} of penicillin/streptomycin at 37 °C in 5% CO_2 atmosphere. Caco-2 cells were seeded at a density of $1 \cdot 10^5$ per well into 48-well polystyrene plates (Sarstedt, Germany) and cultured for 5 days. After an overnight culture in medium without FBS, the cells were stimulated either with SF-loaded nanoparticles or with ΔL-loaded nanoparticles or with dissolved SF (as positive control) in medium without FBS for 6 h. After centrifugation at 2,000 rpm for 10 min at 4 °C, the supernatants were collected and stored at -70 °C for IL-8 and IL-1β measurement by ELISA.[205] The results from the *in vitro* studies indicate that SF have maintained the TLR5 activity and stimulated similar amounts of IL-8 like soluble SF (Figure 3-32). Interestingly, a dilution of one-ten thousandth of CaP/PEI/rSF/HBcAg-FITC/SiO_2 has the same

cytokine secretion effect as a dilution of one-hundredth of the soluble flagellin which might be due to the presence of the silica shell.[206] IL-1β secretion is significantly and unspecifically enhanced by the nanoparticles, possibly through the presence of silicon in the particles.[206] However, in this proof of concept study, the results reveal that calcium phosphate nanoparticles can be used as a carrier for vaccination purposes. Calcium phosphate itself is known as a potent adjuvant which produce high titers of immunoglobulin G2a and neutralising antibodies and can facilitate protection against viral infections. Furthermore, they cause only little or no inflammation at the administration site.[207,208] For the forthcoming research on this topic, antibodies have still to be produced and analysed according to their neutralising efficiency against HBV. Further studies will show how effective such a system might be. Here, the cytokine stimulation through the flagellin-loaded calcium phosphate nanoparticles was tested.

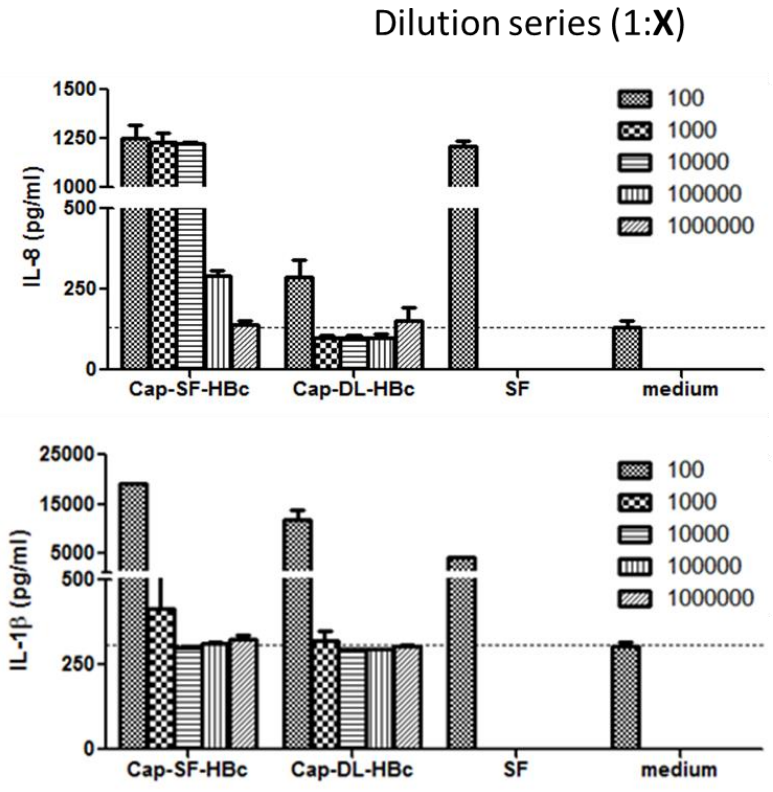

Figure 3-32: Quantitation of cytokines.
Flagellin loaded calcium phosphate nanoparticles induce the TLR5 pathway insignificantly compared to the amounts of IL-8 through soluble rSF. IL-1β secretion is significantly and unspecific enhanced by the nanoparticles, possibly by the presence of silicon in the particles.

In vivo studies with flagellin-functionalised nanoparticles were also carried out earlier where the IL-8 production was detected in C57BL/6 mice after intraperitoneal immunisation.[205] Together, the preliminary results and the herein shown results indicate that flagellin and calcium phosphate nanoparticles can be used as a vaccinal carrier system for immunisation purposes. In conclusion, it could be shown that calcium phosphate nanoparticles can be used as a vehicle for both antigen and adjuvant, giving the possibility to embody a functional carrier system based on biodegradable calcium phosphate nanoparticles that allow the production of cytokines *in vitro*.

3.4.4 Summary

Silica coated, SF flagellin and HBcAg-loaded calcium phosphate nanoparticles were successfully synthesised and characterised. The synthesised nanoparticles showed good colloidal characteristics. The results demonstrated, that calcium phosphate nanoparticles can be used as a vaccine carrier for different immuno-active biomolecules consisting of the adjuvant and the antigen. In a proof of concept, extracted cells released a pronounced amount of inflammatory related cytokines, indicating a good immune stimulation by the nanoparticle-transported biomolecules. However, further immunisation experiments and viability assays with an appropriate cell line need to be carried out to truly validate these results.

3.5 Delivery of poly(I:C) loaded calcium phosphate leads to a significant immunogenic stimulation against HBV in Kupffer cells

This study was a cooperation project between the groups of Prof. Dr. Dongliang Yang (Wuhan, China), Prof. Dr. Astrid Westendorf (Essen, Germany) and Prof. Dr. Matthias Epple (Essen, Germany). The nanoparticle synthesis-related results were provided from the Epple group. This study, the delivery of the Toll-like receptor 3 (TLR3) antagonist polyinosinic:polycytidylic acid (poly(I:C)) by calcium phosphate nanoparticles into murine liver cells was investigated to design a nanoparticle based vaccination system against hepatitis B virus (HBV) infected cells. The double stranded RNA analogue poly(I:C) is a potent immunogenic stimulator of the Toll-like receptor 3 (TLR3) pathway, inducing an immunogenic anti-viral response in numerous cell types.[209-213] Recently, the hydrodynamic injection of poly(I:C) in a mice model was used and led to an interferon-dependent clearance of the hepatitis B virus.[214] The fact that this application method is not clinically transferable to human patients makes it less useful. Thus, alternate pharmaceutical application forms have to be investigated. Herein, calcium phosphate nanoparticles were loaded with the immune-modulative TLR3 antagonist poly(I:C) and coated with a thin silica layer. The nanoparticle uptake was investigated in THP-1 macrophages by fluorescence microscopy. *In vivo*, the nanoparticles were injected intravenously into BALB/c and C57B/6 mice. In addition, the *in vitro* uptake into primary liver cells e.g. Kupffer cells (KC) and liver sinusoidal endothelial cells (LSEC) were also analysed. Furthermore, in our previous studies, we investigated an antibody-targeted approach with a different set of antibodies (IgG1 (Ctrl), anti-F4/80, IgG2 (Ctrl), anit-CD146) for an improved uptake efficiency. These results will be presented first.

3.5.1 Synthesis of poly(I:C)-loaded and thiol-terminated calcium phosphate nanoparticles

Calcium phosphate nanoparticles were prepared as described previously, using a time-scheduled peristaltic pump (solutions were pumped for 1 min in a water-prefilled (20 mL ultrapure water) glass vessel) for the quick precipitation (5 mL Ca^{2+}: 5 mL PO_4^{3-} : 7 mL PEI) of the corresponding aqueous salt solutions (i.e. 18 mM $Ca[CH_3CH(OH)COO]_2 \cdot 5H_2O$ [pH 10], 10.8 mM $(NH_4)_2HPO_4$)

[pH 10]).[58,61,205] These particles were colloidally stabilised by the cationic polyelectrolyte PEI or PEI-Cy5 (2 mg mL^{-1} each) , respectively. After 20 min of stirring at 500 rpm, 100 µL poly(I:C) (1 mg mL^{-1}) (Invivogen, France) was added to 0.9 mL of dispersion, giving 1 mL of a CaP/PEI(-Cy5)/poly(I:C) dispersion. The resulted dispersion was further stirred for 30 min at room temperature. In parallel, non-loaded nanoparticles were also prepared as control without the addition of poly(I:C). Next, the whole CaP/PEI(-Cy5)/poly(I:C) dispersion was poured in a mixture of 4 mL EtOH (p.a., Fisher Scientific, United Kingdom), 5 µL TEOS (Sigma Alrdrich) and 2.6 µL NH_3 (30-33% (v/v), Roth, Germany) and was stirred overnight. On the next day, the mixture was centrifugated at 30,000 rpm (Type 70 Ti Rotor, Beckman&Coulter; SORVALL WX Ultra Series Ultracentrifuge, Thermo Fisher) for 30 min and redispersed with a sonotrode (Hielscher UP50H; sonotrode MS7; cycle 0.8, amplitude 70%, 20 s) in 1 mL ultra-pure water. The resulting CaP/PEI(-Cy5)/poly(I:C)/SiO_2 nanoparticle dispersion was thiol-functionalised by pouring 1 mL of the dispersion in a mixture of 4 mL EtOH and 5 µL MPS. The reaction was stirred for 6-8 h. After stirring, the mixture was centrifuged at 30,000 rpm for 30 min and redispersed with a sonotrode (Hielscher UP50H; sonotrode MS7; cycle 0.8, amplitude 70%, 20 s) in 1 mL ultra-pure water. This led to a thiol-terminated nanoparticle surface for further functionalisation of targeting antibodies by cross-coupling chemistry. Antibodies i.e. anti-mouse F4/80 antigen, anti-CD146, mouse IgG1 K isotype control, rat IgG2a K isotype control for the coupling were all obtained from BD Bioscience (Life Technologies, Carlsbad, USA). 50 µg of each antibody (0.5-1 mg mL^{-1}) was reacted with sulfo-SMCC (4 mM) in PBS using a 300-fold molar excess in a total reaction volume of 500 µL. The reaction was carried out for 2 h at room temperature. The excess of the cross-coupling agent was removed by using an ultrafiltration device (Amicon, MWCO 3k, Merck), following the manufactures' protocol. Herein, the activated antibodies were spun down twice with 12,000 g (Heraeus Fresco 21, Thermo Fisher Scientific) for 30 min at 4 °C to 50 µL and were diluted with 450 µL PBS each centrifugation step. Last, the activated antibodies were spun down again to 50 µL with 12,000 g at 4 °C and were recovered by placing the inverted ultrafiltration device in a fresh collection tube. The collection tube was centrifugated with 2,000 g for 2 min at 4 °C. The collected antibodies were kept on ice. Then, 50 µL of each

antibody was reacted with 1 mL of thiol-terminated CaP/PEI(-Cy5)/poly(I:C)/SiO_2-SH nanoparticles on ice overnight.

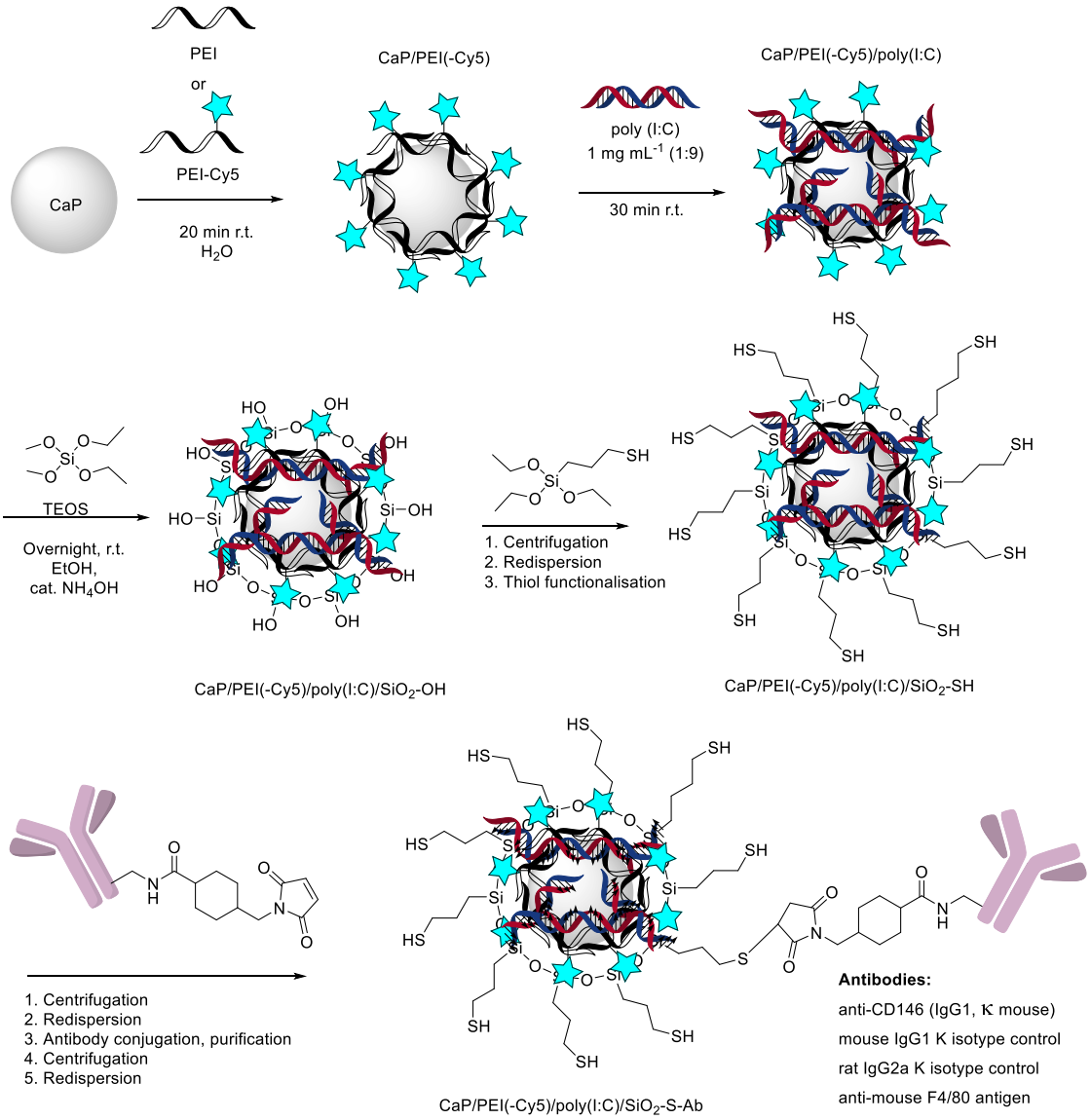

Figure 3-33: Synthesis route of poly(I:C) loaded and thiol-terminated calcium phosphate nanoparticles.
After precipitation and colloidal stabilisation, the particles were purified by ultracentrifugation and redisperison. A thin silica layer which infolds the calcium phosphate nanoparticle core was added by the hydrolysis of TEOS. Further hydrolysis with MPS led to thiol-terminated calcium phosphate nanoparticles. These nanoparticles are accessible for the attachment of antibodies or other proteins by cross coupling chemistry.

On the next day, every coupling reaction were purified by ultracentrifugation (30,000 rpm, 30 min,Type 70 Ti Rotor, SORVALL WX Ultra Series, Thermo Fisher) and the nanoparticles were recovered by subsequent redispersion ((Hielscher UP50H;

sonotrode MS7; cycle 0.8, amplitude 70%, 5 s) in 1 mL ultra-pure water giving the final dispersion of CaP/PEI(-Cy5)/poly(I:C)/SiO_2-S-Ab nanoparticles (Figure 3-33).

3.5.2 Characterisation

Calcium phosphate nanoparticles were characterised by DLS and SEM during all synthetic steps. The final dispersions of all functionalised calcium phosphate nanoparticles were colloidal stable and homogeneous, reflected by the small polydispersity index. A summary of the results can be found in Table 3-12. Analysis by SEM revealed a spherical morphology of the nanoparticles with an average diameter of 120 nm for CaP/PEI/poly(I:C)/SiO_2-SH and CaP/PEI/poly(I:C)/SiO_2-S-F4/80 nanoparticles (Figure 3-34A and B). The average hydrodynamic diameter of CaP/PEI/poly(I:C)/SiO_2-SH nanoparticles was 212 nm (zeta potential +43 mV). The antibody-functionalised calcium phosphate nanoparticles were generally larger, with a hydrodynamic diameter ranging from 290-463 nm with a similar zeta potential (+39-43 mV) (Table 3-13). The SEM diameter of all nanoparticles was generally smaller than the hydrodynamic DLS diameter, indicating a moderate degree of particle agglomeration. SEM analysis revealed a general spherical morphology for all synthesised calcium phosphate nanoparticles.

.

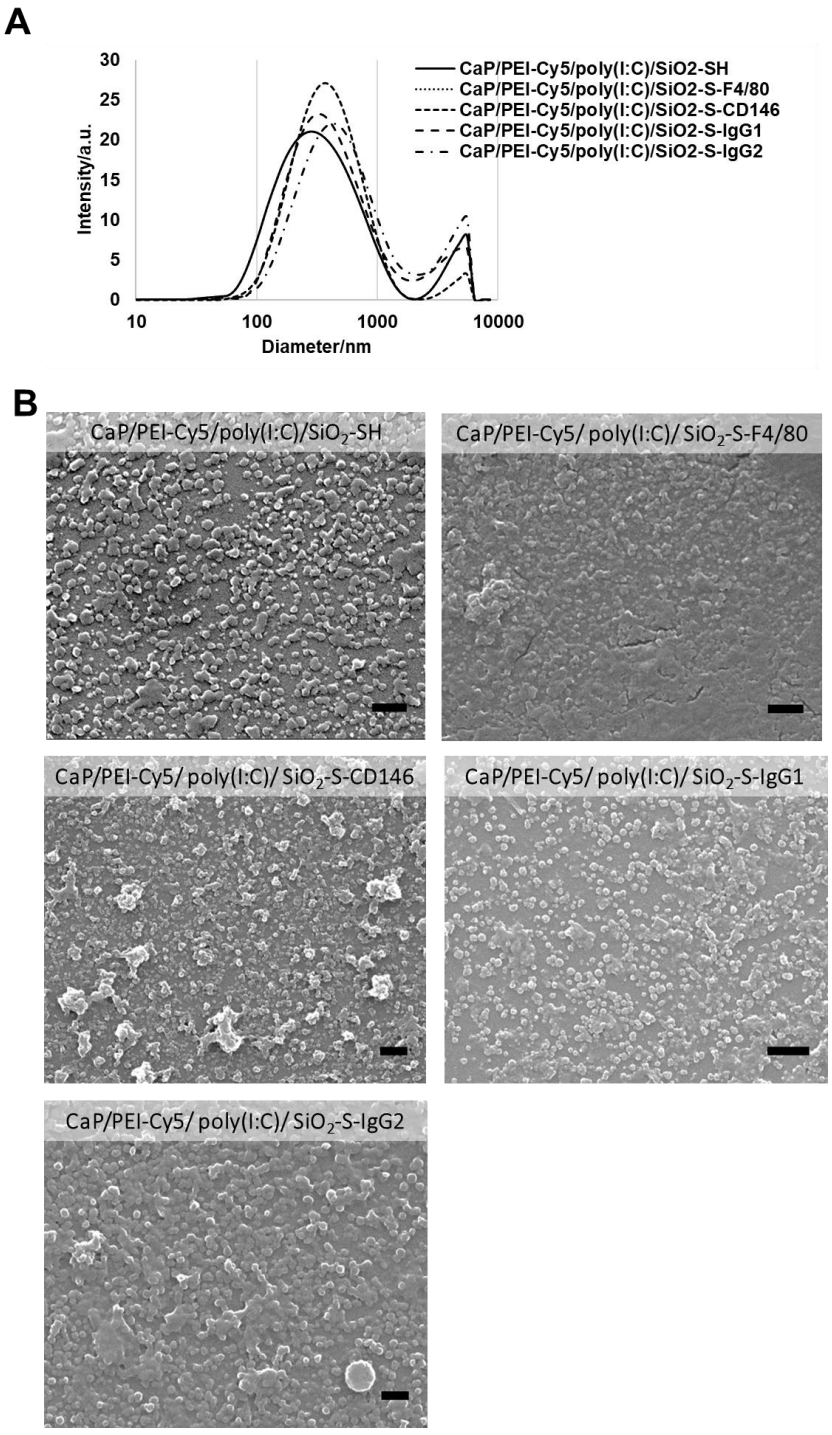

Figure 3-34: DLS and SEM results of the functionalised nanoparticles.
A: DLS of the functionalised calcium phosphate nanoparticles. B: SEM analysis of the functionalised calcium phosphate nanoparticles. The hydrodynamic diameter of the DLS measurement was generally smaller than the core diameter of the SEM analysis. Generally, all synthesised calcium phosphate nanoparticles have shown a spherical morphology. Scale bar 500 nm.

In comparison to the non-functionalised calcium phosphate nanoparticles, without antibodies, the hydrodynamic diameter was increased in all cases.

Table 3-12: Characterisation data of functionalised nanoparticles.

Particle type	d_{DLS}/nm	d_{SEM}/nm	PDI	ζ/mV
CaP/PEI-Cy5/poly(I:C)/SiO_2-SH	212±12	120±6	0.412	43
CaP/PEI-Cy5/poly(I:C)/SiO_2-S-F4/80	290±30	121±3	0.468	39
CaP/PEI-Cy5/poly(I:C)/SiO_2-S-CD146	329±33	131±5	0.314	40
CaP/PEI-Cy5/poly(I:C)/SiO_2-S-IgG1	356±11	152±4	0.432	39
CaP/PEI-Cy5/poly(I:C)/SiO_2-S-IgG2	463±10	132±3	0.479	43

The poly(I:C) concentration was determined by UV spectroscopy, analysing the final supernatants from the last purification step by using its maximal absorbance of poly(I:C) at 266 nm and taking the non-loaded thiol-terminated calcium phosphate nanoparticles as a blank. Figure 3-35 shows the calibration curve and the corresponding results (Table 3-13). Therefore, different amounts of poly(I:C) were found on the surface of the calcium phosphate nanoparticles ranging from 33.8-97.3 µg mL^{-1}. Interestingly, the amount of poly(I:C) was the lowest on non-functionalised calcium phosphate nanoparticles (Table 3-13). This data together with the results from the AAS allows the calculation of the number of nanoparticles per mL, as well as the number of poly(I:C) molecules on one single nanoparticle. With an average length of 0.2-1 kilobases for low molecular weight poly(I:C) and molecular weight for a single I:C base-pair of 653.41 g mol^{-1}, the molecular weight ranges from 131,000-653,000 g mol^{-1} and gives a mean of 460,000 g mol^{-1}.

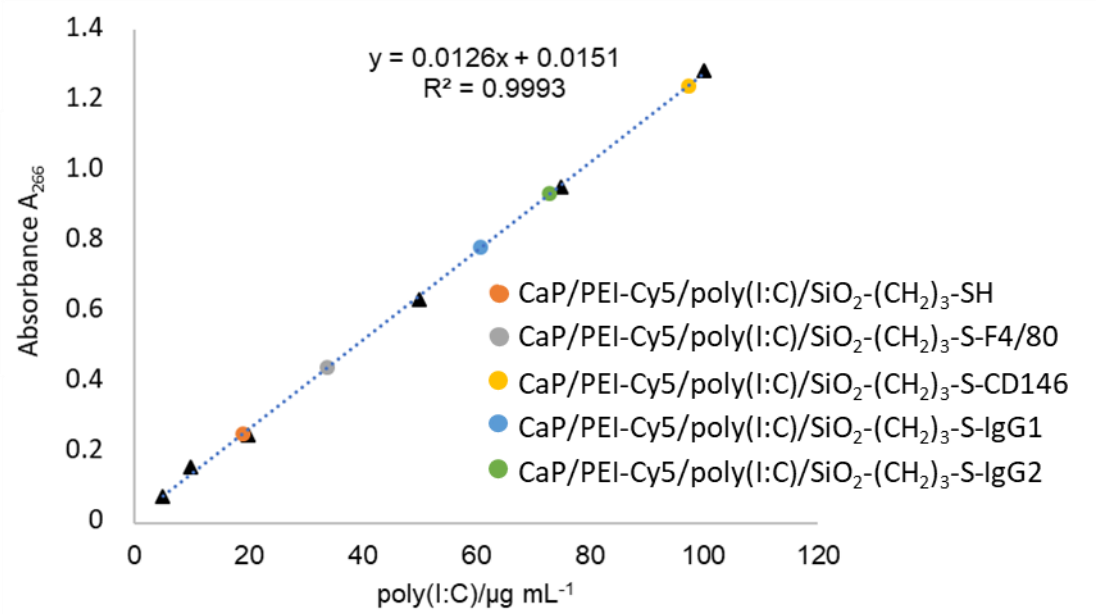

Figure 3-35: Quantitation of poly(I:C).
Poly(I:C) was determined by measuring the absorbance at 266 nm from the supernatant of a freshly prepared and centrifugated calcium phosphate nanoparticle dispersion.

The calculations of the characteristic nanoparticular parameters were carried by using the Eq. 13 and Eq. 14 from chapter 5.5. For example, in the case of F4/80-functionalised nanoparticles, the calcium concentration was 7.3 µg mL^{-1}, corresponding to an equivalent hydroxyapatite concentration of 18.3 µg mL^{-1}. Together with the solid core radius of 60.5 nm, the nanoparticle concentration was calculated giving a nanoparticle concentration of $6.3 \cdot 10^9$ NPs mL^{-1}. Herein, spherical and uniformly shaped nanoparticles and a hydroxyapatite density of $3.14 \cdot 10^3$ kg m^{-3} were assumed. The number of poly(I:C) molecules per mL^{-1} was determined by dividing the nanoparticle bound amount (in µg mL^{-1}) of poly(I:C) through the nanoparticle concentration, giving $4.4 \cdot 10^{13}$ poly(I:C) molecules NP^{-1}. For uniformly shaped and spherical F4/80-functionalised nanoparticles, the total surface area was $4.6 \cdot 10^4$ nm^{-2} where 0.15 poly(I:C) molecules, occupying one nm^2 or $1.5 \cdot 10^5$ poly(I:C) molecules μm^{-2}. F4/80-functionalised nanoparticles consisted of 30% CaP and 70% poly(I:C) indicating that most of the poly(I:C) was encapsulated as stacked multi-layers. Further calculation for the other different types of nanoparticles were carried out analogously (Table 3-13).

Table 3-13: Poly(I:C) loadings on the surface of the functionalised calcium phosphate nanoparticles. Taking 460,000 g mol^{-1} as average molecular weight for poly(I:C).

Type of nanoparticles (CaP/PEI-Cy5/poly(I:C)/SiO_2-S-X; X=…)	**H**	**F4/80**	**CD146**	**IgG1**	**IgG2**
Parameter					
d_{SEM}/nm	120±6	121±3	131±5	152±4	132±3
$V_{NP;\ only\ CaP}/m^3$	$9.0\cdot10^{-22}$	$9.3\cdot10^{-22}$	$1.2\cdot10^{-21}$	$1.8\cdot10^{-21}$	$1.2\cdot10^{-21}$
$A_{NP;\ only\ CaP}/nm^2$	$4.5\cdot10^{4}$	$4.6\cdot10^{4}$	$5.4\cdot10^{4}$	$7.3\cdot10^{4}$	$5.5\cdot10^{4}$
$m_{NP;\ only\ CaP}$/kg	$2.8\cdot10^{-18}$	$2.9\cdot10^{-18}$	$3.7\cdot10^{-18}$	$5.8\cdot10^{-18}$	$3.8\cdot10^{-18}$
$[Ca^{2+}]_{AAS}/\mu g\ mL^{-1}$	10.4	7.3	16.7	13.5	7.5
$[Ca_5(PO_4)_3OH]/\mu g\ mL^{-1}$	26.1	18.3	42.0	33.9	18.9
NPs mL^{-1}	$9.2\cdot10^{9}$	$6.3\cdot10^{9}$	$1.1\cdot10^{10}$	$5.9\cdot10^{9}$	$5.0\cdot10^{9}$
w(poly(I:C))/µg mL^{-1}	19	33.8	97.3	60.8	73
MW(poly(I:C))/g mol^{-1}	$4.6\cdot10^{5}$	$4.6\cdot10^{5}$	$4.6\cdot10^{5}$	$4.6\cdot10^{5}$	$4.6\cdot10^{5}$
poly(I:C) mL^{-1}	$2.5\cdot10^{13}$	$4.4\cdot10^{13}$	$1.3\cdot10^{14}$	$8.0\cdot10^{13}$	$9.6\cdot10^{13}$
m(poly(I:C)) NP^{-1}/kg	$2.1\cdot10^{-18}$	$5.4\cdot10^{-18}$	$8.6\cdot10^{-18}$	$1.0\cdot10^{-17}$	$1.5\cdot10^{-17}$
poly(I:C) NP^{-1}	$2.7\cdot10^{3}$	$7.1\cdot10^{3}$	$1.1\cdot10^{9}$	$1.4\cdot10^{4}$	$1.9\cdot10^{4}$
poly(I:C) μm^{-2}	$6.0\cdot10^{4}$	$1.5\cdot10^{5}$	$2.1\cdot10^{5}$	$1.9\cdot10^{5}$	$3.5\cdot10^{5}$
wt ratio (poly(I:C):CaP)	1:1.4	1:0.5	1:0.4	1:0.6	1:0.3
Particle composition					
CaP/wt-%	57.9	35.1	30.1	35.8	20.5
poly(I:C)/wt-%	42.1	64.9	69.9	64.2	79.5

3.5.3 *In vivo* uptake of functionalised calcium phosphate nanoparticles

The analysis of the *in vivo* uptake was carried out at the Universitätsklinikum Essen by Dr. Annika Frede. Herein, 200 µL of each nanoparticle type was injected intravenously into BALB/c mice, containing $2.4\cdot10^{10}$ nanoparticles and about 14.4 µg poly(I:C). The mice were sacrificed 1 or 3 h after the injection, and lung, liver, spleen, and mesenteric lymph nodes were prepared for FACS analysis.[215] A targeted drug delivery strategy is a major goal in nanomedicine.[216] Therefore, we first proved the potential of the antibody-targeted approach, analysing the different tissue cells for remaining nanoparticles after 1 h incubation by tracking the Cy5-labelled calcium phosphate nanoparticles in a FACS experiment. The results are summarised in Figure 3-36. After 1 h incubation, most of the nanoparticles were found in the liver and the

lung. About 20-40% of the lung tissue cells had taken up the non-targeted (SH) and antibody-functionalised nanoparticles (IgG1, F4/80, IgG2, CD146) as well. The results show that up to 60% of the liver cells had efficiently taken up the non-targeted calcium phosphate nanoparticles, CaP/PEI-Cy5/poly(I:C)/SiO_2-SH, whereas only up to 5% of these cells took up the antibody-functionalised nanoparticles. In about 10% of the spleen cells, non-targeted nanoparticles could be found, whereas less than 5% internalised the antibody-functionalised nanoparticles and less than 3% of the mesenteric lymph nodes (mLN) had incorporated both types of nanoparticles (Figure 3-36).

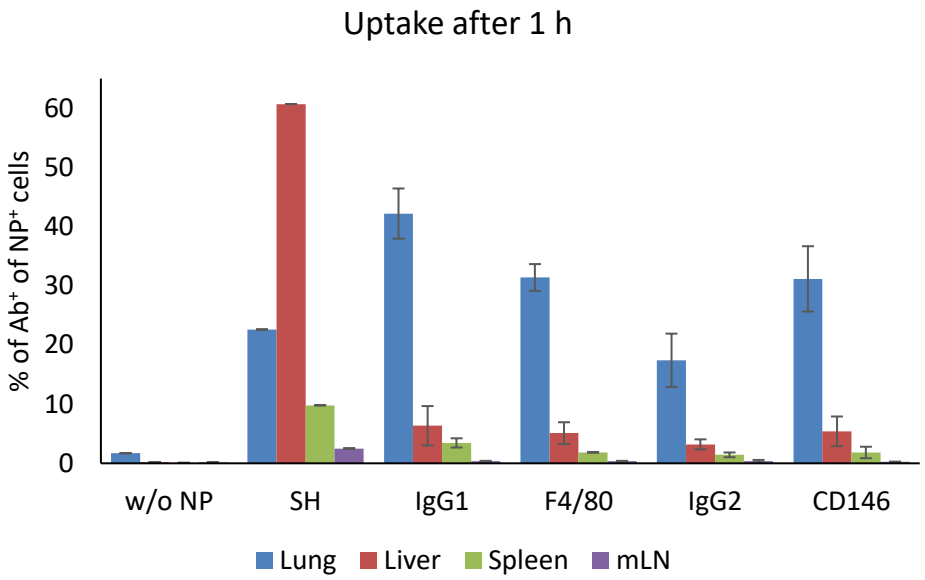

Figure 3-36: *In vivo* uptake analysis of non-targeted and targeted calcium phosphate nanoparticles.

CD146 is a strongly expressed surface molecule on non-parenchymal KCs and LSECs whereas F4/80 is also presented on KCs. Furthermore, CD146 and F4/80 are partially expressed on lung endothelial cells.[217-221] Therefore, these results indicate that the antibody-functionalised nanoparticles are less effective than non-targeted nanoparticles. On one hand, this might be explained through a direct intercepting of the targeted nanoparticles by antibody-recognising receptors within bloodstream.[222] Endothelial cells, thrombocytes, epithelial cells and macrophages within the blood stream bearing membrane-bound and antibody-recognising surface receptors. IgG1,

IgG2, F4/80 and CD146 can be recognised by those which may lead to an untimely clearance of the antibody-functionalised nanoparticles.[222,223] On the other hand, directly after the *i.v.* administration of the dispersion, nanomaterials are immediately influenced by dissolved proteins from biological fluids through unspecific adhesion forces. This leads to the formation of a protein corona surrounding the functionalised nanomaterial and prevent the antibodies from efficient targeting.[224,346] Therefore, non-targeted calcium phosphate nanoparticles may be unrecognised by endogenous receptors, leading in return to a high retrieval of the nanoparticles in the liver cells. Burger *et al*. have shown that mercapto-ethanol and cysteine increase the uptake efficiency in a spleen culture.[225] Thus, a similar effect can be assumed for the non-targeted nanoparticles (propan-1-thiol moiety). After tail vein injection, the venous blood transports the nanoparticles to the lung. From here, the nanoparticles can interact with the widely expressed CD146 and F4/80, whereas IgG1 and IgG2 might interact with inhaled antigens.[217-221] These results correlate with a recently published meta study which have shown that only 0.7% (median) of the administered nanoparticle dose is found to be delivered to a solid tumour by a targeting approach.[226] This emphasises that the design of a nanoparticle-based and targeted vaccine vehicle is not trivial, as it has to meet many biological requirements. To validate our results, we repeated the *in vivo* uptake analysis, taking the non-targeted nanoparticles, the specific targeting anti-CD146-functionalised nanoparticle and the unspecific targeting IgG1-functionalised nanoparticles (control). The results are summarised in Figure 3-37. Therefore, lyophilised CaP/PEI-Cy5/poly(I:C)/SiO_2-SH nanoparticles were reconstituted in 260 µL ultrapure water, giving of nanoparticle dispersions with a concentration of 72 µg mL^{-1}. 200 µL of that dispersion was injected intravenously into BALB/C mice (Harlan Winkelmann GmbH, Borchen, Germany) containing 14.4 µg poly(I:C) and $6.9 \cdot 10^9$ nanoparticles. Analogously, CD146 or IgG1 functionalised nanoparticles were applied, containing 14.4 µg poly(I:C) and $1.7 \cdot 10^9$ or $1.4 \cdot 10^9$ nanoparticles, respectively. After 1 and 3 h mice were sacrificed, and the organs were isolated for the uptake analysis. The liver, the lung, the spleen, and the mesenteric lymph nodes were prepared for analysis. To obtain cells from the lung and the liver tissue, the tissues were digested in collagenase containing media at 37 °C for 60 min or

45 min, respectively. To recover single cell suspension from remaining and undigested tissue, cells were squashed through a 70 µm strainer. Spleens and mesenteric lymph nodes were squashed through 70 µm strainers and washed with erythrocyte lysis buffer or PBS, containing 2% FCS and 2 mM EDTA, respectively. Afterwards, the cells were stained and analysed by FACS.[227]

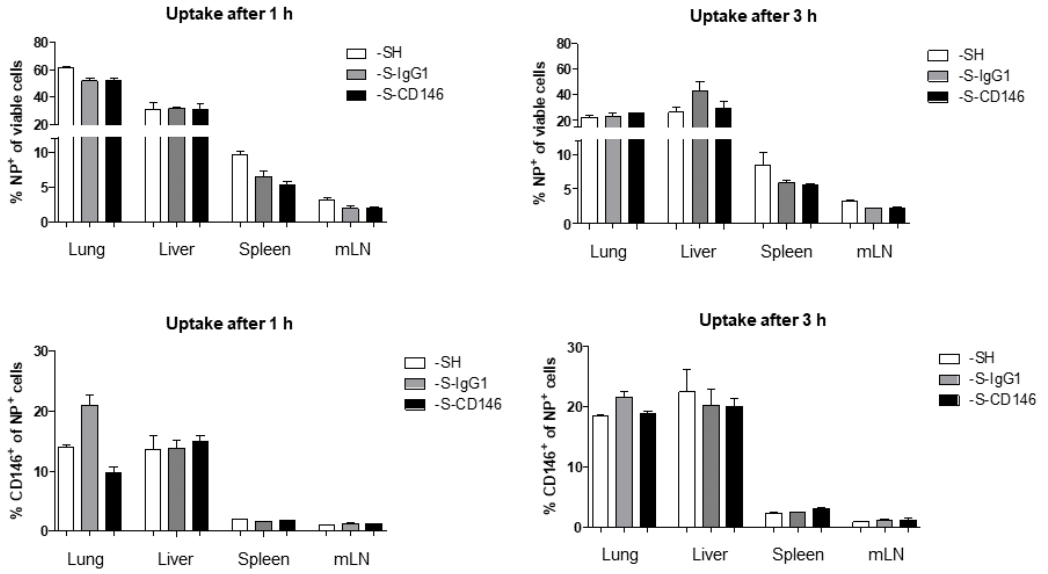

Figure 3-37: *In vivo* uptake analysis of different nanoparticles by different organs of BALB/c mice after 1 and 3 h.
Insignificant differences of the uptake between targeted and non-targeted calcium phosphate nanoparticles was observed. For the *in vivo* uptake analysis by different organs, 200 µl of each nanoparticle dispersion (CaP/PEI-Cy5/poly(I:C)/SiO_2-SH, -CD146 and -IgG1) were injected intravenously into BALB/c mice. The uptake of particles was analysed in lung, liver, spleen, and mesenteric lymph nodes (mLN) after 1 and 3 h by flow cytometric analysis. Herein, 2-3 animals were used per time point.[227]

These data indicate that anti-CD146-functionalised nanoparticles do not significantly enhance the uptake efficiency of $CD146^+$ LSECs. Furthermore, these results corroborate that a targeting strategy is not inevitable when hepatocytes are addressed. However, this experiment showed that poly(I:C) was delivered by non-targeted CaP/PEI-Cy5/poly(I:C)/SiO_2-SH nanoparticles into $CD146^+$ LSECs.

3.5.4 RNA Isolation and real-time reverse transcription (RT)-PCR

The expression levels of the poly(I:C) induced cytokines and chemokines, IL-6, TNFα, IFNβ, IFNy and IP-10 in hepatocytes, LSEC and non-parenchymal cells (NPC) were determined by RT-PCR (Figure 3-38).

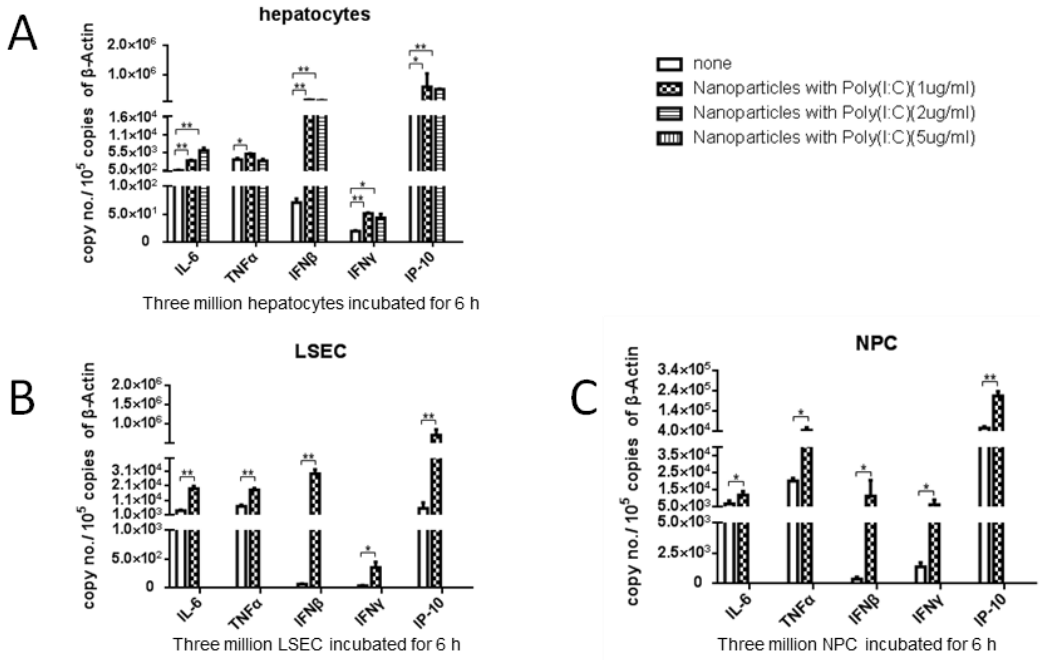

Figure 3-38: Expression levels of poly(I:C) induced cytokines and chemokines.
Gene expression levels of the cytokines and chemokines of IL-6, TNF-α, IFN-β, IFN-γ and IP-10 in hepatocytes (A), LSEC (B) and NPC (C) were determined by RT-PCR. About $3 \cdot 10^6$ cells of each cell type were treated with different concentration of nanoparticles ($1.6 \cdot 10^9$ mL^{-1} (1 µg mL^{-1} poly(I:C)) and $3.3 \cdot 10^9$ mL^{-1} (2 µg mL^{-1} poly(I:C)) for 6 h. The mRNA transcripts were normalised to β-actin (×/100,000 copies of β-actin).[227]

In all cell types, the expression of IFN-α/β, TNF-α, IL-6 and IP-10 was significantly increased, indicating that the treatment with poly(I:C)-loaded calcium phosphate nanoparticles induces a pronounced intrahepatic immune response in a type I interferon dependent manner. These results also correlate with previously found results.[228] However, up to date, effective prophylactic vaccines against HBV are available. The herein designed nanoparticles might be useful for the treatment against HBV chronic infections in the future. The data demonstrated that calcium phosphate nanoparticles can be used as a delivery tool for vaccination purposes.

3.5.1 Summary

Here, we have described the successful synthesis of poly(I:C)-loaded calcium phosphate nanoparticles to address HBV infections. Although, the results of the previously followed antibody-guided approach did not lead to an accumulated concentration of the functionalised nanoparticles in the liver, we could successfully demonstrate that the thiol-functionalised and poly(I:C)-loaded nanoparticles

accumulate in the liver on their own when the nanoparticles are intravenously administered. After blood circulation, the nanoparticles accumulate in the liver within 1 h to 3h. Here, it was shown that calcium phosphate nanoparticles can lead subsequently to a pronounced production of cytokines and chemokines in hepatocytes and might be useful against HBV infection. Therefore, we could show that calcium phosphate nanoparticles can be loaded with bioactive molecules and are a suitable tool to transport compounds to the liver as well as for imaging and vaccination.[227]

3.6 Doxorubicin functionalised calcium phosphate nanoparticles

This study was a DAAD cooperation between the groups of Prof. Dr. Epple (Essen, Germany) and Prof. Dr. Hu (Nanjing, China).

In this study, thiol-terminated and near-infrared fluorescent (NIRF) dye (DY754, Dyomics GmbH, Jena, Germany) equipped calcium phosphate nanoparticles were used to simultaneously conjugate the tumour-targeting and metastasis-inhibiting iRGD peptide and the well-established chemotherapeutic agent doxorubicin (DOX). Previous studies by Dr. Kozlova and Dr. Sokolova have shown a feasible application of NIRF-equipped calcium phosphate nanoparticles for *in vivo* imaging (Haedicke *et al.*).[229] Combining diagnostic visualisation and therapy of a disease is also known as theranostic.[347] These theranostic (imaging and therapy) nanoparticles should be used *in vivo* on H22 cells as a tumour mouse model. For the *in vivo* imaging, the biological distribution of the functionalised nanoparticles into different organs should be investigated by two different routes of administration, such as intraperitoneal (*i.p.*) and intravenous (*i.v.*).

The tumour-targeting and -penetrating peptide iRGD has drawn much attention since the last years. It is a cyclic nonapeptide (CRGDKGPDC) and binds to αv integrins and neuropilin-1 receptors, which are highly expressed in tumour cells and the surfaces of vasculature, leading to apoptosis by direct caspase-3 activation. Thereby, it has been intensively used in drug-targeted cancer therapy.[230-232] Doxorubicin is a broad-range and well-known chemotherapeutic agent for the treatment of diverse types of cancer, including leukemias, the Hodgkin's lymphoma, as well as cancers of the bladder, breast, stomach, lung, ovaries, and others.[233] However, treatment with doxorubicin leads to an 8-fold increase in risk of potentially fatal cardiotoxicity.[234] Therefore, a cancer-targeted strategy would eventually lead to a decrease of that risk and is clinically preferred. In the following chapter, the synthesis and viability assay of the theranostic calcium phosphate nanoparticles are described.

3.6.1 Synthesis and characterisation of theranostic calcium phosphate nanoparticles

Calcium phosphate nanoparticles were prepared as previously described, using a time-scheduled peristaltic pump.[58,61,205] Briefly, 5 mL of 10.8 mM $(NH_4)_2HPO_4$ (pH 10) (Merck, Darmstadt, Germany), 5 mL of 18.0 mM $(CH_3CH(OH)COO)_2Ca{\cdot}5H_2O$ (pH 10) (Seelze, Fluka Analytical, Germany) and 7 mL of 80 µM PEI-DY754 (Surflay Nanotec GmbH, Berlin, Germany) were pumped within 1 min into a water-containing glass vessel (20 mL ultrapure water) and were stirred with 300 rpm for 20 min at room temperature. 10 mL of the resulting CaP/PEI-D754 dispersion were coated with a thin silica layer shell by the hydrolysis of 50 µL TEOS in 40 mL ammonia (26 µL, 30-33% (v/v)) alkaline ethanol. The reaction was stirred overnight at room temperature. On the next day, the mixture was centrifuged at 30,000 rpm with a 70 Ti rotor (Beckman&Coulter, Krefeld, Germany) in a SORVALL WX Ultra Series ultracentrifuge, (Thermo Fisher Scientific, Waltham, USA) for 30 min, and the pellet was dispersed by using a UP50H ultrasonic device (Hielscher Ultrasound Technology, Teltow, Germany). The ultrasonic device was equipped with a sonotrode MS3 (Hielscher, Germany) applying an amplitude of 70% with a cycle of 0.8 for 20 s in 10 mL ultrapure water. 10 mL of the CaP/PEI-DY754/SiO_2-OH dispersion was given to a Stoeber solution containing 50 µL (3-mercaptopropyl)trimethoxysilane in 40 mL ethanol. The reaction was stirred for 6 h at room temperature, giving thiol-terminated calcium phosphate nanoparticles CaP/PEI-DY754/SiO_2-SH. The nanoparticles were centrifugated and purified as described above, using 10 mL ultrapure water for the redispersion. The resulting calcium phosphate nanoparticle dispersion CaP/PEI-DY754/SiO_2-SH was used for the subsequent coupling of Doxorubicin (AppliChem GmbH, Darmstadt, Germany DOX or/and iRGD (Bachem AG, Bubendorf, Switzerland). Different amounts of DOX (100, 200 and 300 µg) and iRGD (100 µg) were activated with a 4-fold molar excess of succinimidyl 3-(2-pyridyldithio)-propionate (SPDP, Thermo Fisher Scientific, Waltham, USA), which is a bifunctional crosslinker, leading to the N-hydroxy-succinimide-activated compound of DOX(act.) or iRGD(act.) (Figure 3-39). The conjugation was carried out for 30 min at room temperature in 100 µL reaction buffer (100 mM sodium phosphate, 150 mM NaCl,

pH 7.5). Then, activated DOX and iRGD were directly used for the coupling with the thiol-terminated calcium phosphate nanoparticle without further purification.

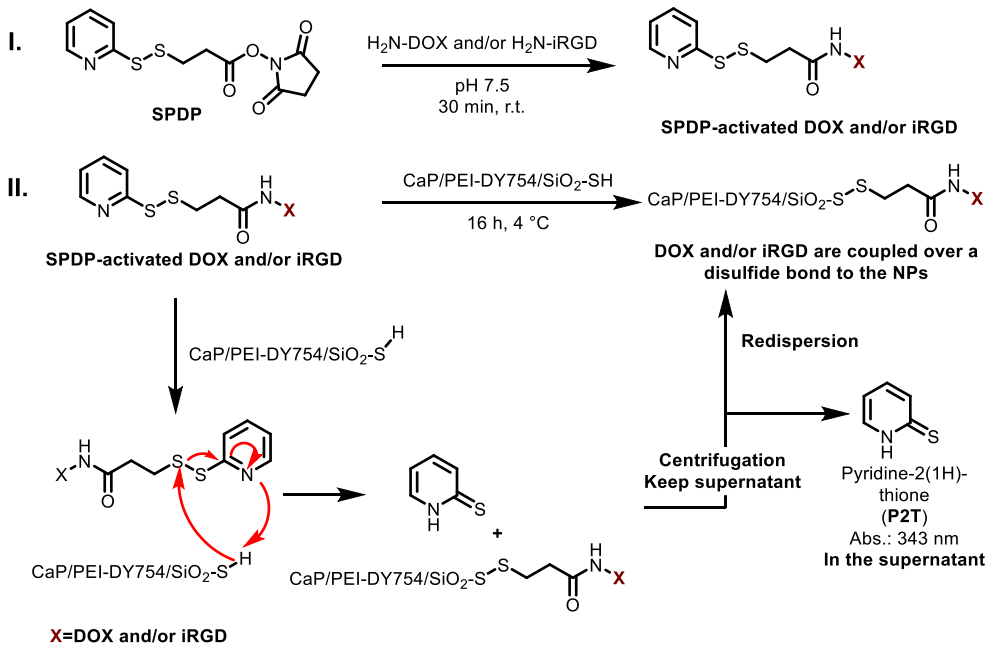

Figure 3-39: NHS-activation of iRGD and/or DOX.
DOX and iRGD were activated with the hetero-specific bifunctional cross-linker SPDP (I.). Conjugation of the activated molecules was monitored by the released by-product pyridine-2-(1H)-thione (II.).

Herein, 100 µL of the activated molecule were given to 1 mL of the CaP/PEI-DY754/SiO_2-SH nanoparticle dispersion. The mixture was incubated overnight at 4 °C. The obtaining doxorubicin-functionalised calcium phosphate nanoparticles CaP/PEI-DY754/SiO_2-S-S-DOX or doxorubicin- and iRGD-functionalised (bifunctional) nanoparticles CaP/PEI-DY754/SiO_2-S-S-DOX/iRGD were purified through ultracentrifugation (21,000 g, 4 °C, Heraeus™ Fresco™ 21 Microcentrifuge, Thermo Fisher) and redispersion in 1 mL ultrapure water (MS7, 70% amplitude, 0.8 cycle for 10 s). A schematic figure of the synthesised nanoparticles is shown in Figure 3-40.

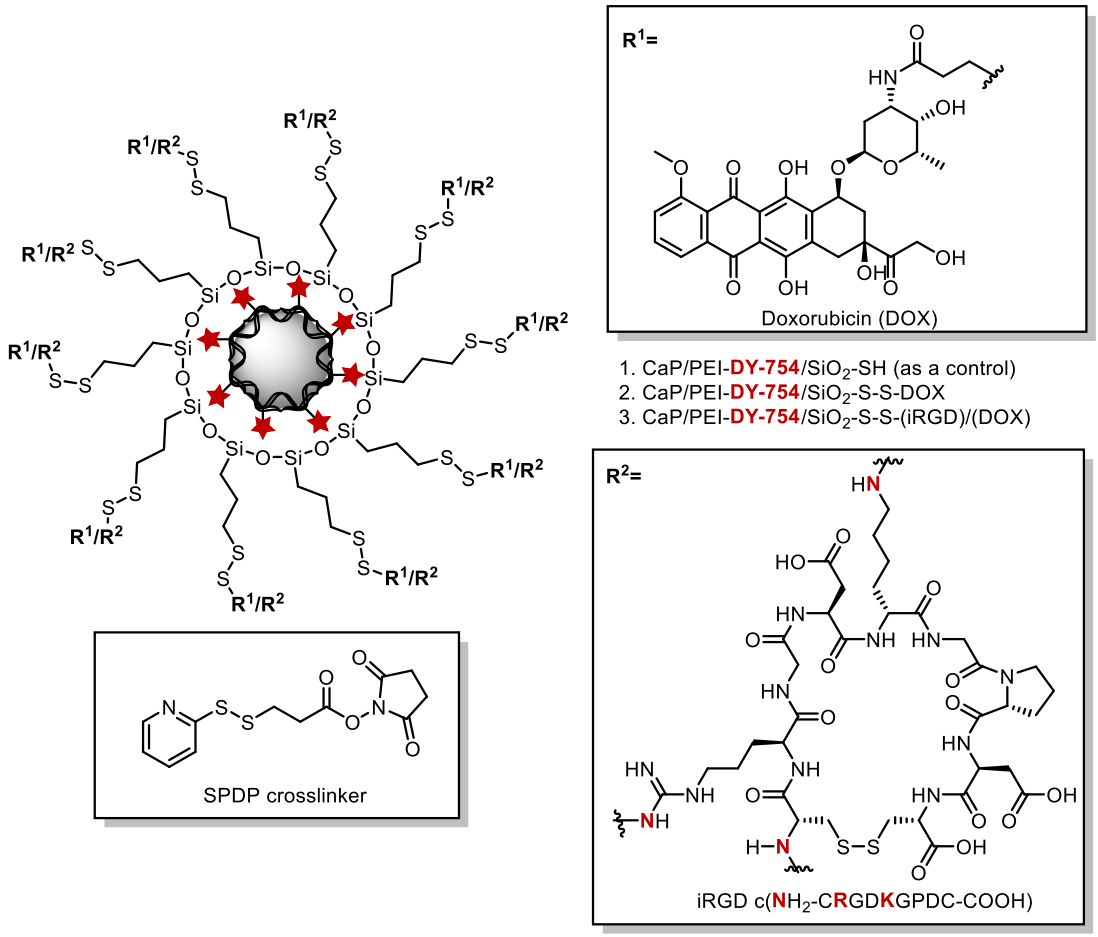

Figure 3-40: Synthesis of theranostic calcium phosphate nanoparticles.
This carrier system bears redox-labile disulphide bonds for a potential release of the covalently conjugated doxorubicin and iRGD. iRGD has three addressable primary amines (red) within its side chains (R^2).

The supernatant of the centrifugation was kept to determine the doxorubicin concentration by UV-spectroscopy. Visually, the red doxorubicin was successfully conjugated on the nanoparticles´ surface, indicated by the red colour of the final dispersion (Figure 3-41).

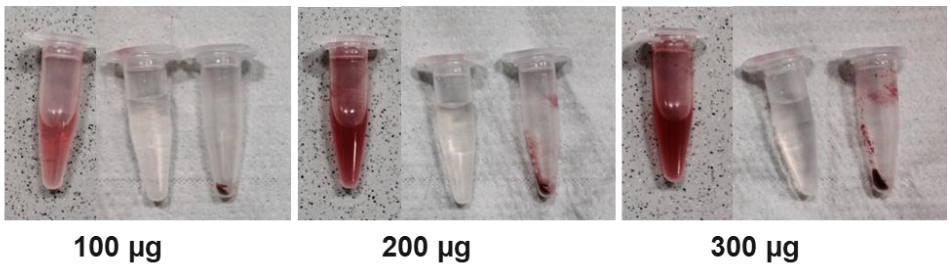

Figure 3-41: Overview of the final dispersions.
CaP/PEI-DY754/SiO_2-SH was incubated with different amounts of NHS-activated doxorubicin. On the left of each image, the final dispersion. On the middle of each image, the supernatant. On the right of each image, the pellet after centrifugation.

The coupling was monitored by the UV-active by-product pyridine-2-(1H)-thione (P2T), which has an absorption maximum at 343 nm. This carrier system bears redox-labile bisulfide bonds for a potential release of the covalently conjugated doxorubicin and iRGD.[235]

To validate this result, the supernatant was analysed by UV-spectroscopy for a by-product formation during the cross-coupling reaction (Figure 3-42).

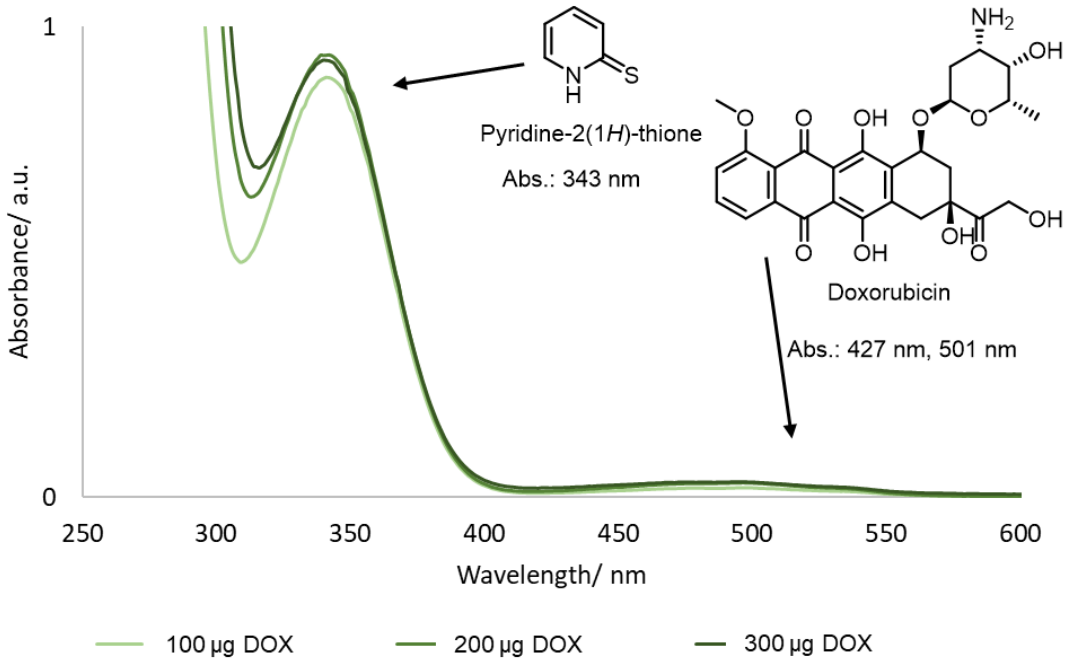

Figure 3-42: Monitoring of the coupling efficiency of NHS-activated DOX.
The coupling of NHS-activated doxorubicin can be visualised by the by-product of SPDP. The positive coupling event is indicated through the UV-active P2T. In all cases, the UV-active P2T was formed and low amounts of activated DOX remained in the supernatant.

This spectrum strongly indicates that nearly all activated doxorubicin molecules were successfully activated and then conjugated on the surface of the nanoparticles which is in turn indicated by the low amounts of DOX remaining in the supernatant. In all cases, the same intensity revealed a limited space for the activated doxorubicin molecules on the surface of thiol-terminated calcium phosphate nanoparticles (CaP/PEI-DY754/SiO_2-SH). This indicates that the necessary amount of activated doxorubicin for subsequent conjugation was exceeded. To determine both, the percental coupling efficiency and the amount on the nanoparticle surface, different amounts of doxorubicin (ranging from 5, 10, 25, 50, 75, 100 µg) were used to activate

the doxorubicin and to let it react with 1 mL CaP/PEI-DY754/SiO_2-SH. In total, 88.9% of initially used doxorubicin was found on the nanoparticles´ surface, whereas 3.7% remained in the supernatant. 7.4% were lost during the cross-coupling reaction (Figure 3-43).

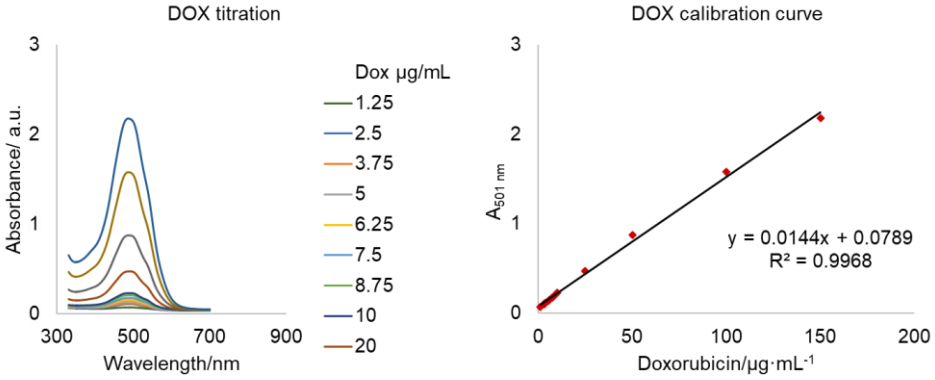

DOX/ µg mL^{-1}	5	10	25	50	75	100
Supernatant	0.3	0.49	0.98	2.12	1.12	1.46
On the nanoparticles	5.45	8.04	19.23	41.79	70.28	90.04

	DOX/ %
Supernatant/ %	3.7
On the nanoparticles/ %	88.9

Figure 3-43: Determination of the percental coupling efficiency.
About 88.9% of the NHS-activated doxorubicin was found on the nanoparticles´ surface, indicating a high coupling efficiency. Only about 4% of doxorubicin remained in the supernatant, while about 7% was lost during the cross-coupling reaction.

The average size of the nanoparticles conjugated with 100, 200 and 300 µg doxorubicin was around 161 nm whereas the non-conjugated nanoparticles had an average size of 34 nm in diameter (Figure 3-44 and Table 3-14). The zeta potential was positive, between +25 and +29 mV indicating a stable colloidal dispersion. Synthesised nanoparticles have shown in almost every case a PDI value lower than 0.3 which is defined as a monodisperse colloidal suspension. The increased size of functionalised calcium phosphate nanoparticles indicated a successful conjugation of doxorubicin on the nanoparticles´ surface.

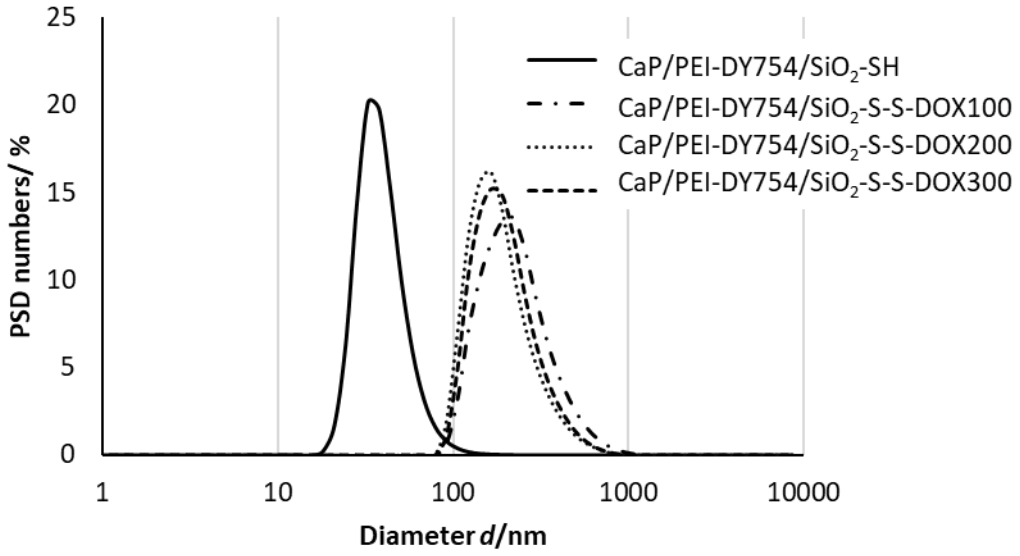

-

Figure 3-44: DLS measurement of non-conjugated and conjugated nanoparticles.
The size between thiol-terminated and doxorubicin conjugated calcium phosphate nanoparticles are different, indicating a successful conjugation of doxorubicin on the nanoparticles´ surface. PSD is given by numbers in %, generally reflecting a closer approximation to the SEM determined size.

Table 3-14: DLS results.

Type	DLS/nm	PDI	ζ/mV
CaP/PEI-DY754/SiO_2-SH	34.4 ± 3	0.32	26.1
CaP/PEI-DY754/SiO_2-S-S-DOX100	158 ± 28	0.271	25.8
CaP/PEI-DY754/SiO_2-S-S-DOX200	162 ±48	0.252	26.3
CaP/PEI-DY754/SiO_2-S-S-DOX300	164 ± 0	0.213	29.1

Next, different amounts of activated doxorubicin (100, 200 and 300 µg) and iRGD peptide (100 µg or 200 µg) were simultaneously conjugated with thiol-terminated calcium phosphate nanoparticles, giving a various set of diverse amounts loaded calcium phosphate nanoparticles "CaP/PEI-DY754-SiO_2-S-S-DOX/iRGD" (s. Table 3-12). The nanoparticle size of each type was slightly increased about +24 nm in average. The particle size was enlarged with an increasing amount of doxorubicin. This indicated a successful conjugation of iRGD. However, neither the PDI nor the zeta potential of any colloidal dispersion was influenced by the second

ligand iRGD, indicating the remaining integrity of the nanoparticular dispersions. The results of the DLS analysis are shown in Figure 3-45.

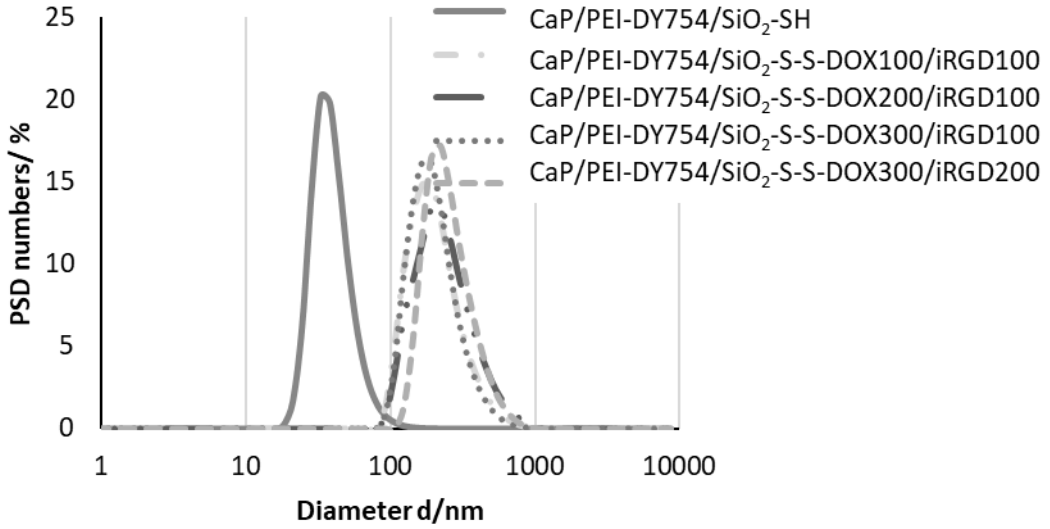

Figure 3-45: DLS measurements of simultaneously conjugated DOX and iRGD calcium phosphate nanoparticles.
DLS measurement of the synthesised calcium phosphate nanoparticles indicated stable dispersions. The size between doxorubicin and bifunctional doxorubicin/iRGD conjugated calcium phosphate nanoparticles is only slightly different (Table 3-11). PSD is given by numbers in %, generally reflecting a plausible approximation to the SEM determined size.

Table 3-15: DLS results.
In all cases, the DLS parameter indicated stable colloidal dispersions. A doxorubicin amount-depending trend was observed, leading to enlarged particle diameter with an increasing amount of doxorubicin. Amounts of the used doxorubicin and iRGD is reflected by number. e.g. DOX100 or iRGD100 in µg.

Type	DLS/nm	PDI	ζ/ mV
CaP/PEI-DY754/SiO_2-SH	34.4 ± 3	0.320	26.1
CaP/PEI-DY754/SiO_2-S-S-DOX100/iRGD100	165 ± 24	0.261	24.0
CaP/PEI-DY754/SiO_2-S-S-DOX200/iRGD100	184 ±39	0.196	25.9
CaP/PEI-DY754/SiO_2-S-S-DOX300/IRGD100	172 ± 15	0.202	29.0
CaP/PEI-DY754/SiO_2-S-S-DOX300/iRGD200	220 ± 0	0.161	25.9

The DLS data showed that a simultaneous conjugation of doxorubicin and iRGD is possible without a loss of the colloidal stability. The SEM data showed some degree of agglomeration and agglutination(Figure 3-46). However, for the later analysis, CaP/PEI-DY754/SiO_2-SH, CaP/PEI-DY754/SiO_2-S-S-DOX100 and CaP/PEI-DY754/SiO_2-S-S-DOX100/iRGD100 were chosen. The amount of doxorubicin per nanoparticle can be calculated from the AAS data and the SEM diameter. Corresponding SEM images

are depicted in Figure 3-46. For example, using the AAS concentration of CaP/PEI-DY754/SiO_2-S-S-DOX100 which was 11.8 µg mL^{-1} and corresponds to an equivalent hydroxyapatite concentration of 30 µg mL^{-1}, the particle concentration per millilitre can be calculated by using the Eq. 13 and Eq. 14 from chapter 5.5. Under the assumption that the synthesised nanoparticles were spherical and uniformly shaped, the solid core diameter from the SEM (*d* = 90 nm; *r* = 45 nm for DOX100-nanoparticels) can be used for the calculation. Herein, the volume of one single nanoparticle was $3.8 \cdot 10^{-22}$ m^3 and a density of 3,140 kg m^3 for hydroxyapatite was used resulting in a nanoparticle concentration of $2.5 \cdot 10^{10}$ NPs mL^{-1}. For the calculation of the number of doxorubicin molecules, the results of the doxorubicin titration were used (Figure 3-43) assuming that up to 90% of the applied doxorubicin were bound on the surface of the calcium phosphate nanoparticles. Therefore, 90 µg mL^{-1} was assumed for 1 mL nanoparticle dispersion giving about $4.0 \cdot 10^6$ doxorubicin molecules per nanoparticle and $1.0 \cdot 10^{17}$ doxorubicin molecules per millilitre. For one nanoparticle, a total surface area of $2.5 \cdot 10^4$ nm^2 was calculated where each nm^2 was occupied with 159 doxorubicin molecules. The data are summarised in Table 3-16. Although the concentration of the targeting moiety iRGD could not be detected by UV-spectroscopy due to the lack of an UV active amino acid (CRGDKGPDC), the determination could be carried out by a fluorescently labelled iRGD. However, according to the results from the doxorubicin titration, it was assumed that a similar or same number of iRGD molecules was coupled to the surface of the bifunctional calcium phosphate nanoparticles CaP/PEI-DY754/SiO_2-S-S-DOX100/iRGD100. Herein, it was expected that both molecules compete for the binding sites on the nanoparticles' surface. This reduces the available binding sites for each molecule to about 50% considering an equal binding affinity for each molecule to the thiol-terminated surface. Therefore, it was assumed that 90% of the half amount (50 µg) of doxorubicin and iRGD were bound to the nanoparticles' surface giving a concentration of 45 µg mL^{-1} for each molecule. Hereby, only an approximative value for the number of iRGD and doxorubicin molecules can be given based on this assumption. In the case of doxorubicin, $2.6 \cdot 10^{16}$ molecules mL^{-1} and $3.4 \cdot 10^6$ molecules NP^{-1} were calculated whereas $2.6 \cdot 10^{15}$ molecules mL^{-1} and $1.9 \cdot 10^5$ molecules NP^{-1} were calculated for iRGD. Further results can be found in

Table 3-16. iRGD is an highly targeting molecule which is even active in the micromolar range.[236]

Table 3-16: Colloidal characteristics and composition of doxorubicin and doxorubicin/iRGD conjugated calcium phosphate nanoparticles.

X[1]			
Parameter	**H**	**DOX100**	**DOX100/iRGD100**
d_{SEM}/nm	51 ± 4	90 ± 8	106 ± 5
$V_{NP;\ only\ CaP}$/m^3	$6.9\cdot10^{-23}$	$3.8\cdot10^{-22}$	$6.2\cdot10^{-22}$
$A_{NP;\ only\ CaP}$/m^2	$8.2\cdot10^{-15}$	$2.5\cdot10^{-14}$	$3.5\cdot10^{-14}$
$m_{NP;\ only\ CaP}$/kg	$2.2\cdot10^{-19}$	$1.2\cdot10^{-18}$	$2.0\cdot10^{-18}$
$[Ca^{2+}]_{AAS}$/µg mL^{-1}	20.1	11.8	10.4
$[Ca_5(PO_4)_3OH]$/µg mL^{-1}	50.5	30.0	26.1
NPs mL^{-1}	$2.3\cdot10^{11}$	$2.5\cdot10^{10}$	$1.3\cdot10^{10}$
w(DOX)/µg mL^{-1}	–	90.0	45.0
MW(DOX)/g mol^{-1}	–	543	543
DOX mL^{-1}	–	$1.0\cdot10^{17}$	$5.0\cdot10^{16}$
m(DOX) NP^{-1}/kg	–	$3.6\cdot10^{-18}$	$3.4\cdot10^{-18}$
DOX NP^{-1}	–	$4.0\cdot10^{6}$	$3.7\cdot10^{6}$
DOX nm^{-2}	–	159	106
wt ratio (DOX:CaP)	–	1:0.33	1:0.58
w(iRGD)/µg mL^{-1}	–	–	45.0
MW(iRGD)/g mol^{-1}	–	–	950
iRGD mL^{-1}	–	–	$2.9\cdot10^{15}$
m(iRGD) NP^{-1}/kg	–	–	$3.4\cdot10^{-18}$
iRGD NP^{-1}	–	–	$2.1\cdot10^{5}$
iRGD nm^{-2}	–	–	6
wt ratio (iRGD: CaP)	–	–	1:0.58
d_{DLS}/nm	34.4 ± 3	158 ± 28	165 ± 24
PDI_{DLS}	0.320	0.271	0.261
ζ_{DLS}/mV	26.0	25.8	24.0
Particle composition			
CaP/wt-%	100	24.8	22.5
DOX/wt-%	0	75.2	38.8
iRGD/wt-%	0	0	38.8

[1](CaP/PEI-DY754/SiO_2-S-S-X, X =)

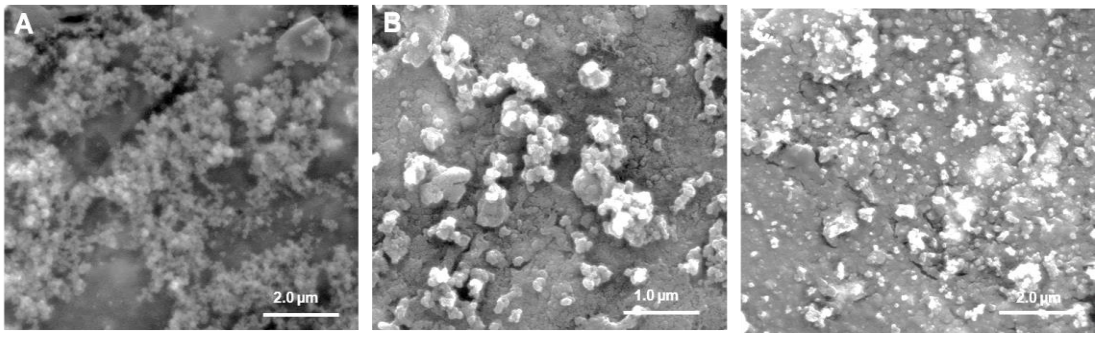

Figure 3-46: SEM images of doxorubicin and doxorubicin/iRGD conjugated calcium phosphate nanoparticles.
A: CaP/PEI-DY-754-SiO_2-SH (30000x magnification, 25 kV); B: CaP/PEI-DY-754-SiO_2-S-S-DOX (60000x magnification, 25 kV); C: CaP/PEI-DY-754-SiO_2-S-S-DOX/ iRGD (100 µg/ 100 µg) (60000x magnification, 25 kV). All synthesised calcium phosphate nanoparticles shown a spherical morphology.

3.6.2 Viability

To determine the cell viability, HeLa cells were incubated comparably for 24 and 72 h with 2.5-7.5 µg doxorubicin hydrochloride, 25-75 µL of CaP/PEI-DY754-SiO_2-S-S-DOX100 or CaP/PEI-DY754-SiO_2-S-S-DOX100/iRGD100. Herein, it was assumed that all of the applied doxorubicin was bound to the nanoparticles' surface. The nanoparticle concentration was normalised to the free doxorubicin hydrochloride, giving a nanoparticle concentration of $6.2 \cdot 10^8$ (25 µL), $1.2 \cdot 10^9$ (50 µL) or $1.9 \cdot 10^9$NPs mL^{-1} (75 µL) which equals 2.5, 5 or 7.5 µg of the doxorubicin hydrochloride. For non-conjugated nanoparticles, the same nanoparticle concentration was chosen. After 24 h of incubation, the doxorubicin and doxorubicin/iRGD-conjugated nanoparticles have shown low cell toxicity. Even for the highest nanoparticle concentration, up to 70% of the cells were still intact whereas most of the doxorubicin hydrochloride treated cells died (30%, 2.5 µg DOX). The viability was further decreased after 72 h for nanoparticle and free doxorubicin treatment (Figure 3-47). The data shows that the nanoparticle conjugate does not exhibit a significantly higher cytotoxicity. Therefore, other concentrations of doxorubicin might be chosen to achieve comparable cytotoxicity results.

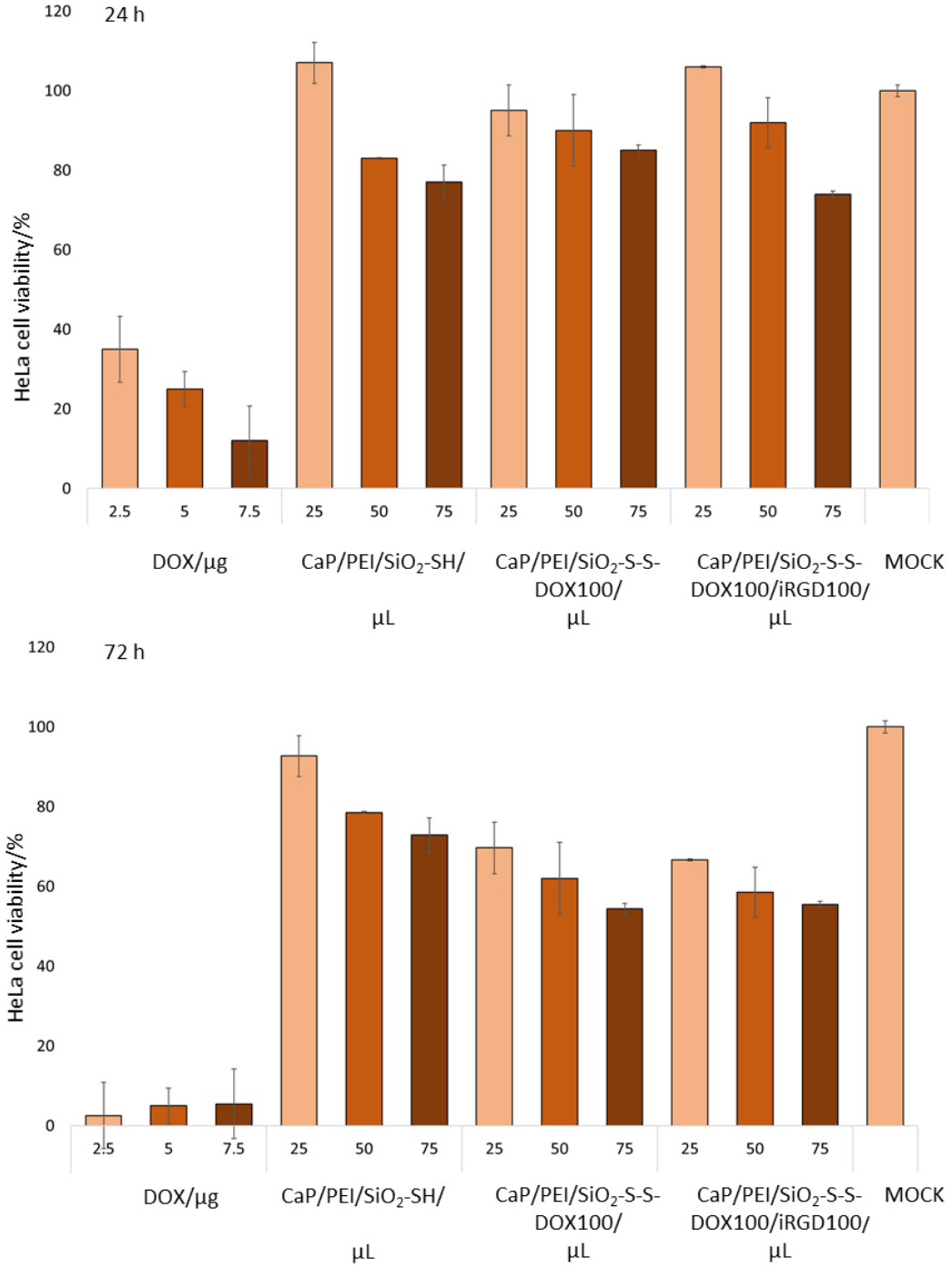

Figure 3-47: MTT viability assay.
Cells were either incubated with the free doxorubicin hydrochloride or with equivalent amounts of doxorubicin or doxorubicin/iRGD-conjugated calcium phosphate nanoparticles. Viability is normalised to the doxorubicin concentration assuming that 1 µL of doxorubicin-loaded nanoparticles equals 0.1 µg of doxorubicin (0.1 µg DOX μL^{-1} nanoparticle dispersion).

.

3.6.3 Summary

The successful synthesis of bifunctional conjugated calcium phosphate nanoparticles was described and validated by different techniques. Nanoparticles can be conjugated with doxorubicin. For iRGD, a quantitation is still necessary, but these results indicate also a successful conjugation of the iRGD which was shown by the characterisation data. Further optimisation of this system may allow a targeted approach for the localisation, visualisation and treatment of cancer-related diseases in the far future.

3.7 Dendritic cells targeting aptamer: Synthesis of chimeric aptamer functionalised calcium phosphate nanoparticles to address the mDEC205 receptor

The inability of conventional proteinogenic vaccines can lead to an abundance of T cell-mediated immunity and limits their use as vaccines for the targeting of diverse diseases including viral infections and cancers.[237,238] An efficient and robust cell-mediated immunity can be facilitated by antigen targeting of dendritic cells (DCs). This plays a pivotal role for eliciting T cell activation and subsequent immunogenicity. However, beside the substantial research interest in these DC-targeted approaches, they are more rapidly becoming therapeutic approaches.[239,240] The fast growing interest results from the capability of DCs to process self and foreign antigens to its cognate T cell receptor, resulting in the surface presentation of the antigens which make DCs attractive as targets for antigen-directed immunogenicity.[95] Furthermore, it has been shown that antigen presentation on the major histocompatibility complex (MHC) class I and II molecule can be enhanced by as much as 1,000- and 50 fold by targeting antigen uptake to DCs via specific DC-enriched receptors.[241] The feasible DC-induced immunotolerance or activation is antigen stimulus depended which reflects the importance of the DCs as targets in the development of novel therapies for treating autoimmune diseases, viral infections, and cancer.[95] In general, antibody-antigen conjugates are used to target antigens of interest to antibody-recognised DCs, usually a transmembrane and partially endocytosed cell surface receptor.[95] Beside well established antibody-antigen conjugate delivery, nucleic acid aptamers provide a promising alternative due to their unique chemical properties and low immunogenicity.[242,243] However, Wengerter *et al.* have identified a RNA aptamer that binds specifically the murine dendritic epidermal complex receptor (mDEC205) in a low nanomolar range. DEC205 is a transmembrane C-type lectin that is predominantly expressed in and presented on the surface of $CD8\alpha^+$ dendritic cells. A minimised version of the identified aptamer (min.2) was biotinylated and combined with the streptavidin cross-linked model antigen ovalbumin (OVA) targeting the model antigen to DEC205 expressing cells. DEC205-targeted antigen cross presentation was verified *in vitro* and *in vivo* by proliferation and cytokine production

by primary murine $CD8^+$ T cells which express a T cell receptor specific for the major histocompatibility complex (MHC).[95] This approach showed that aptamers can be used as a specific and targeting probe to point an antigen to DCs with similar characteristics of a DEC205-antibody. In a similar approach, we successfully immobilised biotin-labelled DEC205 antibodies on the surface of avidin-functionalised (avidin is the structural ancestor of the prominent streptavidin from hen egg white), calcium phosphate nanoparticles and could also attach the DEC205 antibody by sulfo-SMCC cross-coupling. To our knowledge chimeric aptamers are scientifically new. In the following section, the attachment of chimeric aptamers is described.

3.7.1 Chimeric aptamers – motivation and relevance

The idea for chimeric aptamers was resulted from the unique secondary RNA structure of the RNA aptamer scaffold F30 from the F30-2xdBroccoli RNA aptamer (F2B) which was developed by Filonov *et al.*.[116,117] The free energy of the secondary structure of the self-folding F30 scaffold is ΔG^0= -114.6 kJ mol^{-1}. Therefore, it also forces adjacent RNA sequences introduced into the insertion points, i.e. 2xdBroccoli in F2B, into their correct secondary and tertiary conformation (Figure 3-48).[244] The F30 scaffold has several advantages over previously used RNA aptamer scaffolds like t^{Lys}-RNA, including a higher cell biorthogonality, which makes the F30 scaffold undetectable for cell endogenous nucleases and remains stable. Furthermore, it has a three-way junction structure that can be used as an insertion point for aptamers.[117]

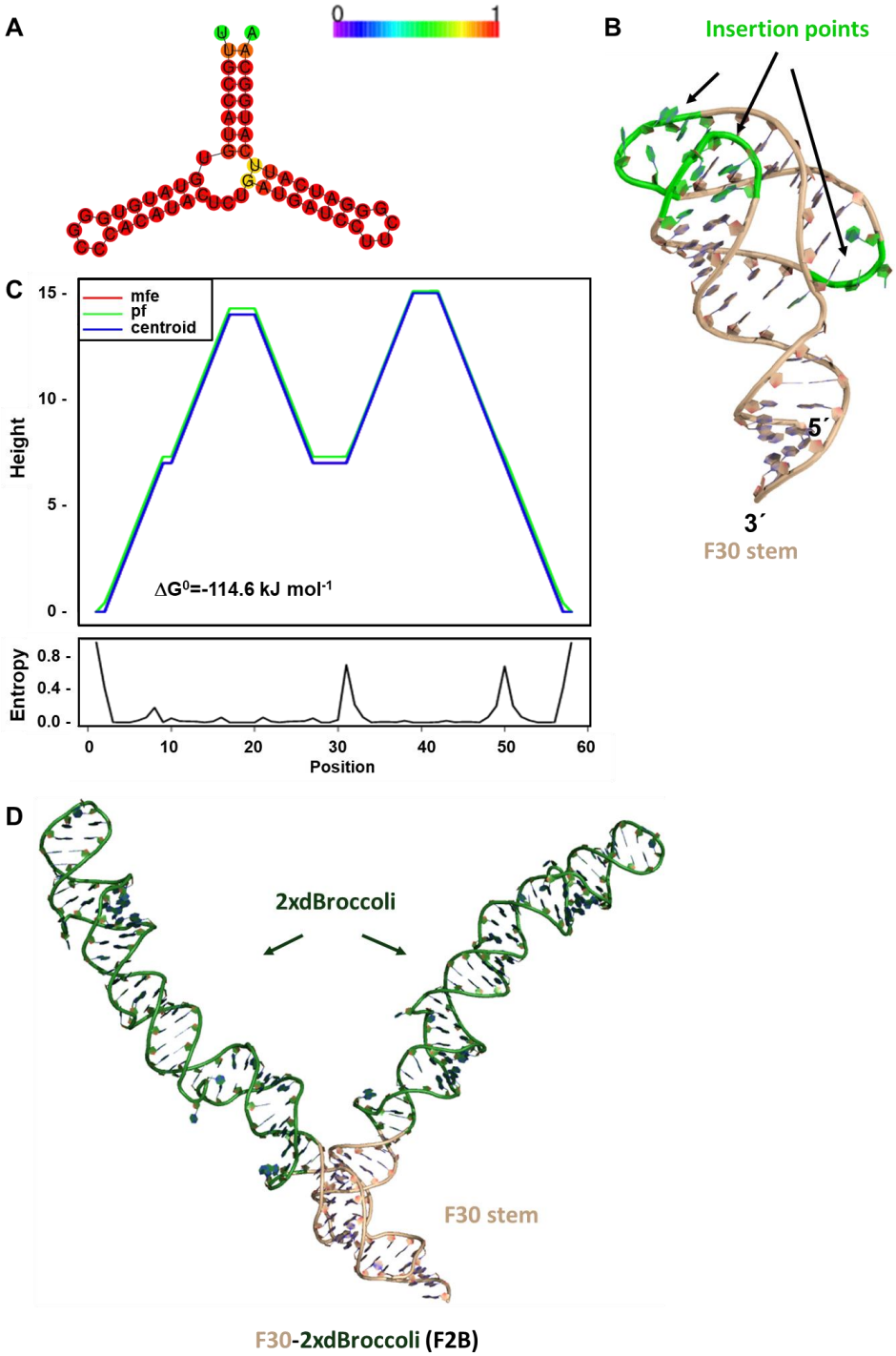

Figure 3-48: Secondary and tertiary structure of the RNA aptamer scaffold F30 and F30-2xBroccoli. A: Base-pair probability plot, showing the most favoured secondary structure of the RNA aptamer scaffold F30. Colour code for the base pair probabilities is reflected by the spectral coloured bar with red: 1.0 (100%) to violet 0.0. B: Tertiary structure of the RNA aptamer scaffold F30. C: Folding and entropy plot. D: Tertiary structure of the RNA aptamer F2B.

For the chimeric aptamers, the F30 aptamer scaffold was used to insert two RNA aptamer effector domains able to bind and image a target molecule. The terminus `chimeric´ is used to denote its bifunctionality. Thus, the cDNA of one of the two RNA

aptamers in FB2 was substituted by the cDNA of the minimised mDEC205 binding aptamer min.2 or by the non-binding control aptamer c36 (Figure 3-49) whereas one of the two dimeric broccoli units remained at the F30 scaffold.

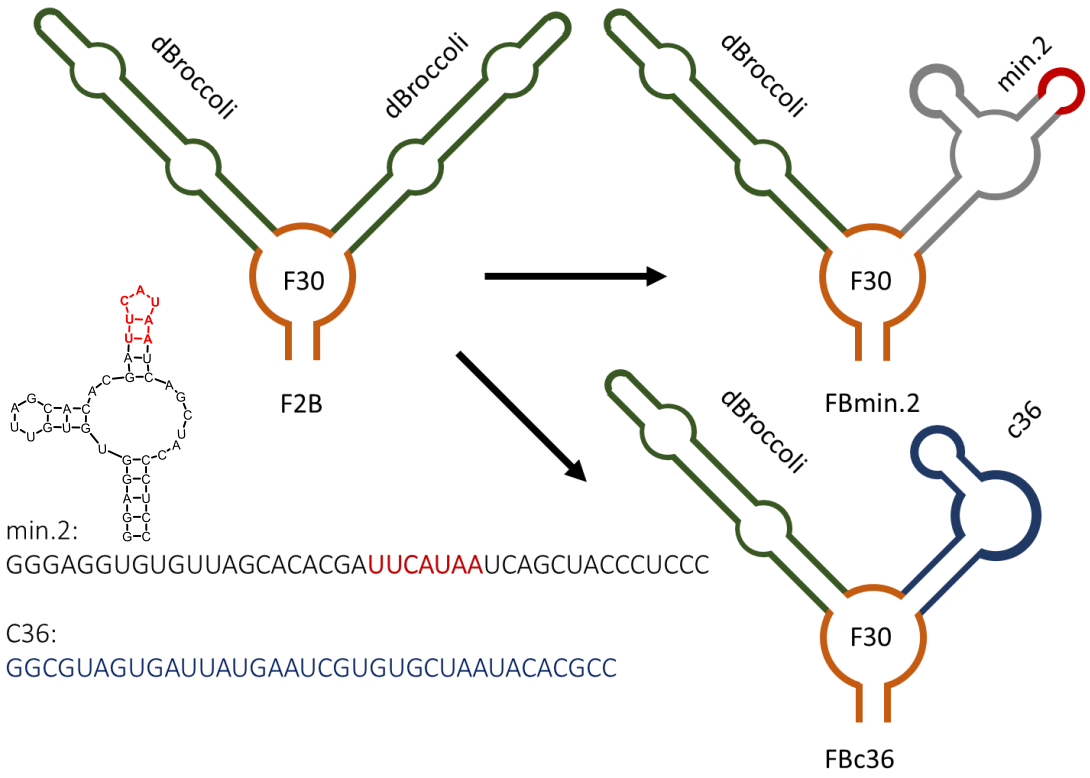

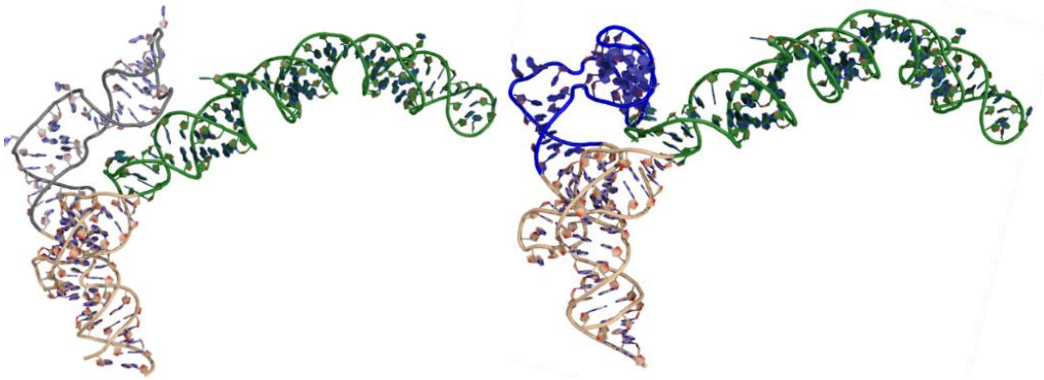

Figure 3-49: Concept for the chimeric aptamer.
Upper section: The conceptual generation of chimeric aptamers and the min.2 2D structure is shown. In this approach, F30-2xdBroccoli was used as a starting point. The second dBroccoli aptamer within F2B was substituted by min.2 or rather with c36 to obtain chimeric aptamers. Bottom section: Computed 3D-Models of the designed chimeric aptamers; left, FBmin.2 and right, FBc36.

Such generated chimeric aptamers would comprise both. On one hand, the fluorescently active G-quadruplex/DFHBI complex of the dBroccoli RNA aptamer is

used for the visual localisation of mDEC205 cells. On the other, the min.2 recognises the mDEC205 receptor (e.g. to guide a nanoparticular encapsulated cargo to the DCs). Such a system would provide an easy synthesisable RNA-based fluorescent analytical probe without any covalent attachment of a fluorescent dye. Wengerter *et al.* described that the effectiveness of a therapeutic vaccine is often restricted to its ability to activate a T cell-mediated immunity.[95] Therefore, they used a multiavidity approach, complexing several biotinylated RNA aptamers with streptavidin. This concept of multiavidity can be easily adapted and addressed by calcium phosphate nanoparticles regarding the possible number of attachable biomolecules on the surface of silanised calcium phosphate nanoparticles. For example, van der Meer *et al.* have shown that up to 240 avidin molecules can be immobilised on one single calcium phosphate nanoparticle, giving up to 600 accessible binding sites for biotinylated molecules.[245] Therefore, even thiol-functionalised calcium phosphate nanoparticles would provide a sufficient area to attach a multiple number of maleimide-activated chimeric aptamers to retain multiavidity. Here, the conjugation of chimeric aptamers on the surface of calcium phosphate nanoparticles is shown with the primary goal to detect mDEC205$^+$ dendritic cells via FACS analysis.

3.7.2 Cloning of pFBmin.2 and pFBc36

To transcribe the genetic information of FBmin.2 and FBc36 *in vitro*, two plasmids pFBmin.2 and pFBc36 were generated by DNA assembly or QuickChange cloning, respectively. Here, the pU19i backbone from pUC19i-Spinach-min-wt-tLys (pUCS) was used as recipient vector. pUCS has a higher plasmid copy number than the original vector pET28c-2xdBroccoli. Therefore, it was used to obtain much higher plasmid yields. pUC19i-Spinach-min-wt-tLys was given to us from Dr. Sven Hennig (Chemical Genomics Centre of the Max Planck Society, Dortmund).

3.7.2.1 Cloning of pFBmin.2

The pFBmin.2 vector (pUC19i-F30-dBroccoli-min.2) should be generated by DNA assembly. The existing restriction sites for *Hind*III, *Xho*I and *Bam*HI from pUCS should

be kept in pFBmin.2 to simplify later cloning experiments. These restriction sites should be flanking the genetic information for the transcription of spinach, including the T7 promotor, spinach and the adjacent T7 terminator. By a restriction double-digest with one of the following enzyme pairs (*Hind*III+*Bam*HI, *Hind*II+*Xho*I), the total gene for the spinach transcription was removed, leaving a gap with sticky ends for subsequent cloning (Figure 3-50).

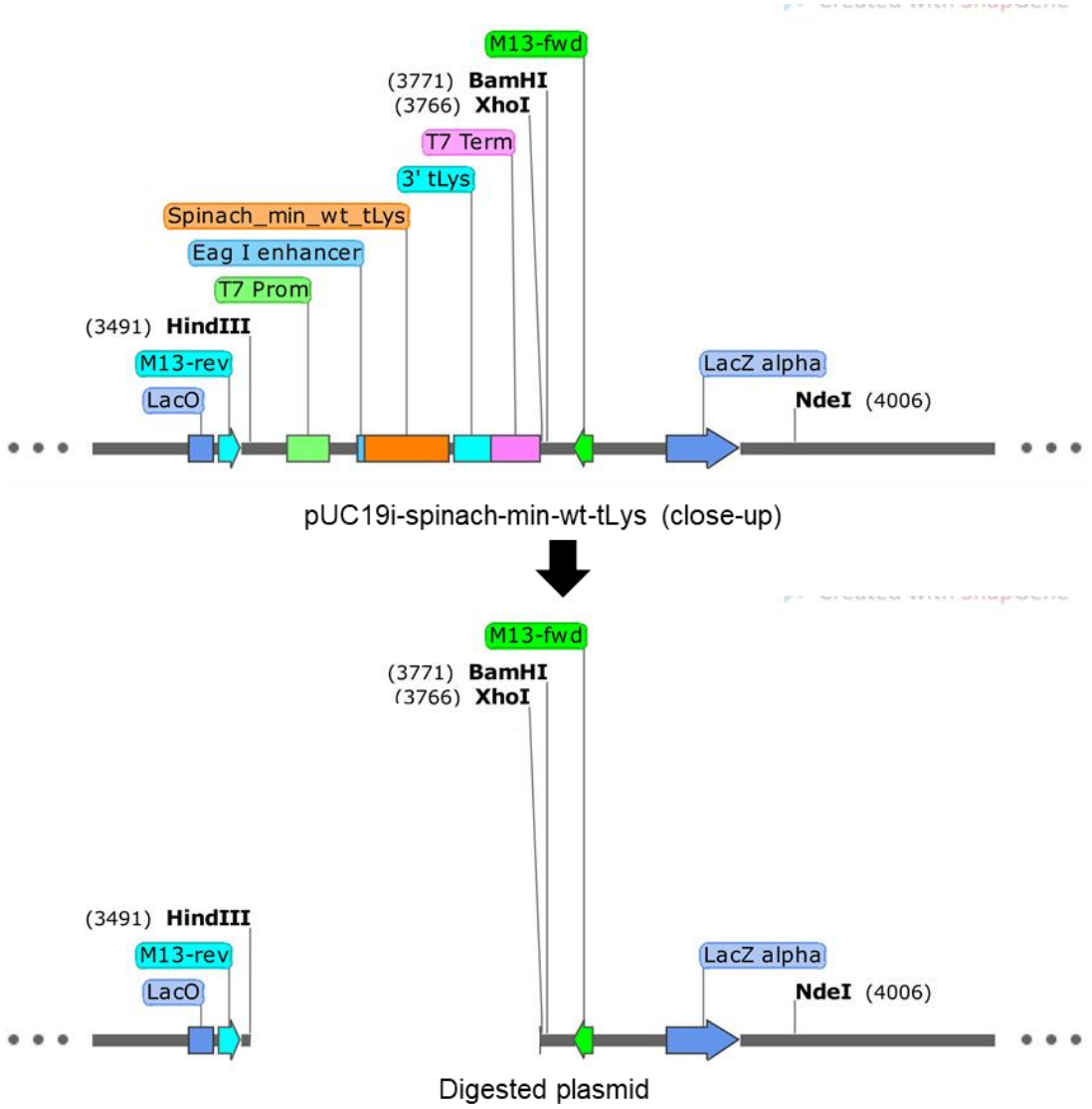

Figure 3-50: Recipient plasmid pUC19i-spinach-min-wt-tLys before and after double-digest.
*Hind*III and *Bam*HI are flanking the gene for spinach transcription. After double digestion, the backbone of pUC19i remains.

The recipient plasmid pUC19i itself is about 4.1 kb long. By double-digestion with each enzyme pair, the plasmid should be separated into two dsDNA fragments with

286 bp and 3.9 kb in size. As it is depicted in Figure 3-51, the test restriction has confirmed the existence of the recognition sites for *Hind*III and *BamH*I, whereas the restriction site of *Xho*I was not detectable. Based on these results, the necessary primers for the DNA assembly were designed.

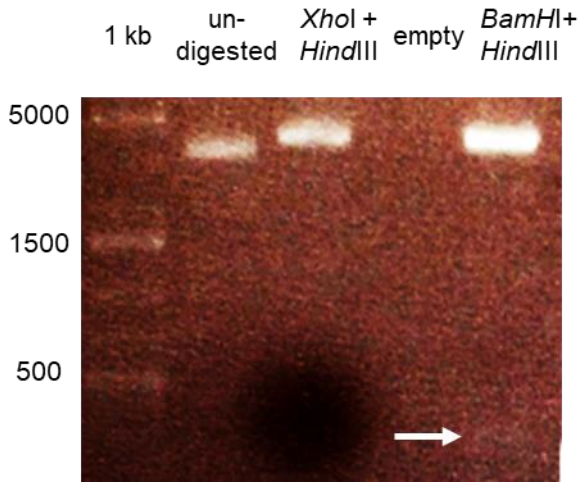

Figure 3-51: 1% agarose gel of double-digested pUC19i-spinach-min-wt-t-Lys.
2 µg of pUCS were double-digested with *Xho*I+*Hind*III, and *Bam*HI

The pFBmin.2 vector was obtained through the HiFi DNA assembly method. 2 µg of the recipient vector pUCS were digested with 40 U of *Hind*III and *Bam*HI each. Through the double digestion, the gene spinach-min-wt-Lys was sliced out and the remaining backbone pUC19i was purified via agarose gel extraction and kept for later cloning. The sequence for one dimeric Broccoli was amplified via PCR from pET28c-2xdBroccoli using the two-following primer sets T7F30_min.2Fwd (5'-AGA TCT CGA TCC CGC GAA-3'; F1), T7F30_min.2Rev (5'-TCG TGT GCT AAC ACA CCT CCC GGA TCA TCA GAG TAT GTG GGA G-3', R1). This generates a first amplicon "amplicon1" bearing one part of the aptamer sequence of min.2. The second primer set, F30-endFwd (5'-TTC ATA ATC AGC TAC CCT CCC GGA TCA TTC ATG GCA AGC TAG C-3'; F2) F30-endRev (5'-TGG TGG TGC TCG AGC AAA AA-3'; R2) generate a second amplicon "amplicon2", carrying the second part of min.2 (Figure 3-52). After the purification of the newly generated amplicons via gel extraction, the amplicons were used for a PCR extension reaction, in which the necessary overhangs for subsequent DNA assembly were built (Figure 3-52). Subsequently, the new extended amplicons

were assembled in one single reaction[164] and transformed into *E. coli* XL-1 Blue chemical competent cells.

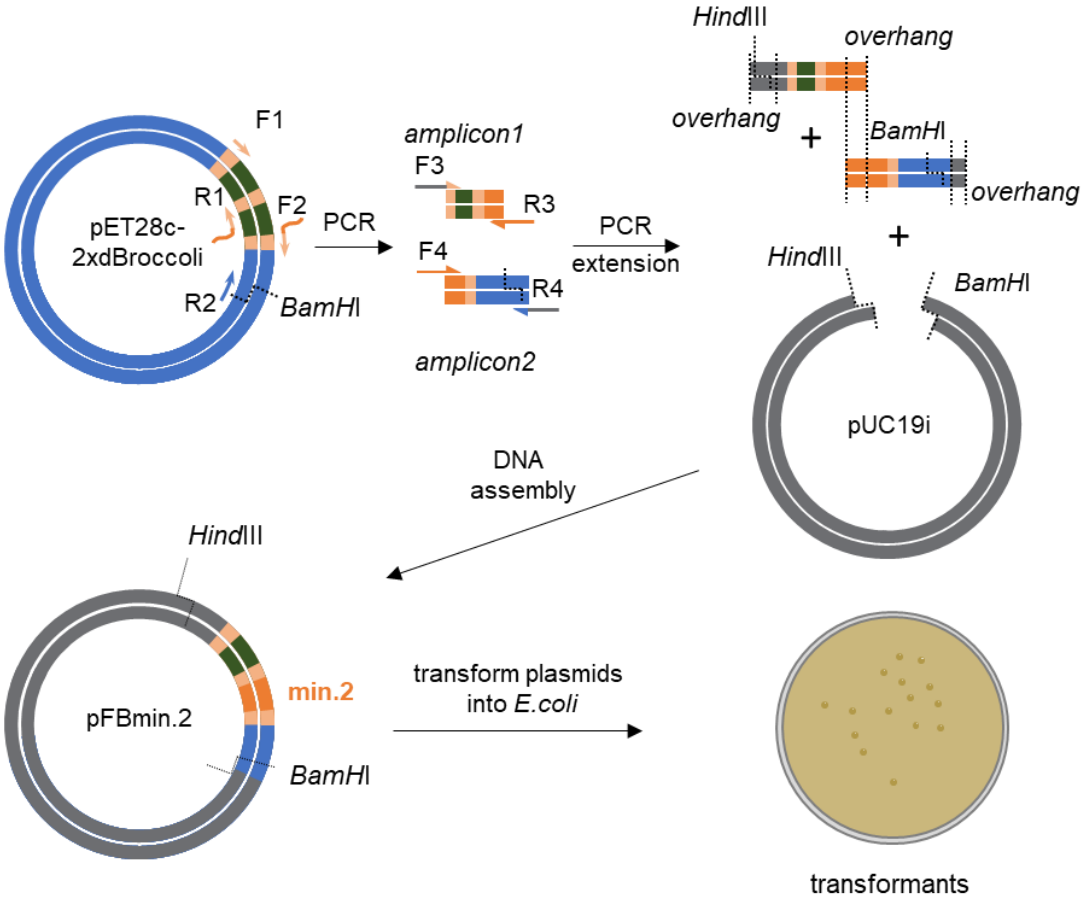

Figure 3-52: Generation of pFBmin.2 and pFBc36 via DNA assembly.
From upper left to down right: The primer set with F1 (T7F30_min.2Fwd) and R1 (T7F30_min.2Rev) generates amplicon1, which bears the full genetic information of dimeric broccoli and partially the min.2 sequence. Whereas the primer set with F2 (F30-endFwd) and R2 (F30-endRev) generates amplicon2. This contains the downstream sequence of pET28c-2xBroccoli and the other half of the min.2 sequence. The generating amplicons are further PCR-extended to generate the necessary overhangs with F3+R3 (Amplicon1 Fwd and Amplicon1 Rev) or F4+R4 (Amplicon2 Fwd and Amplicon2 Rev), respectively (s. Appendix, primer list). Finally, the purified extended amplicons are assembled with the double-digested pUC19i backbone in one DNA assembly reaction and are transformed to obtain the pFBmin.2.

The following day, 5 clones were picked from the agar plate and screened via colony PCR with two different primer sets (1st primer set M13_insert fwd + M13_insert rev (368 bp PCR product); 2nd primer set: T7F30_min.2Fwd + F30_endRev (289 bp PCR product)). The results of the colony PCR are shown in Figure 3-53. Three possible positive clones K3-K5 were detected, then cultivated and after subsequent plasmid

purification, the plasmids were sequenced, revealing a correct sequence for K4. This clone was used for further experiments.

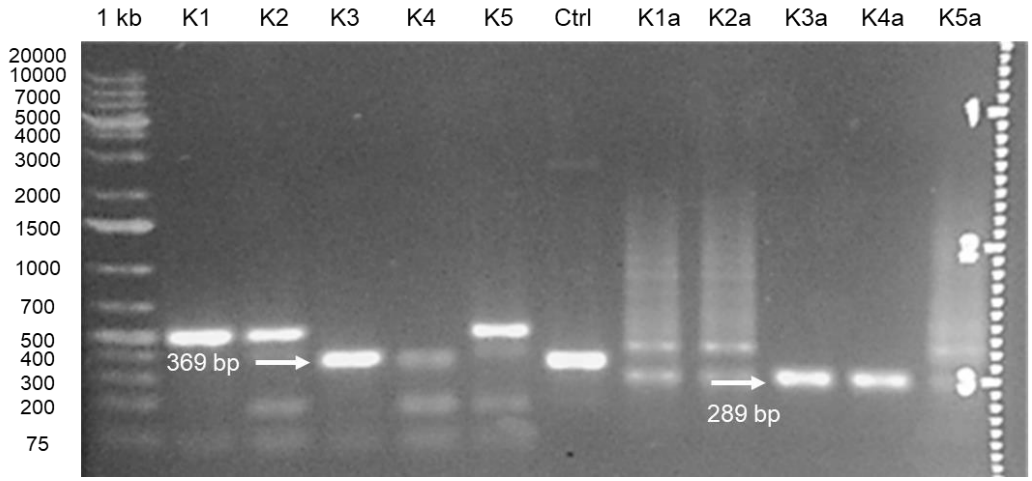

Figure 3-53: Colony PCR.
K1-5: Clones 1-5; 1st primer set should generate a dsDNA fragment with 369 bp. K1a-5a: Clones 1-5; 2nd primer set should generate a dsDNA fragment with 289 bp Ctrl: control amplification of pUCS with 1st primer set generates a control dsDNA fragment with 354 bp for a better size expectation. K3-K5 were taken for further analysis.

3.7.2.2 Cloning of pFBc36

The plasmid for the non-binding control aptamer c36, pFBc36 (pUC19i-F30-dBroccoli-c36) was obtained by site-directed mutagenesis (SDM), using the Q5-site-directed mutagenesis kit (NEB) (Figure 3-54). To substitute min.2, a PCR was performed according to the manufactures' protocol, using the following two primer sets QC_c36_Fwd: 5'-CGT GTG CTA ATA CAC GCC GGA TCA TTC ATG GCA AGC-3'; QC_c36_Rev: 5'-ATT CAT AAT CAC TAC GCC GGA TCA TCA GAG TAT GTG-3'. Both primers bear half of the genetic information for c36. After the treatment with the KLD mix (kinase, ligase, *Dpn*I), 5 µL of the reaction mixture were transformed into *E. coli* DH5α competent cells. The following day, 16 colonies were picked and transferred in 5 mL LB medium each, plasmids were isolated, validated by DNA sequencing. One matching clone was chosen for later template PCR-amplification and *in vitro* transcription.

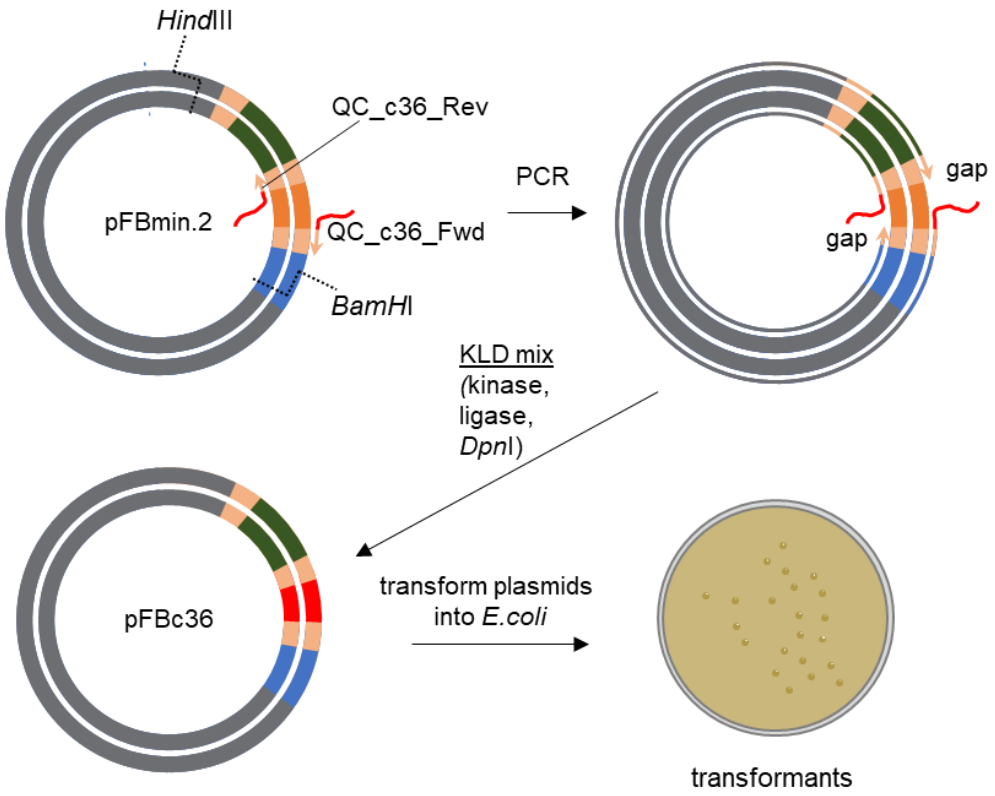

Figure 3-54: Generation of pFBc36 by site directed mutagenesis.
pFBc36 was obtained by site directed mutagenesis. From the upper left to the lower right: Primers anneal to the plasmid pFBmin.2. The plasmid is amplified via PCR, substituting the genetic information for min.2 with the gene for c36. The *Dpn*I digest removes the parental DNA, while the kinase and the ligase seal the remaining gaps. Sealed plasmids are transformed into competent cells.

3.7.3 Template amplification and *in vitro* transcription

In former experiments, *in vitro* transcription was unsuccessfully carried out using restriction enzyme linearised plasmids as template DNA. Linearised plasmids may suffer from incomplete digestion, leading to overlong and wrong transcribed RNA. Therefore, aptamer sequences were amplified via PCR with specific primers to obtain a chimeric aptamer containing PCR product from the corresponding plasmids (Table 3-17).

Table 3-17: Characteristics of PCR and IVT products.

Plasmid	Primer	PCR product (DNA)	IVT product (RNA)
pFBmin.2	T7F30_min.2Fwd F30_Rev_PCRTempl.	T7P-F30-dBroccoli-F30-min.2-F30 (T7P-FBmin2)/ 226 bp	FBmin2 (189 nt)
pFBc36	T7F30_min.2Fwd F30_Rev_PCRTempl.	T7P-F30-dBroccoli-F30-c36-F30 (T7P-FBmin2)/274 bp	FBc36 (183 nt)
pF2B	T7F30_min.2Fwd F30 end IVT_Rev	T7P-F30-dBroccoli-F30-dBroccoli-F30 (T7P-FBmin2)/220 bp	FB2 (237 nt)

The necessary sequence for the T7 promotor was included in the forward primer and allows the subsequent *in vitro* transcription, giving a fully transcribeable PCR product. Generally, the *in vitro* transcription gives higher RNA yields when PCR products are used, since much more micrograms of a 5-kb plasmid are needed compared to a PCR product of 0.5 kb that encodes the same length transcript. For the PCR, five reaction of 100 µL each were used for every construct. This should ensure at least a sufficient amount (i.e. 1 µg) for the following IVT reaction. The results of the PCR amplification are depicted in Figure 3-54. The data shows the successful amplification of the desired cDNA templates with the corresponding lengths. Each in gel PCR product was sliced out, combined and purified through gel extraction (Macherey&Nagel) following the manufacturers' instruction. The PCR product concentration was determined by a µ-volume UV spectrophotometer (NanoDrop 2000c, Thermo Fisher Scientific). The yields are shown in Table 3-18.

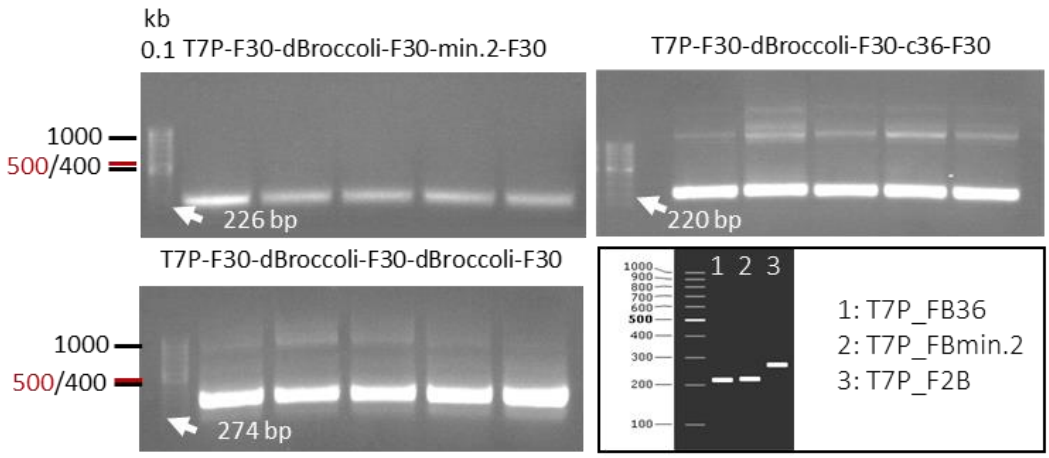

Figure 3-55: 1% agarose gel of the amplified templates.
Amplified PCR products (upper row, lower left) compared to the expected amplified sequences (lower right). PCR products were run on a 1% Agarose gel with 100 V for 20 min.

As the results show, quantities of sufficient and pure DNA for an IVT were produced by PCR which was revealed by the ratio 260/280, an indicator for protein impurities. A 260/280 ratio of ~1.8 is widely considered for pure DNA. This value can be found for all amplified constructs. Thus, the PCR products were used for the following IVT reaction.

Table 3-18: DNA yields after PCR and gel extraction.

PCR product	c(DNA)/ ng µL^{-1}	A260	A280	260/280	260/230
T7P-FBmin.2	140.9	2.818	1.521	1.85	1.61
T7P-FBc36	178.4	3.568	1.940	1.84	0.78
T7P-F2B	230.9	4.617	2.533	1.82	1.28

After PCR amplification, the templates were used for the IVT reaction. Three 40 µL IVT reactions were assembled with 1 µg of the corresponding template. The reaction was carried out for 6 h at 37 °C following the instructions of the manufacturers' manual (MEGAScript T7 Transcription Kit, Life Technologies). RNA was purified and eluted with 2x40 µL NF-H_2O. The results of the RNA yields are displayed in Table 3-19.

Table 3-19: RNA yields and chimeric aptamer characteristic.

Aptamer	RNA/ ng µL^{-1}	A260	A280	260/280	260/230	Factor	m_{RNA} / µg	n_{RNA}/ nmol	*MW*/ g mol^{-1}
FBmin.2	1770.5	54.233	30.199	1.8	2.12	32.65	138.1	2.272	61225
FBc36	1795.4	55.254	29.248	1.9	2.08	32.49	140.02	2.379	59370
F2B	1728.9	52.958	29.521	1.93	2.12	32.65	134.85	2.219	77016

The data form the UV spectroscopy measurements pointed out a successful IVT synthesis of chimeric RNA aptamers, showing good yields and with a sufficient purity. This was reflected by the ratios 260/280 and 260/230. All ratios are close or in the range of the value of pure RNA (2.0-2.2).[348] To validate the full integrity and functionality of the IVT synthesised chimeric aptamers, the aptamers were mixed with 10 µM DFHBI in staining buffer and exposed to UV light (354m) expecting an emission of green fluorescence for the intact constructs. All UV light exposed constructs, FBmin.2 (A), FBc36 (B) and F2B (C) showed strong green fluorescence compared to a negative sample (D) containing no RNA (Figure 3-56).

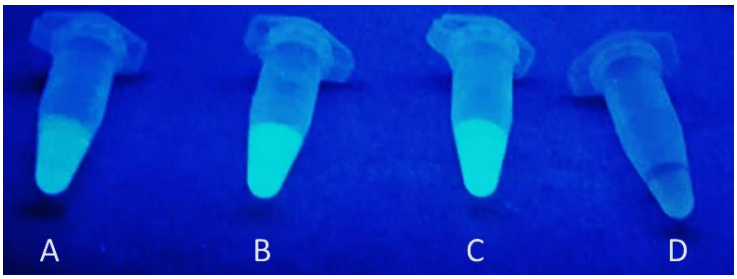

Figure 3-56: UV light exposure of the chimeric RNA aptamer constructs.
The mDEC205 RNA aptamer min.2 and the nonbinding aptamer control c36 were fused with F30-dBroccoli-F30. A: F30-dBroccoli-F30-min.2-F30 (F2B; 189 nt; Control), B: F30-dBroccoli-F30-c36-F30 (183 nt) and C: F30-dBroccoli-F30-dBroccoli -F30 (237 nt). 2 µM of each aptamer were mixed with D: 10 µM DFHBI in staining buffer (40 Mm HEPES [pH 7.4], 100 mM KCl, 1 mM $MgCl_2$, 10 µM DFHBI) containing no RNA.

This result indicated strongly that the chimeric aptamer structure and integrity was fully preserved. It suggests that the F30 scaffold and its conjugated sequences dBroccoli, min.2 or c36 were folded correctly. It further indicates that the F30 scaffold might have forced the adjacent F30-conjugated RNA sequences to fold into their thermodynamically preferred three-dimensional structure. Therefore, it was concluded that F30-adjacent aptamers i.e. dBroccoli and c36, were folded correctly. Moreover, the occurring fluorescence corroborates the correct length of the dBroccoli constructs. Indeed, aborted or rather mutated transcripts from an IVT reaction may also lead to a right fluorescent active 3D structure. The fact that RNA polymerases have an error rate that is about 10^{-4} or 10^{-5}% (1 mistake per 10,000 or 100,000 nts) and short run-off templates were used, makes it less likely that aptamers with a wrong sequence were transcribed. Even with the longest transcript (FB2, 237 nt) there is an error rate of 2.4% for one miss-inserted nucleotide in the whole transcript. This number even decreases for the shorter transcripts of the chimeric aptamers, FBmin.2 (189 nt, 1.89%) and FBc36 (183 nt, 1.83%) and is negligible. Fluorescent aptamers were characterised by fluorescence spectroscopy (Table 3-20). All aptamers had an excitation wavelength of 462 nm and showed an emission wavelength from 497-520 nm which was expected for the dBroccoli/DFHBI complex.[106,108,113,116,117] The observed variations in the emission wavelengths can be explained by the different conjugated sequences (i.e. min.2 and c36) adjacent to dBroccoli.[110] Each adjacent sequence results in a small shift in the emission and

excitation maxima. Titration revealed that the chimeric aptamers can be used down to 62 nM to receive a constant Q-quadruplex/DFHBI fluorescence signal.

Table 3-20: Determination of Excitation and Emission maxima by fluorescence spectroscopy.

Construct	Ex./ nm	Em/ nm
FBmin.2	462	497
FBc36	462	520
F2B	459	504

Finishing the IVT and the fluorescence spectroscopic characterisation, the aptamers were used for the covalent attachment on the surface of calcium phosphate nanoparticles.

3.7.4 Synthesis of chimeric aptamer-functionalised calcium phosphate nanoparticles CaP/PEI/SiO_2-S-aptamer

Chimeric aptamer-functionalised calcium phosphate nanoparticles were obtained by continous precipitation of the calcium lactate and di-ammonium hydrogen phosphate using the same synthesis route as described before (e.g. Ch. 3.2). Briefly, 5 mL of 10.8 mM $(NH_4)_2HPO_4$ (pH 10) (Merck, Darmstadt, Germany), 5 mL of 18.0 mM $(CH_3CH(OH)COO)_2Ca{\cdot}5H_2O$ (pH 10) (Seelze, Fluka Analytical, Germany) and 7 mL of 80 µM PEI were pumped within 1 min into a water-containing glass vessel (20 mL ultrapure water) and were stirred with 1000 rpm for 20 min at room temperature. 10 mL of the resulting CaP/PEI dispersion were coated with a thin silica layer shell by the hydrolysis of 50 µL TEOS in 40 mL ammonia (26 µL, 30-33% (v/v)) alkaline ethanol. The reaction was stirred overnight at room temperature. On the next day, the mixture was centrifuged at 30,000 rpm with a 70 Ti rotor (Beckman&Coulter, Krefeld, Germany) in a SORVALL WX Ultra Series ultracentrifuge, (Thermo Fisher Scientific, Waltham, USA) for 30 min, and the pellet was dispersed by using a UP50H ultrasonic device (Hielscher Ultrasound Technology, Teltow, Germany). The ultrasonic device was equipped with a sonotrode MS3 (Hielscher, Germany) and an amplitude of 70% and a cycle of 0.8 was applied for 20 s) in 10 mL ultrapure water. 10 mL of the resulting CaP/PEI/SiO_2-OH dispersion was given to a

Stoeber solution containing 50 µL (3-mercaptopropyl)trimethoxysilane in 40 mL ethanol. The reaction was stirred for 6 h at room temperature, giving thiol-terminated calcium phosphate nanoparticles CaP/PEI/SiO_2-SH after centrifugation and redispersion using the same settings as described above. The resulting calcium phosphate nanoparticle dispersion CaP/PEI/SiO_2-SH was used for the subsequent coupling of FBmin.2, FBc36 and F2B. For the coupling the RNAs need to be oxidised at the 3' end. Therefore, 60 µg of each RNA was incubated in a total volume of 100 µL 40mM KIO_4 for 1 h at room temperature in the dark. The reaction was stopped with 100 µL of 50% ethylene glycol. Then 1/10th volume of 3M NaOAc (pH 5.2) and 2.5 volumes of 96% ethanol were added to precipitate the RNA. After centrifugation, the pellet was washed with 70% ethanol and air-dried for 30 min. The pellet was dissolved in 100 µL of 10 mM *N*-[κ-maleimidoundecanoic acid] hydrazide (KMUH) and incubated for 2 h at 37 ◦C. After the incubation, 100 µL of 0.2 M $NaBH_4$ and 200 µL of 1 M Tris–HCl pH 8.2 were added and incubated for 30 min on ice in the dark.[90] The RNA was purified by ultrafiltration using a 0.5 mL amicon ultra centrifugal filter device (MWCO = 3 kDa, Merck Millipore, Germany). The RNA was spun down for 15 min at 14,000 g at 4 °C and refilled with 400 µL nuclease-free water and was spun down again for 15 min with 14,000 g at 4 °C. Ultrafiltration steps were repeated twice. RNA was recovered in 20 µL, the concentration was determined by microvolume UV/Vis-spectroscopy (Nanodrop 2000c) and stored at -80 °C. The concentrations of the KMUH-activated were 2.7 µg $µL^{-1}$ (FB2), 2.2 µg $µL^{-1}$ (FBc36) and 1.8 µg $µL^{-1}$ (FBmin.2). 10 µg of each KMUH-activated aptamer was used for the coupling of 1 mL thiol-terminated calcium phosphate nanoparticles CaP/PEI/SiO_2-SH. Particles were purified via centrifugation and redispersion (MS3, 10 s, 70%, 0.8 cyc). After redispersion in staining buffer, the colloidal suspensions were UV light exposed to validate the covalent attachment and the integrity of the aptamers (Figure 3-57). The UV exposure strongly indicated that an intact aptamer was bound on the surface of the nanoparticles. Therefore, a successful covalent attachment of the chimeric aptamers was concluded.

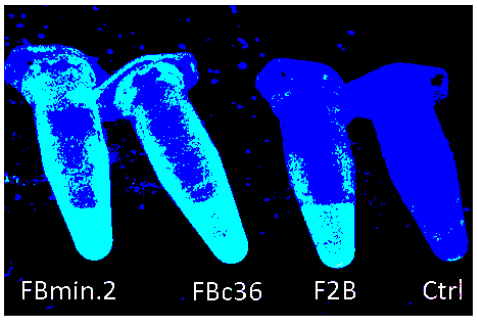

Figure 3-57: Chimeric aptamer-functionalised aptamers.
Chimeric aptamers were covalently attached on the surface of thiol-terminated calcium phosphate nanoparticles. After the conjugation aptamers remain intact, visible by the green fluorescence under UV-light exposure, giving comparable results to the positive control F2B and integrity is confirmed by the negative control (Ctrl, non-conjugated nanoparticles CaP/PEI/SiO_2-SH). The contrast of the image was increased to 100% and brightness was set to -34% to emphasise the differences.

3.7.5 Colloidal characterisation

Chimeric aptamer functionalised calcium phosphate nanoparticles were characterised by DLS and UV-spectroscopy. The results are summarised in Figure 3-58 and Table 3-21.

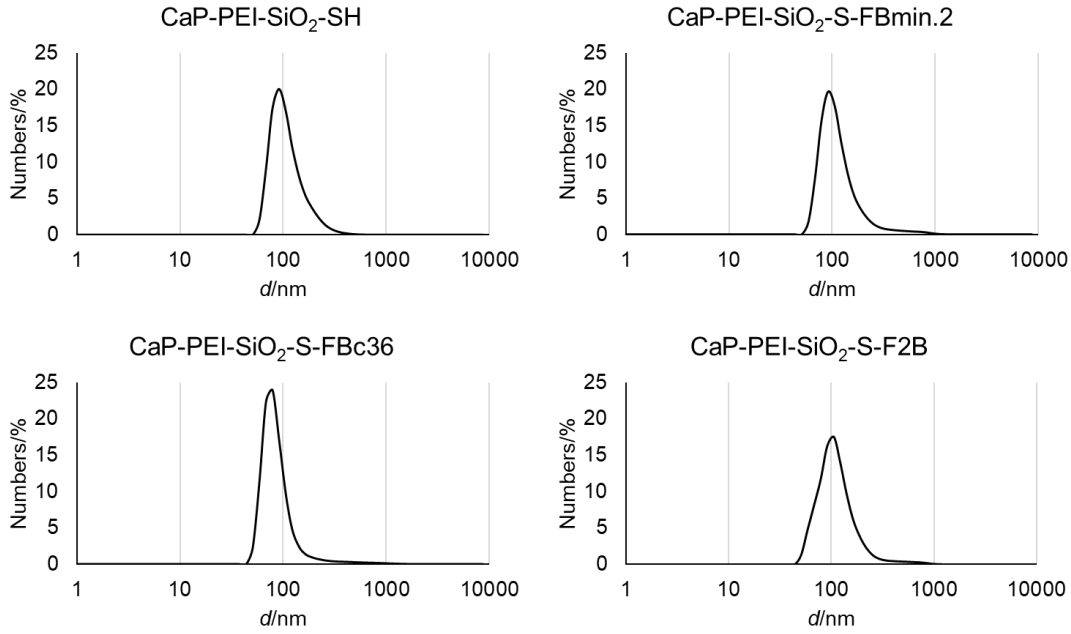

Figure 3-58: DLS results of the aptamer-functionalised calcium phosphate nanoparticles.
The DLS results of chimeric aptamer-functionalised calcium phosphate nanoparticles are shown. The size of the synthesised nanoparticles ranges from 87-106 nm in diameter

Table 3-21: Colloidal characteristics of chimeric aptamer-functionalised calcium phosphate nanoparticles.

Type CaP/PEI/SiO_2-X	H	FBmin.2	FBc36	F2B
Parameter				
d_{SEM}[1]/nm	100	100	100	100
$V_{NP;\ only\ CaP}$/m^3	$5.2\cdot10^{-22}$	$5.2\cdot10^{-22}$	$5.2\cdot10^{-22}$	$5.2\cdot10^{-22}$
$A_{NP;\ only\ CaP}$/m^2	$3.1\cdot10^{-14}$	$3.1\cdot10^{-14}$	$3.1\cdot10^{-14}$	$3.1\cdot10^{-14}$
$m_{NP;\ only\ CaP}$/kg	$1.6\cdot10^{-18}$	$1.6\cdot10^{-18}$	$1.6\cdot10^{-18}$	$1.6\cdot10^{-18}$
$[Ca^{2+}]_{AAS}$/µg mL^{-1}	24.6	42.7	31.2	34.3
$[Ca_5(PO_4)_3OH]$/µg mL^{-1}	61.8	107.2	78.4	86.1
NPs mL^{-1}	$3.8\cdot10^{10}$	$6.5\cdot10^{10}$	$4.8\cdot10^{10}$	$5.2\cdot10^{10}$
w(aptamer)/µg mL^{-1}	–	9.47	9.51	9.87
MW(aptamer)/g mol^{-1}	–	$6.1\cdot10^{4}$	$5.9\cdot10^{4}$	$7.7\cdot10^{4}$
aptamers mL^{-1}	–	$9.3\cdot10^{13}$	$9.6\cdot10^{13}$	$7.7\cdot10^{13}$
m(aptamer) NP^{-1}/kg	–	$1.5\cdot10^{-19}$	$2.0\cdot10^{-19}$	$1.9\cdot10^{-19}$
aptamers NP^{-1}	–	$1.4\cdot10^{3}$	$2.0\cdot10^{3}$	$1.5\cdot10^{3}$
aptamers μm^{-2}	–	$4.6\cdot10^{4}$	$6.4\cdot10^{4}$	$4.7\cdot10^{4}$
wt ratio (aptamer:CaP)	–	1:11.3	1:8.2	1:8.7
d_{DLS}[2]/nm	188 ± 1	455 ± 38	424±30	348±16
d_{DLS}[3]/nm	91	99	87	106
PDI_{DLS}	0.178	0.468	0.449	0.443
ζ_{DLS}/mV	25.5	36.1	32.4	32.6
Particle composition				
CaP/wt-%	100	91.9	89.2	89.7
aptamer/wt-%	0	8.1	10.8	10.3

[1]SEM value of the thiol-terminated nanoparticles was assumed for the aptamer-functionalised nanoparticles.
[2]PSD by intensity /a.u.
[3]PSD by numbers/ %

The measurements show aspects of a stable dispersion regarding the zeta potential (+32-36 mV) but concerning the PDI the chimeric aptamer-functionalised calcium phosphate nanoparticles exceed the ideal value of 0.3. For the calculation of the number of aptamers on the nanoparticles' surface an average solid core diameter of 100 nm was assumed for all nanoparticles since the particle size distribution (PSD) in numbers from the DLS indicated a diameter ranging from 86-106 nm. The PSD expressed in numbers (numbers/%) is a reliable value for the calculation assuming uniformly shaped nanoparticles.[246] Therefore, under the assumption that the synthesised nanoparticles were spherical and uniformly shaped, the solid core diameter from the SEM data of 100 nm (*r* = 50 nm) was used for the calculation. In

the case of un-functionalised nanoparticles, the volume of one single nanoparticle was $5.2 \cdot 10^{-22}$ m^3 and a density of 3,140 kg m^3 for hydroxyapatite was used resulting in a nanoparticle concentration of $3.8 \cdot 10^{10}$ NPs mL^{-1}. For the calculation of the number of FBmin.2 aptamer molecules, the spectroscopically determined concentration was used Table 3-21. Therefore, 9.47 µg mL^{-1} can be assumed for 1 mL dispersion giving about $1.4 \cdot 10^3$ aptamer molecules per nanoparticle and $9.3 \cdot 10^{13}$ aptamers mL^{-1}. After the conjugation, only a small quantity of the RNA aptamers was found in the supernatant (supernatant was collected after removing excess amounts of aptamers by centrifugation) indicating that the initially applied amount was conjugated on the nanoparticles' surface. The calculated number of molecules per nanoparticle ranges from 1400-2000 aptamers per nanoparticle.

3.7.6 FACS analysis

The aptamer-functionalised nanoparticles were tested in a fluorescence assisted cell sorting assay (FACS), carried out at the Universitätsklinikum in Essen (Germany). Herein, dendritic cells (DC) were generated from BDMCs and were harvested from BALB/c mice. The cells were washed and counted. Then, 1250 cells $µL^{-1}$ were seeded in a 12 well plate with a final volume of 400 µL RPMI-1640 medium (supplemented with 5% (v/v) FCS, 0.06 mM β-mercaptoethanol, 1x Pen/Strep, 0.1mg mL^{-1} gentamicin, 20 ng mL^{-1} granulocyte-macrophage colony-stimulating factor (GMCSF)). Then, lyophilised nanoparticles were resuspended in an appropriate volume of staining buffer (40 mM HEPES [pH 7.4], 100 mM KCl, 1 mM $MgCl_2$, 10 µM DFHBI) giving a final aptamer concentration of 1 µM in the reconstituted dispersion. Cells were incubated at 37°C under humidified atmosphere (5% CO_2) with the aptamer-functionalised nanoparticles for 3 h and 24 h, containing a final aptamer concentration of 2.5 nM or 25 nM per well. After the incubation, the cells were harvested and washed with PBS and stained for 30 min in 100 µL antibody solution. The antibody solution was consisting of anti-CD11c (clone HL3-APC conjugate from Bioscience, using a dilution 1:400), anti-F4/80 (clone BM8 Pacific Blue conjugate from Invitrogen, using a dilution 1:400) and fixable viable dye efluor780 from eBioscience (using 1 µL dye mL^{-1} media). Afterwards, the cells were washed with staining buffer (+20 µM DFHBI) once and were resuspended in FACS Buffer (PBS supplemented with

2% FCS and 2 mM EDTA). Then, the cells were analysed via FACS. The obtained results shown in Figure 3-59 give only vague indication of a positive recognition by the nanoparticle-conjugated binding aptamer min.2 and are not significant enough to validate an effective detection of DEC205$^+$ DCs. Herein, the obtained fluorescence signals were plotted as aptamer positive DCs.

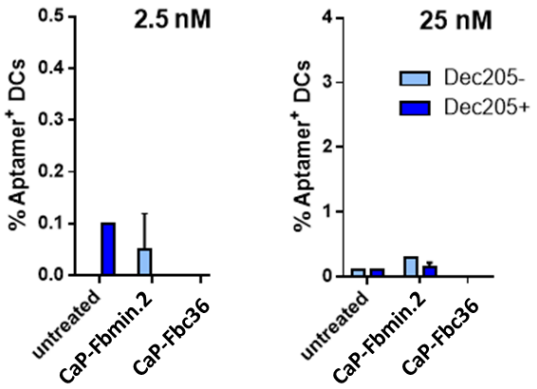

Figure 3-59: FACS analysis of chimeric aptamer-functionalised calcium phosphate nanoparticles. Two different concentrations of the chimeric aptamers were applied to the cells. Non-binding control did not bind to DEC205$^+$ DCs as expected. Only low percentage of the binding aptamer recognised DCs. Concentrations were related on the $K_{d,app}$ of the free min.2 aptamer which is around 23±6 nmol L^{-1}.[95]

However, the experiment needs to be repeated and validated. In the case that the aptamer bound to the DC, a much higher signal would be expected. In a new attempt, the aptamers should be used alone first to validate the binding function and then tested as a functionalised probe.

3.7.7 Summary

The successful synthesis of chimeric aptamers-functionalised nanoparticles was shown. The aptamers were generated by cloning and subsequent *in vitro* transcription and could be obtained in high yield. UV exposure to aptamer-functionalised nanoparticles indicated an intact integrity of the aptamers. Furthermore, successful 3'-end labelling activation and conjugation on the nanoparticles' surface was shown. This was indicated by a remaining fluorescence signal under UV exposure after the final redispersion of the aptamer-functionalised nanoparticles. Therefore, the applied methodology led to aptamers that could bind to calcium phosphate nanoparticles. FACS analysis remained unclear, with

insignificant results that need to be validated. The experiment might be repeated. However, the conceptual idea of chimeric aptamers is still promising due to the diverse application possibilities they can be used for. Future work on this project should focus on the optimisation of the FACS condition, since this project is new and the right FACS conditions (e.g. aptamer concentration, addition of DFHBI) are still needed to be explored.

3.8 Monitoring the dogma of molecular biology with calcium phosphate nanoparticles

The central dogma of molecular biology describes generally the production of a protein in three steps; from DNA over RNA to a matured protein (Figure 3-60).

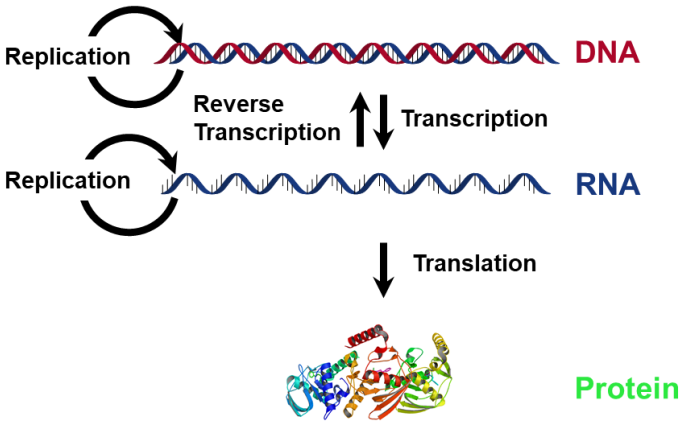

Figure 3-60: Central dogma of molecular biology.

In this chapter the cDNA, mRNA and protein of the green and red fluorescent protein tandem (mRFP-GFP) were transported into HeLa cells with the help of triple-shell calcium phosphate nanoparticles. This approach should elucidate how fast DNA and RNA is translated if nanoparticles are used as a carrier system and how they are distributed in cells. Furthermore, the uptake of the protein itself is comparably analysed. Commercial lipo-based available alternatives for transfection have been shown to be less satisfying concerning its cytotoxicity.[247] Furthermore, uptake studies with nanoparticles are more or less focussing only on single type of a cargo. Here, the objective target was to compare all three transported biomolecules to each other.

3.8.1 Tandem protein

The tandem protein is a fusiogenic protein which consists of the red fluorescent protein, mRFP and the green fluorescent protein, GFP. It is a widely used probe for autophagocytotic processes in cell biology.[248-253] By anchoring the cDNA of the tandem protein to other proteins, it can be used as a marker protein to visualise autophagocytotic processes and herein involved vesicles, exploiting the different pH sensitivities of each monomer within the fusion protein. Whereas mRFP is less pH sensitive and keeps its fluorescence in acidic environments in contrast to GFP. GFP loses its fluorescence in acidic cell compartments or environments e.g. phagolysosomes or lysosomes, enabling the molecular trafficking of those tandem-modified proteins.[248-253] Furthermore, this protein has been attached to other signalling proteins to study trafficking or cellular signal transduction via fluorescence microscopy.[254] Therefore, the protein should be used as a probe for the uptake analysis of calcium phosphate nanoparticles loaded with the tandem protein to elucidate the fate of the transported protein into the cell compartments e.g. cytosol, lysosome by monitoring its distribution through fluorescence microscopy. Furthermore, it should be investigated if the nanoparticle-mediated biomolecule delivery shows any difference between the tandem cDNA, tandem RNA or the tandem protein.

3.8.2 Cloning of pGEX-6P-1tandem.

The genetic information for the tandem protein was cloned into the recipient expression vector pGEX-6P-1. This expression vector encodes a glutathione-S-transferase tag (GST-tag) for protein purification and bridges the tandem gene with the gene for a serine protease recognition sequence to cleave the expressed protein from the affinity tag.[255] The tag was attached to the N-terminus of the tandem protein and was cloned by restriction and ligation. The cloning and expression of the protein was performed with the support of the AG Meyer workgroup, especially with the help of the PhD student Robert Pöhler.

First, we chose three possible host vectors for either His-tag affinity or GST-tag based protein purification and cloned the gene into pET41b+ (His_6-tag), pGEX-6P-1 (GST-tag) and pET15b (His_6-tag). The cDNA of the tandem protein was amplified from ptfLC3

(Addgene Plasmid #21074) via restriction site containing primers. The reverse primer was used to insert a stop codon into the final construct (Table 3-22).

Table 3-22: Primers.

Primer	5'→3'	Length/nt	Host vector	Site
*Apa*IFwd	CAC ACA GGG CCC GAC GTC ATC AAG GAG	27	pET41b+	*ApaI*
*Xho*IRev	GGA CGA GCT GTA CAA GTA ACT CGA G	25	pET41b+/pET15b	*XhoI*
*Bam*IFwd	CAC ACA GGA TCC GAC GTC ATC AAG GAG	27	pGEX-6P-1	*BamHI*
*EcoR*IRev	GGA CGA GCT GTA CAA GTA AGA ATT C	25	pGEX-6P-1	*EcoRI*
*Nde*IFwd	CAC ACA CAT ATG GAC GTC ATC AAG GAG	27	pET15b	*NdeI*

After the amplification of the tandem cDNA, the PCR product was purified via gel extraction. Purified PCR product and 1 µg of each recipient vectors were digested with the specific restriction enzymes and purified via gel extraction again. As it is depicted in Figure 3-61 the digestion for the His-tag based recipient expression vector, pET41b+ was incomplete while the cDNA of tandem was not amplified when the primers *NdeI*Fwd and *XhoI*Rev were used. After gel extraction and purification, the relative inserts and vectors for pET15b and pGEX-6-P1 were ligated and transformed into XL1-Blue chemical competent cells. Next day, some clones were picked and inoculated overnight and harvested on next day for plasmid preparation. After cloning, DNA sequencing revealed that only pGEX6P1 was positively cloned and bared the correct DNA sequence. Thus, the plasmid pGEX-6P1-tandem was obtained and used for the expression of the bi-fluorescent protein mRFP-GFP.

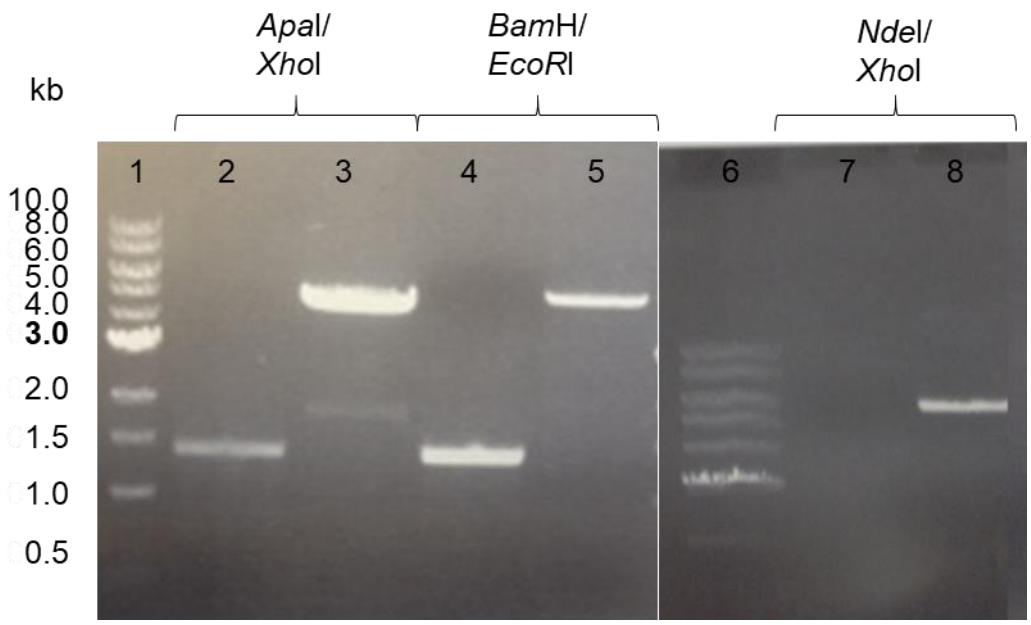

Figure 3-61: Digestion of the amplified insert and the recipient expression vector.
1 and 6: 1 kb DNA ladder (NEB); 2, 4, 7: digested insert;3, 5, 8: digested recipient expression vectors pET41b+, pGEX6P1 and pET15b, respectively.

3.8.3 Cloning of pcDNA3.3tandem.

Another construct of tandem encoding plasmid was generated. The eukaryotic expression vector pcDNA3.3tandem. This vector was obtained by HiFi DNA Assembly by using primers with a specific overhang to the recipient vector. The protocol for the cloning method can be found in previous sections.

3.8.4 Expression of the tandem protein.

A freshly transformed colony of BL21(DE3) pGEX6-1P-tandem was picked and inoculated in 50 mL LB media supplemented with 100 µg mL^{-1} ampicillin overnight at 37 °C with 180 rpm. The following day, the overnight culture was diluted 1/50 in LB media. The culture was grown to an OD of 0.5 and induced with 0.4 mM IPTG and further incubated overnight at 18 °C. Samples were taken prior to and after the induction for SDS/PAGE analysis. Figure 3-62 shows the result of the non- and induced expression culture. Glutathione-S-transferase is a 26 kDa large protein that binds specifically to immobilised glutathione on a cellulose matrix. Together, the GST-tag and the tandem protein has a size of approximately 84 kDa. After the induction with IPTG the protein was detected via SDS-PAGE (Figure 3-61).

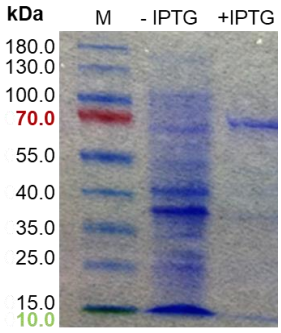

Figure 3-62: SDS-PAGE of non-induced (- IPTG) and induced (+ IPTG) expression culture.
The fusion protein GST-tandem migrates between 70-100 kDa. (13% SDS gel, PageRuler Prestained Protein Ladder Thermos Fisher).

The whole affinity chromatography purification was monitored via SDS-PAGE. As it is depicted in Figure 3-63, the tandem protein could be successfully expressed and purified. The successfully cleavage of the GST-Tag by the precision protease was also demonstrated (Figure 3-63). Both the cleaved GST-Tag and the tandem protein showed the expected mass.

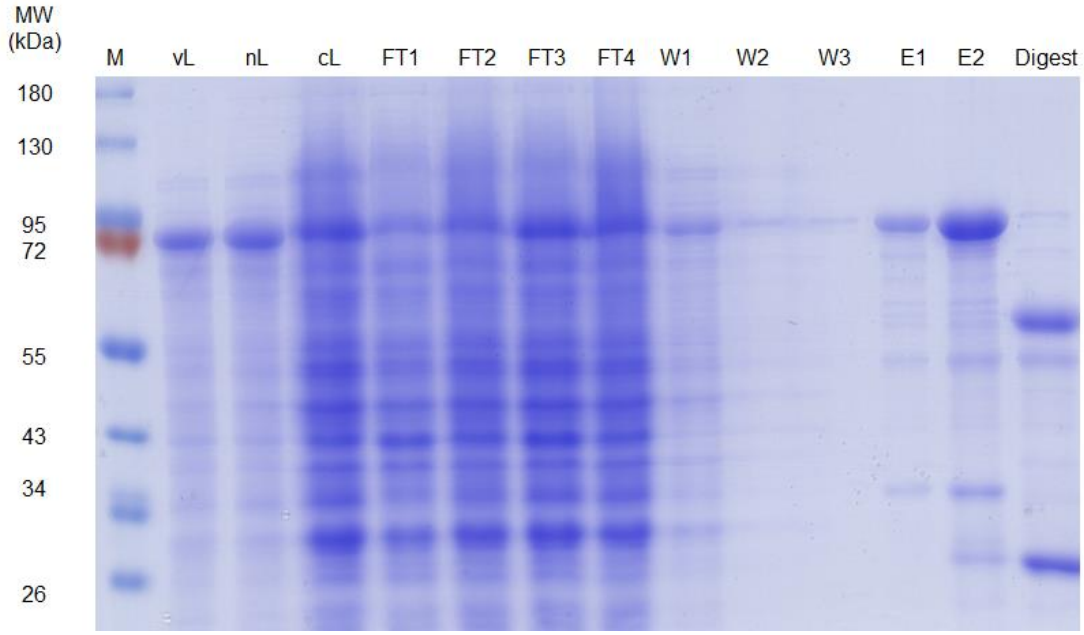

Figure 3-63: Purification of tandem protein
Marker (Thermo Fisher); vL: before lysis; nL: after lysis; cL: cleared lysate; FT1-4: flow through 1-4; W1-W3: wash fractions 1-3; E1-E2: elution 1-2; digestion. (13% SDS gel, PageRuler Prestained Protein Ladder Thermos Fisher).

3.8.5 Size exclusion chromatography (SEC)

For the separation of the cleaved GST-tag from the tandem protein, a size exclusion chromatography was performed, combined with a pre-casted GSTrap column. This experimental set up should ensure the total exclusion of the GST-tag from the protein solution. The passing protein on the column was monitored through an UV/Vis flow through chamber. The protein has been successfully isolated by SEC (Figure 3-64). and the related fractions under the peak were combined, concentrated and analysed via SDS-PAGE.

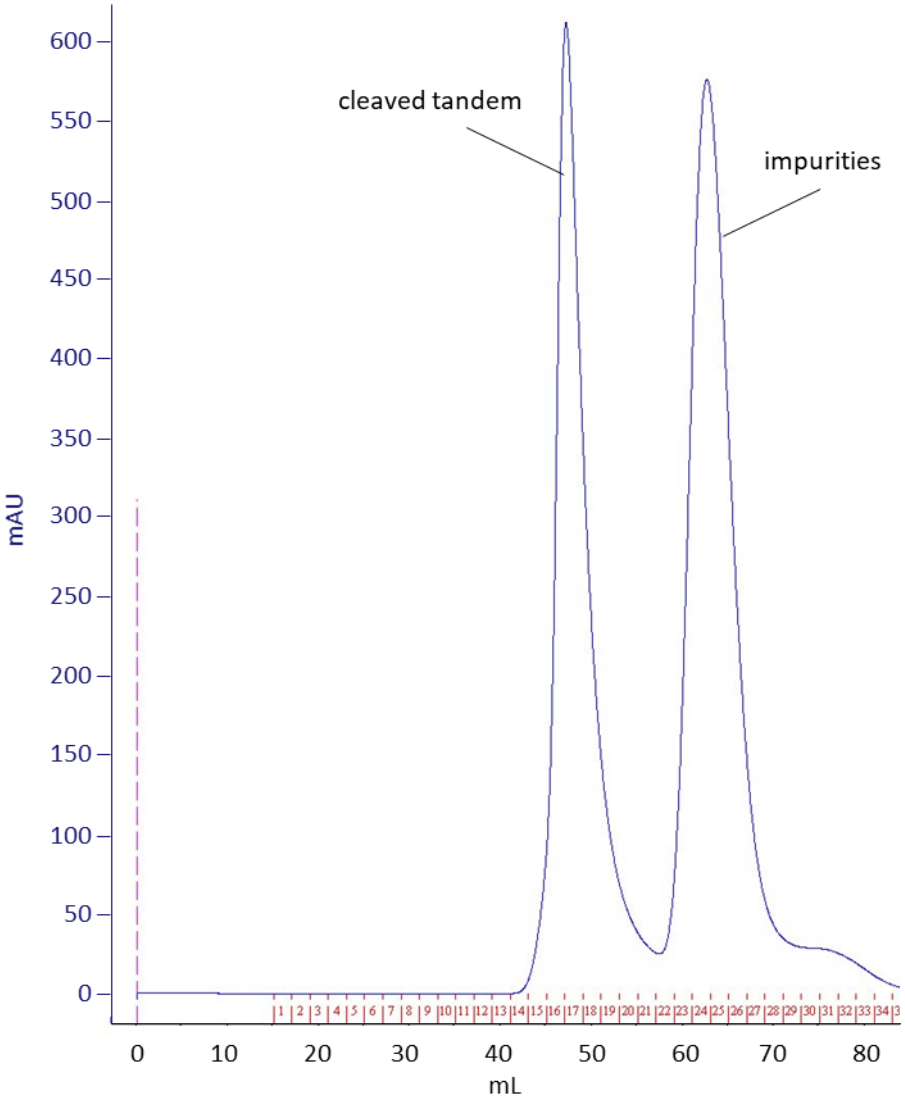

Figure 3-64: Combination of size exclusion and affinity chromatography.
Combined GSTrap and SEC protein purification were used to isolate the cleaved tandem protein. The upstream connected GSTrap captures noncleaved GST-tagged tandem proteins. Cleaved tandem proteins that are eluted first due to the smaller size. A second peak showed some remaining unspecific impurities.

Figure 3-65 shows the purified and concentrated tandem protein. The lanes 3 and 5 showed some impurities. This may be a result of the partial denaturation of the tandem protein by the SDS. SDS is a chaotropic salt that reduces the surface tension which leads to the loss of the protecting solvent surrounding the protein. The tandem protein was successfully separated from the cleaved affinity tag and in all lanes, except lane 6, only the tandem protein (56 kDa) was detected.

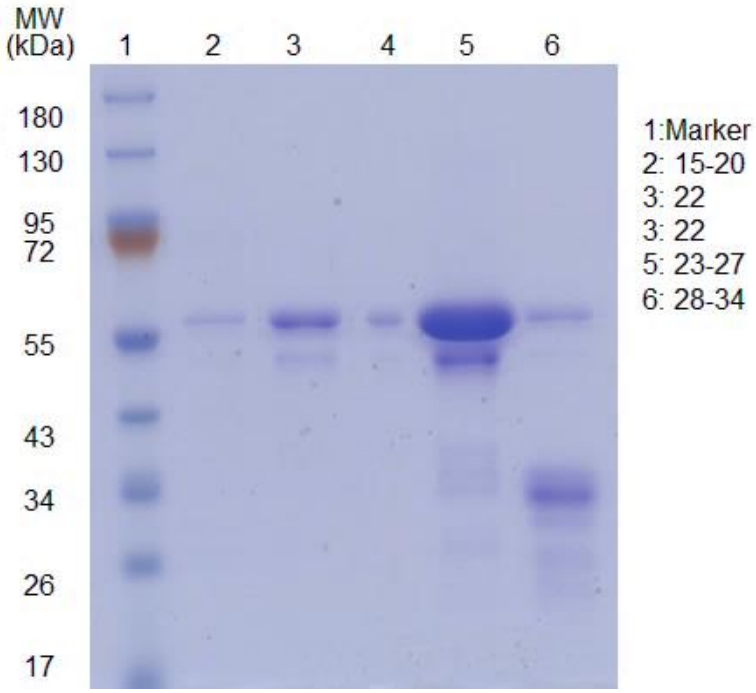

Figure 3-65: SDS-PAGE analysis of the SEC.
All lanes, except lane 6, show the desired protein product.

The overall yield after the protein expression and purification was 7 mg L^{-1} of expression culture. The protein was characterised by UV/Vis spectroscopy and fluorescence microscopy to validate the excitable wavelength and its fluorescence characteristics (Figure 3-66). The data showed the expected excitation/absorption wavelengths for the single monomeric proteins (GFP, 493 nm and mRFP, 563 nm) correlating with the known literature values for each protein.[256-258] Therefore, the tandem protein mRFP-GFP was successfully expressed and characterised.

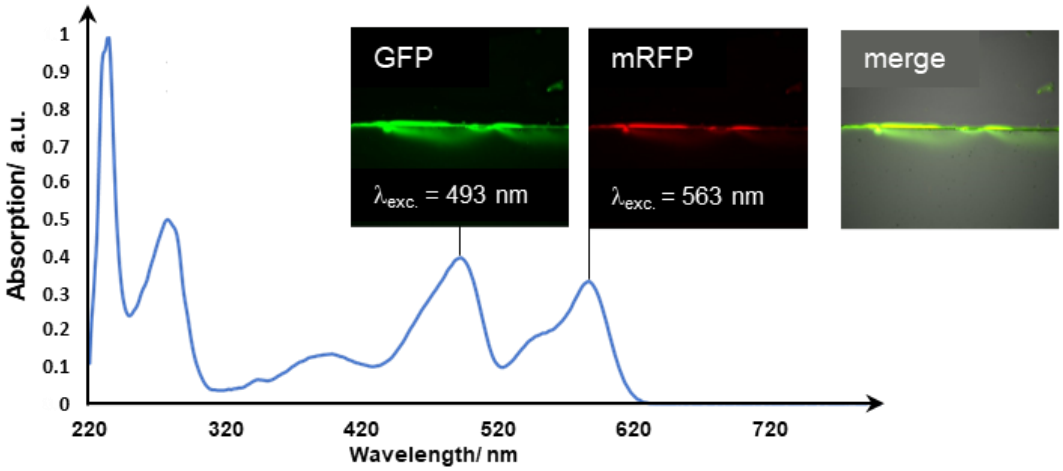

Figure 3-66: UV/Vis characterisation of the tandem protein.

3.8.6 Cloning of pcDNA3.3tandem

For the nanoparticular transport of the tandem cDNA, the gene for the tandem protein was cloned into the plasmid pcDNA3.3 by DNA HiFi assembly from New England Biolabs following the manufactures' protocol. Herein, the gene for the tandem protein was amplified via PCR using the tandem_Fwd (5'-GAA ATA TAA GAG CCA CCA TGG CCT TCT CCG AGG ACG TC-3') as forward and tandem_Rev (5'-GCC CCG CAG AAG GCA GCT TAC TTG TAC AGC TCGT CCAT GC-3') as reverse primer. The backbone fragment was obtained by PCR amplification using the pcDNA3.3_Fwd (5'-CGG CAA TAA AAA GAC AGA ATA AAA C-3') as forward and the pcDNA3.3_Rev 5'-AGG CGA TCT GAC GGT TCA C-3') as reverse primer. Both purified fragments were combined in an assembly reaction in which a 5-molar excess of the tandem gene was used. After the reaction, 2 µL of the assembled plasmid was transferred into chemical competent cells *E. coli* DH5α and the cells were incubated on ice for 20 min and heat-shocked (42 °C, 30 seconds) afterwards. The cells were transferred into SOC medium and cultivated for 1 h at 37°C with 300 rpm in a thermomixer. Then, cells were spun down, resuspended in 100 µL LB medium and stroke out on a LB agar plate supplemented with 100 µg mL^{-1} ampicillin. Positive clones were screened through a colony PCR using the primer set for the tandem gene amplification. About 5 of the positive clones were chosen and cultivated in 5 mL medium (+ 100 µg mL^{-1} ampicillin) overnight at 37°C. The plasmids were isolated from the overnight cultures using a DNA isolation kit (NucleoSpin® Plasmid EasyPure, Macherey&Nagel, Düren,

Germany) and were analysed for the tandem gene through a DNA sequencing service (Seqlab, Göttingen, Germany). Then, the best genetic matching clones were analysed by a test transfection with Lipofectamine 2000.

3.8.6.1 Test transfection

Triplicates of about $1.25 \cdot 10^4$ HeLa cells in a 96-well plate were transfected with 1 µg DNA of the clones of pcDNA3.3tandem C2, C5 and C6 (Invitrogen and 2 µL Lipofectamine 2000, Carlsbad). Previously, the lipoplex complex was incubated for 20 min at room temperature before it was given to the cells. Cells were incubated for 24 h at 37 °C under humidified atmosphere supplied with 5% (v/v) CO_2 before the imaging was started. One clone of C6 was used for later nanoparticular DNA transfection experiments. Figure 3-67 shows the test transfection with Lipofectamine 2000. In all cases, the protein was well expressed by HeLa cells showing a diffuse distribution within the cytosol. This revealed also a successfully cloning of pcDNA3.3tandem.

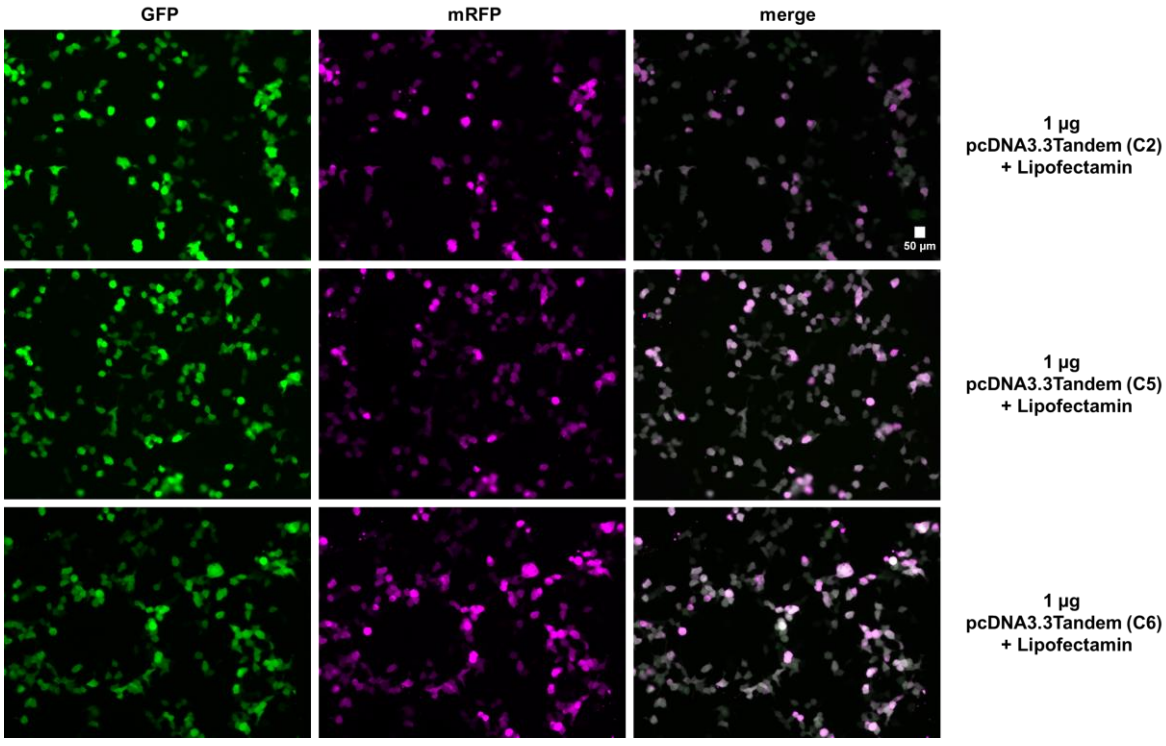

Figure 3-67: Test transfection of HeLa cells with pcDNA3.3tandem.
Different clones of pcDNA3.3tandem (C2, C5 or C6) were transfected with pcDNA3.3tandem by Lipofectamine 2000 and incubated for 24 h to ensure its ability to express the tandem protein. Scale bar 50 µm, 20x.

3.8.7 *In vitro* transcription of polyA$^+$-tandem-mRNA

The *in vitro* transcription (IVT) was carried out following the protocol that was described by Avci-Adali *et al*..[174] A detailed protocol can be found in the materials and method section (5.7.17-5.7.19). The average yield of one IVT reaction for polyA$^+$-tandem-mRNA was 45 µg. The following figure shows the PCR amplified DNA product for the subsequent IVT of T7-tandem-polyA, which is 1710 bp long. The corresponding transcribed RNA is approximately half of the mass of its template. Therefore, the band for the transcribed RNA (polyA$^+$-tandem-mRNA) can be found in the range between 0.7-1.0 kb (Figure 3-68) and fits perfectly well with the expected size of 1673 nt (~836 bp) revealing a successful IVT reaction.

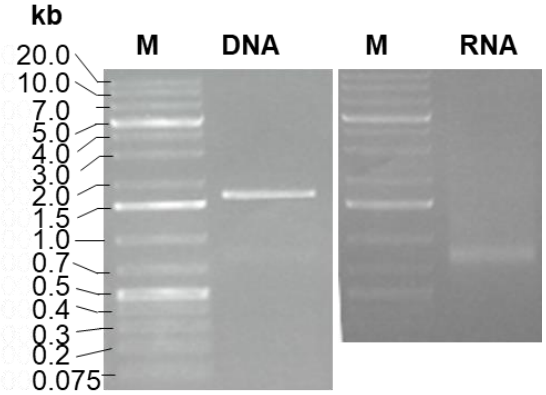

Figure 3-68: PCR product T7-tandem_polyA and polyA$^+$-tandem-mRNA.
1% agarose gel stained with 0.01% ethidium bromide. RNA length is half of the correspondent DNA. M: DNA ladder 1 kb GeneRuler Plus (Thermo Fisher Scientific); DNA: PCR product of T7-tandem-polyA; RNA polyA$^+$-tandem-mRNA.

3.8.7.1 Transfection with polyA$^+$-tandem-mRNA

The transfection was carried out following the protocol that was described by Avci-Adali *et al.*.[174] Briefly, HeLa cells were seeded at $1.5 \cdot 10^5$ cells per well and were cultivated overnight at 37°C under humidified atmosphere with 5% CO_2 in a 6 well plate with DMEM supplemented with 10% FCS, 100 U mL^{-1} penicillin and streptomycin. On the next day, Lipofectamine/mRNA complexes were prepared using 1.5 µg of the polyA$^+$-tandem-mRNA and 2 µL Lipofectamine2000 per well. Cells were incubated for 4 h and were then imaged using a Keyence Biorevo BZ-9000 microscope (Osaka, Japan). The results that are displayed in Figure 3-69 revealed a high

transfection efficiency (up to 80%) after 4 h incubation and indicated a fast expression of mRFP-GFP due to the direct cytosolic availability of the transported mRNA.[174]

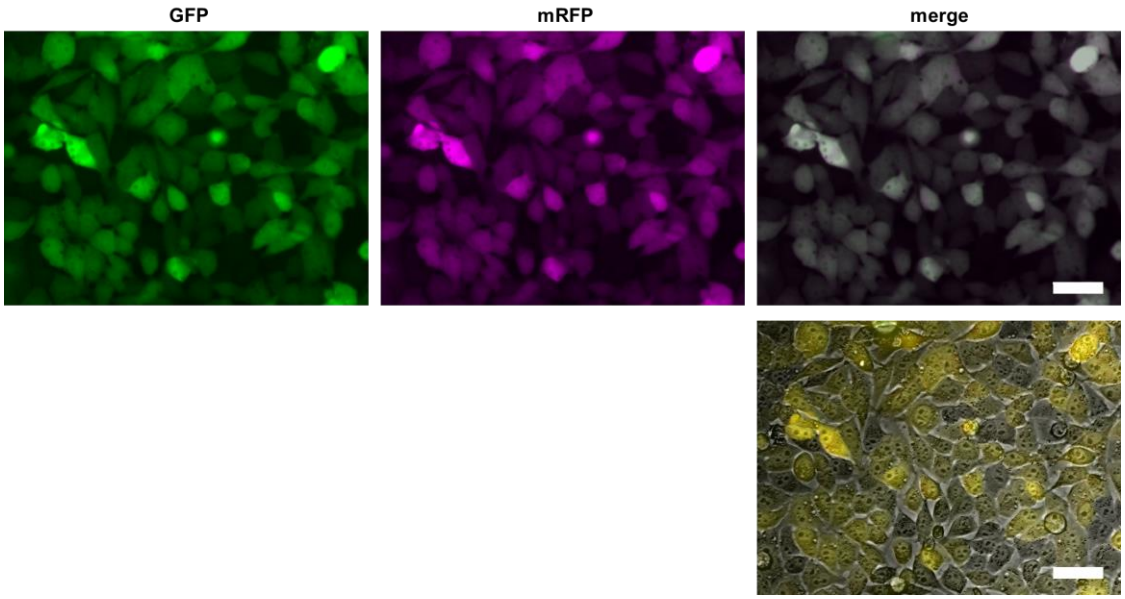

Figure 3-69: Transfection of polyA$^+$-tandem-mRNA with Lipofectamine 2000 after 4 h of incubation. 1.5 µg RNA and 2 µL Lipofectamine 2000 was mixed and applied onto 150,000 HeLa cells per well. These number of cells should compensate the toxicity of the Lipofectamine 2000. Scale bar 50 µm, 40x magnification. In the case of a transfection with Lipofectamine 2000, nearly all cells were expressing the tandem protein after only 4 h. Green: GFP, Mangenta: mRFP; White: merge; Yellow: Overlay of red and green pseudo colours to improve the visualisation of the merge with the brightfield image.

Therefore, the expression of the tandem protein shows a fully intact and readable mRNA and was used for the transfection with calcium phosphate nanoparticles.

3.8.1 Biomolecule characteristics

The dimensions of the transported biomolecules are shown in the following table. The plasmid pcDNA3.3tandem is the heaviest biomolecule ($4.4 \cdot 10^6$ Da). Beside the RNA and protein, they are 8 or 80 magnitudes lighter, respectively. Biomolecule properties are summarised in Table 3-23.

Table 3-23: Used biomolecules.

Biomolecule	*MW*/ g mol^{-1}	Length
pcDNA3.3tandem	4,405,756.00	7137 bp
polyA$^+$-tandem-mRNA	540,646.84	1673 nt (DNA-template: 1710 bp)
tandem protein	52,889.81	470 aa

3.8.2 Synthesis of CaP/PEI/Biomolecule/CaP/PEI particles

Triple-shell calcium phosphate nanoparticles were obtained by rapidly mixing equal volumes of aqueous solutions of 6.25 mM $Ca(NO_3)_2 \cdot 4\ H_2O$ [pH 9] (VWR, p.a.) and 3.74 mM $(NH_4)_2PO_4$ [pH 9] (VWR, p.a.) at room temperature. 1 mL of the fresh dispersion was mixed with 200 µL PEI (2 g L^{-1}) in a new tube to obtain colloidal stability. Then 0.9 mL of this dispersion (CaP/PEI) were transferred into a new 2 mL tube containing either 100 µg of pcDNA3.3tandem, 34 µg of polyA$^+$-tandem mRNA or 100 µg of the tandem protein, respectively. Immediately, 0.5 mL of 6.25 mM $Ca(NO_3)_2 \cdot 4\ H_2O$ [pH 9] (VWR, p.a.), 3.74 mM $(NH_4)_2PO_4$ [pH 9] (VWR, p.a.) each, and 0.2 mL of PEI were added and vortexed briefly. Unabsorbed material and biomolecules were removed by ultracentrifugation at 20,000 g for 20 min at 4 °C (Heraeus Fresco 21, Thermo Fisher Scientific). The supernatants were kept for the quantitation of each biomolecule by UV/Vis spectroscopy with a microvolume spectrophotometer NanoDrop2000c (Thermo Fisher Scientific).

3.8.3 Colloidal characterisation

The results of the DLS measurements are shown in Figure 3-70. The polydispersity index of DNA and protein loaded nanoparticles was 0.284 and 0.342, respectively. The decrease of the zeta potential for these types of nanoparticles might be explained by the counteracting charges of the polyelectrolyte and the biomolecules. For instance, the plasmid pcDNA3.3tandem is a circular dsDNA which can be considered as double negatively charged due to the nucleotide connecting *ortho* phosphate in each strand of the DNA backbone while the tandem protein (pI_{theo} = 5.62)[259] tends to be more negatively charged in a pH neutral medium. This counteracting might have led to the decreased zeta potential of both types of nanoparticles. RNA loaded nanoparticles showed a small degree of agglomeration and an increased PDI, but the zeta potential was twice as high compared to the other nanoparticles. This might be explained by the single negatively charged *ortho* phosphate in the RNA backbone of the single stranded polyA$^+$-tandem-mRNA. Thus, the charges cannot be compensated, resulting in a regular zeta potential of +20 mV. All particles showed a characteristic size distribution, ranging from 106-230 nm in diameter (Figure 3-70).

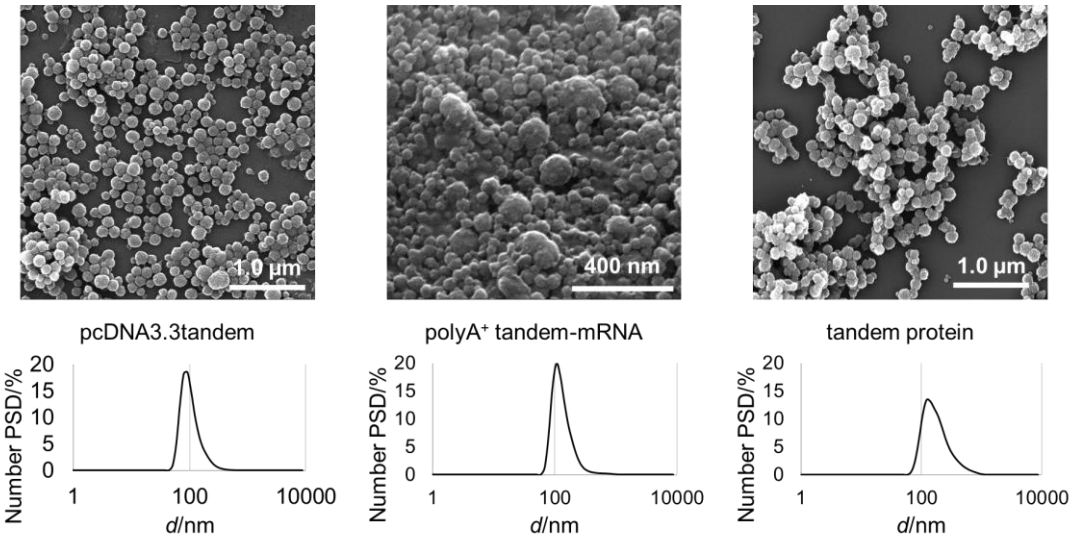

Samples[1] / Parameter	cDNA	mRNA	protein
d_{SEM}/nm	127 ± 10	92 ± 40	138 ± 15.3
DLS d/nm	229 ±27	106 ± 15	143 ± 30
DLS / PDI	0.342	0.510	0.284
ζ/mV	12	20	11
$V_{NP;\ only\ CaP}$/m^3	$1.1\cdot10^{-21}$	$4.0\cdot10^{-22}$	$1.4\cdot10^{-22}$
$A_{NP;\ only\ CaP}$/m^2	$5.1\cdot10^{-14}$	$2.7\cdot10^{-14}$	$6.0\cdot10^{-14}$
$m_{NP;\ only\ CaP}$/kg	$3.3\cdot10^{-18}$	$1.3\cdot10^{-18}$	$4.4\cdot10^{-18}$
$[Ca^{2+}]_{AAS}$/µg mL^{-1}	77.7	85.8	132.0
$[Ca_5(PO_4)_3OH]$/µg mL^{-1}	195.1	215.5	331.5
NPs·mL^{-1}	$5.8\cdot10^{10}$	$1.7\cdot10^{11}$	$7.7\cdot10^{10}$
w(biomolecule)/µg mL^{-1}	90.8	14.4	99.6
Yield(biomolecule)/%	90.3	42.6	96.8
MW(biomolecule)/g mol^{-1}	$4.4\cdot10^{6}$	$5.5\cdot10^{5}$	$5.3\cdot10^{4}$
biomolecules mL^{-1}	$1.2\cdot10^{13}$	$1.6\cdot10^{13}$	$1.1\cdot10^{15}$
m(biomolecule) NP^{-1}/kg	$1.6\cdot10^{-18}$	$8.6\cdot10^{-20}$	$1.3\cdot10^{-18}$
biomolecules NP^{-1}	210	95	15000
biomolecules µm^{-2}	$4.2\cdot10^{3}$	$3.6\cdot10^{3}$	$2.5\cdot10^{5}$
wt ratio (biomolecule:CaP)	1:2.1	1:15.0	1:3.3
Particle composition			
CaP/wt-%	68.2	93.7	76.9
biomolecule/wt-%	31.8	6.3	23.1

Figure 3-70: Summarised results of biomolecule loaded calcium phosphate nanoparticles. Upper row: SEM images of the biomolecule loaded nanoparticles. Middle section: DLS measurements, bottom row: Table with nanoparticle properties. [1]CaP/PEI/X/CaP/PEI (X=…).

The concentration of the encapsulated biomolecules was determined by UV-Vis spectroscopy (NanoDrop2000 device from Thermo Fisher Scientific) measuring the concentration from the supernatant after final centrifugation and calculating the difference between the initial and final concentration. The calcium concentration was determined by AAS. The concentration that was ranging from 78 to 132 µg mL^1 which corresponds to an equivalent hydroxyapatite concentration of 195 to 331 µg mL^{-1}. Under the assumption that the nanoparticles were uniformly and spherical shaped, the volume of one single nanoparticle can be calculated by taking the solid core diameter from the SEM data (92-138 nm) to obtain the radius (ranging from 46 to 69 nm). Thereby, the calculated volume was ranging from $4.0 \cdot 10^{-22}$ m^3 to $1.3 \cdot 10^{-21}$ m^3. Equation 13 from chapter 5.5 was used to calculate the number of nanoparticles per millilitre, assuming a density of hydroxyapatite was of 3,140 kg m^{-3}. The nanoparticle concentration was ranging from 5.8 to $17.0 \cdot 10^{10}$ NPs mL^{-1}. Together with the obtained results from the UV-Vis spectroscopy, the number of biomolecules per millilitre dispersion can be calculated by using the Eq. 14 from chapter 5.5. Thereby, $1.2 \cdot 10^{13}$ to $1.1 \cdot 10^{15}$ biomolecules per millilitre dispersion were assumed. Then, the theoretical number of nanoparticle-encapsulated biomolecules on a single nanoparticle is ranging from 210 to 15000 molecules per nanoparticle reflecting the different molecular weights of each biomolecule (Table 3-23). Nanoparticles could be synthesised with an encapsulated biomolecule loading for DNA and protein of up to 97% in the nanoparticles' core. Together with the PDI and the zeta potential, the synthesised nanoparticles can be considered as stable and could be used for further investigations.

3.8.4 Cell viability

Cell viability results are shown in Figure 3-71. HeLa cells were seeded at 5.0 10^4 cells on a 48 well plate and treated with different dilutions of nanoparticles (1:5, 1:10 and 1:20) for either 3, 6 or 24 h.

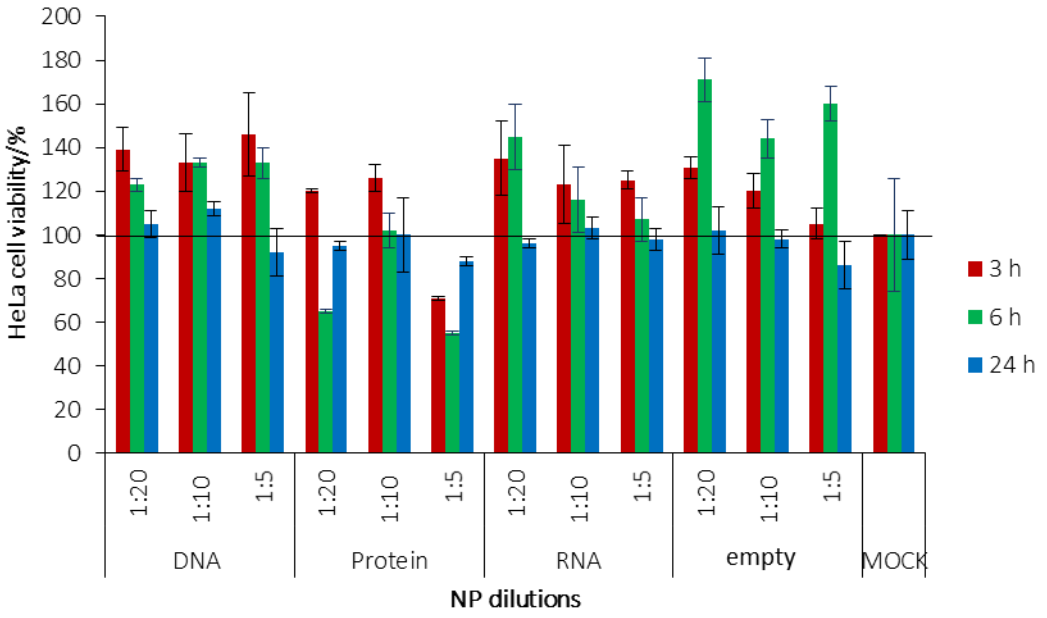

Figure 3-71: MTT assay.
Cell viability assay of HeLa cells. Different dilutions of calcium phosphate nanoparticles were applied to 50,000 cells per well and incubated for different time points. Only low cell toxicity was detected.

The data shows that at any tested concentration, the DNA and RNA-loaded nanoparticles have no significant impact on the cell viability compared to the protein-loaded nanoparticles. As expected, unloaded nanoparticles show no cytotoxicity and corroborate the well-known and proofed biocompatibility and -degradability of calcium phosphate nanoparticles: This leads to the conclusion that no toxic side effects were caused by the nanoparticles itself. The toxicity of the biomolecule-loaded nanoparticles may be due to the fact of some different properties of each transported biomolecule as well as to the used endocytotic pathway. Generally, all nanoparticle-transported molecules are taken up within the first 3 h by endocytosis and must escape after the engulfment from endosomal vesicles to circumvent a premature degradation inside the lysosome.[46,260] The PEI around the calcium phosphate nanoparticle core accelerates the uptake due to its positive charge and contributes to the easy endosomal escape through a diffusion-mediated endosomal rupture ("proton sponge effect").[46] Therefore, all molecules should be released easily in the same manner with the help of PEI. But the molecular properties that allow the biomolecules' endosomal evasion are also needed to be considered. The plasmid pcDNA3.3_tandem harbours a nuclear transport specific guiding sequence (i.e. SV40ori) that facilitates an easy rescue from endosomal vesicles and leads to the

subsequent transport through the cytosol to the nucleus.[261] The transcribed mRNA polyA$^+$-tandem-mRNA is also easily released into the cytosol due to the IVT incorporated modified nucleotides and the ARCA cap analogue at the 5' end, leading to a fast recognition by the ribosome and direct translation of the protein.[262] In contrast to these molecules, the transported protein does not have such evasion helping sequences included, makes it less favoured for an endosomal escape. The continous uptake of the protein follows an enrichment in the lysosome and can cause toxification in the case that the protein is not gradually degraded.[46] The fact that mRFP is less pH sensitive than GFP results in a prolonged resistance time inside the lysosome and probably in toxification. Moreover the monomer mRFP has been reported to be toxic to cells since it is associated with the suppression of Bcl-xL (cellular apoptosis inhibitor) translation.[263] We concluded to avoid such cytotoxic side effects and to use the lowest nanoparticle concentration for later experiments.

3.8.5 Time-lapse monitoring of tandem (DNA, RNA, protein)

HeLa cells were incubated for 6 h with either 50 µL of DNA, RNA or protein loaded nanoparticles (CaP/PEI-Cy5/Biomolecule/CaP/PEI). The nanoparticles were removed, and cells were washed twice with PBS and re-cultivated in fresh media. Imaging positions were set according the signals for PEI-Cy5. The occurring fluorescence was monitored via fluorescence microscopy over 48 h. The results are depicted in Figure 3-72 to Figure 3-74. As the results show, cells took up the nanoparticles and expressed the protein in the case of DNA (Figure 3-72). Here, the first signal was observed 3 h after the removal, which is 9 h after nanoparticle treatment. This result correlates with work from colleagues.[8,45]

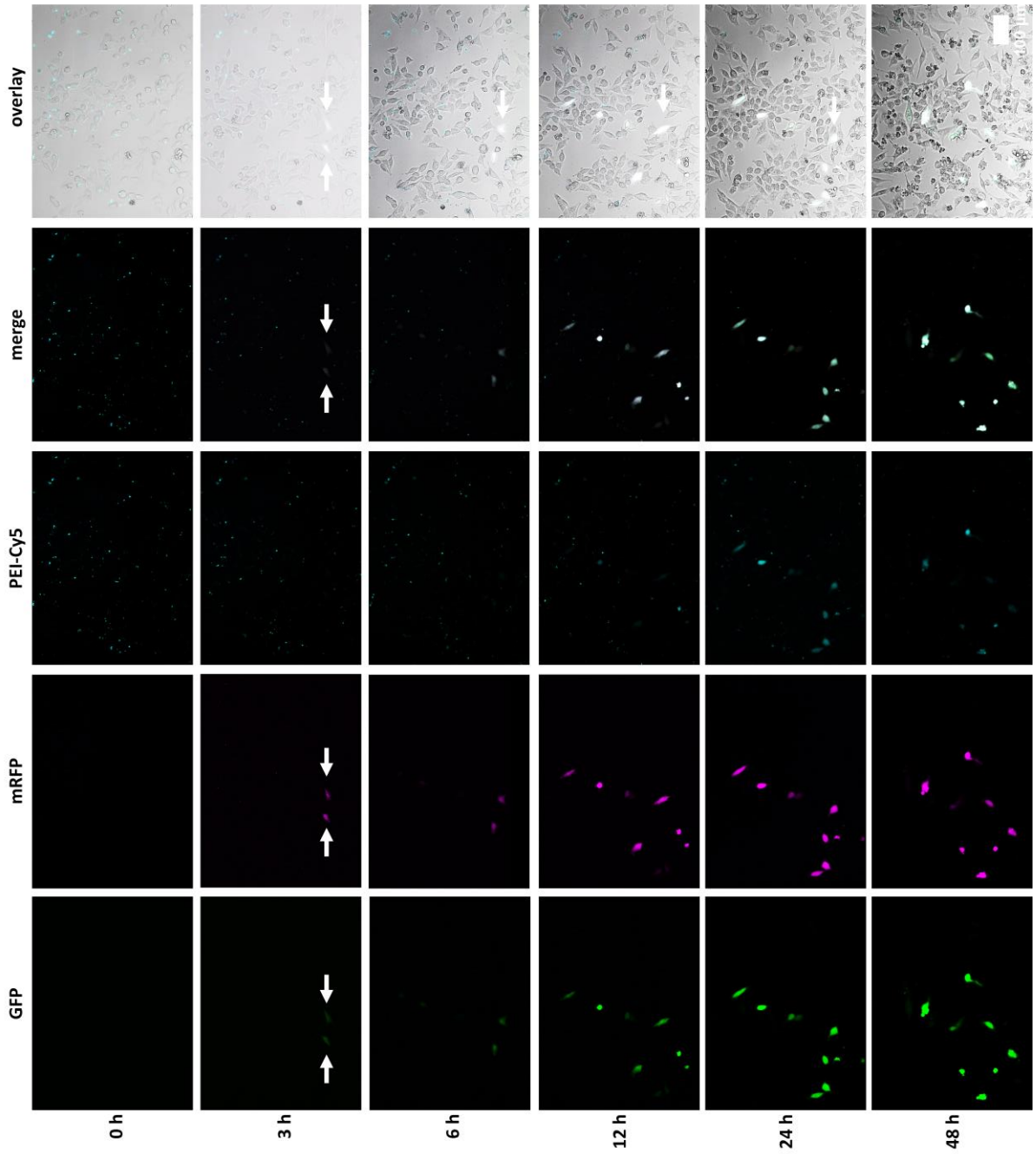

Figure 3-72: DNA transfection with CaP/PEI-Cy5/pcDNA3.3tandem/CaP/PEI.
Time-lapsed monitoring of nanoparticle-transported pcDNA3.3tandemn in HeLa cells. (Scale bar 100 µm, 20x).

The plasmid expressed protein shows a diffuse cytosolic distribution indicating a successful transfection and correct expression of the tandem protein. In contrast to the diffuse cytosolic distribution of the plasmid expressed protein, the protein alone showed right after the removal of the nanoparticles a punctual cytosolic distribution, indicating an entrapment inside lysosomal degrading vesicles (Figure 3-73). This is

further corroborated by the loss of fluorescence for both monomers while GFP loses its fluorescence within 24 h due to its pH sensitivity. mRFP kept its fluorescence over >24h and was completely degraded after 48 h.

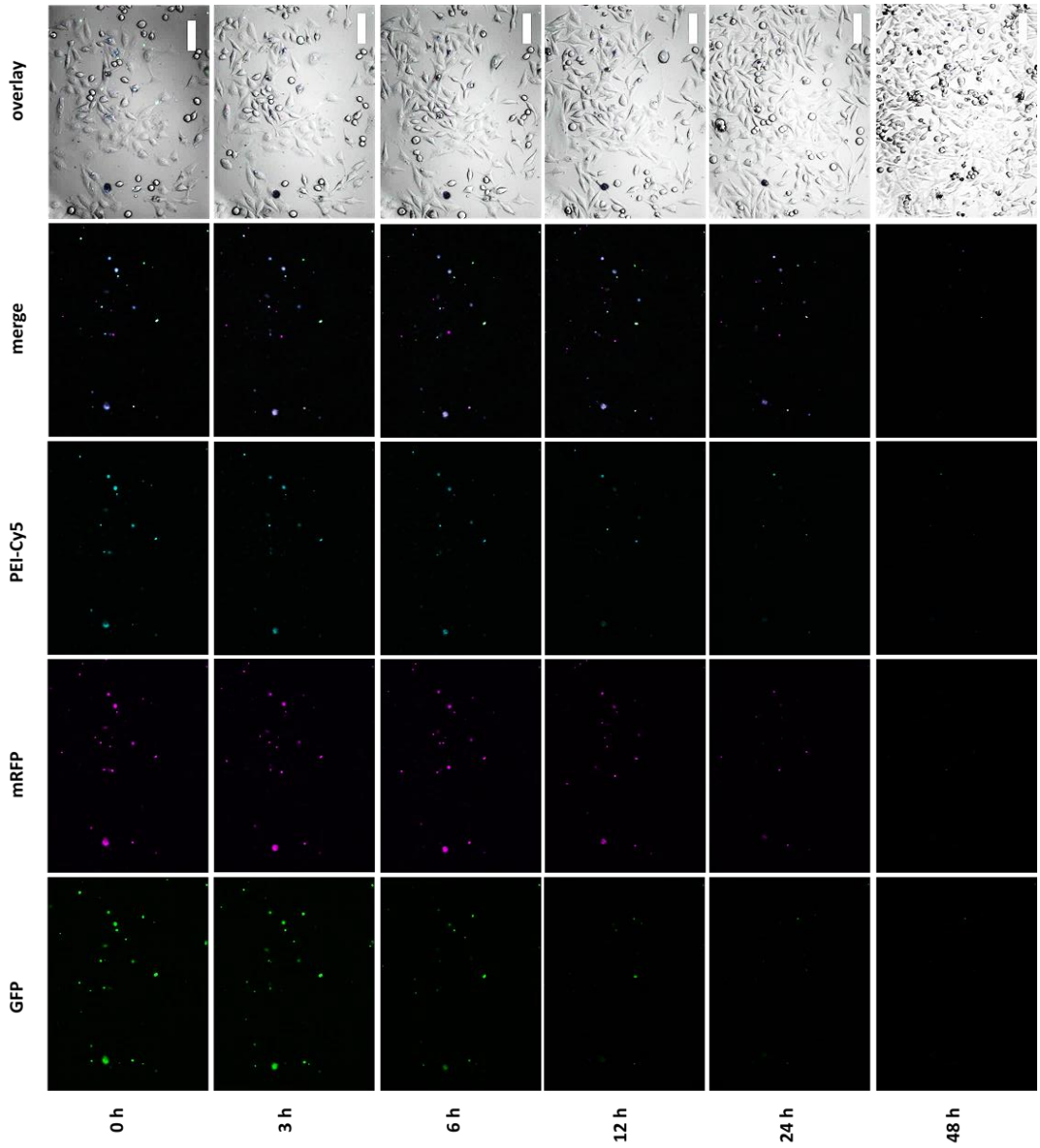

Figure 3-73: Protein transport into HeLa cells with CaP/PEI-Cy5/tandem/CaP/PEI.
Time-lapsed monitoring of nanoparticle-transported tandem protein in HeLa cells. (Scale bars 100 µm, 20x)

Surprisingly, in comparison to the DNA and protein-loaded nanoparticles, we could not observe any fluorescent signals for the RNA loaded calcium phosphate nanoparticles, even though the integrity of the mRNA was validated by a lipo-based

transfection (Figure 3-74). To validate this result, the experiment was repeated triple times, but showed the same result for the applied calcium phosphate nanoparticles.

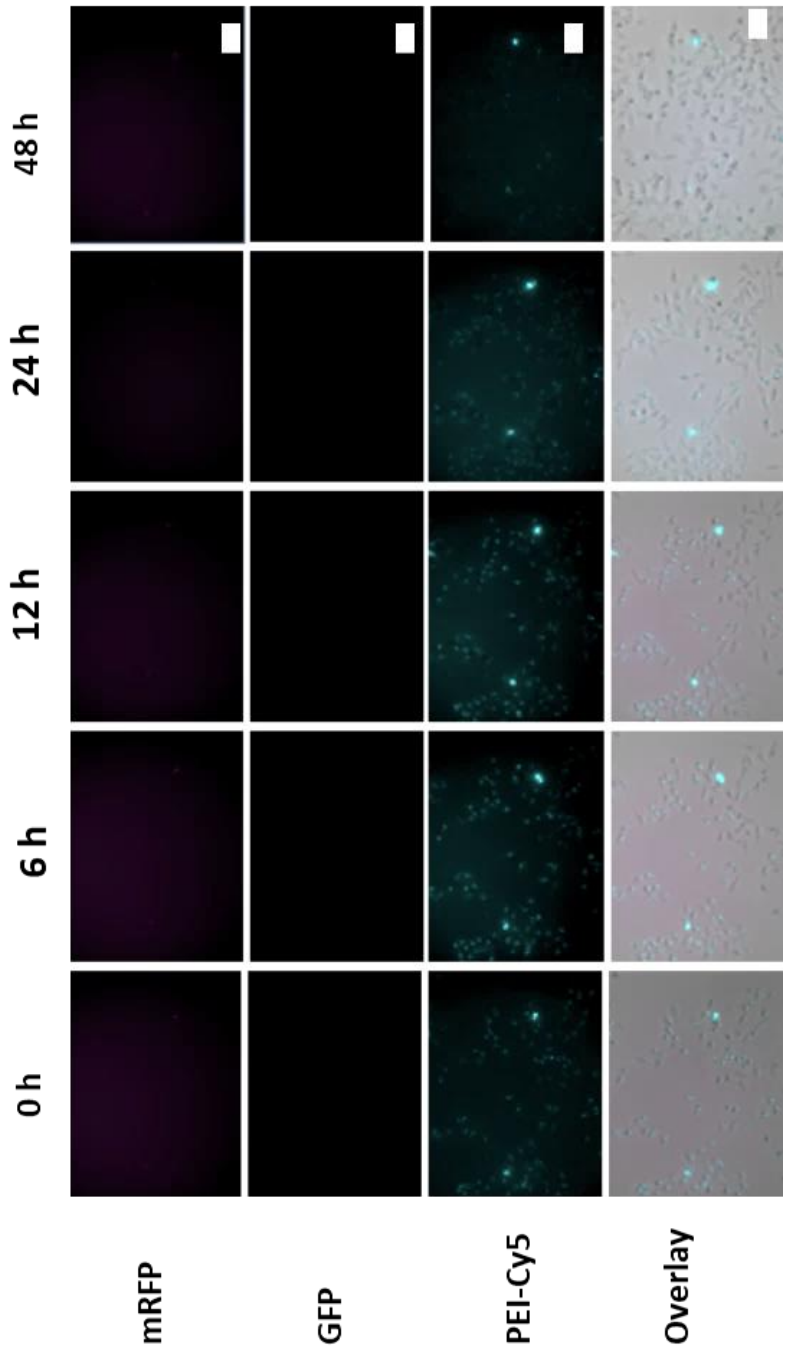

Figure 3-74: PolyA$^+$-tandem-mRNA transport into HeLa cells with CaP/PEI-Cy5/polyA$^+$-tandem-mRNA /CaP/PEI.
Time-lapsed monitoring of nanoparticle-transported tandem polyA$^+$tandem-mRNA in HeLa cells. (Scale bars 100 µm, 20x).

We assumed a premature degradation of the mRNA by ubiquitous RNases. Therefore, we decided to repeat this experiment with freshly prepared RNA. We compared the lipo-based transfection with the nanoparticle-mediated transfection in a time-lapsed manner for 24 h. For the nanoparticle-mediated transfection we received the same results as before (data not shown). Calcium phosphate nanoparticles were not able to transport the polyA^{+}-tandem mRNA inside the cytoplasm of HeLa cells. Since RNA is less stable than DNA due to the second hydroxy groups at the ribose moiety the RNA can be hydrolysed easily under alkaline conditions (pH >7).[264-266] Thereby, we assumed that most of the applied mRNA during the synthesis of calcium phosphate nanoparticles (synthesis is carried out at pH of 9), was hydrolysed and could not reach the cytoplasm of HeLa cells by the nanoparticle-mediated transport. Furthermore, due to the uptake mechanism of calcium phosphate nanoparticles, the encapsulated cargo is transported into lysosomes after the uptake via endocytosis.[46,267] Inside the lysosomes, the RNA could be degraded easily in the presence of the lysosomal nucleases.[268] This would also explain the low loading efficiency of 42% that was found for mRNA loaded nanoparticles (Figure 3-70). Therefore, this experiment might be repeated with another type of calcium phosphate nanoparticles that allows the loading of mRNA on the surface of calcium phosphate. Herein, RNA might be loaded on calcium phosphate nanoparticles after an intermediate centrifugation and redispersion step which would result in a less alkaline synthesis environment and ensure a less degree of mRNA degradation. However, lipofectamine 2000 transfection clearly shows that a transfection with the *in vitro* transcribed RNA is possible. In comparison to DNA and protein transport, the fluorescence signal from the RNA resulting tandem protein occurs within 3 h and 4 h treatment with the transfection agent. Herein, the transported mRNA is directly transported inside the cytosol and translated into the corresponding protein. This leads to a high increase of the transfection efficiency where almost every cell is transfected by the Lipofectamine 2000.

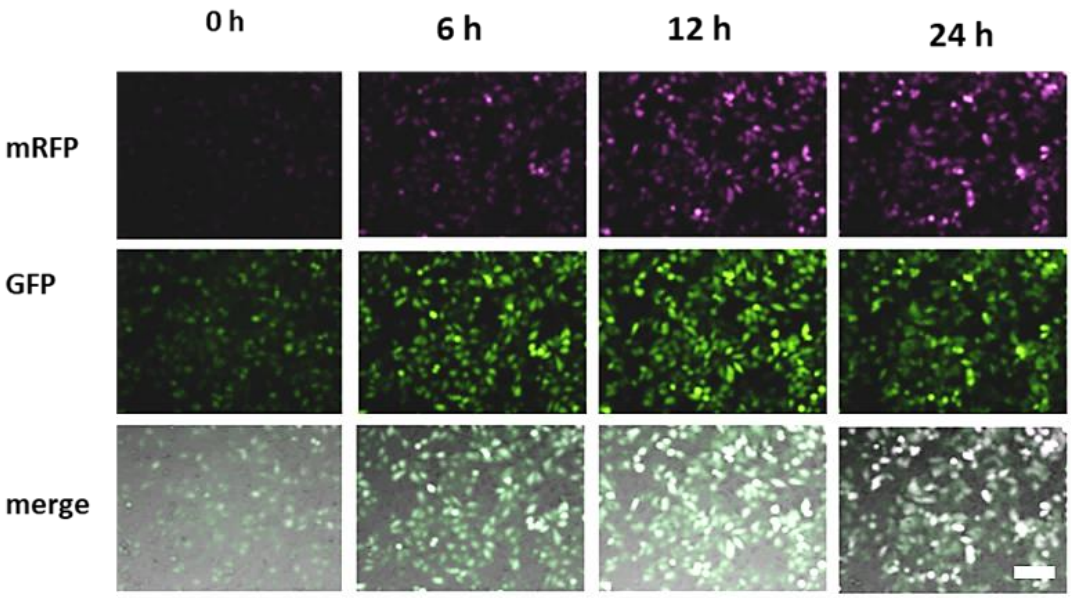

Figure 3-75: Lipofectamine 2000 transfection of polyA$^+$-tandem-mRNA.
Time-lapsed monitoring of polyA$^+$-tandem-mRNA transfected HeLa cells.

Next, the transfection efficiencies were compared to each other. The data in Figure 3-76 clearly demonstrates that the transfection with DNA increases over a period of time whereas the transported protein decreases. These results match with preliminary observation of the nanoparticle mediated transport of DNA and protein where the delivered DNA is expressed by cells after entering the nucleus and the protein is delivered inside lysosome and becomes slowly proteolytic degraded.[8,46] No nanoparticular transport was observed for the polyA$^+$-tandem-mRNA. The Lipofectamine 2000 transfection increases rapidly over time and reach a maximum at 80% (Figure 3-76) and then decreases slowly by time due to degrading proteases inside the cell.

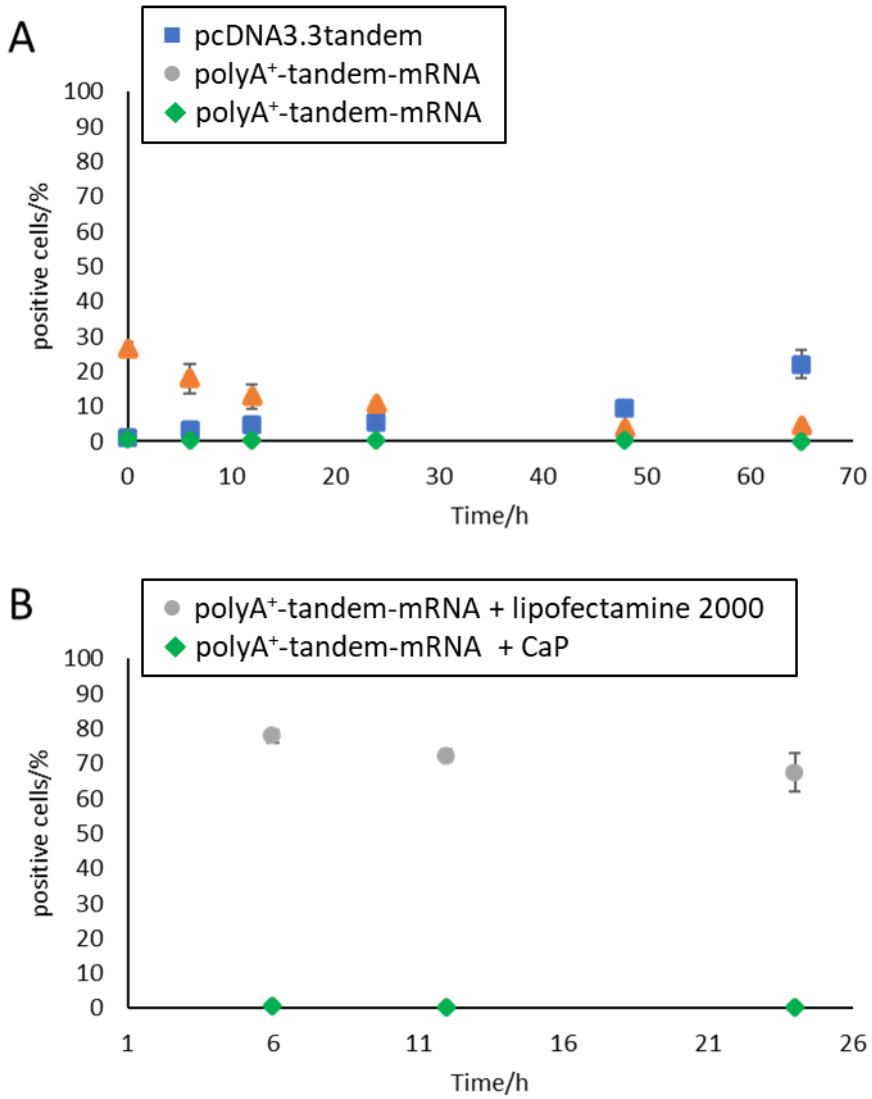

Figure 3-76: Transfection efficiencies of DNA, RNA and protein-loaded calcium phosphate nanoparticles compared to the Lipofectamine 2000 based transfection.
A: Nanoparticle mediated transport. Transported tandem protein is continuously degrading inside the cell (orange), while pcDNA3.3tandem successfully reached the nucleus and initiated the protein expression indicated by the increasing number of tandem protein expressing cells (blue). No transport was observed for the RNA-loaded nanoparticles. B: Lipofectamine 2000-based mRNA transfection (grey) compared to nanoparticle-mediated mRNA transfection (green). Herein, cells were distinguished manually by eye in positive and negative signals through the occurring fluorescence signals.

3.8.6 Summary

The results point out that the efficiency of nanoparticle-mediated biomolecule transport can differ from biomolecule to biomolecule. Here, we described the synthesis and full colloidal characterisation of tandem DNA, RNA and protein loaded calcium phosphate nanoparticles. Tandem-mRNA loaded and PEI-Cy5 stabilised nanoparticles could not be transported due to the alkaline synthesis procedure to obtain calcium phosphate nanoparticles, but the mRNA remained intact when Lipofectamine 2000 was used as transfection agent. Therefore, the nanoparticle-mediated transport could be successfully shown for the tandem protein and DNA.

3.9 Delivery of the auto-fluorescent protein R-phycoerythrin by calcium phosphate nanoparticles into four different eukaryotic cell lines

This work was a cooperative project between the groups of Prof. Meyer and Prof. Epple at the University of Essen.

The bio-distribution and -availability of intact therapeutic proteins like insulin for example, plays a crucial role for patients with *diabetes mellitus* I and II. Though, insulin is a well-known therapeutically used and broadly available protein, where patients take their daily individual dose easily by the injection of an automated insulin pump. Other relevant therapeutic proteins may not be so easily distributed by a simple injection into the human blood stream. However, in the end proteinogenic therapeutics must reach their final target location inside or on the cell to fulfil their function. In many cases, the nanotechnology has proven its applicability transporting even membrane-impermeable proteins into the cell.[269-271] Beside an effective transport of the therapeutic protein, it is also important to know its cellular fate. Many proteins can be well transported into a cell with the help of nanoparticles, but partially end in cellular lysosomes, where the acidic environment and proteases hamper the protein function by degradation, preventing the fulfilment of its therapeutic effect. Studying these processes *in vitro* can elucidate how much of a therapeutic protein may have to be administered. Despite the well-studied uptake mechanisms of nanoparticles by endocytosis, the fact that every cell type is comprised of an individual membrane composition and different numbers of membrane associated, bound and percolated functional proteins, the uptake mechanism can immensely differ from cell type to cell type. Thus, following the uptake process requires a reporting agent, usually a chemically introduced fluorophore, to track the protein of interest. The chemical attachment of such a fluorophore is indeed scientifically well accepted, but the attached dye gives less to no information about its structural or functional integrity. Herein, we decided to investigate the uptake of the red fluorescent phycoerythrin (R-PE) from the phycoerythrobilin protein family for its structural and functional integrity. R-PE from the *Rhodomas spec.* is a 240 kDa multimeric protein comprising several disk-like subunits with up to 10 phycoerythrobilin chromophores. These are bound on the

surface of the protein and complexed by hydrogen bonds and hydrophobic interactions and give the protein its fluorescence (Figure 3-77).[272] Its subunits have an isoelectric point in the range of 4.9 and 5.7, though it is predominantly negatively charged in water at a neutral pH of 7.[273] R-PE is widely used as a reporter protein in immunoassays like fluorescence-assisted cell sorting (FACS) and enzyme-linked immunosorbent assay (ELISA), flow cytometry, multimer/tetramer applications, or conjugate labelling chemistry and Förster resonance energy transfer (FRET)-based assays.[274-278]

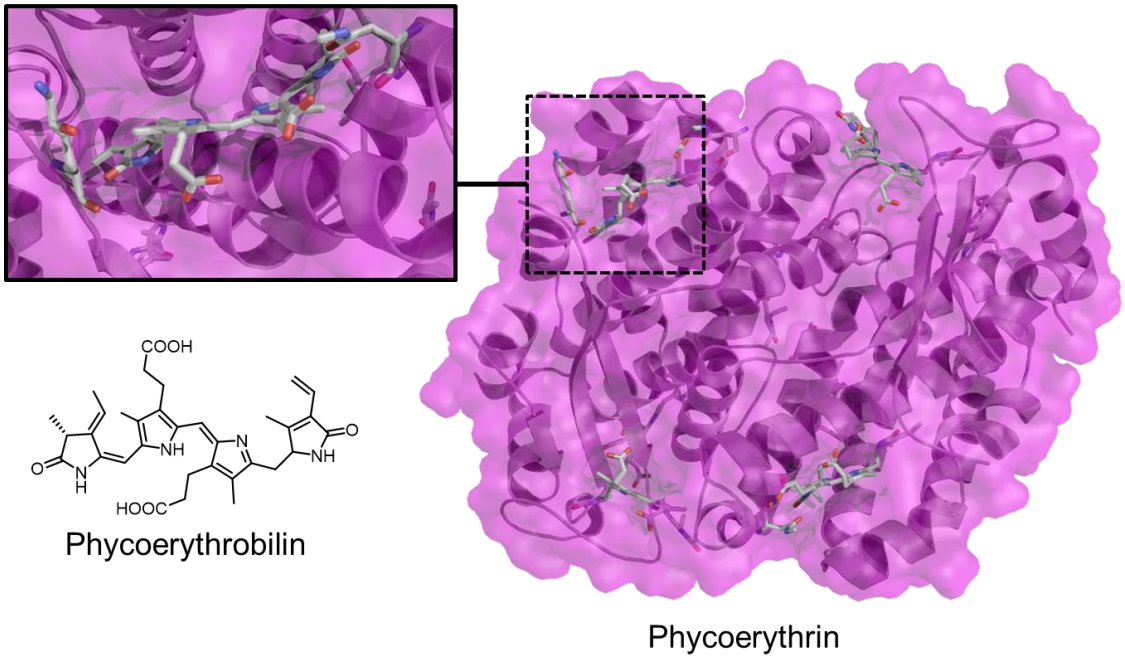

Figure 3-77: 3D Model of the phycoerythrobilin protein Phycoerythrin.
Multimeric disk-like shaped R-PE consists of several α-Helices and few β-sheets, 10 phycoerythrobillin chromophores are responsible for its fluorescence and are bound by hydrogen bonds and hydrophobic interactions (PDB: 1XG0).

Furthermore, R-PE is known to produce a singlet oxygen after radiation and has a potential application as a photosensitizer in photodynamic therapy (PDT).[279] Moreover, it was also shown to be toxic for some cell lines by inducing apoptosis through arresting the cell cycle in the S phase.[279-281]

The fluorogenic characteristics of the protein, with excitation bands of $\lambda_{exc.}$ = 499, 565 nm and a shoulder at 545 nm and emission at $\lambda_{em.}$ = 575 nm, were

used to track the protein alone or together with the nanoparticles during the uptake study (Figure 3-78).

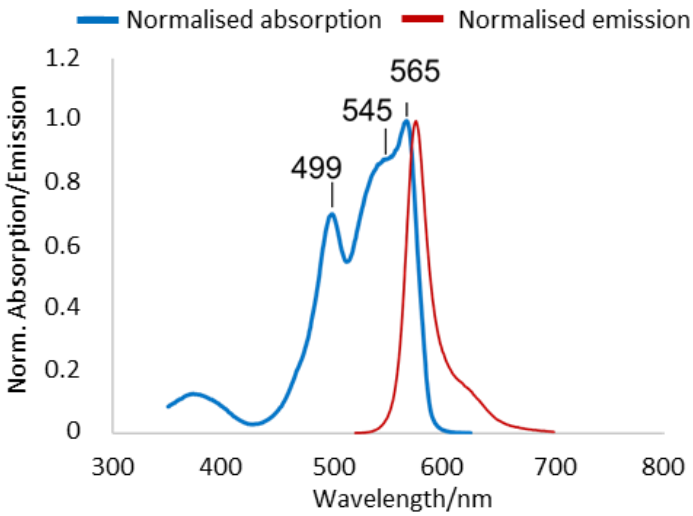

Figure 3-78: Normalised spectra of R-PE.
R-PE shows some excitation bands at $\lambda_{exc.}$ = 499, 565 nm and a shoulder at 545 nm and emits its fluorescence at $\lambda_{em.}$ = 575 nm. (100 mM sodium phosphate, 1 mM EDTA, 0.02% sodium azide, pH 7.00).[282]

The fluorescence should also serve as a reporter for the possible degradation or damage of its functional integrity during the uptake passing cellular compartments. By this approach, the nanoparticular uptake of the R-PE was studied in four different cell lines: HeLa, MG-63, MC3T3-E1 and HEK293T.

3.9.1 Synthesis and characterisation of R-PE loaded calcium phosphate nanoparticles (CaP/PEI/R-PE)

All used inorganic salts were of per analytical (p.a.) quality. Aqueous solutions of the inorganic salts were prepared with ultrapure water (Purelab ultra instrument from ELGA). For the synthesis of calcium phosphate/polyethyleneimine/R-phycoerythrin (CaP/PEI/R-PE) nanoparticles, aqueous solutions of calcium nitrate (6.25 mM, pH 9; Merck, p.a.) and diammonium hydrogen phosphate (3.74 mM, pH 9; Merck, p.a. grade) were rapidly mixed by pipetting equal volumes into a microcentrifuge tube followed by briefly vortexing and transferring 1 mL of the nascent dispersion into a second tube with 0.2 mL of a polyethyleneimine solution (PEI; Sigma-Aldrich, *MW* 25 kDa; 2 mg mL^{-1}). The mixture was rapidly vortexed to achieve the colloidal stability. The positive zeta potential (+30.3 mV) of the formed CaP/PEI nanoparticles indicates a successful colloidal stabilisation by PEI. Then, equal volumes of the nanoparticle dispersion and the R-PE (1 mg mL^{-1}) were mixed under thorough vortexing. Non-adsorbed protein molecules and dissolved counter ions were removed by centrifugation (21,000 g; 30 min; 4 °C) and subsequent redispersion of 1 mL water with a sonotrode (Hielscher UP50H; sonotrode MS3; cycle 0.8, amplitude 60%, 30 s). R-PE from Rhodomonas was obtained from Molecular Probes by LifeTechnologies™ (Eugene, Oregon, USA), and was used as a dilution from 4 mg mL^{-1} in ammonium sulphate/potassium phosphate buffer at pH 7.0 to 1 mg mL^{-1} with ultrapure water. The following table shows the obtain results by SEM, DLS, UV/Vis and AAS (Figure 3-79).

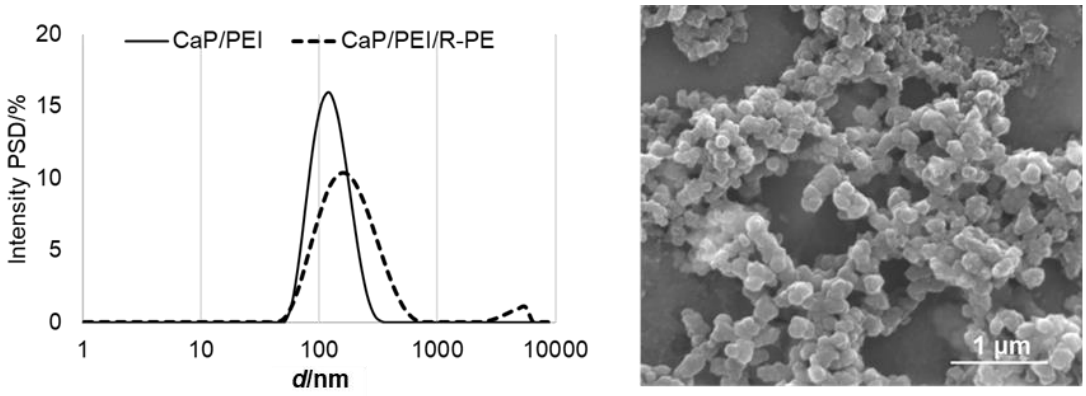

Sample	DLS *d*/nm	PDI	ζ/mV	SEM *d*/nm
CaP/PEI	116±2	0.111	30±1	78±15
CaP/PEI/R-PE	150±4	0.294	-21±1	150±3

Figure 3-79: Characterisation of R-PE loaded calcium phosphate nanoparticles by DLS and SEM.
The R-PE-loaded and non-loaded calcium phosphate nanoparticles showed good colloidally stability regarding their zeta potentials (-21 mV or 31 mV) and showed only a small degree of agglomeration concerning the DLS results. SEM micrograph shows a representative image of R-PE loaded calcium phosphate nanoparticles (SEM micrograph results for the R-PE loaded calcium phosphate nanoparticles were taken from Dr. Olga Rotan)

The particle diameter was determined by scanning electron microscopy with 150 nm (Figure 3-79). Nanoparticles were composed of calcium phosphate which was proved through the presence of calcium, phosphate, and oxygen by energy-dispersive X-ray spectrometry (EDX), recorded on SEM images. The particles are X-ray amorphous, but we have found crystalline domains in similar calcium phosphate nanoparticles by high-resolution transmission electron microscopy in an earlier study.[283]

The resulting dispersion CaP/PEI/R-PE showed a moderate colloidal stability with a zeta potential of –21 mV and a PDI of 0.294. Compared to non-loaded calcium phosphate nanoparticles the size was increased 2-fold concerning the SEM micrograph results, indicating an adsorption by the negatively charged R-PE.[273] The determination of the calcium concentration was carried out by AAS, revealing a concentration of 5.0 µg mL^{-1} of Ca^{2+}. In combination with an assumed stoichiometry of hydroxyapatite, $Ca_5(PO_4)_3OH$, spherical particles with a radius from SEM of 75 nm, and the density of hydroxyapatite ($3.14 \cdot 10^3$ kg m^{-3}), which corresponds to a particle

concentration of $2.27 \cdot 10^9$ particles mL^{-1}, computing the values in the table below. (Table 3-27).

Table 3-24: Characteristics of the CaP/PEI/R-PE dispersion.

Characteristics of the CaP/PEI/R-PE dispersion	Value
Density of hydroxyapatite	$3.14 \cdot 10^3$ kg m^{-3}
Number of particles in one mL	$2.27 \cdot 10^9$ particles mL^{-1}
Concentration of HAP	12.6 µg mL^{-1}
Volume of one particle	$1.77 \cdot 10^{-21}$ m^3
Weight of one particles	$5.54 \cdot 10^{-18}$ kg
R-PE on dispersed particles	443 µg mL^{-1} | 90% yield
R-PE molecules per one particle	$4.9 \cdot 10^5$ RPE
(with $MW_{R\text{-}PE}$ =$2.4 \cdot 10^2$ kg mol^{-1}; $m_{R\text{-}PE}$ = $3.99 \cdot 10^{-16}$ kg)	
R-PE molecules per mL dispersion	$1.11 \cdot 10^{15}$
Surface area of each nanoparticle	$7.07 \cdot 10^{-14}$ m^2
Occupation of one R-PE molecule per nm^2	0.14 nm^2

The high loading of R-PE is explained due to the negatively charged surface of the protein itself at pH 7.0, though the attracting negative and positive forces of protein and colloidal stabiliser, PEI, exceed a protein monolayer, which explains the increased hydrodynamic radius by DLS measurement. Furthermore, the protein was nearly fully adsorbed on the surface of the PEI-stabilised calcium phosphate nanoparticles which can possibly be explained by the incorporation of the protein through the polyelectrolyte, leading to a small degree of colloidal destabilisation. This is also reflecting the increased PDI of the dispersion. This dispersion of CaP/PEI/R-PE was used for all uptake experiments.[46]

3.9.2 Uptake of R-PE loaded calcium phosphate nanoparticles into four different cell lines

For the uptake studies HeLa, HEK293T, MG-63, and MC3T3 cells were either incubated with the R-PE-loaded nanoparticles or with the dissolved protein alone at the same protein concentration for 3 and 6 h. As it is shown in the following figures, R-PE was strongly taken up with the help of the calcium phosphate nanoparticles with an increasing amount from 3 to 6 h. The dissolved R-PE was not taken up at all, indicating an inability to cross the cell-membrane on its own which corroborates with earlier results concerning the calcium phosphate mediated transport of biomolecules.[52,284-286] Interestingly, the dissolved R-PE treated cells showed some morphological changes after 3 and 6 h. Affected cells were decreased in size and appears as round shaped cells which indicates a cytotoxic effect by the dissolved R-PE (Figure 3-80). This correlates with the fact that dissolved R-PE is toxic for some cell lines.[281]

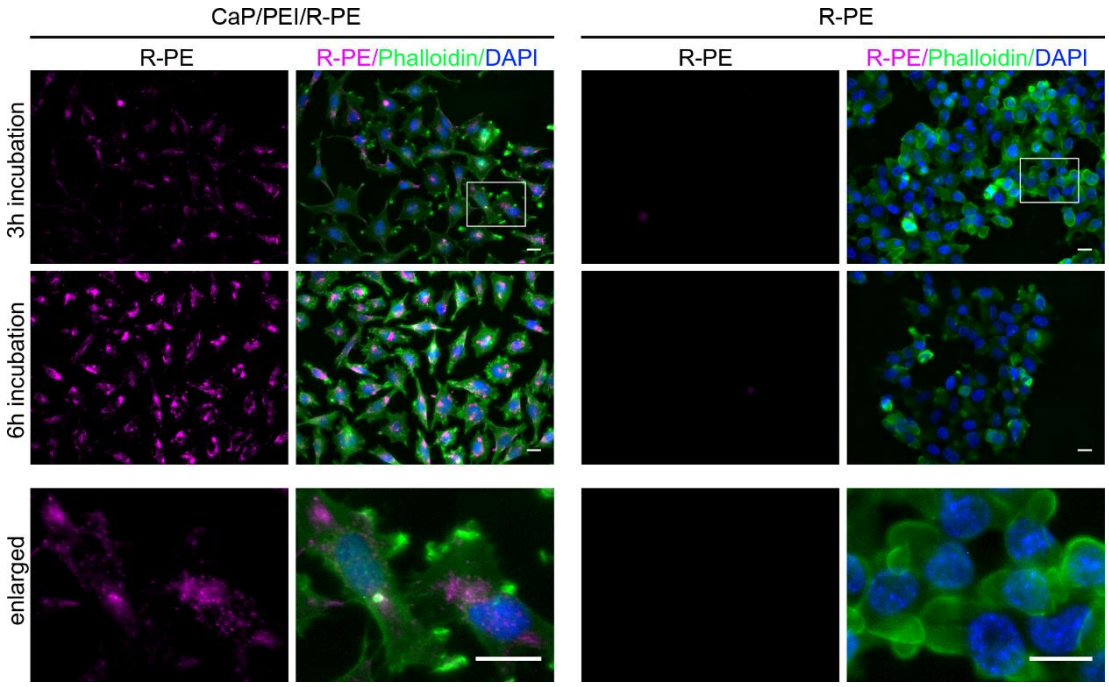

Figure 3-80: Loading in nanoparticles enables R-PE to enter cells.
HeLa cells were incubated with R-PE-loaded nanoparticles (CaP/PEI/R-PE) or dissolved R-PE for 3 h (top row) or 6 h (center row). Cells were fixed and stained with phalloidin (green; actin filaments) and DAPI (blue; nucleus). Bottom row: Magnification of the upper images (white boxes; top row): 3 h incubation R-PE/Phalloidin/DAPI for CaP/PEI/R-PE nanoparticles (left) and 3 h incubation R-PE/Phalloidin/DAPI for R-PE alone (right). All scale bars are 20 µm.

In contrast to the dissolved protein-treated cells, R-PE loaded calcium phosphate nanoparticles seemed to show no influences on cell viability. Cells kept a viable morphology. Components of the nanoparticles, including calcium and PEI might have some adverse effects on cell viability. Since calcium ions are known to act as second messengers in the signal transduction of cells and are involved in the regulation of apoptosis. A toxic effect due to an excess of calcium ions would be expected, but none of the potential adverse effects were observed.[287-289] This might be explained by a very low dose, that was finally used in the well (about 1.1 µg L^{-1} calcium). The low concentration seemed to be manageable for the cells. The concentration of polyethyleneimine, which indeed has a known cytotoxic impact on cells, cannot directly be determined and was estimated to about 0.1 µg mL^{-1}. Based on earlier quantitative analyses of polymer-coated nanoparticle it is known that this PEI concentration is a non-cytotoxic and unharmful for the cells, and correlates with other observations.[290-292] In contrast, MG-63 and MC3T3 cells were less sensitive to R-PE (data not shown). Herein, a viability assay was not conducted since our major focus of this study was the uptake analysis of the R-PE by calcium phosphate nanoparticles and its subsequent fate in the cell. The intracellular localisation of R-PE was analysed by using confocal laser scanning microscopy (CLSM) through lysosomal, lysosome-associated membrane protein 1 (Lamp1), and early endosomal, early endosome-associated protein 1 (EEA1), recognising antibodies. After 6 h of incubation and subsequent immunostaining images were recorded (Figure 3-80). The data show, R-PE-loaded nanoparticles did not change the overall pattern of the endo-lysosomal system compared to untreated cells (Figure 3-81A) and R-PE molecules were distributing both types of early endo- and lysosomal vesicles (Figure 3-81B). These results are consistent to earlier observations and support that calcium phosphate nanoparticles are engulfed by endocytosis and proceed over the degradative endosomal-lysosomal pathway.[293]

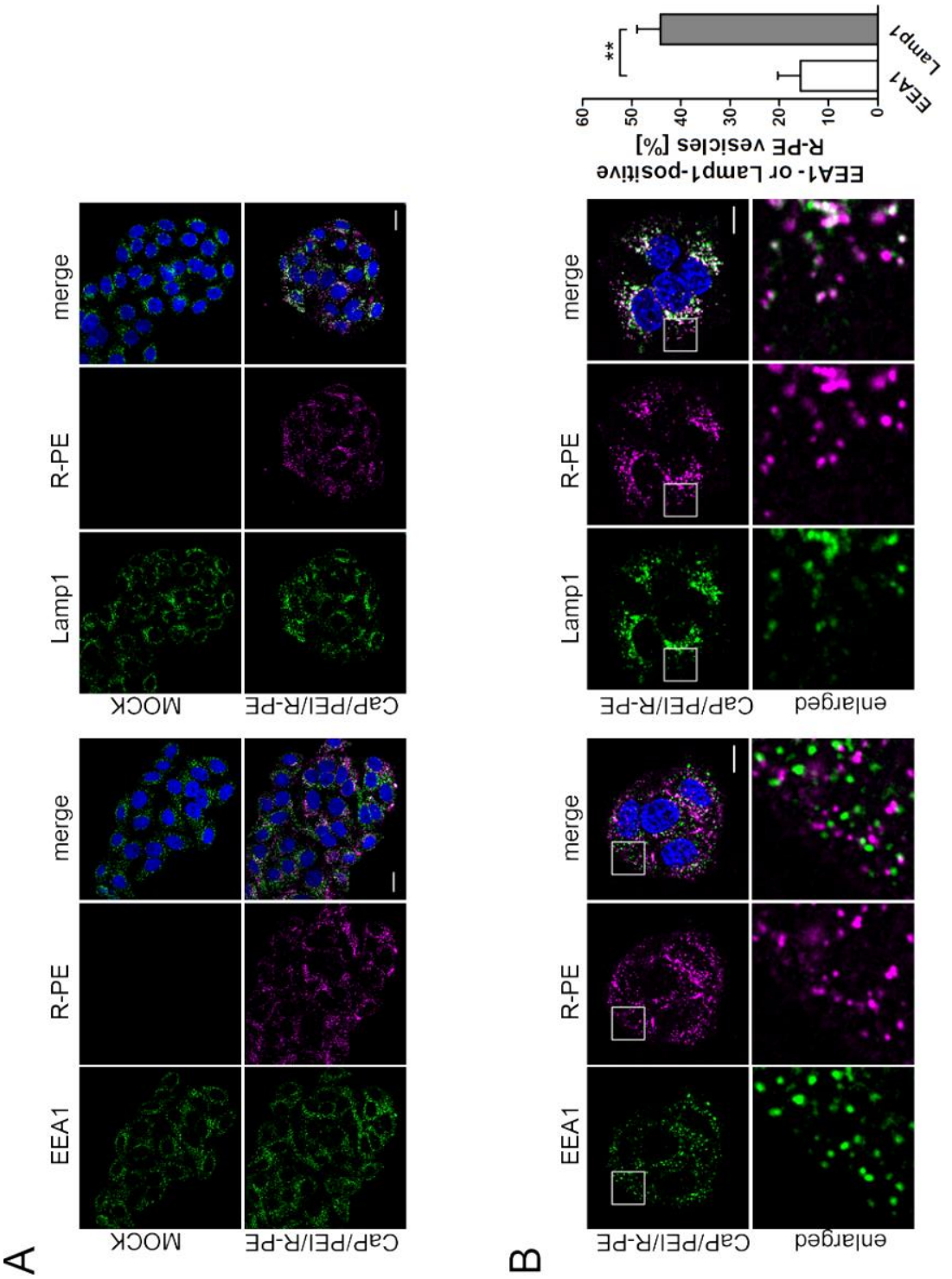

Figure 3-81: CaP/PEI/R-PE nanoparticles enter HeLa cells and co-localise with early endosomes and lysosomes.

A: Confocal laser scanning microscopy on HeLa cells after 6 h of incubation with either CaP/PEI/R-PE nanoparticles or untreated, followed by washing with PBS, fixation and staining with EEA1 (green), Lamp1 (green) and Hoechst33342 (blue). The overall pattern of early endosomes or lysosomes is not affected by incubation with CaP/PEI/R-PE nanoparticles. Scale bar, 20 µm. B: High resolution images to analyse the co-localisation of R-PE with EEA1 or Lamp1. HeLa cells were treated and processed as in (A). An enlargement of the boxed area is shown. Diagram on the right: Quantification of R-PE vesicles showing EAA1 or Lamp1 positive vesicles. Data represent mean ± SD from three independent experiments (student's t-test).**, $p<0.01$. Scale bar 10 µm.

The data of the quantitative analysis of the confocal images demonstrates that about 15% of the R-PE vesicles colocalised with EEA1, whereas about 45% of the R-PE concurred with the signal for the Lamp1 localisation. (Figure 3-81B). It is well accepted that the usual processing of an engulfed cargo from endosome to lysosome can be facilitated within a few minutes up to 3 h. Since in total not all the R-PE amount was co-localised in early endosomes or lysosomes in HeLa cells, which might be explained by slight proteolytic degradation of R-PE during and after the uptake of the protein but can be explained by a different vesicular intermediate localisation that has not been addressed in this study. However, EEA1 and Lamp1 represent only two of possible vesicular intermediate structure associated and endocytic processing involved proteins. Proteins such as the vesicular associated membrane proteins (VAMP-3, -4, -5, -7 and 8), the adaptor protein, phosphotyrosine interacting with PH domain and the leucine zipper 1 (APPL1) or the syntaxin 6 (STX) can also be addressed by immuno-fluorescence.[294-297] Here, we decided to choose anti-EEA1 and anti-Lamp1 as representative probes of an early and middle stage of intracellular vesicle processing. R-PE was concentrated to early endosomal- and lysosomal-vesicular structures and was not widely distributed inside the cytoplasm which is usual for a gene transfected cell with a fluorescent protein (similar to the results of chapter 3.8). In all cases, where R-PE was given without nanoparticles to the cells, no or only non-significant amounts of R-PE were found in the cell, indicating that R-PE is unable to enter the cell on its own. Therefore, R-PE loaded nanoparticles are suggested to be a suitable carrier for the transport of R-PE into HeLa cells. We investigated a possible release of R-PE into the cytoplasm from lysosomes, suggesting that some of the R-PE is transported at later time points, from 6 h to up to 20 h. Depending on a given Bafilomycin A1 (BafA1) concentration, which is a specific inhibitor of vacuolar-type H+-ATPase that inhibits the acidification and protein degradation in lysosomes of cultured cells, we monitor comparably the fate of R-PE in treated or untreated cells by live cell imaging. [46,298] For this purpose, after 6 h of incubation with R-PE-loaded calcium phosphate nanoparticles, we removed the nanoparticles by washing the cells with DBPS and re-cultivated them with 100 nM BafA1 or without any additive in nanoparticle-free medium. For non-treated cells, we observed that the intrinsic red fluorescence of R-PE was vanishing over time,

indicating a continuous lysosomal degradation of R-PE where R-PE did not escape from the lysosome into the cytoplasm.

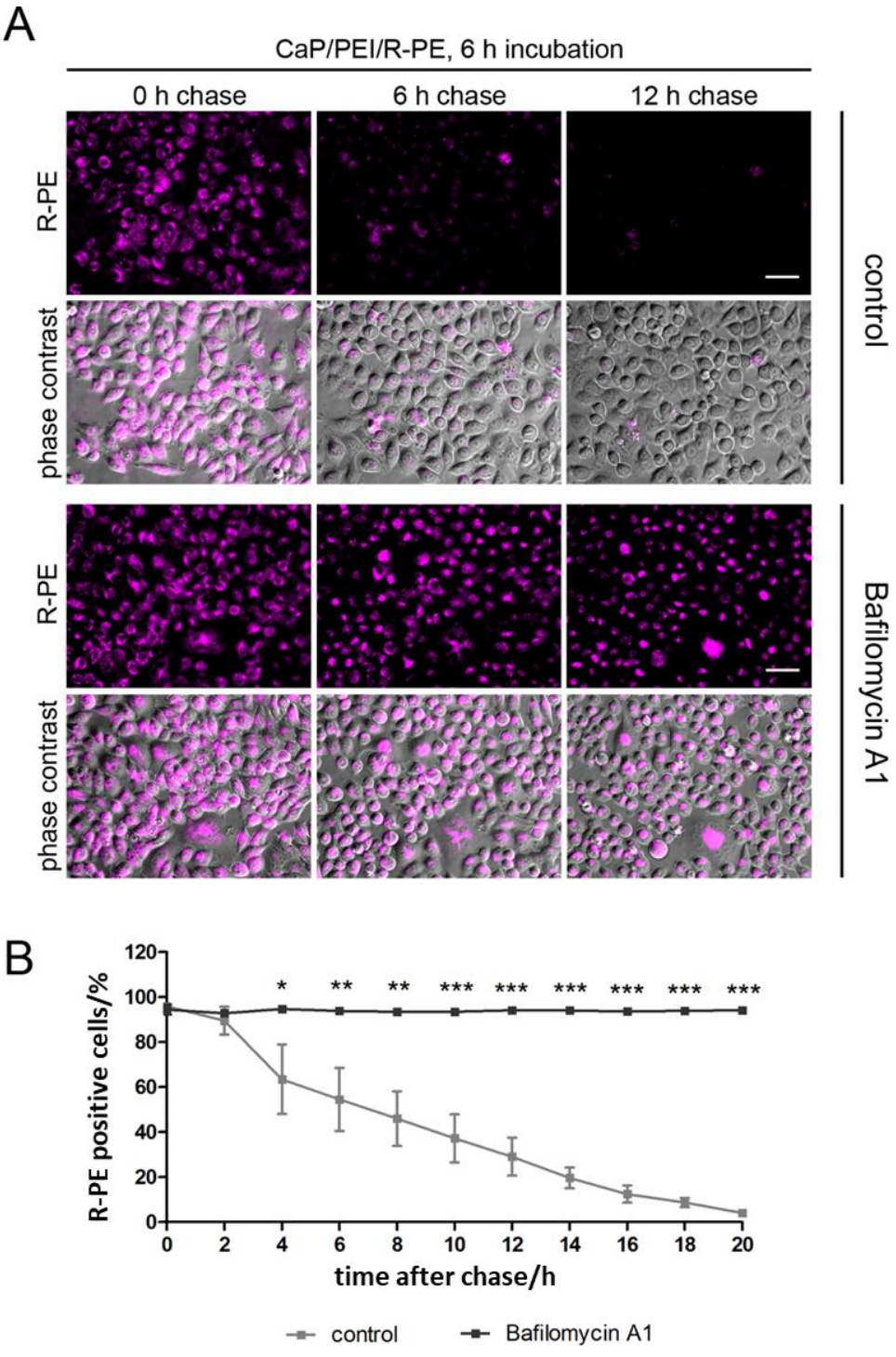

Figure 3-82: R-PE is degraded in lysosomes after nanoparticle-mediated uptake into HeLa cells.
A: After 6 h of incubation with CaP/PEI/R-PE nanoparticles, HeLa cells were washed and chased for up to 20 h. The fluorescence signal of R-PE (magenta) persists after inhibition of lysosomal degradation by BafA1 and vanishes without any treatment (control). The R-PE signal is shown alone or merged with phase contrast to visualise the cells. Scale bar 50 µm. B: Quantification of R-PE positive cells from three independent experiments. Data represent mean ± SD (student's t-test). *, $p<0.05$, **, $p<0.01$, ***, $p<0.001$.

This is corroborated by the fact that we could not observe a clear, diffuse cytoplasmic distribution of R-PE during the whole experiment (Figure 3-82). For treated cells, we observed a preserving intrinsic fluorescence of R-PE during the whole observation time in vesicular structures, which is indeed an indication for the proteolytic degradation of the protein.

To have proof of our results, we further analysed other cell lines, including human epidermal kidney cells (HEK293T), human osteosarcoma cells (MG-63), and mouse osteoblastic preosteoblasts from the calvaria (MC3T3). The cell lines were treated and incubated under the same conditions. In all cases, calcium phosphate nanoparticles could transport the R-PE into all of four cell lines and the lysosomal proteolytic degradation of R-PE was inhibited by BafA1 (Figures 3.83-85). R-PE was not completely degraded in HEK293T cells and MG-63 cells, indicating a less proteolytic activity of these cells. On the contrary, a comparable rapid degradation of R-PE was observed in MC3T3 cells within 6 h (compare HeLa cells).

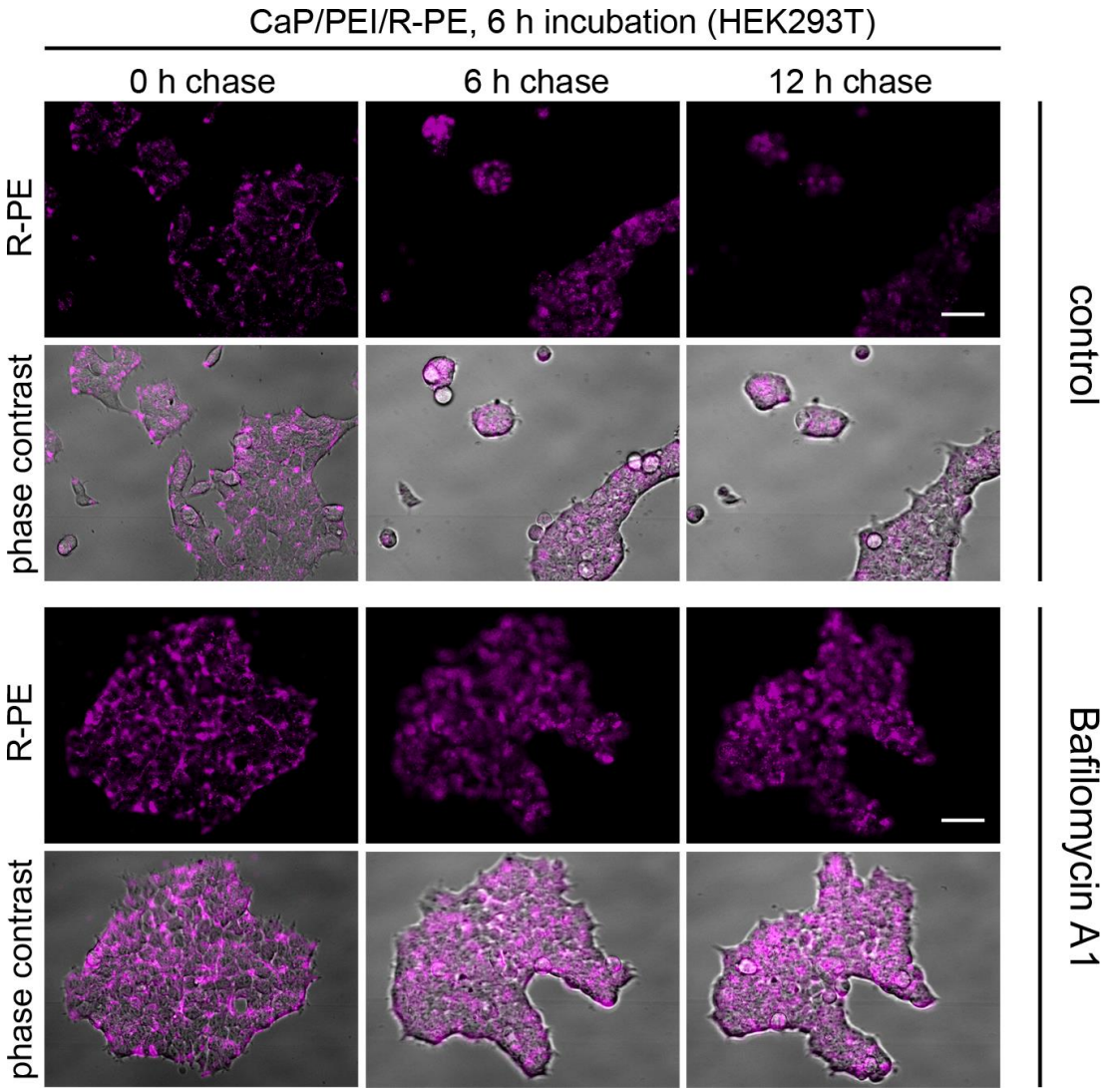

Figure 3-83: R-PE is not degraded in lysosomes after nanoparticle-mediated uptake into HEK293T cells.
After 6 h of incubation with CaP/PEI/R-PE nanoparticles, HEK293T cells were washed and chased to the comparable timepoint for up to 12 h. The fluorescence signal of R-PE (magenta) persists after inhibition of lysosomal degradation by BafA1 and without any treatment (control). The R-PE signal is shown alone or merged with phase contrast to visualise the cells. Scale bar 50 µm.

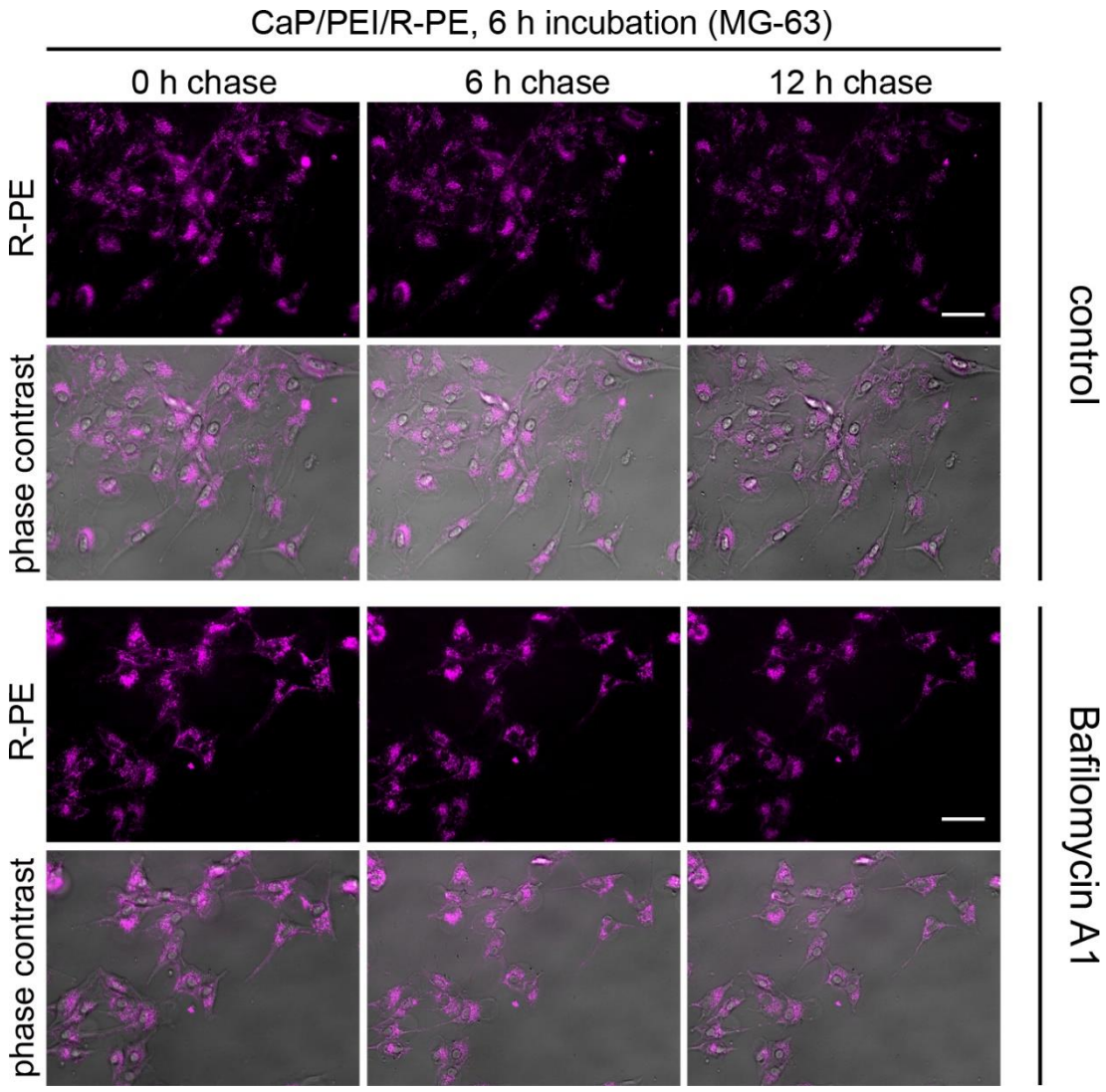

Figure 3-84: R-PE nanoparticles are not degraded in lysosomes after nanoparticle-mediated uptake into MG-63 cells.
After 6 h of incubation with CaP/PEI/R-PE nanoparticles, MG-63 cells were washed and chased to the comparable timepoint for up to 12 h. The fluorescence signal of R-PE (magenta) persists after the inhibition with BafA1 and without any treatment (control). The R-PE signal is shown alone or merged with phase contrast to visualise the cells. Scale bar 50 µm.

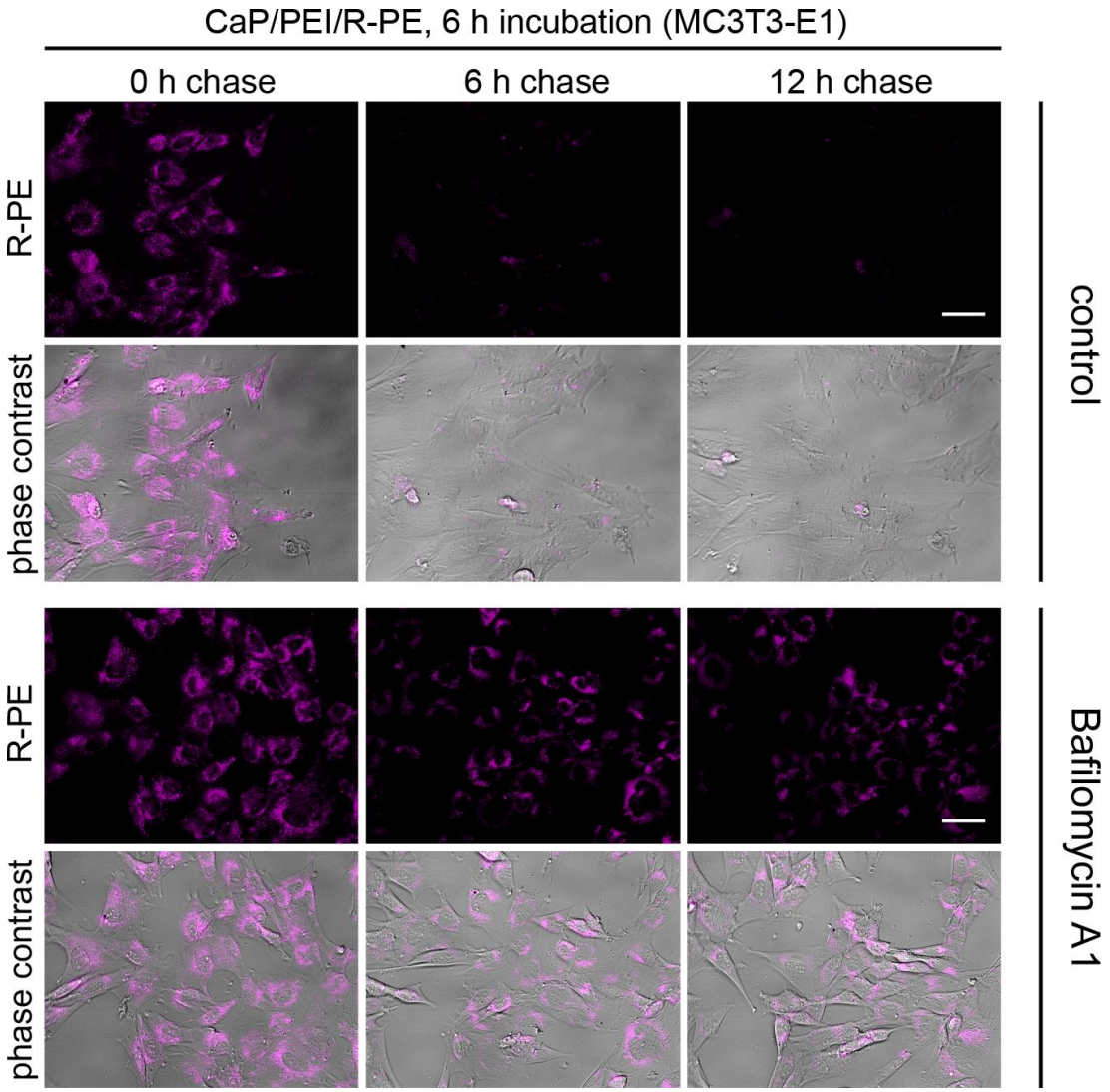

Figure 3-85: R-PE nanoparticles are degraded in lysosomes after nanoparticle-mediated uptake into MC3T3 cells.
After 6 h of incubation with CaP/PEI/R-PE nanoparticles, MG-63 cells were washed and chased to the comparable timepoint for up to 12 h. The fluorescence signal of R-PE (magenta) persists after the inhibition with BafA1 and without any treatment (control). The R-PE signal is shown alone or merged with phase contrast to visualise the cells. Scale bar 50 µm. (Image editing were carried out by Dr. Schulze)

These results show that the delivery of proteins can be facilitated with the help of calcium phosphate nanoparticles. The nanoparticle-mediated transport of proteins or other therapeutic relevant molecules, such as DNA, vaccines or anti-cancer drugs across the cell membrane is still a challenging hurdle and a major goal of nanomedicine.[269,284,299,300] In gene therapy, immunology or tumour therapy, nanotechnology is widely exploited to transport these molecules.[10,301-304] Thus, the structural and functional integrity of these drugs must be assured to preserve the

therapeutic function which works for most of the above mentioned branches of science. The main route of intracellular transport of these drugs goes from endocytosis over early endosomes to degrading lysosomes. An untimely release into the cytoplasm, by the escape of the early endosome is mostly desired to address intracellular receptors or the nucleus of a cell. Nanoparticles can be equipped with early endosome escaping molecules, such as viral peptides, or polycations e.g. PEI.[305,306] Especially PEI has been discussed to facilitate an endosomal escape via the "proton-sponge effect".[307-309] Herein, PEI (pKa ~7) causes a high pH in the endosomes and induces a high proton influx by membrane bound ATPase proton pumps which actively translocate protons into endosomes to compensate the increasing alkaline environment. PEI buffers all inflowing protons and resists the acidification of endosomes. ATPases of the cell keep on pumping protons into the endosome, leading to a high proton concentration and induce a passive chloride ions entry. Hence, the increased ionic concentration causes simultaneously the influx of water, resulting in a high osmotic pressure, swelling and finally the rupture of the cell. [45,309,310]

In the case of R-PE, we could not observe an early endosome escaping effect by the applied nanoparticles and the investigated cell lines, but the red-fluorescing R-PE was indeed taken up by all four cell lines even after 3 h. After 6 h, the phycoerythrin is mainly located in the two analysed vesicular compartments, early endosomes and lysosomes. These vesicles are mainly derived from uptake processes, such as macropinocytosis and endocytosis, and are the principal uptake pathway for calcium phosphate nanoparticles.[293] First, both uptake pathways lead to an early endosome formation that is later fused with lysosomes to degrade engulfed material by proteases and an acidic environment.[311] In the case of an early endosomal or lysosomal escape, we expected a diffuse distribution of the red fluorescent signal over the whole cytosol, but we observed a vesicular distribution which indicated an endo-/lysosomal capture of R-PE. In the cell, R-PE was obviously proteolytic degraded in the lysosomes because the fluorescence of R-PE vanished in the case of HeLa cells and MC3T3 cells, but persisted in the case of HEK293T cells and MG63 cells, indicating that the fate of a nanoparticle-transported protein is specifically depended on the

cell line. Furthermore, each cell line has its unique proteome, that may permit the protein degradation of certain proteins.[312] The assumption of the lysosomal degradation of R-PE is further corroborated by the fact, that R-PE is nearly insensitive to pH changes. It resists even low and high pH values in the pH range between 3.5 and 10.[313] Therefore, with a pH of 4.5 and 5 inside a lysosome, R-PE was not degraded by the acidic environment pH but rather by a proteolytic decomposition.[314] Moreover, calcium phosphate nanoparticles are insoluble at neutral pH, but soluble at low pH, suggesting calcium phosphate nanoparticles were dissolved inside the lysosome.[286,315,316]

Interestingly, the proteolytic degradation of R-PE occurs within a few hours in two out of four investigated cell lines. In earlier studies, the calcium phosphate nanoparticle-mediated transport of nucleic acids, such as plasmid DNA or siRNA was not suffering from degradation. Generally, plasmid DNA contains sequence-specific nuclear import signals i.e. SV40 enhancer sequence, leading to the recruitment of general transcription factors and the subsequent nuclear import.[317] Commercial available siRNA is chemically protected from endogenous RNase degradation by two additional desoxythymidines at each 3' end. Nanoparticle transported proteins may not easily be protected from proteolytic degradation inside an endo- or /lysosome. Here, it might be necessary to modify the system by including some endosomal escaping additives, such as specific peptides like the HA2 peptide from the influenza virus, or by genetic engineering of the protein at its terminal sequences with similar peptide sequences to ensure an early escape from endosomes.[318] However, the presented results are only indicative for this special case and clearly demonstrated that the nanoparticle-mediated transport of the auto-fluorescent R-phycoerythrin into these four cell lines is possible.[46]

3.9.3 Summary

Calcium phosphate nanoparticle easily mediated the transport of the auto-fluorescent R-phycoerythrin into four different cell lines. Dissolved R-PE was not taken up by any of these cells. A fluorescent labelled protein that might have been used for this study instead of the auto-fluorescent protein, had not revealed any information about the functional integrity of the protein itself. The fluorescent label (or organic dye) is usually not effected that much by cellular degradation. Therefore, the following of auto-fluorescent proteins offers an easy way to study the efficiency of new carrier systems for biomolecules, in particular proteins.[46]

4 Summary

This work comprises the syntheses and characterisations of different formulated calcium phosphate nanoparticles for various biomedical and molecular biology applications, including immunisation, vaccination, transfection and cell-targeting. It investigates the transport and the functionalisation of a broad set of biomedically and molecular biology relevant molecules and gives an overview over the feasible applications for the usage of calcium phosphate nanoparticles. This work has successfully shown the cloning of bimodal expression systems for the investigation of translation and transcription. The resulting plasmids could be used for the nanoparticular transfection. Moreover, the successful cloning and production of a new promising class of aptamers (chimeric aptamers) was shown, as well as their conjugation on the surface of calcium phosphate nanoparticles. Different biomolecules, including targeting sequences (iRGD, antibodies, anti-cancer drugs, or antigens) could be covalently attached on the surface of thiol-terminated and silica-coated calcium phosphate nanoparticles using a various set of cross coupling chemicals. These nanoparticles were also successfully used as a carrier for different immunogenic adjuvants (rSF, poly(I:C), CpG^{m}) to improve the immune response of nanoparticle-presented antigens to the host immune system. The usage of triple-shell calcium phosphate nanoparticles allowed the endocytosis-mediated transport of various molecular biology relevant molecules, such as phycoerythrin (R-PE), tandem plasmids or proteins across the cell membrane. It was not possible though to transport the *in vitro* transcribed $polyA^{+}$-tandem-mRNA with the help of calcium phosphate nanoparticles. Triple-shell calcium phosphate nanoparticles were also successfully used as transfection agents for the plasmid pCherries'n'Broccolies, using the fluorescent protein mCherry and the RNA imaging aptamer dBroccoli as probes to analyse transcriptional or translational cellular processes. The transport of the auto-fluorescent protein reveals the fate of a nanoparticle-transported protein. These results were later confirmed, especially by the uptake analysis of the tandem protein. It turned out that the successful nanoparticle-transport is dependent on the biomolecule (DNA, RNA, protein) that is used. Calcium phosphate nanoparticles have demonstrated an extraordinary wide field for applications. Thus, the successful covalent attachment of HSV-1 glycoprotein B derived antigens to the nanoparticles,

leading to a prophylactic protection against HSV infections, which was demonstrated by the high survival rate of treated mice. Although some of the projects could not finally be accomplished, but some interesting indications were found and will be helpful for future projects. However, the usage of calcium phosphate nanoparticles was demonstrated as an effective and valuable carrier or presenting system that will give rise to versatile useful biomedical and molecular biology relevant nanotools in the future.

4.1 Zusammenfassung

Diese Arbeit thematisiert die Synthesen und Charakterisierungen von Calciumphosphat-Nanopartikeln für biomedizinische und molekularbiologische Anwendungen, wie die Immunisierung, Vakzinierung, Transfektion oder spezifische Zellmarkierung. Die Arbeit untersucht den Transport sowie die Funktionalisierungsmöglichkeiten eines breiten Spektrums an biomedizinisch und molekularbiologisch relevanten Molekülen und gibt einen Überblick über mögliche Anwendungen für den Gebrauch von Calciumphosphat-Nanopartikeln. Diese Arbeit konnte erfolgreich die Generierung eines bimodalen Expressionssystems zeigen, welches zur Untersuchung von Transkription und Translation angewendet werden könnte. Die resultierenden Plasmide ließen sich zur nanopartikel-basierten Transfektion nutzen. Darüber hinaus, konnte die erfolgreiche Klonierung und Produktion einer neuen Aptamerklasse (chimäre Aptamere) erfolgreich gezeigt werden und ebenfalls deren Konjugation auf der Oberfläche von Calciumphosphat-Nanopartikeln. Verschiedene Biomoleküle mit zielgerichteter und epitoperkennende Funktion wie dem cyclischen Nonapeptid iRGD sowie Antikörper (CD146, IgG1, IgG2, F4/80), immunogene Antigene (P1 und P2) oder Zytostatika (Doxorubicin) konnten unter Verwendung verschiedener heterobifunktioneller Crosslinker kovalent auf der Oberfläche von thiol-terminierten und silica-umhüllten Calciumphosphat-Nanopartikeln angebracht werden. Diese Nanopartikel wurden ebenfalls erfolgreich als Trägersystem für unterschiedlicher immunogene Adjuvanzien (rSF, poly(I:C), CpG^{m}) verwendet, um die Immunantwort auf die nanopartikel-präsentierten Antigene des Zielorganismus zu verbessern. Die Verwendung von dreischaligen Calciumphosphat-Nanopartikeln erlaubte den endozytose-vermittelten Transport von verschiedenen molekularbiologisch relevanten Molekülen in die Zelle über die Zellmembran, wie zum Beispiel dem Phycoerythrin (R-PE), dem Plasmid zur eukaryotischen Tandemexpression (mRFP-GFP) oder dem Tandemprotein. Es war nicht möglich, die *in vitro* transkribierte $polyA^{+}$-tandem-mRNA mithilfe von dreischaligen Calciumphosphat-Nanopartikeln in Zellen zu transportieren. Dennoch wurden dreischalige Calciumphosphat-Nanopartikel erfolgreich als Transfektionsagens für das Plasmid pCherries'n'Broccolies verwendet, welches über das fluoreszente Protein mCherry

und dem DFHBI-fluoreszenzinduzierbaren RNA-Aptamer dBroccoli als Sonden zur Analyse von transkriptionellen und/oder translationalen zellulären Prozessen nutzen.

Der Transport eines auto-fluoreszenten Proteins in die Zelle wie beispielsweise dem R-PE kann Aufschluss über das Schicksal eines über nanopartikel-transportieren Proteins geben. Die dabei resultierenden Ergebnisse konnten insbesondere durch die Aufnahmestudie des Tandemproteins bestätigt werden. Hierbei zeigte sich, dass der erfolgreiche nanopartikel-basierte Transport von der Art des zu transportierenden Biomoleküls (DNA, RNA, Protein) abhängig ist. Calciumphosphat-Nanopartikel konnten ein äußerst weites Anwendungsspektrum demonstrieren. So auch bei der kovalenten Anbringung von HSV-1 Glykoprotein B abgeleiteten Antigenen auf die Nanopartikeloberfläche, welche nach Immunisierung letztlich zu einem prophylaktischen Schutz gegen HSV-1 Infektionen in Mäusen führte und durch die hohe Überlebensrate der mit Nanopartikeln behandelten Mäuse demonstriert wurde. Trotz der Tatsache, dass Projekte nicht zu Abschluss gebracht werden konnten, so wurden doch interessante Hinweise gefunden die hilfreich für zukünftige Arbeiten sein werden. Die Verwendung von Calciumphosphat-Nanopartikel demonstrierte sich hierbei als ein effektives und wertvolles Träger- oder Präsentationsystem, welches sicherlich auch in Zukunft die Entwicklung einer Vielzahl an verschieden nützlichen biomedizinisch und molekularbiologisch relevanten Nanowerkzeugen ermöglichen wird.

5 Materials and methods

The following chapter describes the methods that have been used during this work.

5.1 Spectroscopic methods

5.1.1 UV/Vis- Spectroscopy

UV/Vis spectrometry enables the determination of the concentration of solubilised molecules. For the determination, molecules must absorb light in the UV to visual range. In this work, the concentration of peptides, DNA and RNA were determined by UV/Vis spectrometry (Cary Bio 300 Spectrophotometer from Varian) and NanoDrop2000c (Thermo Fisher Scientific) to quantify the final amount of the used biomolecules onto the surface of calcium phosphate nanoparticles. The intensity of a light beam passing a specimen can be reduced by absorption, scattering or reflexion. Therefore, the contributions of scattering and reflexion shall be recorded by a blank sample. Usually, the solvent in which the biomolecule is dissolved is used for that purpose. By doing so, the intensity attenuation of a light beam is then only resulted from the dissolved molecules. UV/Vis active molecules absorb, depending on their electronic structure, only the light of a distinct wavelength. The relation between absorption and concentration is given by the Lambert-Beer law.[319-321]

$$A=\lg\frac{I_0}{I}=\varepsilon cd \qquad \text{Eq. 9}$$

A: absorption of a distinct wavelength; I_0: intensity prior passing the specimen; I: intensity, after passing the specimen; ε: molar extinction coefficient; c: concentration given in mol L^{-1}; d: pathlength of the crossing light beam.

The molar extinction coefficient is a substance-specific parameter which can be obtained through a calibration curve. The concentration of nucleic acids can be determined measuring the absorption at 260 nm whereas in proteins only certain amino acids absorb at 280 nm.[322]

5.1.2 Atomic absorption spectroscopy

The atomic absorption spectroscopy can be used to determine the concentration of certain elements. Free atoms are absorbing light at a typical wavelength. In this work, AAS was used to determine the calcium concentration within the dispersion of calcium phosphate nanoparticles. By determination of the calcium concentration, the number of particles per millilitre was calculated. For the analysis by AAS, specimens need to be atomised transferring the element into the gas phase. Atomisation is easily carried out by a flame (2300 °C) where afterwards the monochromatic light absorption of the specific wavelength is recorded. The concentration can then again be received by the Lambert-Beer law.[322,323] The detection limit of AAS is 0.1 mg L^{-1}. Prior to each measurement, dispersions of calcium phosphate were dissolved in aqueous hydrochloric acid. The AAS measurements were carried out by Mrs. Brauner and Mr. Meya. An atomic absorption spectrometer of the M-series (Thermo Electron) was used for all measurements.

5.1.3 Fluorescence spectroscopy

Fluorescence spectroscopy measures the emission of light mediated by fluorescent active molecules. Fluorescence itself is described as the spontaneous emission of light after the turn-off of exciting electromagnetic radiation for over a few nanoseconds and is a product of the different excitation states of the electrons within the molecule. The electronic crossing from the excited to the relaxed state is carried out by the principle of Franck-Condon which is based on the Born-Oppenheimer approximation. Herein, the electron movement is described as fast compared to the atomic nuclei. A fact that relies on the heavier mass of the atomic nuclei in comparison to the electrons. This is illustrated by vertical crossings within the energy diagram from the ground state to the first excited state. After the excitation, the molecule in the excited state stays for a decisive time. This time is also termed as fluorescence life time. An excited molecule can relax to its ground state by different relaxation mechanisms, including the emission of light by luminescence (fluorescence or phosphorescence) or the non-radiative dissipation of energy from the molecule to its surroundings. If the molecule reaches the vibrational ground state of the electronically excited state, the molecule can change into the vibrational state of the

electronic ground state under the emission of fluorescence. A second relaxation mechanism is the energy emission by phosphorescence. By a spin conversion of the molecule, the non-radiative state changes into an electronic triple state which is also known as intersystem crossing (ISC). This nonradiative transition can give rise to phosphorescence in which the molecule relaxes to the electronical ground state by emission of phosphorescence radiation. Another nonradiative relaxation mechanism is the internal conversion. Internal conversion (IC) is the coupling from a vibrational state of an electronically excited state to a vibrational state of a lower excited electronic state and is released by heat.[324-326] The emission of fluorescence basically occurs at a higher wavelength than the absorption does. The different electronical transitions are summarised in the Jablonski-diagram (Figure 5-1). A Cary Eclipse Fluorescence Spectrophotometer (Agilent) was used for all measurements.

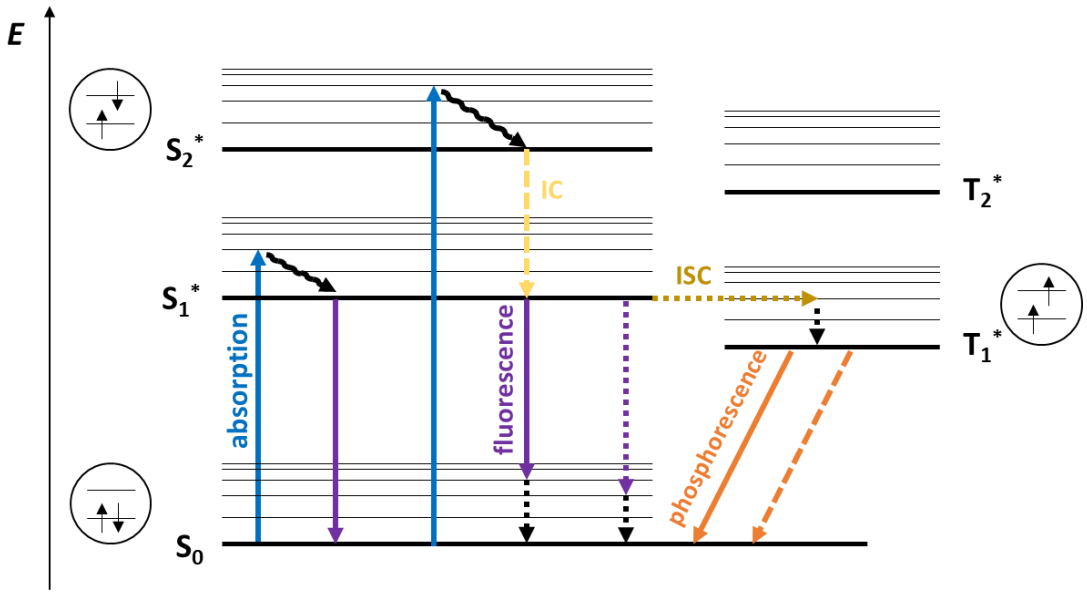

Figure 5-1: Jablonski diagram.
The Jablonski diagram illustrates the electronic states of light-excited molecules and the different transitions between them. The ground state is described as S_0 and excited states are marked with a (*). The absorption (blue) of a photon by an electron leads to the first excited state S_1^*. After the absorption, the electron can return to the ground state by either emitting fluorescence (purple) or phosphorescence (orange). Another non-radiative relaxation mechanisms are marked as dashed lines. Phosphorescence occurs when the electron changes its spin multiplicity to a triplet state (T_1^*) by the intersystem crossing (ISC, gold). The internal conversion (IC, yellow) allows the electron to relax from a second excited state (S_2^*) to the first electronically excited state S_1^*. Retraced from Ref..[327]

5.2 Lyophilisation

Lyophilisation, also known as freeze-drying is used for a conservative drying of aqueous samples. In this work freeze-drying was used to dry a dispersion of calcium phosphate nanoparticles to extend the shelf life time. Prior to the freeze-drying, a cryoprotective D-(+) trehalose was added to the samples (20 mg mL^{-1}). Lyophilisation is based on the sublimation and re-sublimation of water. It is the direct phase transfer from the solid state to the gas phase and vice versa. These changes of states are only realised at 0 °C and 6 mbar. By freeze drying, the water is then sublimated from a sample and re-sublimated on a condenser surface with low temperature. In this work an Alpha 2 – 4 LSC freeze-dryer from Martin Christ was used. Prepared dispersions of calcium phosphate nanoparticles were shock-frozen in liquid nitrogen and sublimated at -10 °C with 0.32 mbar. The condenser had a temperature of -85 °C.

5.3 Microscope techniques

5.3.1 Scanning electron microscopy

Scanning electron microscopy (SEM) is used to image the surface topography of a sample, wherein structures can be visualised down to the sub-nanometre scale. A fine probe of electrons with energies typically up to 40 keV is focused on a specimen and scanned along a pattern of parallel lines. As a result of the impact of the incident electrons, various signals are generated and collected to form an image or to analyse the sample surface (Figure 5.2).[328]

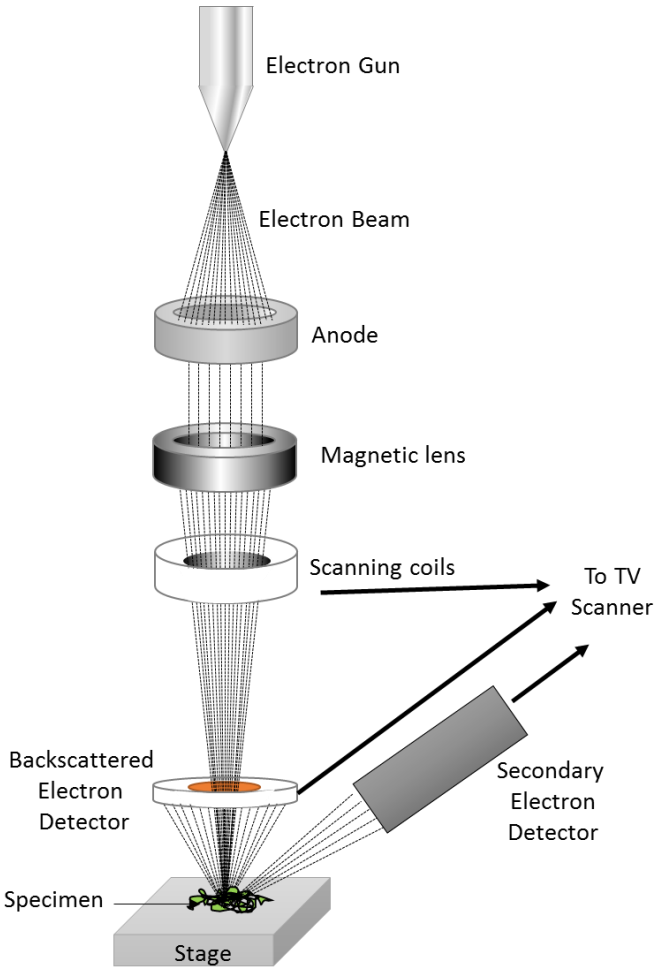

Figure 5-2: Illustration of a SEM aperture setup.
Scheme of a scanning electron microscope (SEM). Electrons with energies up to 40 keV from an electron source are focused on a specimen. Focusing of the beam line is achieved by an anode ring and the following magnetic lens. The impact of the primary high-energy electron beam with the specimen results in a backscattering of the low-energy electrons (~10-100 eV), high energy electrons and X-rays. Signals of backscattered electrons are monitored by electron detectors/scanners.[329]

The backscattered electrons consist mainly of secondary electrons, with energies of a few tens of eV while high-energy electrons from the primary beam and

characteristic X-rays are also backscattered.[328] This technique was used to analyse the synthesised calcium phosphate nanoparticles.

The SEM-images in this thesis were recorded with an ESEM Quanta 400 FEG (FEI, Hilsboro, USA). Samples from dispersions were dripped on a silicium-wafer and air dried. Non-conductive samples were sputter-coated with Au/Pd. All SEM images in this thesis were recorded by Mr. Smail Boukercha, Mrs. Ursula Giebel, Ms. Viktoria Grasmik and Ms. Dr. Kateryna Loza.

For the particle analysis and size determination, the SEM images were analysed by the free image processing and analysis software ImageJ.[330] The average diameter of a spherical particle was determined manually by using the software function "measure", taking the given scale bar as measured reference length. The diameter of 50 particles were measured and the mean and SD were calculated for each image.

5.4 Dynamic light scattering

Dynamic light scattering (DLS) can be used for the characterisation of colloid dispersions. It is the most frequently non-destructive used method to quickly and easily obtain an average diameter of nanoparticles dispersed in liquids.[246] Herein, information about the average particle size distribution (PSD), polydispersity, zeta potential ζ and the colloid stability can be found. Furthermore, the zeta potential gives continuing information about the characteristics of the particle surface and its charge. The dynamic light scattering technique relies on the Rayleigh scattering from the suspended nanoparticles that undergo molecular Brownian motion.[246] By illuminating the sample with a laser source, (usually λ = 532 nm), it is possible to estimate the diffusion speed of the particles and to measure its hydrodynamic diameter, which includes hydration layer, polymer shells or other possible stabilisers.[246] A detector measures the intensity of the backscattered light by the suspended nanoparticles in a defined angle. The intensity of the backscattered light is given by the sum of constructive and destructive interferences, resulting from each impact between the laser beam and the particles. By these interferences and the continuous motion of the particles, the backscattered light intensity is spatiotemporal fluctuated, which is recognised as light and dark dots by the

detector.[331,332] Thus, the correlation of the scattered light is decreased in depending on time. This is in turn described by its auto correlation function. Therefore, fast moving suspended particles lead to an accelerated decrease of the correlation of the scattered light. Typically, intervals of DLS measurements comprises µs to ns. By the autocorrelation function, the diffusion coefficient is calculated. The diffusion coefficient is associated with the hydrodynamic diameter of the particles as follows.[331-333]

$$D = \frac{kT}{6\pi\eta R_h} \qquad \text{Eq. 10}$$

With D: diffusion coefficient; k: Boltzmann constant; T: temperature; η: viscosity; R_h: hydrodynamic radius.

This first correlation leads to reasonable accurate results for strictly monodisperse and spherical uniformed nanoparticles.[246] However, nanoparticles in a real dispersion are usually not monodisperse. In general, they are distinguishing in size and morphology (polydispersity). The intensity of the scattered light is proportional to the sixth power of the particle diameter ($I \sim d^6$), thus the scattered light of larger particles will strongly overlay that of smaller particles, which makes DLS unable to discriminate between nanoparticles with slight differences in diameter or to exactly resolve polydisperse samples.[246,331,334] Thus, it is necessary to use an appropriate algorithm to obtain a particle size distribution from the autocorrelation function. The most common algorithm method that is used, is the cumulant method. Herein, colloidal particles are treated as uniform spherical non-interacting single scattering spheres so that the measured intensity distribution may be converted into relative volume or number distribution of the particle size.[335] The polydispersity index (PDI) is an index for the agglomeration of a sample, ranging from 0.0-1.0. The PDI also shows how much the particles differ from one another and is calculated by the quotient of the average molecular weight (MW) and the number of average molecular weight M_n, leading to the following equation:

$$\text{PDI} = \frac{MW}{M_n} \qquad \text{Eq. 11}$$

Measured size distribution by DLS is only comparable to other methods for a PDI of <0.1. For PDI between 0.1-0.5, the size distribution of dispersions are only comparable to values determined by DLS.[331] Beside the easy measurement and the advantage of simultaneously probing of a large quantity of particles, it is also possible to calculate the zeta potential by DLS. The speed of charged particles in a dispersion is determined by the Laser Doppler Velocimetry (LDV). Herein, the scattered light of charged particles, moving in an electric field, is used to calculate the speed and the electrophoretic mobility of the particles. This is given by the Henry-equation, which is related to the zeta potential.

$$U_E = \frac{2\varepsilon\zeta f(K_a)}{3\eta} \qquad \text{Eq. 12}$$

U_E is the electrophoretic mobility, ε the dielectric constant, ζ the zeta potential, $f(K_a)$ the Henry-function and η the viscosity.

For the determination of the particle size distribution and the zeta potential, the Zetasizer Nano Series ZS DLS device was used for all measurements (Malvern Instruments, Germany). For every measurement, the Smoluchowski approximation was used. The data was taken from the Malvern software without further correction. The scattering intensity distributions (z-average) refers to the particle size data.

5.5 Calculations on calcium phosphate nanoparticles

For the determination of the calcium phosphate nanoparticle concentration, the formation of hydroxyapatite ($Ca_5(PO_4)_3OH$) (MW = 502.31 g mol^{-1}) with a density of ρ(HAP) = 3.14 g cm^3 and uniformly and spherical shaped particles were assumed.

The estimated number N(particles) of particles per mL of colloidal dispersion is given through the following equation:

$$N(\text{particles}) = \frac{V(\text{HAP})}{V(\text{particles})} = \frac{[Ca^{2+}]\cdot 2.5115\cdot 3}{\rho(\text{HAP})\cdot 4\pi r^3} \qquad \text{Eq. 13}$$

With N(particles): number of particles; V(HAP): volume of HAP; V(particles): volume of the particles; [Ca^{2+}]: calcium concentration; ρ: density of HAP; r: radius of SEM

data; the factor 2.5115 is derived from the molecular weight of HAP (502.31 g mol^{-1}) and is used to calculate the volume of HAP.

The amount of bound or loaded molecules per particle *N*(molecules $particle^{-1}$) is then given by:

$$N(\text{molecules particle}^{-1}) = \frac{\beta}{N(\text{particle}) \cdot M_r(\text{molecule})} \cdot N_A \qquad \text{Eq. 14}$$

With β: mass concentration in g m^{-3}; *N*(particles): number of particles from previous equation; *MW*(molecule): molecular weight of the molecule and N_A: Avogadro number ($6.022 \cdot 10^{23}$).

5.6 Buffers

Buffers	**Composition**
GST-Resuspension buffer	50 mM HEPES [pH 7.4, 4 °C], 150 mM KCl, 5 mM $MgCl_2$ add freshly: 1 mM PMSF, 1 mg/mL lysozyme
GST-Elution buffer	50 mM HEPES pH 7.4, 4 °C], 150 mM KCl, 5 mM $MgCl_2$, 20 mM GSH
SEC-Buffer	50 mM HEPES pH 7.4, 4 °C], 150 mM KCl, 5 mM $MgCl_2$,
DFHBI Staining Buffer	40 mM HEPES [pH 7.4], 100 mM KCl, 1 mM $MgCl_2$, 10 µM DFHBI
FACS Buffer	1xPBS, 2% (v/v) FCS, 2mM EDTA
DFHBI Medium	1x DMEM, 40 mM HEPES [pH 7.4], 20 µM DFHBI
Endotoxin removal solution	0.2N NaOH in 95% ethanol

5.7 Molecular biological methods

5.7.1 Bacterial culture

In this thesis, BL21 (DE3), XL1-Blue and DH5α strains of *Escherichia coli* were used and cultivated at 37 °C when there are no other cultivating conditions are mentioned.

5.7.2 Cloning

All plasmid constructs were obtained by regular cloning techniques e.g. the HiFi DNA assembly (New England Biolabs) a variant of the Gibson assembly or by the classical restriction and ligation cloning method.

5.7.3 HiFi-DNA assembly cloning

In a DNA assembly reaction, at least two or up to 6 double-stranded DNA fragments with a complementarity sharing ≥20 bp long overlap, generated by PCR or by the annealing of two complementary single-stranded DNA, are added to an enzyme mixture that consists of a 5'-exonuclease, DNA polymerase and ligase, in a 1.5 mL microcentrifuge tube. The mixture is incubated for 15-60 min at 50 °C. During the assembly reaction, the 5'-exonuclease excises approximately 40 bases min^{-1} bases at the 5' ends of the two double-stranded DNA fragments and generates two complementary single-stranded 3' overhangs.[336] The overhangs facilitate the annealing and within each annealed fragment the DNA polymerase fills in the gaps that have resulted from the 5´exonuclease digestion. In the last reaction step the ligase seals the nicks in the assembled DNA.[164]. The assembled DNA is transformed into a chemical competent bacterial host following the transformation instruction. The individual DNA assemblies for the different constructed vectors are treated capitulary in this thesis.

5.7.4 Plasmid isolation and purification

Plasmids from bacteria were obtained by Plasmid Purification and Isolation Kits from Macherey & Nagel (Düren, Germany). Isolation and purification of plasmid DNA was carried out following the manufacturers' instructions.

5.7.5 RNA isolation

RNA from IVT was purified by using the miRNeasy purification kit from Qiagen (Hilden, Germany). All IVTs were purified as the manufacturers' manual recommended.

5.7.6 Site-directed mutagenesis

For all the site-directed mutagenesis, the Q5-Site-Directed Mutagenesis Kit (NEB) was used. The kit utilises a high-fidelity DNA Polymerase along with custom mutagenic primers to create insertions, deletions and substitutions in designated plasmids by polymerase chain reaction. After PCR, the amplified material is treated for 5 min at room temperature with an enzyme mix of a kinase, ligase and *Dpn*I (KLD) enzyme to circularise the new plasmid and to remove the template. The treated mixture is then transformed into chemical competent cells of *E. coli*.

5.7.7 Restriction and ligation

Restriction and ligation cloning was used for the generation of the expression vector of pGEX-6P-1-tandem(mRFP-EGFP) (chapter 3.8.2). 1 µg of two double-stranded DNA fragments of vector and insert fragment were digested by restriction enzymes and incubated for 1 h at 37 °C. The digested fragments were analysed by gel electrophoresis 100 V, 1 h and were cleaned up by using a gel extraction kit (Macherey-Nagel, Düren, Germany) and assembled in 1.5 mL microcentrifuge tube with a 4-fold molar excess of the insert over the vector. Molar Excess was calculated by using the below-mentioned equation.

$$4 \cdot m(\text{Vector})/\text{ng} \cdot \left(\frac{\text{Insert/bp}}{\text{Vector/bp}}\right) = m(\text{Insert})/\text{ng} \qquad \text{Eq. 15}$$

The reaction mixture was incubated overnight at 16 °C. The next day, 5 µL of the ligation reaction was transformed into XL1-Blue *E. coli* chemical competent cells.

5.7.8 Polymerase chain reaction

For cloning techniques, polymerase chain reactions (PCR) was carried out by using a high-fidelity DNA polymerase, Q5 DNA Polymerase (New England Biolabs) or the

Platinum SuperFi DNA polymerase (Invitrogen). In single cloning, a Taq polymerase (NEB) was used. PCR was carried out by following the manufacturers' instructions.

5.7.9 Colony PCR

Clones resulting from cloning were validated by colony PCR (cPCR). In general, 10 colonies were screened for the desired genetic information. First, each colony was transferred with a pipette tip onto an agar master plate supplemented with an appropriate antibiotic resistance. The colony was further transferred into a prefilled PCR-vial with 15 µL of a PCR master mix (by dipping the tip into the PCR solution). Last, the pipette was dropped into 5 mL LB media with appropriate amount of antibiotic (e.g. 50-100 µg mL^{-1} for Ampicillin) and incubated overnight at 37 °C with 180 rpm.

5.7.10 Transformation of chemically competent cells

50 µL chemical competent cells (e.g. *E. coli* XL1-Blue) were thawed on ice. After that, 2 µL of plasmid DNA were added, mixed and incubated for 30 min on ice. Cells were heat shocked at 42 °C for 30 s and incubated for further 2 min on ice. 950 µL of LB media were added to the cells and incubated for 60 min at 37 °C with approximately 350 rpm in a thermomixer. After incubation, cells were mixed by inverting the tube several times and 100 µL of the cell suspension were streaked out on LB agar plates with corresponding antibiotic resistance. The remaining culture was spun down for 1 min with 4000 g at room temperature. 800 µL of the supernatant were discarded, and the pellet was suspended in the remaining volume and streaked out on a LB-agar plate. The plates were incubated at 37 °C overnight.

5.7.11 Expression

A freshly transformed colony of BL21(DE3) pGEX6-1P-tandem was picked and was inoculated in 50 mL LB media supplemented with 100 µg mL^{-1} ampicillin overnight at 37 °C with 180 rpm. The next day, the overnight culture was diluted 1/100. The culture was grown to an OD of 0.5. 0.4 mM IPTG were used to induce the expression. The culture was further incubated overnight at 18 °C. 50 µL of the culture was kept for SDS-PAGE analysis before and after the induction.

5.7.12 Protein purification of the tandem protein

After the overnight incubation cells (*E. coli* BL21) were harvested at 10,000 g for 15 min at 4 °C. The pellet was resuspended in 30 mL resuspension buffer supplemented with the 1 mM PMSF (a broad range protease inhibitor) and 1 mg mL^{-1} lysozyme. Cells were incubated for 30 min on ice. Again a 50 µL sample for the SDS PAGE analysis was taken from the resuspended cells. Cells were lysated by ultrasonication for 3 rounds (1 min rnd^{-1}, cyc. 0.3, amp. 50% each) and an additional round (1 min rnd^{-1}, cyc 0.3, amp. 60%) via a sonotrode (UP50H, Hielscher). After the lysis, cells were centrifugated for 20 min at 4 °C with 20,000 g. 50 µL of the cleared lysate were kept for SDS-PAGE analysis. The whole lysate was sterile filtrated through a syringe filter (0.2 µm, SARSTEDT). The lysate was kept on ice while equilibrating a 5 mL GSTrap prepacked column (GE Healthcare) with 10 CV resuspension buffer using a peristaltic pump (1 mL min^{-1}) to load the column. After equilibration, the whole lysate was loaded onto the column and the flow through fractions were collected in 5 mL aliquots. The column was washed with 3 CV resuspension buffer and the wash fractions were also collected prior to the elution. The protein was eluted with 2 CV of elution buffer. 50 µL of each fraction was taken for later SDS-PAGE analysis. Both elution fractions were combined, the concentration was measured at A_{280} and digested at 4 °C overnight with a PreScission Protease from GE Healthcare (1 µL protease per 6 mg protein). After digestion, 50 µL was kept for the SDS-PAGE analysis. The digested protein was concentrated by a 30 kDa Vivaspin ultracentrifugal filter (Sartorius) down to 1 mL. The tandem protein was then purified by a combination of size exclusion and affinity chromatography using a GSTrap (5mL) combined HiLoad™ 16/600 Superdex™ 75pg column. The purification was carried out automatically by a FLPC device from GE Healthcare (Äkta). The column was equilibrated for 2 h at 1 mL min^{-1} with degassed resuspension buffer at 4 °C. Later, the concentrated protein was loaded on the column and 2 mL fractions were collected. The tandem protein containing fractions were combined and concentrated down to 1 mL via a 30 kDa ultracentrifugal filter device. The concentration was measured (52.7356 kDa, pI 5.69, ε_{280} = 54780 $M^{-1}cm^{-1}$).

5.7.13 *In vitro* transcription

For the *in vitro* transcription of RNA, 1 µg of a PCR DNA template was used and assembled in a 40 µL reaction containing 10 mM of each NTP, 40 U of Ribolock RNase inhibitor, 1x transcription buffer and 1x Enzyme Mix. All chemicals were purchased from life technologies and carried out following the manufacturers´ protocol.

5.7.14 SDS-PAGE

Size analysis of expressed proteins was carried out through SDS-PAGE. Samples were mixed with 6x SDS loading buffer and boiled for 10 min at 95 °C. After cooling, 10 µL of each sample were applied on a 13% SDS gel. The gel was run for 45 min with 100 V on a PEQLab electrophoresis chamber (VWR, Germany).

5.7.15 Endotoxin and sterility assay

Endotoxin Quantitation was performed with the LAL Chromogenic Endotoxin Quantitation Kit which is based on the Limulus amoebocyte lysate (LAL) assay (Pierce, Thermo Fisher Scientific, Carlsbad, USA), following the manufactures´ instructions.

Sterility was assayed on a sheep-blood agar plate by incubating 10 µL of a dispersion overnight at 37 °C, using 10 µL of sterile ultrapure water as negative and a contaminated tip was used as positive control.

5.7.16 DNA Sequencing

DNA sequencing was carried by Microsynth/Seqlab (Göttingen, Germany). 30 µL of a DNA sample was prepared with 100 ng μL^{-1} in elution buffer (5 mM Tris/HCl, pH 8.5) and was send to the sequencing laboratory.

5.7.17 Amplification of tandem cDNA template for *in vitro* transcription

The tandem cDNA template preparation for ensuing *in vitro* transcription was obtained by a polymerase chain reaction. Using 5'-TTGGACCCTCGTACAGAAGCTAATACG-3' (T7_IVT Fwd) as forward and 5'-T_{120}-CTTCCTACTCAGGCTTTATTCAAAGACCA-3' (T7_IVT_polyA) as reverse primer. Both primers were purchased from Microsynth AG (Switzerland, Balgach) and were purified by PAGE. T7_IVT_polyA has an extension of 120 thymidines adding a polyT-tail to the cDNA template during the PCR, resulting in a polyA-tail after

completion. For the PCR, a reaction volume of 100 µL was used, containing 50 µL of 2x Super Platinum DNA Polymerase PCR, 2x Master Mix (Invitrogen, Carlsbad, USA), 7 µL of 10.0 µM of each forward and reverse primer, 20 µL 5x GC-Enhancer and about 25-50 ng of plasmid DNA. For the PCR protocol: In a first initial activation step, the reaction mixture was heated up to 98 °C for 45 s, followed by 30 cycles of denaturation at 98 °C for 30 s, annealing at 67.7 °C for 30 s, extension at 72 °C for 2 min and final extension at 72 °C for 5 min. After that, the reaction was held at 4 °C after completed cycles. The reaction was performed in a Mastercycler nexus (Eppendorf, Hamburg, Germany). The PCR reaction was purified by a PCR purification Kit (Macherey-Nagel, Düren, Germany) according to the manufacturer's instructions and the DNA was eluted twice using 20 µL nuclease-free water for each elution. Size, quality and integrity of the PCR product were verified on a 1% agarose gel.

5.7.18 *In vitro* transcription polyA$^+$-tandem-mRNA

The purified PCR template harbours the genetic information for the *in vitro* transcription of polyA$^+$-tandem mRNA by a T7 RNA polymerase which can be used for the eukaryotic expression of the tandem protein. IVT was performed by using the MEGAScript® T7 Kit (Life technologies, Darmstadt, Germany). Beside the stabilisation mediating polyA-tail at the 3'-end of mRNAs, other modifications were introduced during its processing e.g. derivatives of ribosyl nucleotide triphosphates like Ψ-UTP and Me-CTP. The 5'-end is normally modified by a 5'-cap structure like 3'-O-Me-m^{7}G(5')ppp(5')G (ARCA cap). This motif is bound by the cap binding complex which recruits the ribosome and therefore plays a crucial role in the initiation of the translation in eukaryotic cells. For efficient mRNA production, *in vitro* the reaction mixture was composed of the following components. At first, a 50 µL of a NTP/Cap-mix were mixed containing 5 µL of 75 mM ATP, 1.25 µL of 75 mM GTP (both from MEGAscript® T7 Kit, Life Technologies), 3.75 µL of 100 mM of Me-CTP, 3.75 µL of 100 mM Ψ-UTP, 1.25 µL of 100 mM 3'-O-Me-m^{7}G(5')ppp(5')G RNA cap structure analogue (all from JenaBioscience, Jena, Germany) and filled up to 40 µL with NF-H_2O (MEGAScript® T7 Kit, Life Technologies). Mixture was mixed thoroughly by pipetting up and down. For the IVT, a reaction volume 40 µL was prepared containing 1 µL of RiboLock RNase inhibitor (40 U µL^{-1}) (Thermo Scientific, Waltham,

USA), 23 µL of the NTP/Cap-mix, 4 µL of 10x reaction buffer, 1 µg PCR product, 4 µL of T7 RNA polymerase enzyme mix. The remaining volume was filled up with NF-H_2O. The IVT reaction mixture was incubated at 37 °C for 6 h in a thermomixer. The template DNA was removed by adding 1 µL TURBO DNase (from MEGAscript® T7 Kit) to the IVT reaction mixture and it was incubated for 15 min at 37 °C. Next, the IVT reaction was purified using RNeasy Mini Kit (Qiagen, Hilden, Germany) according to the manufacturer's instructions. The modified mRNA was eluted from the spin column membrane twice with 40 µL nuclease-free water, flash frozen with liquid nitrogen and stored at -80 °C.

5.7.19 *In vitro* transcription of RNA Aptamers

The *in vitro* transcription of chimeric aptamers was carried out with the MEGAscript® T7 Kit (Life Technologies) was used following the manufactures' protocol. RNA was purified using RNeasy Mini Kit as described above.

5.8 Cell biology methods

In this thesis, different cell lines were used to analyse the viability or the uptake of bio-functionalised calcium phosphate nanoparticles.

5.8.1 HeLa, HEK293T and MG-63 cells: Recovery of cryopreserved cells and cultivation conditions

HeLa cells (human epithelial cervical cancer cells), HEK293T (human epidermal kidney cells) and MG-63 cells (human bone osteosarcoma cells) were recovered by thawing them in a water bath at 37 °C for a couple of minutes. Cell suspensions were given dropwise to 5 mL Dulbecco´s Minimal Essential Media (DMEM) (Gibco Life Technologies, Carlsbad, California) without phenol red and glutamine and were supplemented with 10% (v/v) fetal bovine serum (Gibco), 100 U mL^{-1} penicillin and streptomycin (Gibco); 1×GlutaMax (Gibco), 1×sodium pyruvate (Gibco). The cells were spun down for 3 min at 900 rpm (Multifuge XR, Thermo Fisher; Waltham, Massachusetts, USA). The supernatant was vacuumed, and the cell pellet was resuspended in 5 mL of prewarmed DMEM. 1 mL of that cell suspension was added to 10 mL fresh DMEM in a tissue culture flask (T25, Sarststedt, Nürnbrecht, Germany) and was cultivated for 2-3 days at 37 °C (5% CO_2, humidified atmosphere) according to standard cell culture protocols.[46]

5.8.2 MC3T3-E1 cells

MC3T3-E1 cells (mouse osteoblastic cell line) were recovered under the same conditions as the other cell lines and were cultivated in αMEM, supplemented with 10% FBS, 100 U mL^{-1} penicillin and streptomycin, 1% NEAA (Gibco, Life Technologies, Carlsbad, California) at 37 °C (5% CO_2, humidified atmosphere), according to standard cell culture protocols.[46]

5.8.3 Cell seeding

For uptake or viability studies, cells were regularly seeded in tissue culture plates with a density of ~13,750 cells cm^{-2}. The cells were counted manually under the light microscope by applying 10 µL of a cell suspension on a NEUBAUER counting chamber. For every cell counting, 4 areas with 4x4 squares (1 square = 0.25 mm x 0.25 mm) were counted and the mean was calculated.

5.8.4 Time-lapse monitoring of tandem (DNA, RNA, protein)

HeLa cells were seeded at 50,000 cells in a four-chamber well (500 µL per well) and were either incubated for 6 h with 50 µL of DNA, RNA or protein loaded and PEI-Cy5 stabilised triple-shell calcium phosphate nanoparticles. After incubation, cells were washed twice with PBS and re-cultivated in fresh DMEM. The imaging positions were set according the fluorescence signal from PEI-Cy5. Cells were imaged over 48-65 h.

5.8.5 Immunofluorescence

For immunofluorescence staining, cells were fixed with 4% (w/v) para-formaldehyde for 20 min, washed twice with DPBS and permeabilised using 0.1% (v/v) Triton X-100 in DPBS for 10 min. For indirect immunofluorescence, samples were washed with DPBS and incubated in blocking solution (3% (v/v) BSA, 0.1% (v/v) Triton X-100, 0.1% (v/v) saponin) for 1 h, followed by an incubation with the indicated primary antibodies for 1 h in blocking solution. The cells were washed three times with 0.1% (v/v) Triton X-100 in DPBS and incubated with the fluorescence labelled secondary antibody and Hoechst33342 in blocking solution for 1 h. After washing with 0.1% (v/v) Triton X-100 in DPBS and DPBS alone, the coverslips were mounted on glass slides using ProLong Gold antifade reagent (Thermo Fisher Scientific). For the staining of filamentous actin, the fixation, washing and permeabilisation steps were the same as described above. Afterwards, the cells were blocked with 1% (v/v) BSA, 0.1% (v/v) Triton X-100, and 0.1% (v/v) saponin for 30 min, followed by an incubation with 1 unit of Alexa Fluor 660 Phalloidin (200 U mL^{-1}) per coverslip in blocking solution for 20 min. Cells were washed three times with 0.1% (v/v) Triton X-100 and stained with DAPI in DPBS (300 nM) for 5 min. Then, the coverslips were washed with DPBS and mounted with 5 µL anti-fading medium ProLong (ThermoFisher).

5.8.6 Bafilomycin A1 chase and time-resolved imaging

The lysosomal degradation chase of nanoparticle-transported R-PE was validated by Bafilomycin A1 (BafA1) treatment. In an eight-chamber well (Falcon), $2.0 \cdot 10^4$ cells well were seeded in 400 µL DMEM (1×) supplemented with 10% FBS and 100 U mL^{-1} penicillin and streptomycin each and incubated for 24 h at 37 °C, 5% CO_2. Then, 20 µL of a dispersion of CaP/PEI/R-PE nanoparticles were added to the first row

of the eight-chamber well, whereas 20 µL of dissolved R-PE (443 µg mL^{-1}) were added to the second row. This gives a concentration of $1.08 \cdot 10^8$ nanoparticles per mL (dilution 1:21), $4.53 \cdot 10^7$ nanoparticles per well and about 2,260 nanoparticles per cell. After 6 h of incubation, the chase was initialised. The cells were washed with pre-warmed (37 °C) DPBS twice to ensure the total removal of non-incorporated nanoparticles. The cells in two wells of the first and second row of the eight-chamber slide were incubated in fresh prewarmed (1×) DMEM (37 °C) containing 100 nM BafA1, whereas the remaining wells received (1×) DMEM without BafA1. Cells were imaged with a Keyence Biorevo BZ-9000 microscope (Osaka, Japan) and an air objective S Plan Fluor ELWD 40×/0.60 OFN22 Ph2 WD 3.6±2.8 (Nikon, Japan). Images were taken every 30 min over 24 h. For each well, three positions of one well were recorded in three independent experiments. The red fluorescence of the cells was analysed manually in each image with the same illumination parameters. At least 100 cells were counted for each well.

5.8.7 Transfection with Lipofectamine 2000

Eukaryotic cells were transfected with 1 µg of DNA using 1 µL of Lipofectamine 2000 (Life Technologies, Carlsbad, USA). Then cells were incubated for 24 h and imaged for the desired observation time.

5.8.7.1 Transfection of tandem-RNA with Lipofectamine 2000 and time-lapsed monitoring

The transfection was carried out, following the manufacturers‘ protocol. Briefly, for the mRNA transfection with Lipofectamine 2000, cells were seeded at $1.5 \cdot 10^5$ in a 12 well plate and incubated for 24 h at 37 °C in humified atmosphere (5% CO_2). On the next day, 500 µL Opti-MEM containing 1.5 µg $polyA^+$-tandem mRNA and 2 µL Lipofectamine 2000 were mixed in a microcentrifuge tube and incubated for 20 min at room temperature.

The cells were briefly washed with 500 µL DBPS and re-cultivated with the transfection mixture containing media for 4 h at 37 °C with 5% CO_2. Then transfection mixture was replaced with 1 mL DMEM and were incubated for further 24 h and

monitored with a fluorescence microscope over the whole observation time, taking 1 image h^{-1}.

5.8.8 MTT assay

The assay itself is based on the reduction of the water-soluble yellow tetrazolium salt 2-(4,5-dimethylthiazol-2-yl)-3,5-diphenyl-2*H*-tetrazol-3-ium bromide (MTT) into the violet, water-insoluble formazan compound (*E,Z*)-5-(4,5-dimethylthiazol-2-yl)-1,3-diphenylformazan by NADPH, NAD and succinate depending reductases of viable cells (Figure 5.3).[337] Therefore, the amount of reduced MTT is equal to the glycolysis rate of a cell.[337] The reduction of MTT by NAD and NADPH reductases takes place at the endoplasmic reticulum whereas the succinate reduction is carried out inside the mitochondria of viable cells.[337-339]

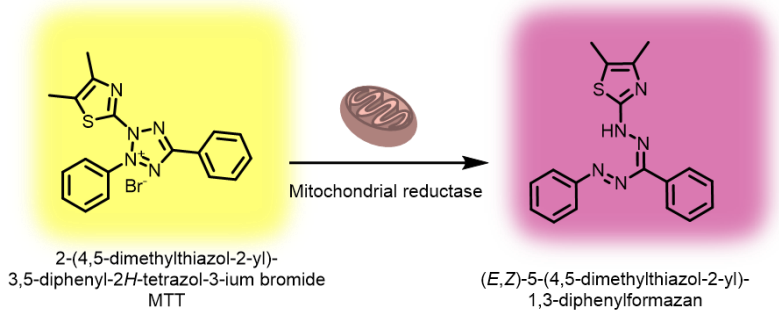

Figure 5-3: MTT reaction.
MTT is reduced by mitochondrial reductases of viable cells.

The cells were incubated with calcium phosphate nanoparticles for several hours (e.g. 3, 6, 24 up to 48 h) at 37 °C under humidified atmosphere with 5% CO_2 in multi-well tissue culture plates. After each incubation, the medium was vacuumed, and the cells were washed twice with prewarmed DBPS. The cells were incubated with a mixture of 1:5 DMEM/DPBS, containing 1 mg mL^{-1} MTT (Life Technologies, Carlsbad, USA) for 1 h at 37 °C and under humidified atmosphere with 5% CO_2. Media was removed, and the formazan crystals were dissolved in 300 µL DSMO p.a. (Carl Roth, Germany) and the plate was incubated for 30 min at 37 °C. The dissolved formazan compound was spread out in 100 µL aliquots on a 96-well microtiter plate, taking triplicates for each well. The absorbance was measured at 592 nm with a multi-scan plate reader (Thermo Fisher Scientific).

5.9 Bioconjugation techniques

5.9.1 3’-end RNA labelling

For the 3’-end selective chemical attachment of a hetero-specific crosslinker, such as EZLink-Hydrazide-LC-Biotin (Thermo Fisher) or KMUH (*N*-[κ-maleimidoundecanoic acid] hydrazide, trifluoroacetic acid salt; Thermo Fisher Scientific), a biotin or a maleimide functionality was introduced through previous potassium periodate oxidation. It is less common, but an advantageous labelling technique and it is not only restricted to newly synthesised RNA. It can therefore be also applied to commercially available or cell-isolated RNA. Furthermore, the incorporation at the 3’-end of the RNA, the diol moiety in the molecule, impede proper folding and yields a rather uniform RNA population in terms of structure and RNA/label ratio.[90] This labelling technique was used for the covalent attachment of chimeric aptamers on the surface of calcium phosphate nanoparticles. The diol oxidation at the 3’-end results in a dialdehyde formation that is highly susceptible to a nucleophilic attack and react with the nucleophilic hydrazide components such as hydrazine derivatives. Finally, the product can be stabilised by borohydride reduction.[90] The conjugation is shown in Figure 5-4.

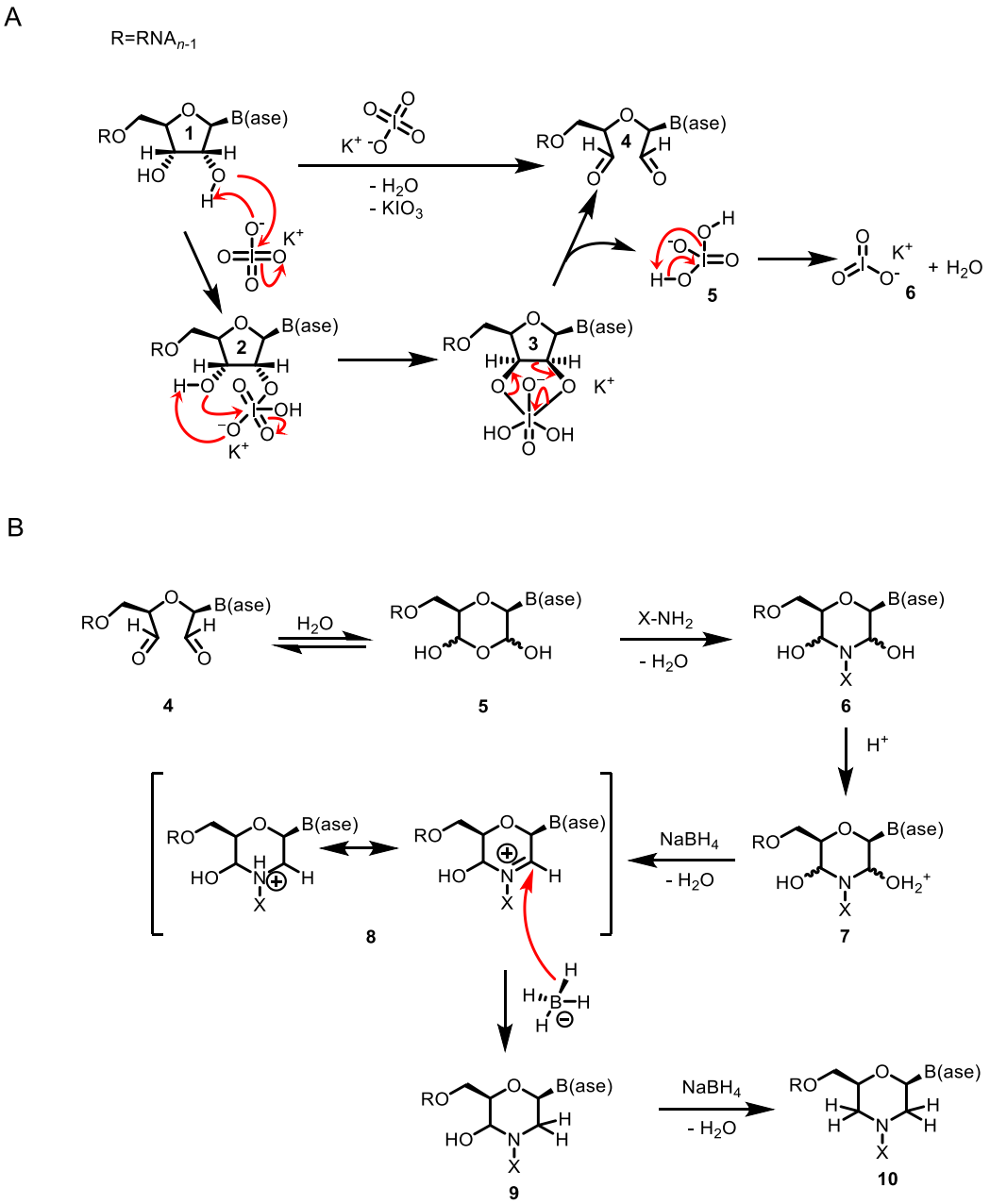

Figure 5-4: Periodate mediated oxidation of the diols and subsequent attachment of a crosslinker. A: periodate oxidation of the 3' end. B: attachment of hydrazide containing crosslinker, followed by subsequent reduction through sodium borohydride.

5.9.1 Periodate oxidation of the 3´-terminal ribose and hydrazide coupling

1-2 nmol of RNA was incubated in a total volume of 100 µL 40mM KIO_4 for 1 h at room temperature in the dark. The reaction was stopped with 100 µL of 50% ethylene glycol. Then 1/10th volume of 3M NaOAc (pH 5.2) and 2.5 volumes of 96% ethanol were added to precipitate the RNA. After centrifugation, the pellet was washed with 70% ethanol and air-dried for 30 min. The pellet was dissolved in 100 µL of 10 mM *N*-[κ-maleimidoundecanoic acid] hydrazide (KMUH) or 10 mM EZ-Link Hydrazide-LC-Biotin and incubated for 2 h at 37 ◦C. After the incubation, 100 µL of 0.2 M $NaBH_4$ and 200 µL of 1 M Tris–HCl pH 8.2 were added and incubated for 30 min on ice in the dark.[90] The RNA was purified by ultrafiltration using a 0.5 mL amicon ultra centrifugal filter device (MWCO = 3 kDa, Merck Millipore, Germany). The RNA was spun down for 15 min at 14,000 g at 4 °C and refilled with 400 µL NF-H_2O and spin down again for 15 min at 14,000 g at 4 °C. Ultrafiltration steps were repeated twice. RNA was recovered, the concentration was determined by microvolume UV/Vis-spectroscopy (Nanodrop 2000c) and stored at -80 °C.

5.9.2 Crosslinking with sulfo-SMCC and SPDP

Two commonly used bifunctional and hetero-specific cross-linkers were utilised for the attachment of amine harbouring peptides or proteins. Proteins or peptides, that had to be covalently attached on the surface of thiol- or amine-terminated and silanised calcium phosphate nanoparticles, were first dissolved or diluted in DPBS to 2 mg mL^{-1}. The dissolved peptide or protein was then reacted with a 10-50 fold molar excess of the cross-linker, either the water-soluble sulfosuccinimidyl 4-(*N*-maleimidomethyl)cyclohexane-1-carboxylate (sulfo-SMCC) or the DMSO-soluble succinimidyl 3-(2-pyridyldithio)propionate (SPDP) in DBPS for 1-2 h at room temperature. The crosslinker excess was removed by ultrafiltration using a 0.5 mL amicon ultra centrifugal filter (MWCO = 3 kDa, Merck Millipore, Germany). Activated biomolecules were centrifuged and washed 3 times with DBPS and then recovered following the manufactures' protocol.

5.10 Bioinformatics

Some bioinformatic tools have been used during this thesis and are briefly described down below section.

5.10.1 RNA 2D-prediction with RNAfold

The analysis of the two-dimensional structures of the generated RNA constructs (e.g. enlarged or truncated) was carried out *in silico* by the RNAfold WebServer tool.[166] The 2D prediction of RNA indicates how the RNA is most likely folded after an insertion, deletion or substitution of ribonucleotides, and reflects its structural integrity which is, by computed base-pair probabilities, ranging from 0.0-1.0. RNA sequences were loaded into the input field of the tool and the data were processed using default settings.[166] After processing, the tool followed a mathematical algorithm that calculates the minimum free energy (MFE) of several 2D structures and highlights the single, most probable secondary RNA structure. This 2D RNA folding prediction tool was used for the generation of a modified version of the F30-2xdBroccoli aptamer.

5.10.2 PyMol

Handling, modelling and visualisation of generated 3D models was carried out with PyMol v1.3 (Schrödinger, LLC).

5.10.3 3D RNA prediction with RNAComposer

3D models of the designed RNA aptamers e.g. chimeric aptamers were generated by the web tool RNAComposer. This tool allows the generation of 3D models of RNA molecules from the primary sequence with up to 500 nt. The tool can distinguish between six different secondary structure prediction methods e.g. Centroidfold, ContextFold, CONTRAfold, IPknot, RNAfold and RNAstructure. For all generated RNA 3D models, the secondary structure prediction method RNAfold was used.[340-342]

5.11 Material arrangements for the preparation of pyrogen/endotoxin-free and sterile calcium phosphate nanoparticles.

Some material precautions have to be made for the syntheses of sterile and pyrogen/endotoxin-free calcium phosphate nanoparticles. All aqueous solutions that

have been prepared in this thesis were prepared with ultrapure water (PURELAB flex 1, ELGA LabWater, Veolia Water Technologies, Celle, Germany). This water has a certificated pyrogen/endotoxin concentration of <0.001 EU mL^{-1} which is known as endotoxin-free.[343] Glassware and magnetic stirring bars were rinsed with sterile filtrated endotoxin removal solution (0.2 M NaOH in 95% ethanol), filled with sterile filtrated 2 M NaCl, incubated for 2 h at room temperature and rinsed thoroughly with sterile ultrapure water. Afterwards, the glassware and magnetic stirring bars were autoclaved for 45 min at 134 °C (Laboklav, SHP Steriltechnik AG, Detzel Schloss/Satuelle, Germany) and baked overnight at 200 °C. Additionally, the prepared solutions were sterile filtrated by using a sterile 0.2 µm syringe filter (Sarstedt AG, Sarstedt, Germany). Flexible tubes that were used to pump solutions were cleaned by rinsing each tube with 50 mL endotoxin removal solution followed by washing each tube with 50 mL of 2 M NaCl dissolved in ultrapure water and finally by wash them with 100 mL ultrapure water prior to the synthesis. Ultrasound sonicator tips (Hielscher Ultrasonics GmbH, Teltow, Germany) and 25 mL ultracentrifugation tubes (Beckmann&Coulter, Krefeld, Germany) were cleaned and incubated in endotoxin removal buffer for 2 h followed by an additional incubation for 2 h in 2 M NaCl at room temperature. After the incubation, the tips and tubes were thoroughly washed with sterile ultrapure water. Then after the removal of the endotoxins, the ultrasound sonicator tip was stored in a 15 mL tube filled with 100% *i*-PrOH. Plastic wares e.g. pipettor tips, pipettes or micro centrifuge tubes (Sarstedt AG,Sarstedt, Germany) were also sterile and pyrogen-free. After the completed synthesis of calcium phosphate nanoparticles, endotoxin contamination was determined by the LAL Chromogenic Endotoxin Quantitation Kit (Pierce, Thermo Fisher Scientific, Carlsbad, California, USA). The sterility test was performed on a sheep-blood agar plate incubating 10 µL of the calcium phosphate nanoparticles dispersion overnight at 37 °C.

5.12 Synthesis of PEI-stabilised calcium phosphate nanoparticles

5.12.1 Synthesis of PEI stabilised single-shell calcium phosphate nanoparticles CaP/PEI

All syntheses were performed at room temperature. For the synthesis of polyethylene imine (PEI) stabilised single-shell calcium phosphate nanoparticles, 0.2 mL of PEI (PEI; Sigma-Aldrich, *MW* 25 kDa; 2 mg mL^{-1}) was prefilled into a 1.5 mL microcentrifuge tube and equal, e.g. 1 mL each, volumes of 6.25 mM $Ca(NO_3)_2 \cdot 4\ H_2O$ [pH 9] (FLUKA) and 3.74 mM $(NH_4)_2HPO_4$ [pH 9] (FLUKA) were pipetted into a 15 mL tube under continuously vortexing. Immediately, after mixing for a few seconds, 1 mL of the formed calcium phosphate nanoparticle dispersion (CaP) was transferred into the PEI-containing microcentrifuge tube and the dispersion was mixed thoroughly by vortexing for 10 seconds to obtain colloidal stability. All chemicals were obtained in p.a. grade. Excess of the stabilising PEI was removed by centrifugation at 21,100 g (Heraeus Fresco 21, Thermo Fisher, Carlsbad). The supernatant was discarded carefully, and the remaining pellet was briefly washed with 1 mL ultrapure water. Left over water was replaced by 1 mL ultrapure water and the pellet was redispersed by ultrasonication using a sonotrode tip (Hielscher UP50H; sonotrode 3; cycle 0.8, amplitude 60%, 30 s). The obtained CaP/PEI dispersion was kept at 4 °C.

5.12.2 Synthesis of PEI stabilised calcium phosphate double-shell nanoparticles CaP/PEI/CaP/PEI

Double-shell calcium phosphate nanoparticles were prepared analogously to the single-shell calcium phosphate nanoparticles as described in the previous section. After preparing 1 mL of single-shell calcium phosphate nanoparticles (w/o centrifugation and redispersion), a second shell was synthesised by adding 500 µL of 6.25 mM $Ca(NO_3)_2 \cdot 4\ H_2O$ [pH 9] (FLUKA) and 500 µL of 3.74 mM $(NH_4)_2HPO_4$ [pH 9] (FLUKA) to the dispersion. The dispersion was thoroughly vortexed and additional 200 µL of PEI (2 mg mL^{-1}) were added and mixed by vortexing again. Excess of the stabilising PEI was removed by centrifugation at 21,100 g (Heraeus Fresco 21, Thermo Fisher, Carlsbad). The supernatant was discarded, and the remaining pellet was briefly washed with 1 mL ultrapure water. Left over water was replaced by 1 mL

ultrapure water and the pellet was redispersed by ultrasonication using a sonotrode tip (Hielscher UP50H; sonotrode 3; cycle 0.8, amplitude 60%, 30 s). The obtained CaP/PEI dispersion was kept at 4 °C.

5.12.3 Synthesis of triple-shell calcium phosphate nanoparticles

Triple-shell calcium phosphate nanoparticles CaP/PEI/X/CaP/PEI were obtained by rapidly mixing a compound X (e.g. DNA, protein, RNA) with single-shell calcium phosphate nanoparticles followed by preparing a third shell of calcium phosphate as it is shown in the previous chapter.

5.12.4 Synthesis of pDNA stabilised calcium phosphate nanoparticles

Plasmid DNA stabilised calcium phosphate nanoparticles (CaP/plasmid/CaP/PEI) were synthesised by rapidly mixing 500 µL of 6.25 mM $Ca(NO_3)_2 \cdot 4\ H_2O$ [pH 9] (FLUKA) and 500 µL of 3.74 mM $(NH_4)_2HPO_4$ [pH 9]. Immediately under continuously vortexing, 100 µg of plasmid DNA (1 mg mL^{-1}) was given to the dispersion, followed by the preparation of a second layer of calcium phosphate, 250 µL 6.25 mM $Ca(NO_3)_2 \cdot 4\ H_2O$ [pH 9], 500 µL of 3.74 mM $(NH_4)_2HPO_4$ [pH 9] and 200 µL PEI. Excess of the stabilising PEI was removed by centrifugation at 21,100 g (Heraeus Fresco 21, Thermo Fisher Scientific, Carlsbad). The supernatant was discarded, and the remaining pellet was briefly washed with 1 mL ultrapure water. Left over water was replaced by 1 mL ultrapure water and the pellet was redispersed by ultrasonication using a sonotrode tip (Hielscher UP50H; sonotrode 3; cycle 0.8, amplitude 60%, 20 s). The obtained CaP/PEI dispersion was kept at 4 °C.

5.12.5 Synthesis of silica-coated calcium phosphate core nanoparticles

Silica-shell and calcium phosphate core nanoparticles were synthesised as follows. All syntheses were performed at room temperature. 20 mL sterile filtrated (0.2 µm) ultrapure water were filled into a 50 mL tube. Under continuous stirring at 1000 rpm, 5 mL of 10.8 mM $(NH_4)_2HPO_4$ [pH 10] (Merck), 5 mL of 18.0 mM $[CH_3CH(OH)COO]_2Ca{\cdot}5\ H_2O$ [pH 10] (Fluka) and 7 mL of 0.08 mM polyethyleneimine (25 kDa branched, Sigma Aldrich) were pumped into the water-prefilled 50 mL tube for 1 minute. The dispersion was stirred for further 20 min. For the preparation of 1 mL of silica-coated calcium phosphate core nanoparticles, 0.9 mL of the CaP/PEI dispersion were transferred into a new tube and 0.1 mL of a biomolecule of choice (1 mg mL^{-1}) were added to the dispersion and the mixture was stirred for 30 min at 500 rpm. For non-loaded dispersion, 1 mL of CaP/PEI was directly proceeded for silanisation. For the preparation of the silica-shell around the calcium phosphate nanoparticles, 1 mL of CaP/PEI or CaP/PEI/biomolecule dispersion were mixed with a Stoeber solution consisting of 4 mL EtOH (p.a.), 5.0 µL tetra orthosilicate (TEOS, Sigma) and 2.6 µL ammonia solution (30-33% (v/v), Carl Roth). The mixture was stirred overnight at 1000 rpm. For a -NH_2 or -SH termination, biomolecule containing or non-containing (CaP/PEI/biomolecule/SiO_2-OH or CaP/PEI/SiO_2-OH), 1 mL of the silanised calcium phosphate nanoparticles were mixed with Stoeber solution consisting of 4 mL EtOH, 5 µL MPS or APTES. The mixtures were stirred at 1000 rpm overnight. The next day, the dispersions were ultracentrifugated at 30,000 rpm (SORAVALL WX 90, Ultra Series, Thermo Scientific) for 30 min to remove non-reacted impurities. The pellets were washed briefly with 0.5 mL sterile filtrated ultrapure water and redispersed by ultrasonication (UP50H, Hielscher, Ultrasound Technology; sonotrode 3, cycle 0.8, amplitude 70%, 20 s) on ice in 1 mL sterile filtrated ultrapure water.

6 Literature

[1] J. Gribbin, "Richard Feynman: A Life in Science"**, Dutton Adult 1st edition** (1997) 1-320.

[2] V. Morigi, A. Tocchio, C. B. Pellegrini, J. H. Sakamoto, M. Arnone, E. Tasciotti, "Nanotechnology in Medicine: From Inception to Market Domination", **Journal of Drug Delivery Volume 2012** (2012) Article ID 389485.

[3] E. M. Goldys, M. A. Sobhan,"Fluorescence of Colloidal Gold Nanoparticles is Controlled by the Surface Adsorbate", **Advanced Functional Materials 22** (2012) 1906-1913.

[4] Daumann, S. "Synthese und Charakterisierung von Nanopartikeln: Anisotrope Edelmetall-Nanopartikel und Zinkoxid-Nanopartikel", Dissertation, **University of Duisburg-Essen** (2016) 1-207.

[5] StatNano "Ranking of Countries in Nanotechnology Publications in 2016", **Nano Science, Technology and Industry Scoreboard** (2017) available online at http://statnano.com/news/57105 (accessed 18.07.2017).

[6] M. G. Krukemeyer, V. Krenn, F. Huebner "History and Possible Uses of Nanomedicine Based on Nanoparticles and Nanotechnological Progress", **Journal of Nanomedicine & Nanotechnology 6** (2015) 2157-7439.

[7] K. Haedicke, D. Kozlova, S. Grafe, U. Teichgraber, M. Epple, I. Hilger, "Multifunctional calcium phosphate nanoparticles for combining near-infrared fluorescence imaging and photodynamic therapy", **Acta Biomaterialia 14** (2015) 197-207.

[8] S. Chernousova, M. Epple, "Live-cell imaging to compare the transfection and gene silencing efficiency of calcium phosphate nanoparticles and a liposomal transfection agent", **Gene Therapy 24** (2017) 282-289.

[9] W. Habraken, P. Habibovic, M. Epple, M. Bohner, "Calcium phosphates in biomedical applications: materials for the future?", **Materials Today 19** (2016) 69-87.

[10] V. Sokolova, A. M. Westendorf, J. Buer, K. Überla, M. Epple, "The potential of nanoparticles for the immunization against viral infections", **J**ournal of **Mat**erials **Chem**istry **B 3** (2015) 4767-4779.

[11] A. Tabaković, M. Kester, J. H. Adair, "Calcium phosphate-based composite nanoparticles in bioimaging and therapeutic delivery applications", **Wiley Interdisciplinary Reviews: Nanomedicine and Nanobiotechnology 4** (2012) 96-112.

[12] A. F. Hollemann, E. Wiberg, N. Wiberg "Anorganische Chemie", **De Gruyter Auflage: 102** (2007) 1-2188.

[13] S. Slomkowski, J. V. Alemán, R. G. Gilbert, M. Hess, K. Horie, R. G. Jones, P. Kubisa, I. Meisel, W. Mormann, S. Penczek, R. F. T. Stepto, "Terminology of polymers and polymerization processes in dispersed systems (IUPAC Recommendations 2011)", **Pure and Applied Chemistry 83** (2011) 2229-2259.

[14] B. Derjaguin, G. Sidorenkov, "Thermoosmosis at ordinary temperatures and its analogy with the thermomechanical effect in helium II", **Cr Acad Sci Urss 32** (1941) 622-626.

[15] E. J. W. Verwey, T. G. Overbeek, K. van Nes "Theory of the stability of lyophobic colloids. The interaction of particles having an electric double layer." **Elsevier**, **New York-Amsterdam** (1948) 1-216.

[16] Malvern Instruments "Zeta potential - An introduction in 30 minutes", **Malvern** available online at https://www.malvern.com/en/support/resource-center/technical-notes/TN101104ZetaPotentialIntroduction (accessed 29.06 2017).

[17] B. Derjaguin, "A Theory of Interaction of Particles in Presence of Electric Double-Layers and the Stability of Lyophobe Colloids and Disperse Systems", **Progress in Surface Science 43** (1993) 1-14.

[18] B. Derjaguin, "A theory of interaction of particles in presence of electric double layers and the stability of lyophobe colloids and disperse systems", **Acta Physicochim Urs 10** (1939) 333-346.

[19] E. J. W. Verwey, "Theory of the Stability of Lyophobic Colloids". **Journal of Physical Chemistry 51** (1947) 631-636.

[20] G. Trefalt, M. Borkovec "Overview of DLVO Theory", **Laboratory of Colloid and Surface Chemistry LCSC - University of Geneva** (2017) available online at www.colloid.ch/dlvo (accessed 29.06. 2017).

[21] International Union of Pure and Applied Chemistry "IUPAC Compendium of Chemical Terminology Gold Book ", **IUPAC Version 2.3.3** (2014) available online at http://goldbook.iupac.org/pdf/goldbook.pdf (accessed 30.06. 2017).

(22] S. Abott, N. Holmes "Nanocaotings: Principles and Practice from Research to Production" **Destech Publications** (2013) 1-350.

[23] O. Rotan, "Calcium Phosphate Nanoparticles for Medical Application: Drug and Vaccine Delivery", Dissertation **University of Duisburg-Essen** (2016) 1-217.

[24] T. F. Tadros, "Polymers in Colloid Systems: Adsorption, Stability and Flow", **Elsevier Amsterdam** (1988) 1-412.

[25] M. Epple, E. Bäuerlein, W. Pompe, "Handbook of Biomineralization", **Wiley-VCH, Weinheim 1st edition** (2009) 1-424.

[26] M. P. Ferraz, F. J. Monteiro, C. M. Manuel, "Hydroxyapatite nanoparticles: A review of preparation methodologies", **Journal of applied biomaterials & biomechanics**:**JABB 2** (2004) 74-80.

[27] S. V. Dorozhkin, M. Epple, "Biological and medical significance of calcium phosphates", **Angewandte Chemie International Edition 41** (2002) 3130-3146.

[28] P. Kumar, B. Vinitha, G. Fathima, "Bone grafts in dentistry", **Journal of Pharmacy & Bioallied Sciences 5** (2013) 125-127.

[29] M. Goldberg, A. B. Kulkarni, M. Young, A. Boskey, "Dentin: Structure, Composition and Mineralization: The role of dentin ECM in dentin formation and mineralization", **Frontiers in Bioscience (Elite Edition) 3** (2011) 711-735.

[30] M. Epple, E. Bäuerlein, "Handbook of Biomineralization", **WILEY-VCH Verlag GmbH & Co. KGaA,: Weinheim** 1st edition (2007) 1-1269 Published online at http://onlinelibrary.wiley.com/book/10.1002/9783527619443

[31] V. Uskokovic, D. P. Uskokovic, "Nanosized hydroxyapatite and other calcium phosphates: chemistry of formation and application as drug and gene delivery agents", **Journal of biomedical materials research. Part B, Applied biomaterials 96** (2011) 152-191.

[32] S. V. Dorozhkin, "Calcium Orthophosphates in Nature, Biology and Medicine",**Materials 2** (2009) 399-498.

[33] M. Yashima, Y. Yonehara, H. Fujimori, "Experimental Visualization of Chemical Bonding and Structural Disorder in Hydroxyapatite through Charge and Nuclear-Density Analysis", **The Journal of Physical Chemistry C 115** (2011) 25077-25087.

[34] D. Aquilano, M. Bruno, M. Rubbo, F. R. Massaro, L. Pastero, "Low Symmetry Polymorph of Hydroxyapatite. Theoretical Equilibrium Morphology of the Monoclinic $Ca_5(OH)(PO_4)_3$", **Crystal Growth & Design 14** (2014) 2846-2852.

[35] F. Z. Ren, X. Lu, Y. Leng, "Ab initio simulation on the crystal structure and elastic properties of carbonated apatite", **J Mech Behav Biomed 26** (2013) 59-67.

[36] B. Clarke, "Normal Bone Anatomy and Physiology", **C**linical **J**ournal **of the A**merican **S**ociety **of N**ephrology **3** (2008) 131-139.

[37] L. Pei, T. Tsuzuki, A. Dodd, M. Saunders, "Synthesis of calcium chlorapatite nanoparticles and nanorods via a mechanically-induced solid-state displacement reaction and subsequent heat treatment", **Ceramics International 43** (2017) 11410-11414.

[38] L. Sun, L. C. Chow, S. A. Frukhtbeyn, J. E. Bonevich, "Preparation and Properties of Nanoparticles of Calcium Phosphates With Various Ca/P Ratios", **J Res Natl Inst Stand Technol 115** (2010) 243-255.

[39] X. Ying, C. Yun, S. Minjie, P. A Qineng, "Mini Review of Biodegradable Calcium Phosphate Nanoparticles for Gene Delivery", **Current Pharmaceutical Biotechnology 14** (2013) 918-925.

[40] P.-A. Mouthuy, A. Crossley, H. Ye, "Fabrication of calcium phosphate fibres through electrospinning and sintering of hydroxyapatite nanoparticles", **Materials Letters 106** (2013) 145-150.

[41] X. Guo, T. Xia, H. Wang, F. Chen, R. Cheng, X. Luo, X. Li, "Electrosprayed Microparticles with Loaded pDNA-Calcium Phosphate Nanoparticles to Promote the Regeneration of Mature Blood Vessels", **Pharmaceutical Research 31** (2014) 874-886.

[42] Y. Cai, H. Pan, X. Xu, Q. Hu, L. Li, R. Tang, "Ultrasonic Controlled Morphology Transformation of Hollow Calcium Phosphate Nanospheres: A Smart and Biocompatible Drug Release System", **Chemistry of Materials 19** (2007) 3081-3083.

[43] M. Nakamura, A. Oyane, "Physicochemical fabrication of calcium phosphate-based thin layers and nanospheres using laser processing in solutions", **Journal of Materials Chemistry B 4** (2016) 6289-6301.

[44] M. Epple, K. Ganesan, R. Heumann, J. Klesing, A. Kovtun, S. Neumann, V. Sokolova, "Application of calcium phosphate nanoparticles in biomedicine", **Journal of Materials Chemistry 20** (2010) 18-23.

[45] B. Neuhaus, B. Tosun, O. Rotan, A. Frede, A. M. Westendorf, M. Epple, "Nanoparticles as transfection agents: a comprehensive study with ten different cell lines", **RSC Advances 6** (2016) 18102-18112.

[46] M. Kopp, O. Rotan, C. Papadopoulos, N. Schulze, H. Meyer, M. Epple, "Delivery of the autofluorescent protein R-phycoerythrin by calcium phosphate nanoparticles into four different eukaryotic cell lines (HeLa, HEK293T, MG-63, MC3T3): Highly efficient, but leading to endolysosomal proteolysis in HeLa and MC3T3 cells", **PLOS ONE 12** (2017) e0178260.

[47] X. Xu, Z. Li, X. Zhao, L. Keen, X. Kong, "Calcium phosphate nanoparticles-based systems for siRNA delivery", **Regenerative Biomaterials 3** (2016) 187-195.

[48] O. Rotan, K. N. Severin, S. Popsel, A. Peetsch, M. Merdanovic, M. Ehrmann, M. Epple, "Uptake of the proteins HTRA1 and HTRA2 by cells mediated by calcium phosphate nanoparticles", **Beilstein J Nanotechnol 8** (2017) 381-393.

[49] X. Cheng, L. Kuhn, "Chemotherapy drug delivery from calcium phosphate nanoparticles", **Int J Nanomedicine 2** (2007) 667-674.

[50] A. Frede, B. Neuhaus, R. Klopfleisch, C. Walker, J. Buer, W. Müller, M. Epple, A. M. Westendorf, "Colonic gene silencing using siRNA-loaded calcium phosphate/PLGA nanoparticles ameliorates intestinal inflammation in vivo", **Journal of Controlled Release 222** (2016) 86-96.

[51] T. Knuschke, W. Bayer, O. Rotan, V. Sokolova, M. Wadwa, C. J. Kirschning, W. Hansen, U. Dittmer, M. Epple, J. Buer, A. M. Westendorf, "Prophylactic and therapeutic vaccination with a nanoparticle-based peptide vaccine induces

efficient protective immunity during acute and chronic retroviral infection", **Nanomedicine : nanotechnology, biology, and medicine 10** (2014) 1787-1798.

[52] V. Sokolova, O. Rotan, J. Klesing, P. Nalbant, J. Buer, T. Knuschke, A. M. Westendorf, M. Epple, "Calcium phosphate nanoparticles as versatile carrier for small and large molecules across cell membranes", **Journal of Nanoparticle Research 14** (2012) 910.

[53] S. S. A. Abidi, Q. Murtaza, "Synthesis and Characterization of Nano-hydroxyapatite Powder Using Wet Chemical Precipitation Reaction", **Journal of Materials Science & Technology 30** (2014) 307-310.

[54] S. P. Mondejar, A. Kovtun, M. Epple, "Lanthanide-doped calcium phosphate nanoparticles with high internal crystallinity and with a shell of DNA as fluorescent probes in cell experiments", **Journal of Materials Chemistry 17** (2007) 4153-4159.

[55] E. V. Giger, B. Castagner, J. Raikkonen, J. Monkkonen, J. C. Leroux, "siRNA transfection with calcium phosphate nanoparticles stabilized with PEGylated chelators", **Adv Healthc Mater 2** (2013) 134-144.

[56] M. Junginger, K. Bleek, K. Kita-Tokarczyk, J. Reiche, A. Shkilnyy, F. Schacher, A. H. E. Muller, A. Taubert, "Calcium phosphate growth beneath a polycationic monolayer at the air-water interface: effects of oscillating surface pressure on mineralization", **Nanoscale 2** (2010) 2440-2446.

[57] M. Junginger, K. Kita-Tokarczyk, T. Schuster, J. Reiche, F. Schacher, A. H. E. Muller, H. Colfen, A. Taubert, "Calcium Phosphate Mineralization beneath a Polycationic Monolayer at the Air-Water Interface", **Macromol Biosci 10** (2010) 1084-1092.

[58] D. Kozlova, S. Chernousova, T. Knuschke, J. Buer, A. M. Westendorf, M. Epple, "Cell targeting by antibody-functionalized calcium phosphate nanoparticles", **Journal of Materials Chemistry 22** (2012) 396-404.

[59] W. Stöber, A. Fink, E. Bohn, "Controlled growth of monodisperse silica spheres in the micron size range", **Journal of Colloid and Interface Science 26** (1968) 62-69.

[60] G. Kolbe, " Das komplexchemische Verhalten der Kieselsäure", Dissertation, **University of Jena** (1956) 1-130.

[61] D. Kozlova. "Kovalent funktionalisierte Calciumphosphat-Nanopartikel zur selektiven Adressierung von Zellen", Dissertation, **Universität Duisburg-Essen** (2014) 1-220.

[62] V. P. Chauhan, T. Stylianopoulos, J. D. Martin, Z. Popovic, O. Chen, W. S. Kamoun, M. G. Bawendi, D. Fukumura, R. K. Jain, "Normalization of tumour blood vessels improves the delivery of nanomedicines in a size-dependent manner", **Nat Nano 7** (2012) 383-388.

[63] M. Zhao, H. Li, X. Bu, C. Lei, Q. Fang, Z. Hu, "Quantitative Proteomic Analysis of Cellular Resistance to the Nanoparticle Abraxane", **ACS Nano 9** (2015) 10099-10112.

[64] A. Magarkar, T. Róg, A. Bunker, "Molecular Dynamics Simulation of PEGylated Membranes with Cholesterol: Building Toward the DOXIL Formulation", **The Journal of Physical Chemistry C 118** (2014) 15541-15549.

[65] Y. Barenholz, "Doxil(R)--the first FDA-approved nano-drug: lessons learned", **Journal of controlled release : official journal of the Controlled Release Society 160** (2012) 117-134.

[66] P. Milla, F. Dosio, L. Cattel, "PEGylation of proteins and liposomes: a powerful and flexible strategy to improve the drug delivery", **Current drug metabolism 13** (2012) 105-119.

[67] A. A. Gabizon, "Pegylated liposomal doxorubicin: metamorphosis of an old drug into a new form of chemotherapy", **Cancer investigation 19** (2001) 424-436.

[68] E. C. Wang, A. Z. Wang, "Nanoparticles and their applications in cell and molecular biology", **Integrative Biology 6** (2014) 9-26.

[69] H. Jo, C. Ban, "Aptamer–nanoparticle complexes as powerful diagnostic and therapeutic tools", **Experimental & Molecular Medicine 48** (2016) e230.

[70] M. M. Cardoso, I. N. Peca, A. C. Roque, "Antibody-conjugated nanoparticles for therapeutic applications", **Current medicinal chemistry 19** (2012) 3103-3127.

[71] K. Ouadahi, E. Allard, B. Oberleitner, C. Larpent, "Synthesis of azide-functionalized nanoparticles by microemulsion polymerization and surface modification by click chemistry in aqueous medium", **Journal of Polymer Science Part A: Polymer Chemistry 50** (2012) 314-328.

[72] Z.-L. Song, Z. Chen, X. Bian, L.-Y. Zhou, D. Ding, H. Liang, Y.-X. Zou, S.-S. Wang, L. Chen, C. Yang, X.-B. Zhang, W. Tan, "Alkyne-Functionalized Superstable Graphitic Silver Nanoparticles for Raman Imaging", **Journal of the American Chemical Society 136** (2014) 13558-13561.

[73] N. A. Campbell, "Biology : concepts & connections", **Pearson Custom Pub.: New York 7th Edition** (2011) 1-779.

[74] A. Sorkin, M. von Zastrow, "Endocytosis and signalling: intertwining molecular networks", **Nat Rev Mol Cell Biol 10** (2009) 609-622.

[75] L. M. Traub, "Tickets to ride: selecting cargo for clathrin-regulated internalization", **Nat Rev Mol Cell Biol 10** (2009) 583-596.

[76] J. P. Lim, P. A. Gleeson, "Macropinocytosis: an endocytic pathway for internalising large gulps", **Immunology and cell biology 89** (2011) 836-843.

[77] B. D. Grant, J. G. Donaldson, "Pathways and mechanisms of endocytic recycling", **Nat Rev Mol Cell Biol 10** (2009) 597-608.

[78] T. Devarasu, R. Saad, A. Ouadi, B. Frisch, E. Robinet, P. Laquerriere, J.-C. Voegel, T. Baumert, J. Ogier, F. Meyer, "Potent calcium phosphate nanoparticle surface coating for in vitro and in vivo siRNA delivery: a step toward multifunctional nanovectors", **Journal of Materials Chemistry B 1** (2013) 4692-4700.

[79] S. Tenzer, D. Docter, J. Kuharev, A. Musyanovych, V. Fetz, R. Hecht, F. Schlenk, D. Fischer, K. Kiouptsi, C. Reinhardt, K. Landfester, H. Schild, M. Maskos, S. K. Knauer, R. H. Stauber, "Rapid formation of plasma protein corona critically affects nanoparticle pathophysiology", **Nature nanotechnology 8** (2013) 772-781.

[80] Y. Jin, Y. Song, X. Zhu, D. Zhou, C. Chen, Z. Zhang, Y. Huang, "Goblet cell-targeting nanoparticles for oral insulin delivery and the influence of mucus on insulin transport", **Biomaterials 33** (2012) 1573-1582.

[81] Z. Mao, X. Zhou, C. Gao, "Influence of structure and properties of colloidal biomaterials on cellular uptake and cell functions", **Biomaterials Science 1** (2013) 896-911.

[82] P. Saftig, J. Klumperman, "Lysosome biogenesis and lysosomal membrane proteins: trafficking meets function", **Nat Rev Mol Cell Biol 10** (2009) 623-635.

[83] G. Sahay, D. Y. Alakhova, A. V. Kabanov, "Endocytosis of nanomedicines", **Journal of Controlled Release : Official Journal of the Controlled Release Society 145** (2010) 182-195.

[84] G. Settanni, J. Zhou, T. Suo, S. Schottler, K. Landfester, F. Schmid, V. Mailander, "Protein corona composition of poly(ethylene glycol)- and poly(phosphoester)-coated nanoparticles correlates strongly with the amino acid composition of the protein surface", **Nanoscale 9** (2017) 2138-2144.

[85] M. Mahmoudi, S. E. Lohse, C. J. Murphy, A. Fathizadeh, A. Montazeri, K. S. Suslick, "Variation of protein corona composition of gold nanoparticles following plasmonic heating", **Nano Letters 14** (2014) 6-12.

[86] V. Mirshafiee, R. Kim, S. Park, M. Mahmoudi, M. L. Kraft, "Impact of protein pre-coating on the protein corona composition and nanoparticle cellular uptake", **Biomaterials 75** (2016) 295-304.

[87] Y. Grigoryev, "Principles and Mechanisms of Mammalian Cell Transfection", BitesieBio (2017) available online at http://bitesizebio.com/9288/principles-and-mechanisms-of-mammalian-cell-transfection/.(accessed 26.7.2017).

[88] B. Beckert, B. Masquida, "Synthesis of RNA by in vitro transcription", **Methods in Molecular Biology 703** (2011) 29-41.

[89] J. M. Berg, J. L. Tymoczko, L. Stryer, "Biochemistry", **New York: W H Freeman 7th Edition** (2002) 1-1198.

[90] R. K. Hartmann, A. Bindereif, A.Schön, E. Westhof, "Handbook of RNA Biochemistry", **Wiley-VCH Verlag GmbH & Co. 2nd Edition** (2014) 1-1314.

[91] A. D. Ellington, J. W. Szostak, "In vitro selection of RNA molecules that bind specific ligands", **Nature 346** (1990) 818-822.

[92] M. Darmostuk, S. Rimpelova, H. Gbelcova, T. Ruml, "Current approaches in SELEX: An update to aptamer selection technology", **Biotechnology advances 33** (2015) 1141-1161.

[93] R. Stoltenburg, C. Reinemann, B. Strehlitz, "SELEX--a (r)evolutionary method to generate high-affinity nucleic acid ligands", **Biomolecular engineering 24** (2007) 381-403.

[94] K. N. Kang, Y. S. Lee, "RNA aptamers: a review of recent trends and applications", **Advances in biochemical engineering/biotechnology 131** (2013) 153-169.

[95] B. C. Wengerter, J. A. Katakowski, J. M. Rosenberg, C. G. Park, S. C. Almo, D. Palliser, M. Levy, "Aptamer-targeted antigen delivery", **Molecular therapy : the journal of the American Society of Gene Therapy 22** (2014) 1375-1387.

[96] M. Blind, M. Blank, "Aptamer Selection Technology and Recent Advances", **Molecular Therapy. Nucleic Acids 4** (2015) e223.

[97] A. D. Keefe, S. Pai, A. Ellington, "Aptamers as therapeutics", **Nature reviews. Drug discovery 9** (2010) 537-550.

[98] H. Rehm, T. Letzel, "Der Experimentator: Proteinbiochemie/Proteomics", **Springer Berlin Heidelberg 7th Edition** (2016) 1-406.

[99] A. V. Lakhin, V. Z. Tarantul, L. V. Gening, "Aptamers: Problems, Solutions and Prospects", **Acta Naturae 5** (2013) 34-43.

[100] T.-H. Ku, T. Zhang, H. Luo, T. M. Yen, P.-W. Chen, Y. Han, Y.-H. Lo, "Nucleic Acid Aptamers: An Emerging Tool for Biotechnology and Biomedical Sensing", **Sensors (Basel, Switzerland) 15** (2015) 16281-16313.

[101] Z. Cao, R. Tong, A. Mishra, W. Xu, G. C. Wong, J. Cheng, Y. Lu, "Reversible cell-specific drug delivery with aptamer-functionalized liposomes", **Angew Chem Int Ed Engl 48** (2009) 6494-6498.

[102] C. S. Ferreira, M. C. Cheung, S. Missailidis, S. Bisland, J. Gariepy, "Phototoxic aptamers selectively enter and kill epithelial cancer cells", **Nucleic Acids Res 37** (2009) 866-876.

[103] S. D. Jayasena, "Aptamers: An emerging class of molecules that rival antibodies in diagnostics", **Clin Chem 45** (1999) 1628-1650.

[104] H. Sun, X. Zhu, P. Y. Lu, R. R. Rosato, W. Tan, Y. Zu, "Oligonucleotide aptamers: new tools for targeted cancer therapy", **Mol Ther Nucleic Acids 3** (2014) e182.

[105] P. Dua, S. Kim, D. K. Lee, "Patents on SELEX and therapeutic aptamers", **Recent patents on DNA & gene sequences 2** (2008) 172-186.

[106] R. L. Strack, S. R. Jaffrey, "Live-cell imaging of mammalian RNAs with Spinach2", **Methods Enzymol 550** (2015) 129-146.

[107] H. Huang, N. B Suslov, N.-S. Li, S. Shelke, M. Evans, Y. Koldobskaya, P. Rice, J. A Piccirilli, "A G-Quadruplex-Containing RNA Activates Fluorescence in a GFP-Like Fluorophore", **Nat Chem Biol 10** (2014) 686-691.

[108] W. Song, R. L. Strack, N. Svensen, S. R. Jaffrey, "Plug-and-play fluorophores extend the spectral properties of Spinach", **J Am Chem Soc 136** (2014) 1198-1201.

[109] L. Greenbaum, C. Rothmann, R. Lavie, Z. Malik, "Green fluorescent protein photobleaching: a model for protein damage by endogenous and exogenous singlet oxygen", **Biological chemistry 381** (2000) 1251-1258.

[110] K. Y. Han, B. J. Leslie, J. Fei, J. Zhang, T. Ha, "Understanding the Photophysics of the Spinach-DFHBI RNA Aptamer-Fluorogen Complex to Improve Live Cell RNA Imaging", **Journal of the American Chemical Society 135** (2013) 19033-19038.

[111] J. Zhang, J. Fei, B. J. Leslie, K. Y. Han, T. E. Kuhlman, T. Ha, "Tandem Spinach Array for mRNA Imaging in Living Bacterial Cells", **Scientific Reports 5** (2015) 17295.

[112] G. Pothoulakis, F. Ceroni, B. Reeve, T. Ellis, "The Spinach RNA Aptamer as a Characterization Tool for Synthetic Biology", **ACS Synthetic Biology 3** (2014) 182-187.

[113] N. Svensen, S. R. Jaffrey, "Fluorescent RNA Aptamers as a Tool to Study RNA-Modifying Enzymes", **Cell Chem Biol 23** (2016) 415-425.

[114] K. Y. Han, B. J. Leslie, J. Fei, J. Zhang, T. Ha, "Photophysical Properties of the Spinach-DFHBI RNA Aptamer-Fluorogen Complex and its Applications to Live Cell Imaging with Improved Fluorescence Signal", **Biophysical Journal 106** 486a-487a.

[115] M. Okuda, D. Fourmy, S. Yoshizawa, "Use of Baby Spinach and Broccoli for imaging of structured cellular RNAs", **Nucleic Acids Research 45** (2017) 1404-1415.

[116] G. S. Filonov, C. W. Kam, W. Song, S. R. Jaffrey, "In-gel imaging of RNA processing using Broccoli reveals optimal aptamer expression strategies", **Chemistry & biology 22** (2015) 649-660.

[117] G. S. Filonov, S. R. Jaffrey, "RNA Imaging with Dimeric Broccoli in Live Bacterial and Mammalian Cells", **Curr Protoc Chem Biol 8** (2016) 1-28.

[118] Nature.com, "Immune system", **Macmillan Publishers Limited** (2018) available online at https://www.nature.com/subjects/immune-system (accessed 01.07.2017 2017).

[119] Nature.com, "Innate immune cells", **Macmillan Publishers Limited** (2018) available online at https://www.nature.com/subjects/innate-immune-cells (accessed 01.07.2017).

[120] P. H. Raven, G. B. Johnson, "Biology", **McGraw-Hill Science/Engineering/Math; 6 edition** (2001) 1-1344.

[121] S. Liao, P.-Y. von der Weid, S. I. f. C. D. "Inflammation Research Network: Lymphatic System: An Active Pathway for Immune Protection", **Seminars in cell & developmental biology 38** (2015) 83-89.

[122] OERServices "Microbiology", **Lumencandela** (2018) available online at https://courses.lumenlearning.com/suny-microbiology/ (accessed 01.07.2017).

[123] J. Haller Hasskamp, J. L. Zapas, E. G. Elias, "Dendritic cell counts in the peripheral blood of healthy adults", **American journal of hematology 78** (2005) 314-315.

[124] M. Ciofani, J. C. Zuniga-Pflucker, "The thymus as an inductive site for T lymphopoiesis", **Annual review of cell and developmental biology 23** (2007) 463-493.

[125] R. E. Mebius, G. Kraal, "Structure and function of the spleen", **Nat Rev Immunol 5** (2005) 606-616.

[126] I. W. Lugton, "Mucosa-associated lymphoid tissues as sites for uptake, carriage and excretion of tubercle bacilli and other pathogenic mycobacteria", **Immunology and cell biology 77** (1999) 364-372.

[127] Nature.com, "Macrophages: Arteriogenic macrophages protect against ischaemia", **Nat Rev Immunol 11** (2011) 716-716.

[128] O. Leavy, "Immunotherapy: Stopping monocytes in their tracks", **Nat Rev Immunol 11** (2011) 715-715.

[129] D. Voehringer, "Protective and pathological roles of mast cells and basophils", **Nat Rev Immunol 13** (2013) 362-375.

[130] E. Kolaczkowska, P. Kubes, "Neutrophil recruitment and function in health and inflammation", **Nat Rev Immunol 13** (2013) 159-175.

[131] H. F. Rosenberg, K. D. Dyer, P. S. Foster, "Eosinophils: changing perspectives in health and disease", **Nat Rev Immunol 13** (2013) 9-22.

[132] H. Karasuyama, K. Mukai, Y. Tsujimura, K. Obata, "Newly discovered roles for basophils: a neglected minority gains new respect", **Nat Rev Immunol 9** (2009) 9-13.

[133] A. Erdei, M. Andrasfalvy, H. Peterfy, G. Toth, I. Pecht, "Regulation of mast cell activation by complement-derived peptides", **Immunology letters 92** (2004) 39-42.

[134] E. a. U. Vivier, S.: NK cells: receptors and functions. Nature, 2010; Vol. Poster.

[135] E. L. Fitzgerald, K. A. Fitzgerald: "Innate immunity: sensing and signalling", **Nature Reviews Immunology** (2017) online available at http://www.nature.com/nri/posters/innate/index.html (accessed 02.07.2017).

[136] S. L. Zhou, Z. J. Zhou, Z. Q. Hu, X. W. Huang, Z. Wang, E. B. Chen, J. Fan, Y. Cao, Z. Dai, J. Zhou, "Tumor-Associated Neutrophils Recruit Macrophages and T-Regulatory Cells to Promote Progression of Hepatocellular Carcinoma and Resistance to Sorafenib", **Gastroenterology 150** (2016) 1646-1658.e1617.

[137] L. Boiocchi, U. Gianelli, A. Iurlo, F. Fend, I. Bonzheim, D. Cattaneo, D. M. Knowles, A. Orazi, "Neutrophilic leukocytosis in advanced stage polycythemia vera: hematopathologic features and prognostic implications", **Mod Pathol 28** (2015) 1448-1457.

[138] J. R. Dunkelberger, W.-C. Song, "Complement and its role in innate and adaptive immune responses", **Cell Res 20** (2009) 34-50.

[139] Nature.com, "Humoral Immunity", **Macmillan Publishers Limited** (2018) available online at https://www.nature.com/subjects/humoral-immunity (accessed 01.07.2017).

[140] C. A. Janeway, P. Traves, M. Walport, "Immunobiology: The Immune System in Health and Disease", **Garland Science: New York 5th edition** (2001) .

[141] J. Parkin, B. Cohen, "An overview of the immune system", **Lancet (London, England) 357** (2001) 1777-1789.

[142] A. H. Lucas: Immunoglobulin Gene Construction: Human. In *eLS*; John Wiley & Sons, Ltd, 2001.

[143] Nature.com, "Adaptive immunity", **Macmillan Publishers Limited** (2017) available online at https://www.nature.com/subjects/adaptive-immunity (accessed 01.07.2017).

[144] B. K. Tischer, N. Osterrieder, "Herpesviruses - a zoonotic threat?", **Veterinary microbiology 140** (2010) 266.

[145] M. Schmid, T. Speiseder, T. Dobner, R. A. Gonzalez, "DNA Virus Replication Compartments", **Journal of Virology 88** (2014) 1404-1420.

[146] T. C. Mettenleiter, "Herpesvirus Assembly and Egress", **Journal of Virology 76** (2002) 1537-1547.

[147] Y. Wu, "The Role of the Cytomegalovirus Glycoprotein Complex gHgLgO in Virus Entry", Dissertation **Ludwig-Maximilians-Universität zu München** (2017) 1-107.

[148] M. Komuro, M. Tajima, K. Kato, "Transformation of Golgi membrane into the envelope of herpes simplex virus in rat anterior pituitary cells", **European journal of cell biology 50** (1989) 398-406.

[149] J. D. Baines, "Envelopment of herpes simplex virus nucleocapsids at the inner nuclear membrane", published in "Human Herpesviruses: Biology, Therapy, and Immunoprophylaxis", A. Arvin, G. Campadelli-Fiume, E. Mocarski, P. S. Moore, B. Roizman, R. Whitley, K. Yamanishi, Eds.: **Cambridge: Cambridge University Press**, (2007) Chapter 11. available online at https://www.ncbi.nlm.nih.gov/books/NBK47361/ (accessed 02.07.2017).

[150] B. Herbert, "Viral Keys for Molecular Locks" **HELIX** (2010) available online at https://helix.northwestern.edu/article/viral-keys-molecular-locks (accessed 21.05.2017).

[151] K. Grunewald, P. Desai, D. C. Winkler, J. B. Heymann, D. M. Belnap, W. Baumeister, A. C. Steven, "Three-dimensional structure of herpes simplex virus from cryo-electron tomography", **Science 302** (2003) 1396-1398.

[152] S. F. Modrow, Dietrich; Truyen, Uwe; Schätzl, Hermann *Molekulare Virologie*; Spektrum Akademischer Verlag Heidelberg 2010, 2010; Vol. 3. Auflage.

[153] A. Wald, L. Corey: Persistence in the population: epidemiology, transmission. In *Human Herpesviruses: Biology, Therapy, and Immunoprophylaxis*; A. Arvin, G. Campadelli-Fiume, E. Mocarski, P. S. Moore, B. Roizman, R. Whitley, K. Yamanishi, Eds.: Cambridge, 2007.

[154] "WHO updates fact sheet on Herpes Simplex Virus (31 January 2017)- Part 1: HSV-1", **Communitymedicine4asses** (2017) available online at https://communitymedicine4asses.wordpress.com/2017/02/02/who-updates-fact-sheet-on-herpes-simplex-virus-31-january-2017-part-1-hsv-1/ (accessed 21.05.2017 2017).

[155] G. B. Lowhagen, P. Tunback, T. Bergstrom, "Proportion of herpes simplex virus (HSV) type 1 and type 2 among genital and extragenital HSV isolates", **Acta Derm Venereol 82** (2002) 118-120.

[156] World Health Organization, "Herpes simplex virus" **WHO** (2017) available online at http://www.who.int/mediacentre/factsheets/fs400/en/ (accessed 17.05.2017 2017).

[157] The New Zealand Herpes Foundation " Herpes – the key facts" **NZHF** (2014) available online at https://www.herpes.org.nz/patient-info/key-facts/ (accessed 21.05.2017 2017).

[158] A. Krawczyk, M. Dirks, M. Kasper, A. Buch, U. Dittmer, B. Giebel, L. Wildschutz, M. Busch, A. Goergens, K. E. Schneweis, A. M. Eis-Hubinger, B. Sodeik, A. Heiligenhaus, M. Roggendorf, D. Bauer, "Prevention of herpes simplex virus induced stromal keratitis by a glycoprotein B-specific monoclonal antibody", **PLoS One 10** (2015) e0116800.

[159] A. Krawczyk, M. A. E. Arndt, L. Grosse-Hovest, W. Weichert, B. Giebel, U. Dittmer, H. Hengel, D. Jäger, K. E. Schneweis, A. M. Eis-Hübinger, M. Roggendorf, J. Krauss, "Overcoming drug-resistant herpes simplex virus (HSV)

infection by a humanized antibody", **Proceedings of the National Academy of Sciences of the United States of America 110** (2013) 6760-6765.

[160] F. Morfin, D. Thouvenot, "Herpes simplex virus resistance to antiviral drugs", **Journal of clinical virology : the official publication of the Pan American Society for Clinical Virology 26** (2003) 29-37.

[161] M. Bystricka, G. Russ, "Immunity in latent Herpes simplex virus infection", **Acta virologica 49** (2005) 159-167.

[162] K. Grünewald, "Herpesvirus in 3D", **Max-Planck-Institut für Biochemie/NIH** (2003) available online at https://www.mpg.de/680524/zoom-1293749866.jpeg (accessed 19.05.2017).

[163] A. Krawczyk, J. Krauss, A. M. Eis-Hubinger, M. P. Daumer, R. Schwarzenbacher, U. Dittmer, K. E. Schneweis, D. Jager, M. Roggendorf, M. A. Arndt, "Impact of valency of a glycoprotein B-specific monoclonal antibody on neutralization of herpes simplex virus", **J Virol 85** (2011) 1793-1803.

[164] N. E. Biolabs: NEBuilder ® HiFi DNA Assembly Master Mix/NEBuilder HiFi DNA Assembly Cloning Kit 2015; Vol. Version 1.2 12/15; pp 26.

[165] F. Li, Q. Zheng, L. E. Vandivier, M. R. Willmann, Y. Chen, B. D. Gregory, "Regulatory impact of RNA secondary structure across the Arabidopsis transcriptome", **The Plant cell 24** (2012) 4346-4359.

[166] A. R. Gruber, R. Lorenz, S. H. Bernhart, R. Neubock, I. L. Hofacker, "The Vienna RNA websuite", **Nucleic Acids Res 36** (2008) 70-74. online available at http://rna.tbi.univie.ac.at/cgi-bin/RNAWebSuite/RNAfold.cgi (accessed 05.07.2017).

[167] K. Romøren, B. J. Thu, N. C. Bols, Ø. Evensen, "Transfection efficiency and cytotoxicity of cationic liposomes in salmonid cell lines of hepatocyte and macrophage origin", **Biochimica et Biophysica Acta (BBA) - Biomembranes 1663** (2004) 127-134.

[168] S. Kuersten, E. B. Goodwin, "The power of the 3[prime] UTR: translational control and development", **Nat Rev Genet 4** (2003) 626-637.

[169] E. V. Koonin, "Does the central dogma still stand?", **Biology Direct 7** (2012) 27-27.

[170] E. V. Koonin, "Why the Central Dogma: on the nature of the great biological exclusion principle", **Biology Direct 10** (2015) 52.

[171] O. V. Stepanenko, O. V. Stepanenko, I. M. Kuznetsova, V. V. Verkhusha, K. K. Turoverov, "Beta-Barrel Scaffold of Fluorescent Proteins: Folding, Stability and Role in Chromophore Formation", **International review of cell and molecular biology 302** (2013) 221-278.

[172] K. Norrman, Y. Fischer, B. Bonnamy, F. Wolfhagen Sand, P. Ravassard, H. Semb, "Quantitative Comparison of Constitutive Promoters in Human ES cells", **PLoS ONE 5** (2010) e12413.

[173] C. Gealy, M. Denson, C. Humphreys, B. McSharry, G. Wilkinson, R. Caswell, "Posttranscriptional Suppression of Interleukin-6 Production by Human Cytomegalovirus", **Journal of Virology 79** (2005) 472-485.

[174] M. Avci-Adali, A. Behring, T. Keller, S. Krajewski, C. Schlensak, H. P. Wendel, "Optimized conditions for successful transfection of human endothelial cells with in vitro synthesized and modified mRNA for induction of protein expression", **Journal of Biological Engineering 8** (2014) 8-8.

[175] H.-y. Yang, L. A. Vonk, R. Licht, A. M. G. van Boxtel, J. E. J. Bekkers, A. H. M. Kragten, S. Hein, O. P. Varghese, K. A. Howard, F. Cumhur Öner, W. J. A. Dhert, L. B. Creemers, "Cell type and transfection reagent-dependent effects on viability, cell content, cell cycle and inflammation of RNAi in human primary mesenchymal cells", **European Journal of Pharmaceutical Sciences 53** (2014) 35-44.

[176] E. Figueroa, P. Bugga, V. Asthana, A. L. Chen, J. Stephen Yan, E. R. Evans, R. A. Drezek, "A mechanistic investigation exploring the differential transfection efficiencies between the easy-to-transfect SK-BR3 and difficult-to-transfect CT26 cell lines", **Journal of Nanobiotechnology 15** (2017) 36.

[177] T. N. Azher, X.-T. Yin, D. Tajfirouz, A. J. W. Huang, P. M. Stuart, "Herpes simplex keratitis: challenges in diagnosis and clinical management", **Clinical Ophthalmology 11** (2017) 185-191.

[178] A. Krawczyk, J. Krauss, A. M. Eis-Hübinger, M. P. Däumer, R. Schwarzenbacher, U. Dittmer, K. E. Schneweis, D. Jäger, M. Roggendorf, M. A. E. Arndt, "Impact of Valency of a Glycoprotein B-Specific Monoclonal Antibody on

Neutralization of Herpes Simplex Virus", **Journal of Virology 85** (2011) 1793-1803.

[179] R. E. Levitz, "Herpes simplex encephalitis: a review", **Heart & lung : the journal of critical care 27** (1998) 209-212.

[180] N. J. Anthis, G. M. Clore, "Sequence-specific determination of protein and peptide concentrations by absorbance at 205 nm", **Protein Science : A Publication of the Protein Society 22** (2013) 851-858.

[181] X. Wang, P. J. Quinn, "Endotoxins: lipopolysaccharides of gram-negative bacteria", **Sub-cellular biochemistry 53** (2010) 3-25.

[182] A. M. Sharifi, F. E. Hoda, A. M. Noor, "Studying the effect of LPS on cytotoxicity and apoptosis in PC12 neuronal cells: role of Bax, Bcl-2, and Caspase-3 protein expression", **Toxicology mechanisms and methods 20** (2010) 316-320.

[183] T. N. Ellis, M. J. Kuehn, "Virulence and Immunomodulatory Roles of Bacterial Outer Membrane Vesicles", **Microbiology and Molecular Biology Reviews : MMBR 74** (2010) 81-94.

[184] L. Hoareau, K. Bencharif, P. Rondeau, R. Murumalla, P. Ravanan, F. Tallet, P. Delarue, M. Cesari, R. Roche, F. Festy, "Signaling pathways involved in LPS induced TNFalpha production in human adipocytes", **Journal of Inflammation (London, England) 7** (2010) 1-1.

[185] Y.-C. Lu, W.-C. Yeh, P. S. Ohashi, "LPS/TLR4 signal transduction pathway", **Cytokine 42** (2008) 145-151.

[186] C. Vaure, Y. Liu, "A Comparative Review of Toll-Like Receptor 4 Expression and Functionality in Different Animal Species", **Frontiers in Immunology 5** (2014) 316.

[187] C. A. Janeway, Jr., R. Medzhitov, "Innate immune recognition", **Annu Rev Immunol 20** (2002) 197-216.

[188] K. L. Comstock, K. A. Krown, M. T. Page, D. Martin, P. Ho, M. Pedraza, E. N. Castro, N. Nakajima, C. C. Glembotski, P. J. Quintana, R. A. Sabbadini, "LPS-induced TNF-alpha release from and apoptosis in rat cardiomyocytes: obligatory role for CD14 in mediating the LPS response", **Journal of molecular and cellular cardiology 30** (1998) 2761-2775.

[189] J. Xaus, M. Comalada, A. F. Valledor, J. Lloberas, F. Lopez-Soriano, J. M. Argiles, C. Bogdan, A. Celada, "LPS induces apoptosis in macrophages mostly through the autocrine production of TNF-alpha", **Blood 95** (2000) 3823-3831.

[190] X. Qin, X. Jiang, X. Jiang, Y. Wang, Z. Miao, W. He, G. Yang, Z. Lv, Y. Yu, Y. Zheng, "Micheliolide inhibits LPS-induced inflammatory response and protects mice from LPS challenge", **Scientific Reports 6** (2016) 23240.

[191] R. Rylander, "Endotoxin in the environment--exposure and effects", **J Endotoxin Res 8** (2002) 241-252.

[192] M. O. Freire, T. E. Van Dyke, "Natural resolution of inflammation", **Periodontology 2000 63** (2013) 149-164.

[193] Y. Li, M. Fujita, D. Boraschi, "Endotoxin Contamination in Nanomaterials Leads to the Misinterpretation of Immunosafety Results", **Frontiers in Immunology 8** (2017) 472.

[194] S. Smulders, J.-P. Kaiser, S. Zuin, K. L. Van Landuyt, L. Golanski, J. Vanoirbeek, P. Wick, P. H. Hoet, "Contamination of nanoparticles by endotoxin: evaluation of different test methods", **Particle and Fibre Toxicology 9** (2012) 41.

[195] I. K. Gordonova, Z. K. Nikitina, V. A. Bykov, "Comparative study of Saccharomyces cerevisiae LPS", **Bulletin of experimental biology and medicine 134** (2002) 370-373.

[196] L. A. Brito, M. Singh, "COMMENTARY: Acceptable Levels of Endotoxin in Vaccine Formulations During Preclinical Research", **Journal of Pharmaceutical Sciences 100** 34-37.

[197] M. Kucki, C. Cavelius, A. Kraegeloh, "Endotoxin Case Study: Interference of Nanoparticles with the Traditional Limulus Amebocyte Lysate Gel Clot Assay" published in "Handbook of Immunological Properties of Engineered Nanomaterials" **Frontiers in Nanobiomedical Research 6** (2016) 187-206.

[198] Y. Li, D. Boraschi, "Endotoxin contamination: a key element in the interpretation of nanosafety studies", **Nanomedicine : nanotechnology, biology, and medicine 11** (2016) 269-287.

[199] S. Riebe, C. Vallet, F. van der Vight, D. Gonzalez-Abradelo, C. Wölper, C. A. Strassert, G. Jansen, S. Knauer, J. Voskuhl, "Aromatic Thioethers as Novel

Luminophores with Aggregation-Induced Fluorescence and Phosphorescence", **Chemistry – A European Journal 23** (2017) 13660-13668.

[200] N. G. Zhegalova, S. He, H. Zhou, D. M. Kim, M. Y. Berezin, "Minimization of self-quenching fluorescence on dyes conjugated to biomolecules with multiple labeling sites via asymmetrically charged NIR fluorophores", **Contrast media & molecular imaging 9** (2014) 355-362.

[201] "PEI transfection protocol", available online at http://www.dartmouth.edu/~tonyz/PEI.pdf (accessed 10.02 2018).

[202] O. Leavy, "New PAMP discovered", **Nature Reviews Immunology 15** (2015) 402.

[203] S. B. Mizel, J. T. Bates, "Flagellin as an Adjuvant: Cellular Mechanisms and Potential", **Journal of immunology 185** (2010) 5677-5682.

[204] W. Li, J. Yang, E. Zhang, M. Zhong, Y. Xiao, J. Yu, D. Zhou, Y. Cao, Y. Yang, Y. Li, H. Yan, "Activation of NLRC4 downregulates TLR5-mediated antibody immune responses against flagellin", **Cell Mol Immunol 13** (2016) 514-523.

[205] D. Kozlova, V. Sokolova, M. Zhong, E. Zhang, J. Yang, W. Li, Y. Yang, J. Buer, A. M. Westendorf, M. Epple, H. Yan, "Calcium phosphate nanoparticles show an effective activation of the innate immune response in vitro and in vivo after functionalization with flagellin", **Virologica Sinica 29** (2014) 33-39.

[206] A. Mendoza, J. A. Torres-Hernandez, J. G. Ault, J. H. Pedersen-Lane, D. Gao, D. A. Lawrence, "Silica nanoparticles induce oxidative stress and inflammation of human peripheral blood mononuclear cells", **Cell Stress & Chaperones 19** (2014) 777-790.

[207] J. P. Baker, "Mercury, Vaccines, and Autism: One Controversy, Three Histories", **American Journal of Public Health 98** (2008) 244-253.

[208] Q. He, A. R. Mitchell, S. L. Johnson, C. Wagner-Bartak, T. Morcol, S. J. D. Bell, "Calcium Phosphate Nanoparticle Adjuvant", **Clinical and Diagnostic Laboratory Immunology 7** (2000) 899-903.

[209] A. Kumar, J. Zhang, F.-S. X. Yu, "Toll-like receptor 3 agonist poly(I:C)-induced antiviral response in human corneal epithelial cells", **Immunology 117** (2006) 11-21.

[210] V. Kunzmann, E. Kretzschmar, T. Herrmann, M. Wilhelm, "Polyinosinic-polycytidylic acid-mediated stimulation of human γδ T cells via CD11c(+) dendritic cell-derived type I interferons", **Immunology 112** (2004) 369-377.

[211] K. Li, Z. Chen, N. Kato, M. Gale, Jr., S. M. Lemon, "Distinct poly(I-C) and virus-activated signaling pathways leading to interferon-beta production in hepatocytes", **J Biol Chem 280** (2005) 16739-16747.

[212] S. Trapp, N. R. Derby, R. Singer, A. Shaw, V. G. Williams, S. G. Turville, J. W. Bess, Jr., J. D. Lifson, M. Robbiani, "Double-stranded RNA analog poly(I:C) inhibits human immunodeficiency virus amplification in dendritic cells via type I interferon-mediated activation of APOBEC3G", **J Virol 83** (2009) 884-895.

[213] J. Wu, M. Lu, Z. Meng, M. Trippler, R. Broering, A. Szczeponek, F. Krux, U. Dittmer, M. Roggendorf, G. Gerken, J. F. Schlaak, "Toll-like receptor-mediated control of HBV replication by nonparenchymal liver cells in mice", **Hepatology (Baltimore, Md.) 46** (2007) 1769-1778.

[214] J. Wu, S. Huang, X. Zhao, M. Chen, Y. Lin, Y. Xia, C. Sun, X. Yang, J. Wang, Y. Guo, J. Song, E. Zhang, B. Wang, X. Zheng, J. F. Schlaak, M. Lu, D. Yang, "Poly(I:C) Treatment Leads to Interferon-Dependent Clearance of Hepatitis B Virus in a Hydrodynamic Injection Mouse Model", **Journal of Virology 88** (2014) 10421-10431.

[215] Y.-R. A. Yu, E. G. O'Koren, D. F. Hotten, M. J. Kan, D. Kopin, E. R. Nelson, L. Que, M. D. Gunn, "A Protocol for the Comprehensive Flow Cytometric Analysis of Immune Cells in Normal and Inflamed Murine Non-Lymphoid Tissues", **PLoS ONE 11** (2016) e0150606.

[216] C. Ruggiero, L. Pastorino, O. L. Herrera, "Nanotechnology based targeted drug delivery", **Conference proceedings : Annual International Conference of the IEEE Engineering in Medicine and Biology Society. IEEE Engineering in Medicine and Biology Society. Annual Conference 2010** (2010) 3731-3732.

[217] Systemic Administration of Clodronate Liposomes via Intravenous (IV) Injection. http://www.liposomes.org/2012/07/systemic-administration-of-clodronate.html.

[218] A. Schrage, C. Loddenkemper, U. Erben, U. Lauer, G. Hausdorf, P. R. Jungblut, J. Johnson, P. A. Knolle, M. Zeitz, A. Hamann, K. Klugewitz, "Murine CD146 is

widely expressed on endothelial cells and is recognized by the monoclonal antibody ME-9F1", **Histochemistry and Cell Biology 129** (2008) 441-451.

[219] R. Zaynagetdinov, T. P. Sherrill, P. L. Kendall, B. H. Segal, K. P. Weller, R. M. Tighe, T. S. Blackwell, "Identification of myeloid cell subsets in murine lungs using flow cytometry", **American journal of respiratory cell and molecular biology 49** (2013) 180-189.

[220] S. H. Park, W. C. Chen, N. Durmus, B. Bleck, J. Reibman, G. Riemekasten, G. Grunig, "The Effects of Antigen-Specific IgG1 Antibody for the Pulmonary-Hypertension-Phenotype and B Cells for Inflammation in Mice Exposed to Antigen and Fine Particles from Air Pollution", **PLoS One 10** (2015) e0129910.

[221] W. D. Geoghegan, C. A. Dawson, N. J. Calvanico, "The effect of IgG and IgG fragments on the absorption of inhaled antigens across the air-blood barrier of isolated perfused rabbit lungs", **Immunology 44** (1981) 331-337.

[222] P. Starlinger, P. Brugger, C. Reiter, D. Schauer, S. Sommerfeldt, D. Tamandl, I. Kuehrer, S. F. Schoppmann, M. Gnant, C. Brostjan, "Discrimination between Circulating Endothelial Cells and Blood Cell Populations with Overlapping Phenotype Reveals Distinct Regulation and Predictive Potential in Cancer Therapy", **Neoplasia (New York, N.Y.) 13** (2011) 980-990.

[223] H.-H. Lin, D. E. Faunce, M. Stacey, A. Terajewicz, T. Nakamura, J. Zhang-Hoover, M. Kerley, M. L. Mucenski, S. Gordon, J. Stein-Streilein, "The macrophage F4/80 receptor is required for the induction of antigen-specific efferent regulatory T cells in peripheral tolerance", **The Journal of Experimental Medicine 201** (2005) 1615-1625.

[224] C. Harrison, "Nanotechnology: Biological proteins knock nanoparticles off target", **Nature reviews. Drug discovery 12** (2013) 264-264.

[225] M. Burger, M. W. Hess, H. Cottier, "The role of 2-mercaptoethanol in the stimulation of spleen cell cultures: increased uptake of cystine into the TCA-soluble pool", **Immunology letters 4** (1982) 193-197.

[226] S. Wilhelm, A. J. Tavares, Q. Dai, S. Ohta, J. Audet, H. F. Dvorak, W. C. W. Chan, "Analysis of nanoparticle delivery to tumours", **Nature Reviews Materials 1** (2016) 16014.

[227] V. S. Sokolova, Z.; Huang, S.; Du, Y.; Kopp, M.; Frede, A.; Knuschke, T.; Buer, J.; Yang, D.; Wu, J.; Westendorf, A. M.; Epple, M., "Delivery of the TLR ligand

poly(I:C) to liver cells in vitro and in vivo by calcium phosphate nanoparticles leads to a pronounced immunostimulation", **Acta Biomaterialia 64** (2017) 401-410.

[228] J. Wu, Z. Meng, M. Jiang, E. Zhang, M. Trippler, R. Broering, A. Bucchi, F. Krux, U. Dittmer, D. Yang, M. Roggendorf, G. Gerken, M. Lu, J. F. Schlaak, "Toll-like receptor-induced innate immune responses in non-parenchymal liver cells are cell type-specific", **Immunology 129** (2010) 363-374.

[229] K. Haedicke, S. Gräfe, F. Lehmann, I. Hilger, "Multiplexed in vivo fluorescence optical imaging of the therapeutic efficacy of photodynamic therapy", **Biomaterials 34** (2013) 10075-10083.

[230] H. Yin, J. Yang, Q. Zhang, J. Yang, H. Wang, J. Xu, J. Zheng, "iRGD as a tumorpenetrating peptide for cancer therapy (Review)", **Molecular medicine reports 15** (2017) 2925-2930.

[231] K. N. Sugahara, G. B. Braun, T. H. de Mendoza, V. R. Kotamraju, R. P. French, A. M. Lowy, T. Teesalu, E. Ruoslahti, "Tumor-penetrating iRGD peptide inhibits metastasis", **Molecular cancer therapeutics 14** (2015) 120-128.

[232] C. D. Buckley, D. Pilling, N. V. Henriquez, G. Parsonage, K. Threlfall, D. Scheel-Toellner, D. L. Simmons, A. N. Akbar, J. M. Lord, M. Salmon, "RGD peptides induce apoptosis by direct caspase-3 activation", **Nature 397** (1999) 534-539.

[233] Medscape, "doxorubicin (Rx)" **Medscape** (2017) available online at http://reference.medscape.com/drug/doxorubicin-342120#showall (Accessed 05.07.2017)

[234] B. J. Cusack, S. P. Young, R. D. Olson, "Daunorubicin and daunorubicinol pharmacokinetics in plasma and tissues in the rat", **Cancer chemotherapy and pharmacology 35** (1995) 213-218.

[235] C. Metcalfe, P. Cresswell, A. N. Barclay, "Interleukin-2 signalling is modulated by a labile disulfide bond in the CD132 chain of its receptor", **Open Biology 2** (2012) 110036.

[236] Q.-H. Zhou, Y.-Z. You, C. Wu, Y. I. Huang, D. OupickÝ, "Cyclic RGD-targeting of reversibly-stabilized DNA nanoparticles enhances cell uptake and transfection in vitro", **Journal of drug targeting 17** (2009) 364-373.

[237] D. A. D'Argenio, C. B. Wilson, "A decade of vaccines: Integrating immunology and vaccinology for rational vaccine design", **Immunity 33** (2010) 437-440.

[238] K. Palucka, H. Ueno, J. Banchereau, "Recent developments in cancer vaccines", **J Immunol 186** (2011) 1325-1331.

[239] R. M. Steinman, J. Banchereau, "Taking dendritic cells into medicine", **Nature 449** (2007) 419-426.

[240] R. O. Dillman, "Cancer immunotherapy", **Cancer Biotherapy & Radiopharmaceuticals 26** (2011) 1-64.

[241] L. C. Bonifaz, D. P. Bonnyay, A. Charalambous, D. I. Darguste, S. Fujii, H. Soares, M. K. Brimnes, B. Moltedo, T. M. Moran, R. M. Steinman, "In vivo targeting of antigens to maturing dendritic cells via the DEC-205 receptor improves T cell vaccination", **J Exp Med 199** (2004) 815-824.

[242] A. C. Yan, M. Levy, "Aptamers and aptamer targeted delivery", **RNA biology 6** (2009) 316-320.

[243] M. A. Syed, S. Pervaiz, "Advances in aptamers", **Oligonucleotides 20** (2010) 215-224.

[244] R. Lorenz, S. H. Bernhart, C. Honer Zu Siederdissen, H. Tafer, C. Flamm, P. F. Stadler, I. L. Hofacker, "ViennaRNA Package 2.0", **Algorithms Mol Biol 6** (2011) 26.

[245] S. B. van der Meer, T. Knuschke, A. Frede, N. Schulze, A. M. Westendorf, M. Epple, "Avidin-conjugated calcium phosphate nanoparticles as a modular targeting system for the attachment of biotinylated molecules in vitro and in vivo", **Acta Biomaterialia** (2017).

[246] H. Fissan, S. Ristig, H. Kaminski, C. Asbach, M. Epple, "Comparison of different characterization methods for nanoparticle dispersions before and after aerosolization", **Analytical Methods 6** (2014) 7324-7334.

[247] S. Chernousova, M. Epple, "Live-cell imaging to compare the transfection and gene silencing efficiency of calcium phosphate nanoparticles and a liposomal transfection agent", **Gene Ther 24** (2017) 282-289.

[248] R. V. Flores, H. M. Sola, J. C. Torres, R. E. Torres, E. E. Guzman, "Effect of pH on the Heat-Induced Denaturation and Renaturation of Green Fluorescent Protein: A Laboratory Experiment", **J Chem Educ 90** (2013) 248-251.

[249] M. Kneen, J. Farinas, Y. Li, A. S. Verkman, "Green fluorescent protein as a noninvasive intracellular pH indicator", **Biophys J 74** (1998) 1591-1599.

[250] M. Perez-Neut, L. Haar, V. Rao, S. Santha, K. Lansu, B. Rana, W. K. Jones, S. Gentile, "Activation of hERG3 channel stimulates autophagy and promotes cellular senescence in melanoma", **Oncotarget 7** (2016) 21991-22004.

[251] P. C. Shivalingappa, R. Hole, C. V. Westphal, N. Vij, "Airway Exposure to E-Cigarette Vapors Impairs Autophagy and Induces Aggresome Formation", **Antioxid Redox Signal** (2015).

[252] N. Vij, P. Chandramani, C. V. Westphal, R. Hole, M. Bodas, "Cigarette smoke induced autophagy-impairment accelerates lung aging, COPD-emphysema exacerbations and pathogenesis", **Am J Physiol Cell Physiol** (2016) ajpcell 00110 02016.

[253] D. J. Klionsky, E. L. Eskelinen, V. Deretic, "Autophagosomes, phagosomes, autolysosomes, phagolysosomes, autophagolysosomes... wait, I'm confused", **Autophagy 10** (2014) 549-551.

[254] M. Sato, T. Ozawa, K. Inukai, T. Asano, Y. Umezawa, "Fluorescent indicators for imaging protein phosphorylation in single living cells", **Nature biotechnology 20** (2002) 287-294.

[255] Sino Biological, "HRV 3C Protease Human Rhinovirus 3C Protease, PreScission Site" **Sino Biological Inc.** (2017) available online at http://www.sinobiological.com/HRV-3C-Protease-(Human-Rhinovirus-3C-Protease,-PreScission-Site)_ps3cp01.html (accessed 06.06.2017).

[256] T. Nakagawa, T. Kurose, T. Hino, K. Tanaka, M. Kawamukai, Y. Niwa, K. Toyooka, K. Matsuoka, T. Jinbo, T. Kimura, "Development of series of gateway binary vectors, pGWBs, for realizing efficient construction of fusion genes for plant transformation", **J Biosci Bioeng 104** (2007) 34-41.

[257] N. C. Shaner, R. E. Campbell, P. A. Steinbach, B. N. G. Giepmans, A. E. Palmer, R. Y. Tsien, "Improved monomeric red, orange and yellow fluorescent proteins derived from Discosoma sp. red fluorescent protein", **Nat Biotech 22** (2004) 1567-1572.

[258] R. Y. Tsien, "The green fluorescent protein", **Annu Rev Biochem 67** (1998) 509-544.

[259] E. Gasteiger, C. Hoogland, A. Gattiker, S. Duvaud, M. R. Wilkins, R. D. Appel, A. Bairoch, "Protein Identification and Analysis Tools on the ExPASy Server" published in J.M. Walker "The Proteomics Protocols Handbook" **Humana Press** (2005) 571-607.

[260] B. Yameen, W. I. Choi, C. Vilos, A. Swami, J. Shi, O. C. Farokhzad, "Insight into nanoparticle cellular uptake and intracellular targeting", **Journal of controlled release : official journal of the Controlled Release Society 190** (2014) 485-499.

[261] D. A. Dean, B. S. Dean, S. Muller, L. C. Smith, "Sequence requirements for plasmid nuclear import", **Exp Cell Res 253** (1999) 713-722.

[262] H. Youn, J.-K. Chung, "Modified mRNA as an alternative to plasmid DNA (pDNA) for transcript replacement and vaccination therapy", **Expert Opinion on Biological Therapy 15** (2015) 1337-1348.

[263] J. Zhou, J. Lin, C. Zhou, X. Deng, B. Xia, "Cytotoxicity of red fluorescent protein DsRed is associated with the suppression of Bcl-xL translation", **FEBS letters 585** (2011) 821-827.

[264] H. S. Bernhardt, W. P. Tate, "Primordial soup or vinaigrette: did the RNA world evolve at acidic pH?", **Biol Direct 7** (2012) 4.

[265] X. Wu, G. Brewer, "The regulation of mRNA stability in mammalian cells: 2.0", **Gene 500** (2012) 10-21.

[266] H. Li, T. Lee, T. Dziubla, F. Pi, S. Guo, J. Xu, C. Li, F. Haque, X.-J. Liang, P. Guo, "RNA as a stable polymer to build controllable and defined nanostructures for material and biomedical applications", **Nano Today 10** (2015) 631-655.

[267] O. Rotan, K. N. Severin, S. Pöpsel, A. Peetsch, M. Merdanovic, M. Ehrmann, M. Epple, "Uptake of the proteins HTRA1 and HTRA2 by cells mediated by calcium phosphate nanoparticles", **Beilstein Journal of Nanotechnology 8** (2017) 381-393.

[268] U. Maivali, A. Paier, T. Tenson, "When stable RNA becomes unstable: the degradation of ribosomes in bacteria and beyond", **Biological chemistry 394** (2013) 845-855.

[269] A. Fu, R. Tang, J. Hardie, M. E. Farkas, V. M. Rotello, "Promises and pitfalls of intracellular delivery of proteins", **Bioconjug Chem 25** (2014) 1602-1608.

[270] L. H. Estrada, S. Chu, J. A. Champion, "Protein nanoparticles for intracellular delivery of therapeutic enzymes", **J Pharm Sci 103** (2014) 1863-1871.

[271] J. N. Barry, A. A. Vertegel, "Nanomaterials for Protein Mediated Therapy and Delivery", **Nano Life 3** (2013).

[272] R. Ficner, R. Huber, "Refined crystal structure of phycoerythrin from Porphyridium cruentum at 0.23-nm resolution and localization of the gamma subunit", **Eur J Biochem 218** (1993) 103-106.

[273] X. S. Fu, L.; Yang, G; Lu,W.; Zhao, M.;Gong, X., "The subunits analysis of R-phycoerythrin from marine red algae by isoelectric focusing", **10** (2011).

[274] R. MacColl, D. Guard-Friar, T. J. Ryan, "Biliprotein light-harvesting strategies, phycoerythrin 566", **Biochemistry 29** (1990) 430-435.

[275] C. Huang, D. S. Berns, R. MacColl, "Kinetics of allophycocyanin's trimer-monomer equilibrium", **Biochemistry 26** (1987) 243-245.

[276] A. N. Glazer, C. S. Hixson, "Characterization of R-phycocyanin. Chromophore content of R-phycocyanin and C-phycoerythrin", **J Biol Chem 250** (1975) 5487-5495.

[277] K. Csatorday, R. MacColl, D. Guard-Friar, C. A. Hanzlik, "Excitation energy transfer between sensitizing chromophores of phycocyanin 612", **Photochemistry and photobiology 45** (1987) 845-848.

[278] K. Csatorday, D. Guard-Friar, R. MacColl, D. S. Berns, "The development of exciton migration routes for phycocyanin 645 and allophycocyanin", **Photochemistry and photobiology 47** (1988) 285-291.

[279] W. G.-C. Huang Bei, Zeng Chen-Kui, and Li Zhen-gang., "The Experimental Research of R-Phycoerythrin Subunits on Cancer Treatment: A New Photosensitizer in PDT", **Cancer Biotherapy and Radiopharmaceuticals 17** (2004) 8.

[280] H. Tan, S. Gao, Y. Zhuang, Y. Dong, W. Guan, K. Zhang, J. Xu, J. Cui, "R-Phycoerythrin Induces SGC-7901 Apoptosis by Arresting Cell Cycle at S Phase", **Marine Drugs 14** (2016) 166.

[281] Q. Pan, M. Chen, J. Li, Y. Wu, C. Zhen, B. Liang, "Antitumor function and mechanism of phycoerythrin from Porphyra haitanensis", **Biological research 46** (2013) 87-95.

[282] T. Mayr, M. Bayer, "Fluorophores.org Database of Fluorecent Dyes, Properties and Applications", **Technical University of Graz** (2017) available online at . http://www.fluorophores.tugraz.at/substance/320 (accessed 16.07.2017).

[283] H. Urch, M. Vallet-Regi, L. Ruiz, J. M. Gonzalez-Calbet, M. Epple, "Calcium phosphate nanoparticles with adjustable dispersability and crystallinity", **Journal of Materials Chemistry 19** (2009) 2166-2171.

[284] A. Fu, R. Tang, J. Hardie, M. E. Farkas, V. M. Rotello, "Promises and Pitfalls of Intracellular Delivery of Proteins", **Bioconjugate Chemistry 25** (2014) 1602-1608.

[285] P. Ghosh, X. Yang, R. Arvizo, Z. J. Zhu, S. S. Agasti, Z. Mo, V. M. Rotello, "Intracellular delivery of a membrane-impermeable enzyme in active form using functionalized gold nanoparticles", **J Am Chem Soc 132** (2010) 2642-2645.

[286] S. Neumann, A. Kovtun, I. D. Dietzel, M. Epple, R. Heumann, "The use of size-defined DNA-functionalized calcium phosphate nanoparticles to minimise intracellular calcium disturbance during transfection", **Biomaterials 30** (2009) 6794-6802.

[287] D. E. Clapham, "Calcium Signaling", **Cell 131** 1047-1058.

[288] S. Orrenius, P. Nicotera, "The calcium ion and cell death", **Journal of neural transmission. Supplementum 43** (1994) 1-11.

[289] G. Ermak, K. J. A. Davies, "Calcium and oxidative stress: from cell signaling to cell death", **Molecular Immunology 38** (2002) 713-721.

[290] V. Sokolova, T. Knuschke, J. Buer, A. M. Westendorf, M. Epple, "Quantitative determination of the composition of multi-shell calcium phosphate-oligonucleotide nanoparticles and their application for the activation of dendritic cells", **Acta Biomaterialia 7** (2011) 4029-4036.

[291] V. Kafil, Y. Omidi, "Cytotoxic Impacts of Linear and Branched Polyethylenimine Nanostructures in A431 Cells", **BioImpacts : BI 1** (2011) 23-30.

[292] W. T. Godbey, K. K. Wu, A. G. Mikos, "Size matters: molecular weight affects the efficiency of poly(ethylenimine) as a gene delivery vehicle", **J Biomed Mater Res 45** (1999) 268-275.

[293] V. Sokolova, D. Kozlova, T. Knuschke, J. Buer, A. M. Westendorf, M. Epple, "Mechanism of the uptake of cationic and anionic calcium phosphate nanoparticles by cells", **Acta biomaterialia 9** (2013) 7527-7535.

[294] J. J. Jung, S. M. Inamdar, A. Tiwari, A. Choudhury, "Regulation of intracellular membrane trafficking and cell dynamics by syntaxin-6", **Bioscience reports 32** (2012) 383-391.

[295] A. Heinrichs, "Membrane trafficking: Earliest endosomes", **Nat Rev Mol Cell Biol 10** (2009) 302-302.

[296] N. Hasan, D. Corbin, C. Hu, "Fusogenic Pairings of Vesicle-Associated Membrane Proteins (VAMPs) and Plasma Membrane t-SNAREs – VAMP5 as the Exception", **PLOS ONE 5** (2010) e14238.

[297] J. Huotari, A. Helenius, "Endosome maturation", **EMBO J 30** (2011) 3481-3500.

[298] T. Yoshimori, A. Yamamoto, Y. Moriyama, M. Futai, Y. Tashiro, "Bafilomycin A1, a specific inhibitor of vacuolar-type H(+)-ATPase, inhibits acidification and protein degradation in lysosomes of cultured cells", **J Biol Chem 266** (1991) 17707-17712.

[299] O. C. Farokhzad, R. Langer, "Impact of nanotechnology on drug delivery", **ACS Nano 3** (2009) 16-20.

[300] K. Riehemann, S. W. Schneider, T. A. Luger, B. Godin, M. Ferrari, H. Fuchs, "Nanomedicine--challenge and perspectives", **Angew Chem Int Ed Engl 48** (2009) 872-897.

[301] J. M. Silva, M. Videira, R. Gaspar, V. Preat, H. F. Florindo, "Immune system targeting by biodegradable nanoparticles for cancer vaccines", **Journal of controlled release : official journal of the Controlled Release Society 168** (2013) 179-199.

[302] A. E. Gregory, R. Titball, D. Williamson, "Vaccine delivery using nanoparticles", **Frontiers in cellular and infection microbiology 3** (2013) 13.

[303] R. Mathaes, G. Winter, A. Besheer, J. Engert, "Non-spherical micro- and nanoparticles: fabrication, characterization and drug delivery applications", **Expert opinion on drug delivery 12** (2015) 481-492.

[304] D. E. Kozlova, M., "Biological targeting with nanoparticles: state of the art", **BioNanoMaterials. 14** (2013) 161-170.

[305] N. A. Alhakamy, A. S. Nigatu, C. J. Berkland, J. D. Ramsey, "Noncovalently associated -penetrating peptides for gene delivery applications", **Therapeutic delivery 4** (2013) 741-757.

[306] L. D. Cervia, C.-C. Chang, L. Wang, F. Yuan, "Distinct effects of endosomal escape and inhibition of endosomal trafficking on gene delivery via electrotransfection", **PLoS ONE 12** (2017) e0171699.

[307] R. V. Benjaminsen, M. A. Mattebjerg, J. R. Henriksen, S. M. Moghimi, T. L. Andresen, "The Possible “Proton Sponge ” Effect of Polyethylenimine (PEI) Does Not Include Change in Lysosomal pH", **Molecular Therapy 21** (2013) 149-157.

[308] A. Akinc, M. Thomas, A. M. Klibanov, R. Langer, "Exploring polyethylenimine-mediated DNA transfection and the proton sponge hypothesis", **The journal of gene medicine 7** (2005) 657-663.

[309] W. Liang, J. K. W. Lam, "Endosomal Escape Pathways for Non-Viral Nucleic Acid Delivery Systems" published in B. Ceresa, "Molecular Regulation of Endocytosis" **InTech: Rijeka** (2012) Ch. 17.

[310] K. A. Curtis, D. Miller, P. Millard, S. Basu, F. Horkay, P. L. Chandran, "Unusual Salt and pH Induced Changes in Polyethylenimine Solutions", **PLOS ONE 11** (2016) e0158147.

[311] M. Jovic, M. Sharma, J. Rahajeng, S. Caplan, "The early endosome: a busy sorting station for proteins at the crossroads", **Histol Histopathol 25** (2010) 99-112.

[312] R. C. Krieg, C. P. Paweletz, L. A. Liotta, E. F. Petricoin, 3rd, "Clinical proteomics for cancer biomarker discovery and therapeutic targeting", **Technology in cancer research & treatment 1** (2002) 263-272.

[313] L. N. Liu, H. N. Su, S. G. Yan, S. M. Shao, B. B. Xie, X. L. Chen, X. Y. Zhang, B. C. Zhou, Y. Z. Zhang, "Probing the pH sensitivity of R-phycoerythrin: investigations of active conformational and functional variation", **Biochimica et biophysica acta 1787** (2009) 939-946.

[314] J. A. Mindell, "Lysosomal acidification mechanisms", **Annual review of physiology 74** (2012) 69-86.

[315] A. E. Ewence, M. Bootman, H. L. Roderick, J. N. Skepper, G. McCarthy, M. Epple, M. Neumann, C. M. Shanahan, D. Proudfoot, "Calcium phosphate crystals induce cell death in human vascular smooth muscle cells: a potential mechanism in atherosclerotic plaque destabilization", **Circulation research 103** (2008) e28-34.

[316] Z. Liu, Y. Xiao, W. Chen, Y. Wang, B. Wang, G. Wang, X. Xu, R. Tang, "Calcium phosphate nanoparticles primarily induce cell necrosis through lysosomal rupture: the origination of material cytotoxicity", **Journal of Materials Chemistry B 2** (2014) 3480-3489.

[317] J. Vacik, B. S. Dean, W. E. Zimmer, D. A. Dean, "Cell-specific nuclear import of plasmid DNA", **Gene therapy 6** (1999) 1006-1014.

[318] J. S. Wadia, R. V. Stan, S. F. Dowdy, "Transducible TAT-HA fusogenic peptide enhances escape of TAT-fusion proteins after lipid raft macropinocytosis", **Nature medicine 10** (2004) 310-315.

[319] B. M. Tissue "Ultraviolet and Visible Absorption Spectroscopy" published in "Characterization of Materials" **John Wiley & Sons, Inc**. 2nd Edition (2002) 1-13.

[320] S. Bhat, N. Curach, T. Mostyn, G. S. Bains, K. R. Griffiths, K. R. Emslie, "Comparison of Methods for Accurate Quantification of DNA Mass Concentration with Traceability to the International System of Units", **Analytical Chemistry 82** (2010) 7185-7192.

[321] M. Hesse, H. Meier, B. Zeeh "Spektroskopische Methoden in der organischen Chemie", **Georg Thieme Verlag: Stuttgart 7th Edition** (2005) 1-468.

[322] F. E. Lottspeich, Joachim W., "Bioanalytik", **Springer Spektrum 3 ed.** (2012) 1-1208.

[323] B. Welz, M. Sperling: "The Techniques of Atomic Absorption Spectrometry", published in Atomic Absorption Spectrometry", **Wiley-VCH Verlag GmbH Third Edition** (2007) 335-475.

[324] Y. Engelborghs, Antonie J.W.G. Visser,: "Fluorescence Spectroscopy and Microscopy", **Humana Press 1 ed.** (2014).

[325] J. R. Albani "Principles and Applications of Fluorescence Spectroscopy", **Blackwell Publishing Ltd**, (2007) 1-264.

[326] J. R. Lakowicz "Principles of Fluorescence Spectroscopy", **Springer US** 3rd Edtion (2006) 1-954.

[327] B. Riedel, "Effizienzsteigerung in organischen Leuchtdioden", **KIT Scientific Publishing** (2011).

[328] A. Bogner, P. H. Jouneau, G. Thollet, D. Basset, C. Gauthier, "A history of scanning electron microscopy developments: Towards "wet-STEM" imaging", **Micron 38** (2007) 390-401.

[329] S. A. Mohanty, M.; Al-Askalany, A.; Radamson H., H.: Scanning Electron Microscope. **Royal Institute of Technology, Stockholm**, (2015) available online at https://www.slideshare.net/Askalany/scanning-electron-microscope-49091382 (accessed 23.04.2017).

[330] C. A. Schneider, W. S. Rasband, K. W. Eliceiri, "NIH Image to ImageJ: 25 years of image analysis", **Nature methods 9** (2012) 671-675, available online at https://imagej.nih.gov/ij/. (accessed 24.04.2017)

[331] P. A. Hassan, S. Rana, G. Verma, "Making Sense of Brownian Motion: Colloid Characterization by Dynamic Light Scattering", **Langmuir 31** (2015) 3-12.

[332] Malvern-Instruments, "Zetasizer NanoSeries User Manual", **Malvern-Instruments**

MAN0317 (2003) 1-270 online available at http://www.biophysics.bioc.cam.ac.uk/files/Zetasizer_Nano_user_manual_Man0317-1.1.pdf (accessed 04.02.2017)

[333] M. Hassellov, J. W. Readman, J. F. Ranville, K. Tiede, "Nanoparticle analysis and characterization methodologies in environmental risk assessment of engineered nanoparticles", **Ecotoxicology (London, England) 17** (2008) 344-361.

[334] D. Mahl, J. Diendorf, W. Meyer-Zaika, M. Epple, "Possibilities and limitations of different analytical methods for the size determination of a bimodal dispersion of metallic nanoparticles", **Colloids and Surfaces A: Physicochemical and Engineering Aspects 377** (2011) 386-392.

[335] B. N. Khlebtsov, N. G. Khlebtsov, "On the measurement of gold nanoparticle sizes by the dynamic light scattering method", **Colloid Journal 73** (2011) 118-127.

[336] L. Rittié, B. Perbal, "Enzymes used in molecular biology: a useful guide", **Journal of Cell Communication and Signaling 2** (2008) 25-45.

[337] M. V. Berridge, Tan, A. S., McCoy, K. D. & Wang, R, "The Biochemical and Cellular Basis of Cell Proliferation Assays That Use Tetrazolium Salts", **Biochemica** (1996).

[338] T. Mosmann, "Rapid Colorimetric Assay for Cellular Growth and Survival - Application to Proliferation and Cyto-Toxicity Assays", **J Immunol Methods 65** (1983) 55-63.

[339] M. V. Berridge, A. S. Tan, "Characterization of the cellular reduction of 3-(4,5-dimethylthiazol-2-yl)-2,5-diphenyltetrazolium bromide (MTT): subcellular localization, substrate dependence, and involvement of mitochondrial electron transport in MTT reduction", **Archives of biochemistry and biophysics 303** (1993) 474-482.

[340] M. Popenda, M. Szachniuk, M. Antczak, K. J. Purzycka, P. Lukasiak, N. Bartol, J. Blazewicz, R. W. Adamiak, "Automated 3D structure composition for large RNAs", **Nucleic Acids Research 40** (2012) e112-e112.

[341] K. J. Purzycka, M. Popenda, M. Szachniuk, M. Antczak, P. Lukasiak, J. Blazewicz, R. W. Adamiak, "Chapter One - Automated 3D RNA Structure Prediction Using the RNAComposer Method for Riboswitches" published in "Methods in Enzymology" **Academic Press 553** (2015) 3-34.

[342] M. Biesiada, K.J. Purzycka, M. Szachniuk, J. Blazewicz, R.W. Adamiak, "Automated RNA 3D structure prediction with RNAComposer" pubplished in "RNA Structure Determination: Methods and Protocols" **Springer Protocols 1st Edition** (2016) 199-215.

[343] Hyglos creative bioscience solutions, "EndoGrade® Endotoxin-freies Wasser", **Hyglos GmbH - a bioMérieux company** (2017) online available at http://www.hyglos.de/de/produkte-services/produkte/endotoxinfreie-reagenzien/endograder-endotoxin-freies-wasser.html (accessed 01.06.2017).

[344] R. G. Taylor, D. C. Walker, R. R. McInnes, "E. coli host strains significantly affect the quality of small scale plasmid DNA preparations used for sequencing", **Nucleic Acids Res 21** (1993) 1677-1678.

[345] J. Davison, "Genetic exchange between bacteria in the environment", **Plasmid 42** (1999) 73-91.

[346] M. Kopp, S. Kollenda, M. Epple, "Nanoparticle-protein interactions: Therapeutic approaches and supramolecular chemistry", **Acc**ounts of **Chem**ical **Res**earch **50** (2017) 1383-1390.

[347] J. Xie, S. Lee, X. Chen, "Nanoparticle-based theranostic agents", **Advanced drug delivery reviews 62** (2010) 1064-1079.

[348] Thermo Fisher Scientific Nanodrop Products, "Interpretation of Nucleic Acid 260/280 Ratios ", **Technical Bulletin NanoDrop Lite T123 Rev1** (2012) 1 available online at https://tools.thermofisher.com/content/sfs/brochures/T123-NanoDrop-Lite-Interpretation-of-Nucleic-Acid-260-280-Ratios.pdf (accessed 26.02.2018)

7 Annex

7.1 Abbreviations

2D	two-dimensional
3D	three-dimensional
AAS	atomic absorption spectroscopy
ACV	acyclovir
AIEL	aggregation inducible emitting luminescence
Apt.	aptamer
ATP	adenosine triphosphosphate
BafA1	bafilomycin A1
***Bam*HI**	restriction enzyme from *Bacillus amyloliquefaciens*
bp	base pair
CaP	calcium phosphate
CD146	cluster of differentiation 146 also known as melanoma cell adhesion molecule
CD4+T	T helper cells
CD8+T	T killer cells
ch.	chapter
CLRs	C-type lectin receptors
CLSM	confocal laser scanning microscopy
CMC	carboxymethyl cellulose
cPCR	colony Polymerase Chain Reaction
CpG^{m}	class B CpG oligonucleotide - Murine TLR9 ligand; 20mer:5'- t*c*c*a*t*g*a*c*g*t*t*c*c*t*g*a*c*g*t*t-3' (*phosphothioate backbone)
CTP	cytidine triphosphosphate
DAI	DNA-dependent activator of IRFs receptors
dBroccoli	dimeric Broccoli
DC	dendritic cells
DEC205	C-type lectin receptor
DFHBI	3,5-difluoro-4-hydroxybenzylidene imidazoline
DLS	differential light scattering
DMEM	Dulbecco´s Minimal Essential Medium
DNA	deoxyribonucleic acid
DOX	doxorubicin
DPBS	Dulbecco´s phosphate buffered saline
***Dpn*I**	restriction enzyme from *Diplococcus pneumoniae*
dsDNA	double stranded DNA
E. coli	*Escherichia coli*
EF-H_2O	endotoxin-free water
EtBr	ethidium bromide
EtOH	ethanol
F4/80	EGF-like module-containing mucin-like hormone receptor-like 1 EMR also known as F4/80
FB2	RNA aptamer consisting of F30-dBroccoli-F30-dBroccoli-F30 (F30-2xdBroccoli)

FBc36	RNA aptamer consisting of F30-dBroccoli-F30-c36-F30
FBmin.2	RNA aptamer consisting of F30-dBroccoli-F30-min.2-F30
FCV	famciclovir
Fwd	forward
GFP	green fluorescent protein
GOI	gene of interest
GST	glutathione S transferase
GTP	guanosine triphosphate
HAP	hydroxyapatite
HEK293T	human epidermal kidney cells
HeLa	Henrietta Lacks cervix carcinoma
***Hind*III**	restriction enzyme from *Haemophilus influenzae*
HSV-1	Herpes Simplex Virus Type 1
IgG1	immunoglobin G1
IgG2	immunoglobin G2
IgA	immunoglobin A
IgD	immunoglobin D
IgE	immunoglobin E
IgM	immunoglobin M
IgW	immunoglobin W
IgY	immunoglobin Y
i.m.	intramuscularly
***i*-PrOH**	propan-2-ol
IPTG	isopropyl β-D-1-thiogalactopyranoside
IVT	*in vitro* transcription
kb	kilo base pair
KC	Kupffer cells
kDa	kilo Dalton (1 Da = 1 g mol^{-1})
KLD	kinase-ligase-*Dpn*I
KMUH	*N*-[κ-maleimidoundecanoic acid] hydrazide, trifluoroacetic acid salt
LAL	limulus amoebocyte lysate assay
LB	lysogeny broth
LSEC	liver sinusoidal endothelial cells
MALT	mucosa-associated lymphoid tissues
MASPs	MBL-associated serine proteases
MBL	mannose-binding lectin
MC3T3	mouse osteoblastic preosteoblasts from the calvaria
MFE	minimum free energy
MG-63	human osteosarcoma cells
MHC	major histocompatibility complex
MHSC	multipotential haematopoietic stem cell
min	minute
min.2	minimised anti-DEC205 aptamer
MREL	maximum recommended endotoxin level
mRNA	messenger RNA
MTT	2-(4,5-dimethylthiazol-2-yl)-3,5-diphenyl-2*H*-tetrazol-3-ium bromide
MWCO	molecular weight cut off

MW	Molecular weight
n.d.	no data
NEAA	non-essential amino acids
NEB	New England Biolabs
NF-H_2O	nuclease-free water
NK	natural killer
NPC	non-parenchymal cells
NPs	nanoparticles
nt	nucleotide
nts	nucleotides
NTPs	nucleoside triphosphate
overnight	over night
PAMP	pathogen-associated molecular patterns
pBr	plasmid pcDNA3.3-F31-2xdBroccoli
PBS	phosphate buffered saline
pChBr	plasmid pcDNA3.3-mCherry-F31-2xdBroccoli
PCR	polymerase chain reaction
pΔBr	plasmid pcDNA3.3-F31-2xdBroccoli ΔUTRs
pΔChBr	plasmid pcDNA3.3-mCherry-F31-2xdBroccoli ΔUTRs
PEI	polyethene imine
pFB2	plasmid pET28c-F30-2xdBroccoli
pFBc36	plasmid pUC19i-F30-dBroccoli-c36
pFBmin.2	plasmid pUC19i-F30-dBroccoli-min.2
PRRs	pattern-recognition receptors
PSD	particle size distribution
pUCS	pUC19i-spinach-min-wt-tLys
Rev	reverse
RF-H_2O	RNase-free water
RLRs	RIG-I-like dependent activator of IRFs receptors
RNA	ribonucleic acid
R-PE	R-phycoerythrin
rpm	rounds per minute
r.t.	room temperature
RT-PCR	real-time polymerase chain reaction
s	seconds
SELEX	systematic evolution of ligands by exponential enrichment
SEM	scanning electron microscopy
SPDP	succinimidyl 3-(2-pyridyldithio)-propionate
Sulfo-SMCC	sulfo-succinimidyl 4-(N-maleimidomethyl)cyclohexane-1-carboxylate
TCID	tissue culture infective dose.
TLR4	toll-like receptor 4
TLRs	toll-like receptors
U	unit
UTP	uridine triphosphate
UTR	untranslated region
VCV	valacyclovir
w/o	without

***Xho*I**	restriction enzyme from *Xanthomonas holcicola*

7.2 Chemicals and laboratory devices

Table 7.1: Overview of the used chemicals.

Chemicals	Manufacturer	Purity
Diammonium hydrogenphosphate	Fluka, Merck, VWR	p.a.
TEOS	Sigma Aldrich	98%
Ethanol, absolute	Fisher Scientific	p.a.
KMUH	Thermo Fisher	97%
Calcium nitrate tetra hydrate	Fluka, Merck, VWR	≥99%
Calcium lactate penta hydrate	VWR, Fluka	99%
MPS	Sigma Aldrich	95%
Sulfo-SMCC	Merck Co KG	90%
SPDP	Thermo Fisher	99%
Ammonia solution	Carl Roth	30-33%
Ultrapure water	ELGA	n.d.
APTES	Sigma Aldrich	99%

Table 7.2: Laboratory devices.

Device and manufacturer	Model
Bench Thermo Scientific	MSC Advantage
Centrifuge ThermoFisher scientific	Hereaus Fresco 21
Centrifuge ThermoFisher scientific	Multifuge XR1
Dynamic Light Scattering Malvern	Zetasizer Nano ZS
FACS Becton Dickinson	FACS LSR II
FACS Becton Dickinson	FACS Aria II
Fluorescence microscope Keyence	BZ9000
Fluorescence microscope Zeiss	Axiovert 40 CFL
Lyophilisator Christ	Alpha 2-4 LSC
Multi-Plate Reader Multiscan FC	ThermoFisher
Scanning electron microscope FEI	Quanta 400 FEG
Ultrapure water purification system Elga	Purelab Ultra Bioscience
Ultrasonic sonotrodes Hielscher	UP50 H
Ultracentrifuge Thermo Scientific	SORVALL WX Ultra Series
Ultracentrifuge Rotor 70 Ti rotor	Beckman&Coulter
UV-Vis-Spectrophotometer Thermo Fisher Scientific	NanoDrop2000c
UV-Vis-Spectrophotometer Varian	Cary 300 Bio
PCR device Eppendorf	MasterCycler Nexus
SDS-PAGE Biorad	Mini-PROTEAN Tetra cel
Agarose gel electrophoresis chamber PEQLab	PerfectBlue

7.3 Bacterial strains

Strain	Chromosomal Genotype
E. coli DH5 alpha[344]	*fhuA2 lac(del)U169 phoA glnV44 Φ80' Δ(lacZ)*M15 *gyrA96 recA1 relA1 endA1 thi-1 hsdR17*
E. coli XL1 Blue	*recA1 endA1 gyrA96 thi-1 hsdR17 supE44 relA1 lac* [F´ *proAB lacI*^{q} *ZΔM15* Tn *10* (Tet ^{r})].
E. coli BL21 (DE3)	B F^{-} *dcm*$^{+}$ *ompT hsdS*($r_B^- m_B^-$) *gal* λ (DE3)

7.4 Enzymes and Kits

Purification Kits were purchased from Macherey and Nagel (Macherey&Nagel, Düren, Germany). All cloning or IVT involved enzymes were purchased either from Life Technologies (Thermo Fisher Scientific, Waltham, USA) or New England Biolabs (NEB, Ipswich, USA).

7.4.1 Chimeric aptamers

Aptamer	RNA sequence
FB2	UUG CCA UGU GUA UGU GGG AGA CGG UCG GGU CCA UCU GAG ACG GUC GGG UCC AGA UAU UCG UAU CUG UCG AGU AGA GUG UGG GCU CAG AUG UCG AGU AGA GUG UGG GCU CCC ACA UAC UCU GAU GAU CCA GAC GGU CGG GUC CAU CUG AGA CGG UCG GGU CCA GAU AUU CGU AUC UGU CGA GUA GAG UGU GGG CUC AGA UGU CGA GUA GAG UGU GGG CUG GAU CAU UCA UGG CAA
FBmin.2	UUG CCA UGU GUA UGU GGG AGA CGG UCG GGU CCA UCU GAG ACG GUC GGG UCC AGA UAU UCG UAU CUG UCG AGU AGA GUG UGG GCU CAG AUG UCG AGU AGA GUG UGG GCU CCC ACA UAC UCU GAU GAU CCG GGA GGU GUG UUA GCA CAC GAU UCA UAA UCA GCU ACC CUC CCG GAU CAU UCA UGG CAA
FBc36	UUG CCA UGU GUA UGU GGG AGA CGG UCG GGU CCA UCU GAG ACG GUC GGG UCC AGA UAU UCG UAU CUG UCG AGU AGA GUG UGG GCU CAG AUG UCG AGU AGA GUG UGG GCU CCC ACA UAC UCU GAU GAU CCG GCG UAG UGA UUA UGA AUC GUG UGC UAA UAC ACG CCG GAU CAU UCA UGG CAA

7.5 Primer list

Primers were purchased from Microsynth AG (Balgach,Switzerland).

Name	5'->3'
2xdBroccoli_Fwd	AGT GAA CCG TCA GAT CGC CTG GGT TGC CAT GTG TAT GTG
2xdBroccoli_Rev	ATT CTG TCT TTT TAT TGC CGC TTG CCA TGA ATG ATC CAG
Amplicon1Fwd	GAC CAT GAT TAC GCC AAG CTT AGA TCT CGA TCC CGC GAA
Amplicon1Rev	TGA TTA TGA ATC GTG TGC TAA CAC ACC TC
Amplicon2Fwd	GCA CAC GAT TCA TAA TCA GCT ACC CTC CC
Amplicon2Rev	AGC TCG GTA CCC GGG GAT CCT GGT GGT GCT CGA GCA AA
c36_IVT_Rev	GG CGT GTA TTA GCA CAC G
F30_endRev	TGG TGG TGC TCG AGC AAA AA
F30_Rev_PCRTempl.	TTG CCA TGA ATG ATC CGG
F30-endFwd	TTC ATA ATC AGC TAC CCT CCC GGA TCA TTC ATG GCA AGC TAG C
F30endIVT_Rev	TTG CCA TGA ATG ATC CAG CCC AC
F30min2F30fwd	ACA TAC TCT GAT GAT CCG GGA GGT GTG TTA GCA CAC GAT TCA TAA TCA GCT ACC CTC CCG GAT CAT TCA TGG CAA GC
F30min2F30rev	GCT TGC CAT GAA TGA TCC GGG AGG GTA GCT GAT TAT GAA TCG TGT GCT AAC ACA CC TCC CGG ATC ATC AGA GTA TGT
F312xdBrCrtlFwd	TAA GAA GAA ATA TAA GAG CCA CCT TGG CGT AGC TAC CAT GTG
F312xdBrCrtlRev	GCC CCG CAG AAG GCA GCT TAT TGG CGT AGC TAC CAT GAA TG
F312xdBroccoliFwd	GTA CAA GTA ATT GGC GTA GCT ACC ATG TG
F312xdBroccoliRev	GCC CCG CAG AAG GCA GCT TAC TTG GCG TAG CTA CCA TG
F31-Fwd	TTG GCG TAG CTA CCA TGT GTA TGT GGG AGA
F31-Rev	CTT GGC GTA GCT ACC ATG AAT GAT CCA GCC C
mCherry_BamHI_Rev	CGG GCC CCG GAT CCT TAC TTG TAC AGC TCG TCC ATG
mCherry_Fwd	GAA ATA TAA GAG CCA CCA TGG TGA GCA AGG GCG AGG AG
mCherry_NheI_Fwd	AGT AAG AAG AAA TAT AAG AGC CAC CGC TAG CAT GGT GAG CAA GGG CGAG
mCherry_Rev	GCC CCG CAG AAG GCA GCT TAT TAC TTG TACA GCT CGT CCA TG
mcherryFwd	TAA GAA GAA ATA TAA GAG CCA CCA TGG TGA GCA AGG GCG AG
mcherryRev	GCT ACG CCA ATT ACT TGT ACA GCT CGT CCA TG
min.2_IVT_Rev	GGG AGG GTA GCT GAT TAT G
mRFP_Fwd	GAA ATA TAA GAG CCA CCA TGG CCT TCT CCG AGG ACG TCA TCA AGG AG
mRFP_Rev	GCC CCG CAG AAG GCA GCT TAG GCG CCG GTG GAG TGG CG
pcDNA3.3_Fwd	CGG CAA TAA AAA GAC AGA ATA AAA C
pcDNA3.3_Rev	AGG CGA TCT GAC GGT TCA C
pcDNA3.3c62GFPRev	CAT GGT GGC TCT TAT ATT TCT TCT TAC TC
pcDNA3.3eGFP_Rev	GGT GGC TCT TAT ATT TCT TCT TAC TCT TC
pcDNA3.3eGFPFwd	TAA GCT GCC TTC TGC GG G
pcDNAGFP_NheI_Rev	GCT AGC GGT GGC TCT TAT ATT TCT TCT TAC TCT TC
pcDNAGFP_XhoI_Fwd	CTC GAG TAA GCT GCC TTC TGC GGG
pET28cF302xdBrFwd	GGA TCA TTC ATG GCA AGC
pET28cF302xdBrRev	GGA TCA TCA GAG TAT GTG G
pGEX6P1_emGFP_fwd_neu	GTG AGC AAG GGC GAG GAG
PrimerF30min.2Fwd	ACA TAC TCT GAT GAT CCG

PrimerF30min.2Rev	GCT TGC CAT GAA TGA TCC
pUC19iSpinachtlysIVT_fwd	AGA TCT CGA TCC CGC GAA ATT AAT ACG AC
Q5SDM_2016822_Fwd	CGG AGT AAG AGA GAA AAG AAG AGT AAG
Q5SDM_2016822_Rev	CGA TTG TGA GTC GTA TTA GCT TC
Q5SDM_2xdB_Fwd	CGG AGG TTG CCA TGT GTA TGT GG
Q5SDM_2xdB_Rev	CGA TTG TGA GTC GTA TTA ATT TCGC
Q5SDM_pUC19c62Fwd	CGG AGG GGC CCG GAT AGC TCA G
Q5SDM_pUC19c62Rev	CGA TTG TGA GTC GTA TTA ATT TCG CGG G
QC_c36_Fwd	CGT GTG CTA ATA CAC GCC GGA TCA TTC ATG GCA AGC
QC_c36_Rev	ATT CAT AAT CAC TAC GCC GGA TCA TCA GAG TAT GTG
Seq_CMVFwd	CGC AAA TGG GCG GTA GGC GTG
Seq_TKpA_Rev	TTG TCT CCT TCC GTG TTT CA
SeqGSTend_fwd	TGG CGA CCA TCC TCC AAA ATC G
T7_c36_04Fwd	GCT ATG ACC ATG ATT ACG CCT CTA GAC GAT CCC GCG AA
T7_c36_04Rev	AGC TCG GTA CCC GGG GAT CCT CGA GGC GTG TAT TAG CAC ACG
T7_IVT_polyA	TTT TTT TTT TTT TTT TTT TTT TTT TTT TTT TTT TTT TTT TTT TTT TTT TTT TTT TTT TTT TTT TTT TTT TTT TTT TTT TTT TTT TTT TTT TTT TTT TTT TTT TTT TTT TTT TTT TTT TTT CTT CCT ACT CAG GCT TTA TTC AAA GAC CA
T7_Prom_Fwd	TAA TAC GAC TCA CTA TAG GGT TGC CAT GTG TAT G
T7F30_min.2Fwd	AGA TCT CGA TCC CGC GAA
T7F30_min.2Rev	TCG TGT GCT AAC ACA CCT CCC GGA TCA TCA GAG TAT GTG GGA G
T7-IVT_rev	TGG TCT TTG AAT AAA GCC TGA GTA GGA AG
T7-IVTFwd	TTG GAC CCT CGT ACA GAA GCT AAT ACG
tandem_Fwd	GAA ATA TAA GAG CCA CCA TGG CCT TCT CCG AGG ACG TC
tandem_Rev	GCC CCG CAG AAG GCA GCT TAC TTG TAC AGC TCG TCC ATG C
tlysIVT_Rev	TGG CGC CCG AAC AGG GAC TT

7.6 Publications

Peer-reviewed Publications

M. Kopp, S. Kollenda, M. Epple, "Nanoparticle-protein interactions: Therapeutic approaches and supramolecular chemistry", **Acc**ounts of **Chem**ical **Res**earch **50** (2017) 1383-1390.

M. Kopp, O. Rotan, C. Papadopoulos, N. Schulze, H. Meyer, M. Epple, "Delivery of the autofluorescent protein R-phycoerythrin by calcium phosphate nanoparticles into four different eukaryotic cell lines (HeLa, HEK293T, MG-63, MC3T3): Highly efficient, but leading to endolysosomal proteolysis in HeLa and MC3T3 cells", **PLoS ONE 12** (2017) e0178260.

Other Publications

M. Nitschke, O. Rotan, K. Severin, S. Pöpsel, M. Ehrmann, M. Epple, "Calcium phosphate nanoparticles as delivery system for proteins across the cell membrane of living cells", **BioNanoMaterials 16** (2015) 90.

V. Sokolova, Z. Shi, S. Huang, Y. Duc, M. Kopp, A. Frede, T. Knuschke, J. Buer, D. Yang, J. Wu, A.M. Westendorf, M. Epple, "Delivery of the TLR ligand poly(I:C) to liver cells in vitro and in vivo by calcium phosphate nanoparticles leads to a pronounced immunostimulation", **Acta Biomaterialia 64** (2017) 401-410.

Contributions to Conferences

Jahrestagung der Deutschen Gesellschaft für Biomaterialien, Freiburg i. Br., 12-14.11.2015, M. Nitschke, O. Rotan, K. Severin, S. Pöpsel, M. Ehrmann, M. Epple, "Calcium phosphate nanoparticles as delivery system for proteins across the cell membrane of living cells" (**V/P**)

IMB Conference "Gene Regulation by the Numbers: Quantitative Approaches to Study Transcription", Mainz, 19.-21.06.2017, M. Kopp, M. Epple, "Time-resolved trafficking of 2xdBroccoli aptamer-labelled mRNA in eukaryotic cells by calcium phosphate nanoparticle transfection" (**P**)

CRC 1093 Evaluation, 11.-12.07.2017, T. Ruks, S. van der Meer, M. Kopp, S. Kollenda, V. Sokolova, M. Epple, "Ultrasmall nanoparticles for protein-specific targeting" (**P**)

CRC1093 International Symposium on Supramolecular Chemistry on Proteins, Essen, 20.-21.09.2017, M. Kopp, M. Epple, "Nanoparticle-mediated transport of an aptamer-labelled mRNA enables time-resolved trafficking of transcription and translation in eukaryotic cells" (**P**)

Aptamers in Bordeaux, Bordeaux, Frankreich, 22.-23.09.2017, M. Kopp, M. Epple, "About cherries and broccolies – Simultaneous monitoring of transcription and translation by calcium phosphate nanoparticle transfection" (**P**)

TRR60 International Symposium - New approaches to prevent or cure chronic viral infections, Essen, Deutschland, 6-8.11.2017, V. Sokolova, Z. Shi, S. Huang, Y. Du, M. Kopp, A. Frede, T. Knuschke, J. Buer, D. Yang, J. Wu, A. M. Westendorf and M. Epple "Delivery of the TLR ligand poly(I:C) *in vitro* and *in vivo* by calcium phosphate nanoparticles" (**P**)

7.7 Statutory declaration

I hereby declare that the presented thesis with the following title:

„Biofunctionalisation of calcium phosphate nanoparticles for biomedical and molecular biology applications“

is my own work and independently written, I further declare that I neither used the help of a second individual nor other helping materials than listed in the references.

I also declare that this thesis is being presented for the first time and it has never been submitted in any other possible way to other chemical faculties.

Essen, 2nd March

Mathis Kopp

7.8 Curriculum vitae

Der Lebenslauf ist in der Online-Version aus Gründen des Datenschutzes nicht enthalten.

8 Danksagung

Zuerst möchte ich mich an dieser Stelle ganz herzlich bei Herrn Prof. Dr. rer. nat. Matthias Epple für die äußerst interessante und interdisziplinäre Aufgabenstellung bedanken. Ich fühlte mich jederzeit sehr gut betreut und in meiner Arbeit unterstützt. Während der gesamten Bearbeitungszeit meines Promotionsthemas konnte ich durch sein mir entgegengebrachtes Vertrauen eigene Ideen verfolgen und umsetzen. Darüber hinaus bin für die Möglichkeit dankbar, meine resultierenden Forschungsergebnisse auf (inter-)nationalen Konferenzen präsentieren zu dürfen und so aktiv am internationalen Forschungsgeschehen teilnehmen zu können. Ferner möchte ich erwähnen, dass mir die vielen Auslandsaufenthalte und die Austauschmöglichkeiten durch die Kooperationen mit chinesischen und deutschen Kollegen neue Erfahrungen innerhalb verschiedener Forschungsthemen brachten, die ich gewinnbringend nutzen konnte.

Ich bedanke mich ganz herzlich bei Frau Prof. Dr. rer. nat. Shirley Knauer für die Begutachtung der Dissertation als Zweitgutachterin.
In diesem Zusammenhang möchte ich besonders für die Mitbenutzung ihres Labors Danke sagen. Ohne das dortige Photometer wäre eine schnelle Quantifizierung der vielen Proben unmöglich gewesen.

Herrn Prof. Dr. rer. nat. Hemmo Meyer danke ich für die zur Verfügungstellung seines zell- und molekularbiologischen Labors. Nur mithilfe des PCR Cycler und einem eigenen Gefrierfach konnten die vielen Plasmide und die Aptamere das Licht der Welt erblicken.

Ganz herzlich möchte ich mich bei den wissenschaftlichen Mitarbeitern, Herrn Dr. rer. nat. Christoph Papadopoulos und Frau Dr. rer. nat. Nina Schulze für die gute Zusammenarbeit während der zahllos erforderlichen Experimente zur Erstellung meiner ersten Publikation bedanken.

Herrn Prof. Dr. rer. nat. Hans Peter Wendel der Universitätsklinikum Tübingen danke ich für die Zusendung des sequenzierten Plasmids pcDNA3.3eGFP und polyA^{+}-eGFP-

mRNA und Herrn Dr. rer. nat. Sven Hennig vom CGC Dortmund danke ich für die Zusendung des DFHBI Moleküls sowie den Vektor für Spinach, welcher Ausgang meiner Klonierungsarbeiten war.

Herrn Dr. rer. nat. Krawczyk und Herrn Ulrich Aufderhorst danke ich für die förderliche Zusammenarbeit während meiner Promotion.

Herrn Dr. rer. nat. Jens Nelsen danke für ein stets offenes Ohr und den guten kollegialen Austausch.

Frau Dr. rer. nat. Sabrina Daumann und Karolin Wey teilten sich mit mir während der Promotion das Labor. Für die gemeinsame Zeit in einer netten und kollegialen Atmosphäre, sowie den anregenden Gesprächen, möchte ich mich herzlich bei ihnen bedanken.

Des Weiteren möchte ich mich bei Frau Prof. Dr. rer. nat. Astrid Westendorf und ihrem Team, insbesondere bei Herrn Dr. rer. nat. Torben Knuschke und Frau Dr. rer. nat. Annika Frede für ihr Engagement und die Übernahme der FACS Messungen der Aptamer-Nanopartikel bedanken.

Auch möchte ich mich bei Herrn Sebastian Kollenda für die gute kollegiale Zusammenarbeit bedanken, gemeinsam konnten wir das Thema „Aptamere“ weiter fokussieren und voranbringen.

Frau Jasmin Wens danke ich für ihre stets motivierte Mitarbeit sowie für die guten Ergebnisse im Rahmen ihres Praxissemesters und Bachelorarbeit.

Ein Dankschön möchte ich auch an Kerstin Brauner und Robin Meya richten, sie übernahmen die zuverlässige Bestimmung des Calciumgehaltes meiner Proben.

Bei Dr. rer. nat. Kateryna Loza und Herrn Dipl. Ing. Smail Boukercha bedanke ich mich für die Erstellung der REM-Bilder.

Carola Fischer, Sabine Kiefer und Sabine Bollmann möchte ich ganz herzlich für ihre uneingeschränkte Unterstützung bei allen administrativen Angelegenheiten danken.

Zudem möchte ich mich bei allen ehemaligen und aktuellen Mitarbeitern des AK Epple für die gute Kooperation im Laboralltag als auch die vielfältigen und interessanten Diskussionen während der Kaffeepausen bedanken.

Ein ganz besonderes Dankeschön und daher zuletzt genannt, gilt meiner lieben Frau Elena und unserer ganzen Familie, die mir in dieser Zeit sehr viel Verständnis entgegenbrachten und stets den „Rücken freihielten“. Ich bin dankbar für ihre bedingungslose und stetige Unterstützung, aufmunternden und auffordernden Worte in schwierigen Phasen meiner Promotion.

Vielen herzlichen Dank!